PhD. Thesis

Active Galactic Nuclei Obscuration at the Peak of the Super Massive Black Hole Growth

(超大質量ブラックホール成長の最盛期における
活動銀河中心核の遮蔽)

Bovornpratch Vijarnwannaluk

A Thesis Presented for the Degree of
Doctor of Philosophy

Astronomical Institute
Tohoku University
Japan
September 2023

Acknowledgment

This small piece of work is the result of my cumulative effort over the past 5 years at Tohoku University. While the majority of my work was done by myself, this thesis would never be complete without the support of my family and my community both in Japan and Thailand. Here, I would like to acknowledge their contribution to this work. I apologize in advance if I had left out anyone.

First and foremost important, I would like to thank my family for their unwavering support during my time in Japan. I thank my parents for always allowing their selfish son to pursue a subject of virtually no real-life value and supporting me both financially and emotionally. It is difficult to quantify their support into value but without them, I would have not been able to achieve anything meaningful.

Second, I would like to thank Professor Masayuki Akiyama, my advisor, for the opportunity to pursue an education in astronomy and astrophysics. I apologize if I were (and I believe I was) a difficult student. Yet, Akiyama-san has always been consistently kind and understanding. Without Akiyama-san's tutelage, I would never have completed my post-graduate education.

The true unsung heroes of myself and my fellow students are the post-doctoral research staff in and outside the astronomical institute. While the senior staff provide insight and experience, the post-doc member provided the technical know-how and the most up-to-date discussion. I would like to thank Dr. Koki Terao, Dr. Jose Manuel Perez Martinez, and Dr. Mitsuru Kokubo. Special recognition goes to Assoc. Prof Kohei Ichikawa, who I consider a second advisor, I thank you for the valuable career advice, academic discussion, as well as continued support throughout the years.

The astronomical institute of Tohoku University is a wonderful education and research environment thanks to the effort of the department staff members. I would like to express my thanks to the staff of the institute, especially to Prof. Tadayuki Kodama, Prof. Masashi Chiba, Assoc. Prof. Masaomi Tanaka, and Assoc. Prof. Kengo Tomida who been a positive impact on my graduate studies and has kept me interested in studying astronomy and astrophysics. A special thanks to Nozomi Okamoto, who has supported me and international students in our everyday lives.

Research is hard and sometimes downright depressing. During the hard times, I always had my fellow students to relax with. Hence, I would express my sincere thanks to my fellow students who have always been there for me and for their great tolerance against the mischief and chaos that I cook up regularly. A special thanks to Hajime Ogane, my fellow Ph.D. graduate who has assisted me with the various administrative procedures over the past 5 years.

Lastly, I would like to thank the Japanese government for providing the MEXT scholarship. MEXT has been a beacon of hope for third-world students such as myself in our pursuit of higher education. Without the financial support from MEXT, none of this would have been possible.

Contents

Chapter 1

Introduction

1.1 An Overview of an Active Galactic Nuclei

Active Galaxies are a sub-class of galaxies whose central supermassive black hole is in a phase of active accretion growth, commonly known as active galactic nuclei (AGN). Our current understanding of AGN suggests that they are powered by the accretion of gas onto the supermassive black hole (SMBH) which resides in the nuclear regions of a galaxy. Typical SMBH has a mass larger than $\log M_{\rm BH}/M_{\odot} > 6$ and their existence is now well accepted due to their detection in several galaxies in the local universe including the Milky Way (Genzel et al., 1997; Ghez et al., 1998). It is also well believed that every massive galaxy, those with stellar masses exceeding $\log M_{*}/M_{\odot} > 9$, contains a SMBH in the nucleus.

AGNs are considered the most luminous persistent source of emission in the universe. In cases of luminous quasars, their luminosity can completely outshine the integrated luminosity of a whole galaxy. The source of the luminous emission comes from the ongoing accretion activity through an accretion disk and onto the SMBH which is emitting as a blue optical/UV continuum. Besides the massive luminosity output from the accretion activity, AGN emission is also panchromatic, spanning over 10 decades of frequency from gamma rays to radio emission. The current understanding of the panchromatic nature of AGN is that each emission (eg. optical, X-ray, and so on) comes from different components in the AGN structure. The spectral energy distribution of AGN is further complicated through obscuration[1] by dust and gas which can hide most of the typical AGN signatures detected in the optical/infrared.

AGN activity is a short phenomenon when compared to the typical time scales of galaxies. Comparison between the number density of galaxies and AGN would show that galaxies typically outnumber AGN by a factor of 100-10,000 depending on luminosity and redshift. This put constraints on the typical lifetime of the AGN phase to be only a few hundred megayears compared to the gigayear time scales in galaxies. Although this is only a few percent of a galaxy's life cycle, it has been suggested that the AGN phase is a key component in regulating the star-formation activity in galaxies through outflows driven by their immense luminosity. Evidence of massive AGN-driven outflows has already been found in samples of luminous AGN. In addition, observations of massive black holes in the local universe show strong correlations with the host galaxy. These observations suggest that the build-up of stellar mass and black hole mass may occur simultaneously (Often coined as co-evolution). AGN which are de facto SMBH which are actively growing mass represent an ideal laboratory to investigate the co-evolution while it is occurring. So while AGN are small in numbers, they are still an integral component in the theories of galaxy evolution which cannot be neglected.

1.2 Cosmological Evolution of AGN

X-ray datasets provide several advantages for statistical AGN studies. First, X-ray emission is a ubiquitous tracer of AGN activity. X-ray emission is produced in the coronal of the SMBH by inverse Compton scattering of soft UV photons. Second, the contamination from stellar emission is low even for starburst galaxies. Third, X-ray emission is optically-thin to dust and hence is strong against absorption therefore

[1] In this work, the term "obscuration" refers to the process which creates absorption in the emission.

obscured sources can also be detected. These qualities make X-rays ideal to study the statistical evolution of the AGN population and have been used to study the number density and luminosity function over the past 30 years.

X-ray studies of AGN show that the luminosity function of AGN can be expressed with a double power law function. For example, Ueda et al. (2014) constructed the hard X-ray AGN luminosity function which describes the number density of Compton-Thin AGN (CTN-AGN), which are AGN with hydrogen column density between $\log N_{\rm H}$ [cm^{-2}] $= 20 - 24$. The evolution of the X-ray luminosity function depends on the X-ray luminosity of the AGN, hence the model is called the "Luminosity-dependent density evolution" model (LDDE model). The hard X-ray luminosity function of CTN-AGN in the local universe is described as the following

$$\frac{d\Phi^{\rm CTN}(L_X, z=0)}{d\log L_X} = A\left[\left(\frac{L_X}{L_*}\right)^{\gamma_1} + \left(\frac{L_X}{L_*}\right)^{\gamma_2}\right]^{-1}$$

where A is the normalization of the luminosity function, L_* is the break luminosity, and γ_1 and γ_2 are the slopes of the connected power-laws. The luminosity function beyond the local universe follows a luminosity and redshift-dependent evolution:

$$\frac{d\Phi^{\rm CTN}(L_X, z)}{d\log L_X} = \frac{d\Phi^{\rm CTN}(L_X, z=0)}{d\log L_X} e(L_X, z)$$

where $e(L_X, z)$ is the evolutionary term, which describes the change in the shape of the luminosity function as

$$e(L_X, z) = \begin{cases} (1+z)^{p1} & [z \le z_{c1}](L_X \\ (1+z_{c1})^{p1}(\frac{1+z}{1+z_{c1}})^{p2} & [z_{c1}(L_X) < z \le z_{c2}] \\ (1+z_{c1})^{p1}(\frac{1+z_{c2}}{1+z_{c1}})^{p2}(\frac{1+z}{1+z_{c2}})^{p3} & [z > z_{c2}] \end{cases} \tag{1.1}$$

where z_{c1} and z_{c2} are two redshift limits where the power of the evolution smoothly changes from $p1$ to $p2$ to $p3$. The name "luminosity-dependent density evolution" comes from this term which is a function of the AGN luminosity. The power index $p1$ is described

$$p1(L_X) = p1^* + \beta_1(\log L_X - \log L_p)$$

where $\log L_p = 44$. The remaining power indexes $p2$ and $p3$ were set to -1.5 and -6.2, respectively. Besides the power indexes, the redshift limits are also a function of redshift, given as

$$z_{c1}(L_X) = \begin{cases} z^*_{c1}(L_X/L_{a1})^{\alpha 1} & [L_X \le L_{a1}] \\ z^*_{c1} & [L_X > L_{a1}] \end{cases} \tag{1.2}$$

and

$$z_{c2}(L_X) = \begin{cases} z^*_{c2}(L_X/L_{a2})^{\alpha 2} & [L_X \le L_{a2}] \\ z^*_{c2} & [L_X > L_{a2}] \end{cases} \tag{1.3}$$

where $z_{c2} = 3.0$ and $\log L_{a2} = 44$ and $\alpha 2 = -0.1$. All parameters are summarized in table 1.1 for the case of the 2-10 keV luminosity function.

Parameter	A	$\log L_*$	γ_1	γ_2	$p1^*$
Value	2.91 ± 0.07	43.97 ± 0.06	0.96 ± 0.04	2.71 ± 0.09	4.78 ± 0.16
Parameter	β_1	z^*_{c1}	$\log L_{a1}$	α_1	
value	0.84 ± 0.18	1.86 ± 0.07	44.61 ± 0.07	0.29 ± 0.02	

Table 1.1: Best-fitted parameters of the 2-10 keV luminosity function

The integration of the X-ray luminosity functions in luminosity shows the evolution of the number density of AGN as a function of redshift. Figure 1.1 (left) shows the evolution of the AGN number density in bins of 2-10 keV luminosity $\log L_{\rm X} = 43 - 45$. The number density of luminous AGN $\log L_{\rm X} = 43 - 45$ peaks between $z \sim 1 - 3$. This epoch is often described in the literature as the cosmic noon as it is where the accretion density and star-formation density are at their highest (Delvecchio et al., 2014; Madau and Dickinson, 2014). The mass gained through accretion during the AGN phase through cosmic history accumulates into the local supermassive black hole mass density as shown in figure 1.1 (right). The bulk of the SMBH mass density was obtained during cosmic noon where $\sim$ 70% of the local SMBH mass density was grown through accretion. During this time, the majority of the mass was grown in AGN with bolometric luminosity of $\log L_{\mathrm{Bol}}$ [erg s^{-1}] $= 45 - 47$ which corresponds to an 2-10 keV X-ray luminosity of $\log L_{\mathrm{X}}$ [erg s^{-1}] $= 43.5 - 45$ assuming the bolometric correction of Duras et al. (2020). In order to forward the model of the luminosity function to the observed number density of AGN, the obscured fraction and estimation of the survey bias are needed to account for AGN missed by the survey. The obscured fraction is discussed in the following section 1.4.

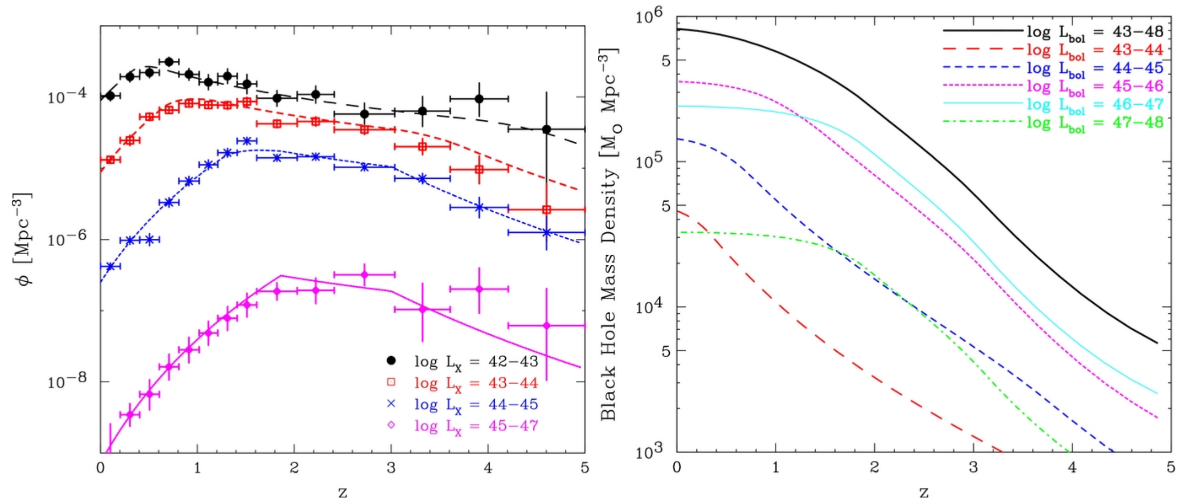

Figure 1.1: (Left) The number density of AGN in bins of 2-10 keV X-ray luminosity as a function of redshift. (Right) The Comoving mass density as a function of redshift and in bins of AGN bolometric luminosity. The black line shows the total mass density grown by the AGN population. This figure was reproduced with permission from figures 12 and 21 of Ueda et al. (2014).

1.3 AGN Classification

1.3.1 Optical Classification : Type-1 vs. Type-2 AGN

From the optical/infrared point of view, AGN can be broadly classified into type-1 AGN and type-2 AGN based on the spectral properties and colors of the UV/optical continuum. Figure 1.2 shows the optical spectrum and optical infrared spectral energy distribution of type-1 and type-2 AGN. Type-1 AGN shows strong and broad emission lines with velocities of a few thousand to ten thousand kilometers per second in the rest frame optical spectra. The typical broad emission lines of AGN include the Balmer and Paschen line series, MgII, CIII, CIV, SiIV, and Lyman-α emission lines. The emitting region of broad emission lines comes from the broad line region (BLR). Type-1 AGN also shows strong narrow permitted and forbidden lines such as Hα, Hβ, [OIII], [NII], [NeV] that have larger equivalent widths than that observed in typical galaxies. In contrast to the broad emission lines, the velocity of narrow lines is a few hundred kilometers per second, These emission lines are emitted from low-density gas at a kpc scale distance from the central engine, called the narrow-line region (NLR). The optical/infrared SED of type-1 AGN has a flat or power-law-like shape due to the dominance of the AGN accretion disk emission in the optical infrared continuum. This results in bluish colors for type-1 AGN which is different from the reddish colors of typical galaxies. This unique luminous blue continuum is used to identify AGN candidates with optical color selection.

On the other hand, type-2 AGN lacks the broad emission lines typically observed among type-1 AGN but still contains strong narrow emission lines. The optical infrared continuum of type-2 AGN is dominated by the host galaxy stellar emission which is characterized by the redden continuum due to dust attenuation. The host-dominated continuum of type-2 AGN means that the optical & near-infrared colors of type-2 AGN are similar to normal galaxies with no AGN activity. Therefore, identification of type-2 AGN often requires additional information from other wavelengths such as X-ray, mid-infrared,

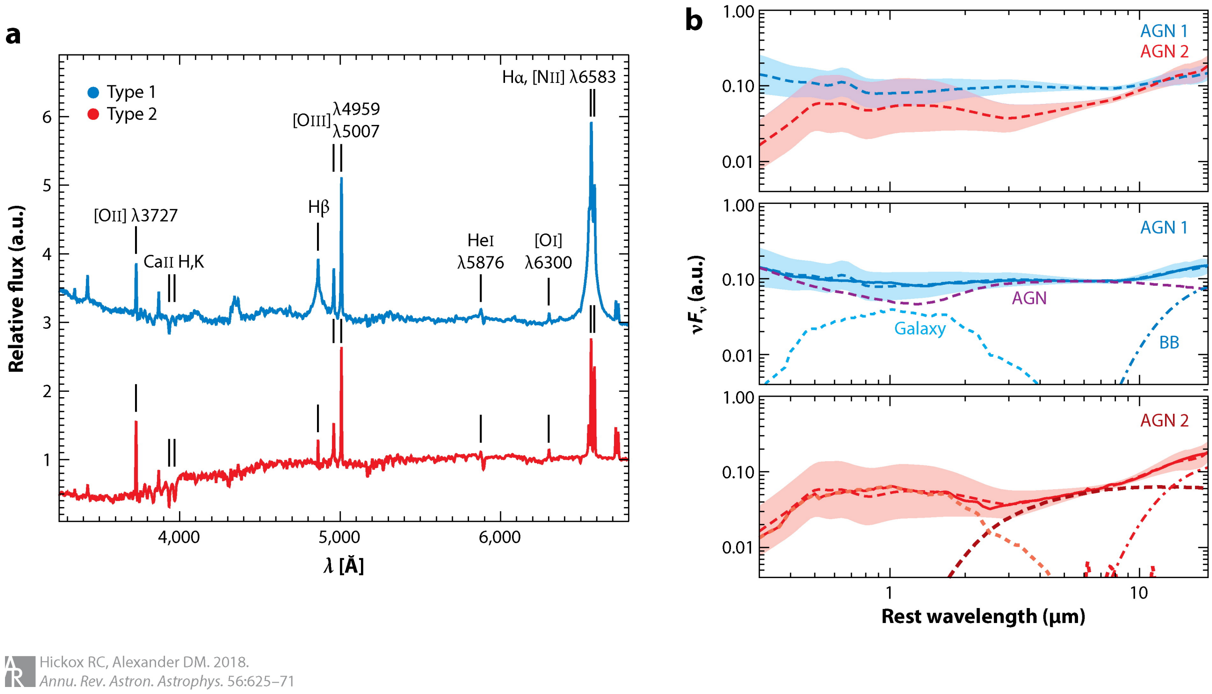

Figure 1.2: (Left) Comparison of the optical spectra of type-1 and type-2 AGN. (Right) Comparison between the optical-infrared spectral energy distribution of type-1 and type-2 AGN. In both panels, type-1 AGN is shown in blue while type-2 AGN is shown in red. This figure was reproduced with permission from figure 3 of Hickox and Alexander (2018).

or radio emission that are less sensitive to dust attenuation or spectral analysis such as Baldwin, Phillips & Terlevich (BPT) diagrams (Baldwin et al., 1981).

The disappearance of the broad emission lines and the blue AGN continuum led to the development of the unified model of AGN (Antonucci, 1993; Urry and Padovani, 1995). The unified model suggests that the spectral diversity of AGN is due to different observed lines of sight towards the AGN with a fraction of them intersecting with a phenomenological dusty torus. As shown in figure 1.3, the dusty torus hides the accretion disk and the BLR on edge-on lines of sights. On the other hand, the typical type-1 AGN characteristic (broad-line & blue continuum) are observable from face-on lines of sight. The NLR which resides several kiloparsecs away from the AGN is always observable regardless of the orientation of the line of sight. Under this model, the fraction of type-2 AGN solely depends on the fraction of sky solid angle obscured by the AGN torus. Hence, the fraction of type-2 AGN can be expressed as

$$f_{\rm obs} = \frac{\Omega_{\rm T}}{4\pi} = \frac{2}{4\pi}(2\pi - \int\int \sin\theta_{\rm S}\ d\theta d\phi) = \cos\theta_{\rm S} = \sin\theta_{\rm T} \tag{1.4}$$

where $\Omega_{\rm T}$ is the solid angle subtend by the torus, $\theta_{\rm S}$ is the sky opening angle, and $\theta_{\rm T} = 90 - \theta_{\rm S}$ is the torus angle. There are two important outcomes of the unified model. First, assuming that all AGNs are randomly oriented on the sky, the unified model suggests that the fraction of type-2 AGN is constant and depends solely on the fraction of sky obscured by the torus. Second, there should be no difference in the host galaxy or environment between type-1 and type-2 AGN as the difference is due to orientation.

1.3.2 X-ray Classification: Unobscured vs. Obscured

Further insight into AGN obscuration came from statistical hard X-ray AGN studies (≥ 10 keV) which are mildly affected by X-ray absorption. Unlike optical/UV light which is sensitive to dust attenuation, X-ray absorption occurs primarily due to metals associated with a gas column density under an assumption of metal abundance in the gas (Morrison and McCammon, 1983). The degree of absorption is represented by the hydrogen column density ($\log N_{\rm H}$) including both atomic and molecular hydrogen (Willingale et al., 2013).

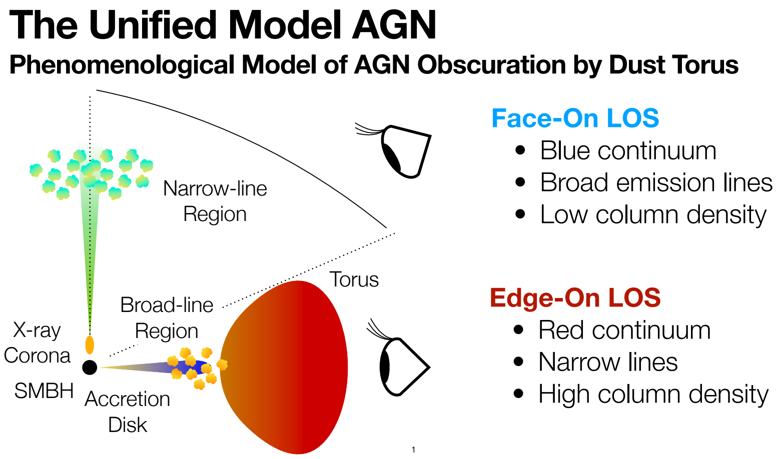

Figure 1.3: Schematic image of the AGN structure under the unified model. The AGN accretion disk and broad-line regions (BLR) are unobscured from face-one lines of sight. For edge-on lines of sights, the disk and BLR are obscured by the dusty torus.

X-ray vs. OIR Classification		X-ray Obscuration			
		Compton-Thin AGN (CTN-AGN)			Compton-Thick AGN (CTK-AGN)
		Log N_H = <22	Log N_H = 22-23	Log N_H = 23-24	Log N_H = 24-26
		Unobscured	Obscured		CTK
Dust Obscuration	Type-1 AGN	• Broad-lines • Blue continuum	• Broad-lines • Outflows (Some cases) • Blue/Flat/Red continuum		
	Type-2 AGN		• Host galaxy continuum • Narrow line \w Large EW		

Figure 1.4: Comparison between the optical and infrared classification of AGN.

In the literature of statistical X-ray AGN studies, the classification of X-ray AGN is defined by the amount of X-ray absorption traced by the hydrogen column density. Figure 1.4 shows a diagram detailing the X-ray classification of AGN compared with optical/IR classification. AGN with hydrogen column densities below $\log N_\mathrm{H}$ [cm^{-2}] ≤ 24 are called Compton-thin AGN (CTN-AGN) while those with hydrogen column densities exceeding $\log N_\mathrm{H}$ [cm^{-2}] ≥ 24 are called Compton-thick AGN. The majority of the literature classifies "obscured AGN" as AGN with hydrogen column density $\log N_\mathrm{H}$ [cm^{-2}] $= 22-24$.[2] The amount of X-ray absorption which is represented by the hydrogen column density (N_H) is linked to dust attenuation (A_V) by a gas-to-attenuation ratio ($N_\mathrm{H}/A_\mathrm{V}$). For dusty gas such as that in the dusty torus, the classification in X-ray and optical broadly agrees with each other. That is, type-1 AGN which shows broad emission lines generally has mild X-ray absorption $\log N_\mathrm{H}$ [cm^{-2}] < 22 while type-2 AGN which lacks emission lines has $\log N_\mathrm{H}$ [cm^{-2}] ≥ 22. Exceptions of these trends can occur because the optical attenuation and X-ray absorption are due to different components (gas & metals vs. dust) and gas-rich dust-free can exist in regions with high temperature such as that within the dust sublimation radius of AGN (Kishimoto et al., 2007). However, such cases of obscuration are rare compared to the

[2]The definition of obscured AGN can vary between studies.

general population of AGN and will be further discussed in chapter 4.

1.4 Trends of the CTN-AGN Obscured fraction

1.4.1 Trends with AGN Luminosity

In the local universe, statistical X-ray studies show that approximately $\sim 60\%$ of all AGN population have absorption larger than $\log N_{\rm H}$ [cm^{-2}] ≥ 22(Comastri et al., 1995; Ueda et al., 2003; Ballantyne et al., 2006; Gilli et al., 2007; Treister et al., 2009). Compton-thick AGN make up approximately $\sim 30\%$ (Ueda et al., 2014; Buchner et al., 2015) and obscured Compton-thin AGN ($\log N_{\rm H}$ [cm^{-2}] $= 22 - 24$) make up the other $\sim 30\%$ of the AGN population. Figure 1.5 shows the fraction of absorbed lines of sights through the torus with hydrogen column density $N_{\rm H}$. This implies that the majority of black hole growth shown in figure 1.1 (right) were grown under heavy obscuration by gas and dust.

The obscured fraction is generally defined as the fraction of obscured AGN with $\log N_{\rm H}$ [cm^{-2}] $= 22-24$ among the Compton-thin population. In studies at low redshifts ($z < 2$), the obscured fraction of Compton-thin AGN shows a clear anti-correlation with AGN luminosity where more luminous quasars are less likely to be obscured. Figure 1.6 shows the obscured fraction as a function of 14-55 keV luminosity. Above $\log L_{\rm X}$ [erg s^{-1}] ≥ 42, which is the canonical luminosity limit for AGN selection[3], the obscured fraction shows a strong decline towards high luminosity. This trend has been observed ubiquitously in various AGN samples selected by optical emission lines, X-rays, and mid-infrared emission (Simpson, 2005; La Franca et al., 2005; Maiolino et al., 2007; Hasinger, 2008; Burlon et al., 2011; Toba et al., 2013, 2021).

Under the unified model, the trend can be explained by an opening angle ($\theta_{\rm S}$) which increases with luminosity. Due to strong illumination and sublimation of dust (Lawrence, 1991; Toba et al., 2014), the inner edge of the dusty torus structure receding outwards. Hence, the accretion disk is directly observable. The obscured fraction may also be a result of radiation pressure on dusty gas. Luminous AGN with a high Eddington ratio can blow out the obscuring material after exceeding an $N_{\rm H}$-dependent critical Eddington ratio (Fabian et al., 2006, 2008, 2009).

1.4.2 Trends with Redshift

The Compton-thin obscured fraction also shows a trend with redshift. The obscured fraction has been shown to increase from the local universe up to redshift 2 (Ueda et al., 2003; La Franca et al., 2005; Ballantyne et al., 2006; Treister and Urry, 2006; Hasinger, 2008; Treister et al., 2009; Ueda et al., 2014; Aird et al., 2015; Buchner et al., 2015). Figure 1.7 shows the obscured fraction in different redshift bins as a function of X-ray luminosity. Towards high redshift, the fraction of obscured AGN increases at all luminosity.

The behavior of the obscured fraction of luminous AGN with $\log L_{\rm X}$ [erg s^{-1}] ≥ 44 is still not well constrained. Overall, the obscured fraction of luminous AGN during cosmic noon is larger than in the local universe. Some studies suggest that the obscured fraction has no evolution beyond redshift two and that it has reached the maximum value[4] (Hasinger, 2008; Kalfountzou et al., 2014; Vito et al., 2016, 2014). In contrast to studies below redshift 2, (Vito et al., 2014, 2018) suggest that the fraction of AGN with $\log N_{\rm H}$ (cm^{-2}) ≥ 23 at redshift 3 to 5 is independent of the X-ray luminosity, indicating that the trend with luminosity has disappeared at high redshift. At the same time, (Georgakakis et al., 2015) suggests that the obscured fraction decreases with decreasing X-ray luminosity.

At face value under the unified model, the increased obscured fraction at a fixed luminosity suggests that the height of the torus has increased. However, there is currently no evidence of such evolution in the literature yet. Alternatively, the X-ray absorption may come from the denser ISM in the nuclear region (Buchner et al., 2015, 2017; Buchner and Bauer, 2017) of the galaxy similar to the larger gas fraction seen in high redshift galaxies (Tacconi et al., 2010; Carilli and Walter, 2013).

[3]Below $\log L_{\rm X} = 42$ [erg s^{-1}], the selection of AGN can be contaminated by star formation
[4]Sometimes referred to as saturated in the literature.

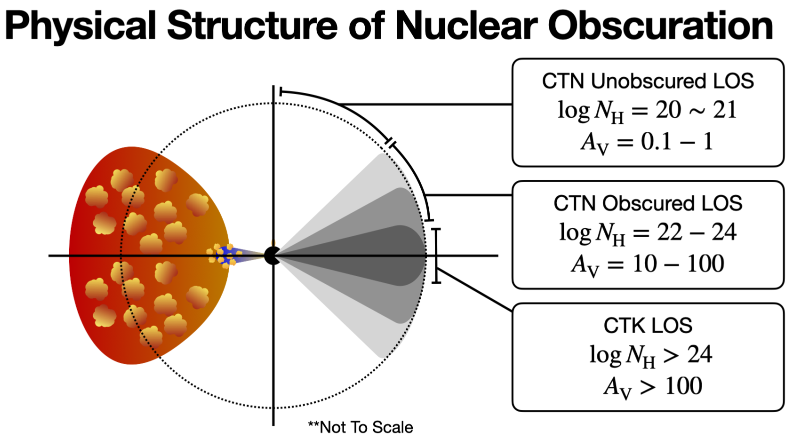

Figure 1.5: Phenomenological distribution of obscured lines of sights through the torus.

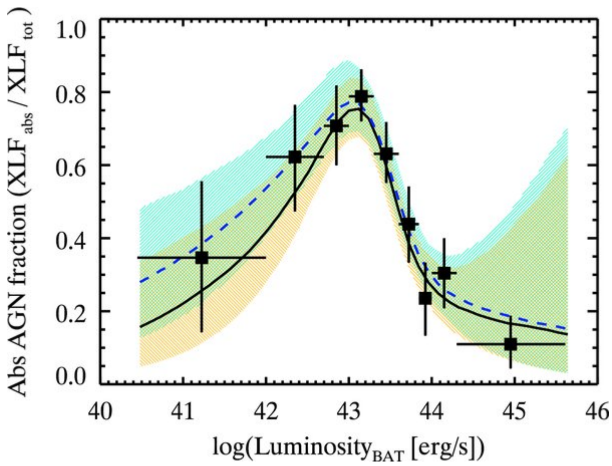

Figure 1.6: The obscured fraction of AGN as seen from hard X-rays ($\geq$ 10) keV as a function of 14-55 keV luminosity. The lines show the ratio between the best-fitted luminosity functions for the whole sample (thick line) and for those with $L_X > 2 \times 10^{42}$ erg s^{-1}. The 1σ uncertainty for each case is shown in blue and orange shaded areas respectively. This figure was reproduced with permission from figure 16 of Burlon et al. (2011).

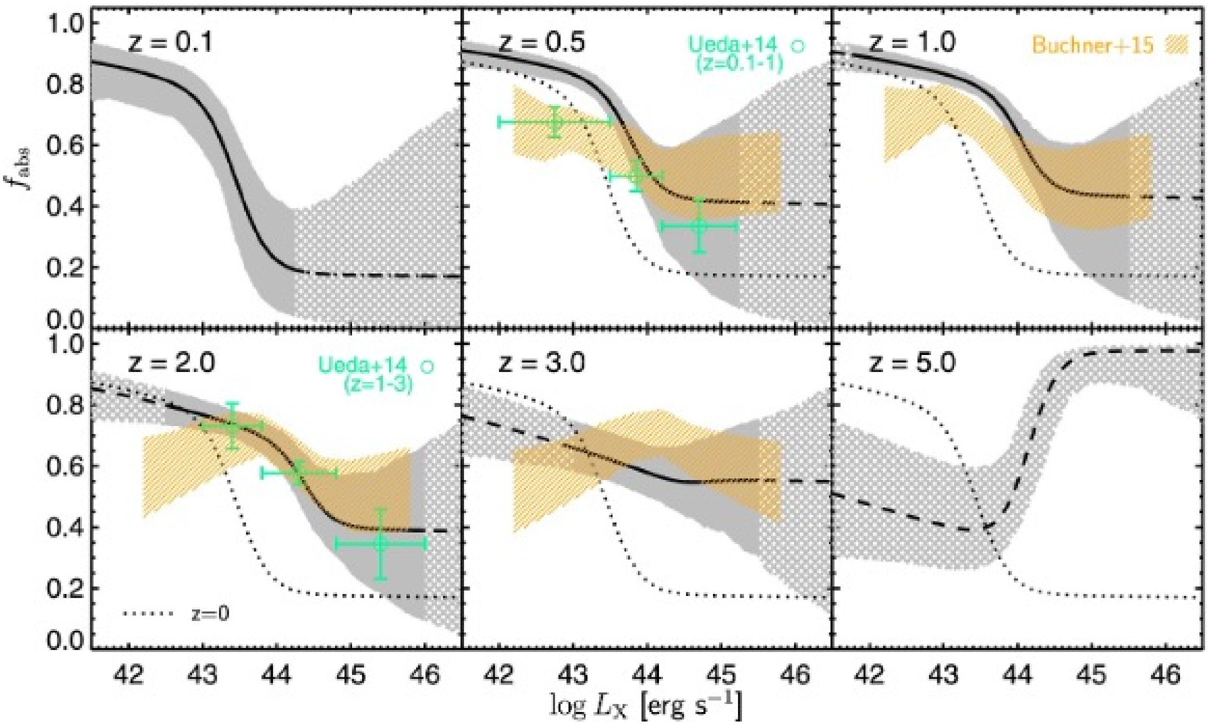

Figure 1.7: The obscured fraction as a function of 2-10 keV luminosity in different redshift bins between $z = 0.1 - 5$. The thick black lines show the luminosity range that the sample covers while the gray shaded area shows the 1σ uncertainty. The results are compared with the obscured fraction determined by Ueda et al. (2014) and Buchner et al. (2015). This figure was reproduced with permission from figure 11 of Aird et al. (2015).

1.5 The Mechanism of AGN Obscuration

1.5.1 Radiation Pressure Regulated Unified Model

The classical physics of radiation pressure in AGN is the discussion of Eddington luminosity by the AGN. Within the sphere of influence of AGN, the gravitational force is balanced by the radiation pressure by electron scattering from the AGN emission.

$$F_{\mathrm{rad}} = F_{\mathrm{Grav}} = \frac{\sigma_{\mathrm{T}}}{c}\frac{L}{4\pi r^2} = \frac{GM_{\mathrm{BH}}m_p}{r^2}$$

where σ_{T} is the Thomson scattering cross-section, c is the speed of light, m_p is the proton mass, M_{BH} is the black hole mass, G is the gravitational constant, L is the luminosity, and r is the distance from the black hole. For dust-free gas, the critical luminosity require to unbind a proton from the gravitational influence of the black hole is given by the Eddington luminosity (L_{Edd}).

$$L_{\mathrm{Edd}} = \frac{4\pi G m_p c}{\sigma_{\mathrm{T}}} M_{\mathrm{BH}} = 1.26 \times 10^{38} \left(\frac{M_{\mathrm{BH}}}{M_{\odot}}\right) \text{ erg s}^{-1} \tag{1.5}$$

Our current understanding of nuclear obscuration of AGN revolves around the concept of radiation pressure regulated unified model (Fabian et al., 2008, 2009; Wada, 2012; Wada et al., 2016; Ishibashi et al., 2018). Here I present a modified version of the discussion of radiation pressure presented in Ishibashi et al. (2018). For a spherical shell of mass with a hydrogen column density of N_{H}, the magnitude of the total gravitational force on the shell of mass is

$$F_{\mathrm{Grav}} = -\frac{GM_{\mathrm{BH}}(4\pi r^2 m_p N_{\mathrm{H}})}{r^2}$$

where N_{H} is the hydrogen column density, and r is the radius to the shell.

Fabian et al. (2006) reasoned[5] that the optical depth of a column of fully ionized gas which is given by the Thomson scattering optical depth (τ_{T}) is smaller than that of dusty or partially ionized gas ($\tau_i = [\tau_{\mathrm{T}}, 1]$). The radiation pressure upon the shell of gas by radiation from the AGN is expressed as

$$F_{\mathrm{rad}} = F_{\mathrm{UV}} = \frac{(L - Le^{-\tau_{\mathrm{UV}}})}{c}$$

where L is the total luminosity of the AGN, c is the speed of light, τ_{UV} is the UV optical depth. both of the optical depths depend on the hydrogen column density which can be expressed as $\tau_{\mathrm{UV}} = \tau_{\mathrm{UV}}(N_{\mathrm{H}}) = \kappa_{\mathrm{UV}} m_p N_{\mathrm{H}}$ where κ_{UV} is the UV opacity. The fiducial value of the UV opacity is $\kappa_{\mathrm{UV}} = 200 f_{\mathrm{dust,MW}}$ cm^{2}g^{-1} where $f_{dust,MW}$ is the dust-to-gas ratio normalized to the Milky way value. The equation of motion of the shell can be expressed as

$$F_{tot} = -4\pi G M_{\mathrm{BH}} m_p N_{\mathrm{H}} + \frac{L}{c}(1 - e^{-\tau_{\mathrm{UV}}}) \tag{1.6}$$

The critical luminosity is the luminosity in which the radiation pressure balances the gravitational force of the gas shell. Therefore, the total force is set to zero and rearranged in terms of luminosity.

$$L_{\mathrm{Eff}} = \frac{4\pi G M_{\mathrm{BH}} c m_p N_{\mathrm{H}}}{(1 - e^{-\tau_{\mathrm{UV}}})} \tag{1.7}$$

Here, L_{Eff} is the effective Eddington luminosity of partially ionized or dusty gas. The generalized Eddington ratio is then expressed as $\Lambda = L/L_{\mathrm{Eff}}$. The generalized Eddington can also be expressed in terms of the classical Eddington ratio limit

$$\Lambda = \frac{L}{L_{\mathrm{Eff}}} = \frac{\lambda L_{\mathrm{Edd}}}{L_{\mathrm{Eff}}} = \frac{(1 - e^{-\tau_{\mathrm{UV}}})}{\sigma_{\mathrm{T}} N_{\mathrm{H}}}\lambda$$

.

[5] For a generalized case of radiation pressure including infrared radiation trapping, please refer to appendix B.

By setting $\Lambda = 1$ where the AGN luminosity has reached the effective Eddington luminosity, the effective Eddington ratio can be expressed in terms of the hydrogen column density.

$$\lambda_{\rm Eff} = \frac{\sigma_{\rm T}}{(1 - e^{-\tau_{\rm UV}})} N_{\rm H} \tag{1.8}$$

Assuming a Milky way gas to dust ratio and at low hydrogen column density (and hence low optical depth), the term $e^{\tau_{\rm UV}}$ can be approximated as $e^{-\tau_{\rm UV}} \sim 1 + \tau_{\rm UV}$ and therefore equation 1.8 can be written as

$$\lambda_{\rm Eff} \sim \frac{\sigma_{\rm T}}{\tau_{\rm UV}} N_{\rm H} = \frac{\sigma_{\rm T}}{\kappa_{\rm UV} m_p} = \frac{6 \times 10^{-25}}{200 \cdot 1 \cdot 1.66 \times 10^{-24}} \sim 0.002$$

.

At $\log N_{\rm H}$ [cm^{-2}] > 22, the UV optical depth becomes optically thick ($\tau_{\rm UV} = 200 \cdot 1.66 \times 10^{-24} \cdot 10^{22} > 1$). Hence, the term $e^{-\tau_{\rm UV}}$ can be approximated as $e^{-\tau_{\rm UV}} \sim 0$, therefore $\lambda_{\rm Eff} \sim \sigma_{\rm T} N_{\rm H}$. This results in a linearly increasing effective Eddington radio as a function of hydrogen column density. At large hydrogen column density (and large optical depth), the radiation pressure is at maximum. The excess hydrogen column density acts as a dead weight in which a much larger Eddington ratio is required to push out the dusty gas.

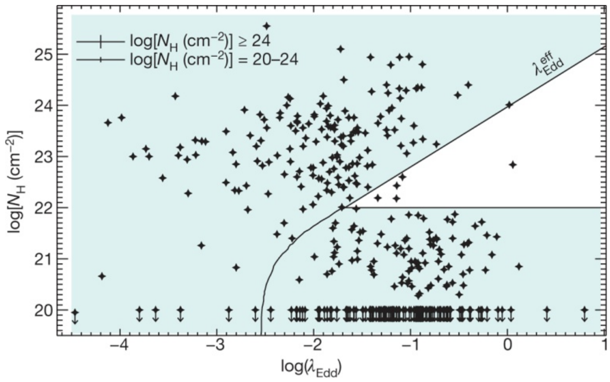

Figure 1.8: The distribution of local SWIFT/BAT detected AGN in the $\log N_{\rm H} - \lambda_{\rm Edd}$ diagram. The forbidden region is shown as a white wedge area. The effective Eddington ratio is shown as the curved line. The upper limit of the host galaxy ISM column density is shown with the horizontal line. This figure was reproduced with permission from figure 3 of Ricci et al. (2017c).

Fabian et al. (2008) showed that the $N_{\rm H} - \lambda_{\rm Edd}$ diagram can be separated into 3 distinct regions as shown in figure 1.8. First, the region below the effective Eddington limit which line-of-sight obscuration is stable. Second, the forbidden zone where the AGN is expected to drive dusty outflows. By producing outflows, line-of-sight is cleared from obscuring dust and gas therefore the AGN is allowed to change from being obscured to unobscured (Fabian et al., 2008; Ishibashi et al., 2018; Jun et al., 2021; Ricci et al., 2022). Last is the ISM absorbed regions where the fiducial limit of ISM absorption in the local universe is $\log N_{\rm H}$ [cm^{-2}] ~ 22.

This model is consistent with the distribution of local hard X-ray selected AGN on the $N_{\rm H} - \lambda_{\rm Edd}$ diagram which shows that obscured AGN tends to avoid the forbidden zone (Fabian et al., 2009; Ricci et al., 2017c, 2022). On the other hand, AGN which shows signs of dusty outflows resides in the forbidden zone (Kakkad et al., 2016; Yamada et al., 2021; Stacey et al., 2022). Hydrodynamic simulations which apply the concept of radiation pressure regulation were able to produce structures of accretion flows analogous to a torus and qualitatively reproduce the trends in the obscured fraction with AGN luminosity (Wada, 2015).

1.5.2 Interstellar Obscuration

In local late-type galaxies, atomic hydrogen (HI) gas shows a flat distribution through the disk with a typical HI surface density is 1-10 M$_\odot$pc^{-2} (Bigiel and Blitz, 2012). This corresponds to a HI column density of $\log N_{\rm HI}$ [cm^{-2}] $= 20 - 21$ and $\log N_{\rm HI}$ [cm^{-2}] $= 21 - 22$ for face-on and edge-on view respectively. On the other hand, molecular hydrogen (H_2) is concentrated within the 5 kpc radius with an exponentially declining density profile (Bigiel and Blitz, 2012; Saintonge and Catinella, 2022). The typical H_2 surface density is 10-100 $M_\odot pc^{-2}$ reaching 1000 $M_\odot pc^{-2}$ in some rare cases (Bigiel and Blitz, 2012). Hence, the corresponds H_2 column density can be substantially higher reaching $\log N_{H_2}$ [cm^{-2}] $= 20 - 22$. Based on these observations, a fiducial limit of $\log N_H$ [cm^{-2}] $= 22$ can be set for the ISM obscuration in the local universe.

On the other hand, the situation at high redshift may be much different than in the local universe. It has been suggested that at high redshift the X-ray absorption in obscured AGN may be due to heavy ISM absorption instead of a dusty torus (Buchner et al., 2017; Gilli et al., 2022). Submillimeter observations of high redshift galaxies have a higher gas fraction and are more compact than galaxies in the local universe with similar mass (Daddi et al., 2010; Tacconi et al., 2010; Carilli and Walter, 2013; Tacconi et al., 2018; van der Wel et al., 2014; Mowla et al., 2019). Hence higher gas densities are expected for the same stellar mass leading to higher column densities. Gilli et al. (2022) suggest that the ISM column density increases as a function of redshift as shown in the thick and long dashed lines of figure 1.9 which may explain the evolution of the CTN-AGN obscured fraction.

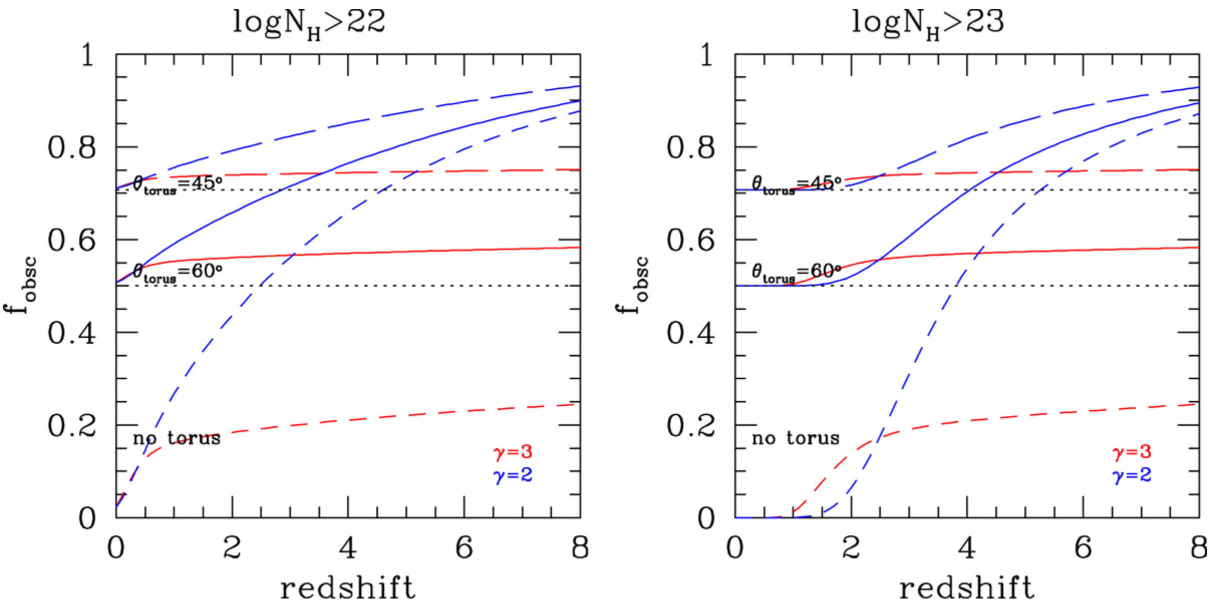

Figure 1.9: Fraction of obscured AGN with $\log N_H$ [cm^{-2}] $= 22 - 24$ (left panel) and $\log N_H$ [cm^{-2}] $=$ $23 - 24$ (right panel) against redshift for various combinations of ISM and torus obscuration. The surface density of ISM clouds evolves as $\propto (1+z)^\gamma$, with $\gamma = 2$ and $\gamma = 3$ shown as blue and red curves, respectively. ISM-only obscuration is shown with short dashed lines. The long dashed and solid lines show the total obscured AGN fraction including the torus at 40 and 60 degrees, respectively. The horizontal dotted lines show the torus-only obscuration. This figure was reproduced with permission from figure 13 of Gilli et al. (2022).

For type-1 AGN, absorption may be due to gas and dust in the polar regions of the AGN, also known as polar dust. Polar dust occurs much closer to the AGN and may be different from typical ISM dust due to the larger gas content (Mizukoshi et al., 2022) and lower abundance of small grain dust due to destruction by the strong AGN luminosity (Tazaki et al., 2020; Tazaki and Ichikawa, 2020). In the literature, SMC dust extinction curves and SMC gas-to-attenuation ratios (Dobashi et al., 2009) are often assumed to represent the polar-dust obscuration. For the same column density, ISM absorption such as the milky way (Zhu et al., 2017) has a lower gas-to-attenuation ratio than SMC gas-to-attenuation (Dobashi et al., 2009). However, it is currently unclear wherever polar dust occurs from AGN outflows or if it is part of the nuclear ISM.

1.5.3 Merger triggered Obscuration

Hydro-dynamical simulations show that the gravitational disturbance during merging events can trigger massive inflows of gas and dust towards the nuclear regions of a galaxy (Hopkins et al., 2005, 2006; Blecha

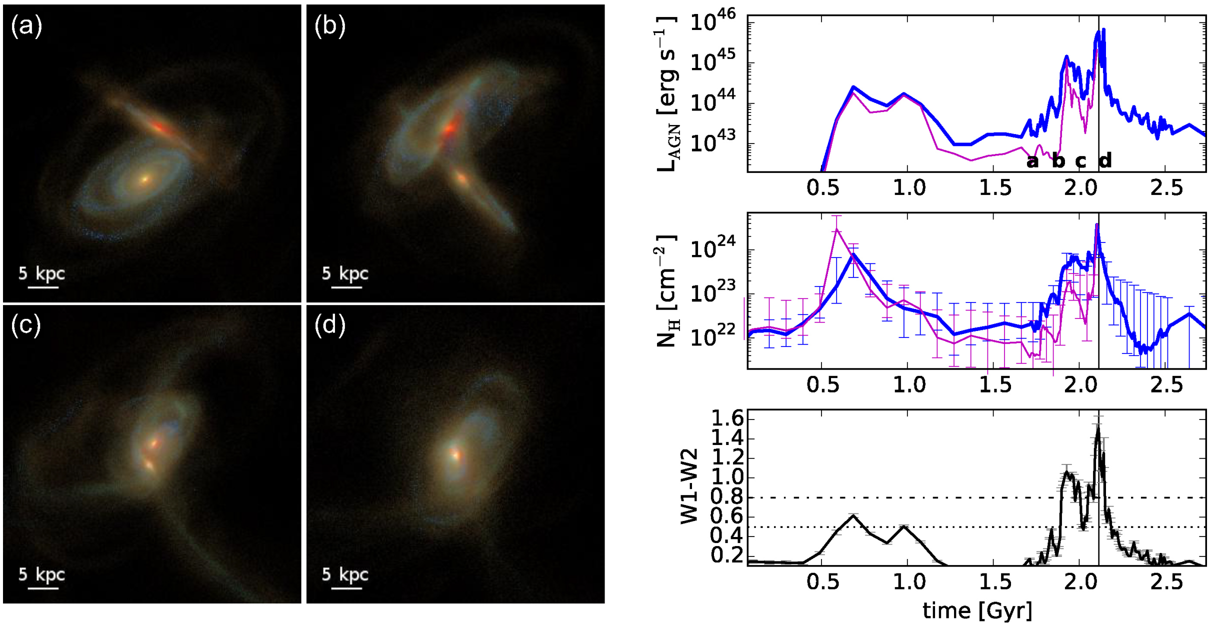

Figure 1.10: (left) Simulated image along the merger sequence from a to d. (right) The evolution of the AGN luminosity, hydrogen column density, and WISE1-WISE2 colors as a function to time along the merger sequence. The figure was reproduced with permission from figure 1 of Blecha et al. (2018).

et al., 2018). Figure 1.10 shows the evolution of the AGN luminosity and hydrogen column density as a function of time along the merger sequence. During this phase, AGN activity occurs under larger amounts of gas and dust where AGN appears obscured or Compton-thick. After an extended obscured phase, strong AGN outflows clear the line of sight toward the observer and the AGN becomes unobscured. Often called the evolutionary scenario of AGN, it suggests a fundamental difference between unobscured AGN and those with obscured or CTK absorption since the obscured phase precedes the unobscured AGN phase (Hickox and Alexander, 2018). In the local universe, ultra-luminous infrared galaxies (ULIRGS) may represent such a case of AGN obscuration. Typically defined as galaxies with infrared luminosity exceeding $\log L_{\rm IR} > 10^{12}\ L_\odot$ (Sanders and Mirabel, 1996), local ULIRGs tend to house luminous AGN with large amounts of X-ray absorption, dust extinction and tend to be in late-stage gas-rich mergers (Goto et al., 2011; Ricci et al., 2021; Yamada et al., 2021). Moreover, AGN dominates the luminous end of the infrared luminosity function above $\log L_{\rm IR}/L_\odot \geq 10^{12}$ up to redshift 2.5 (Goto et al., 2011; Symeonidis and Page, 2021). This may explain the increased fraction of obscured AGN if the frequency of merger trigger obscuration increases towards high redshift therefore high-z redshift observations observe more AGN during the obscured phase.

1.6 The Need for Deep & Wide Survey

The luminosity function of AGN shows a break (or knee) where the number density of AGN sharply declines with luminosity. Therefore a large survey area (and volume) is needed in order to obtain a statistically significant sample of luminous AGN. In the case of obscured AGN, the metals in the gas column along the line of sight make the AGN fainter compared to AGN of the same intrinsic X-ray luminosity. This means that a deeper survey depth is required in order to detect obscured AGN when compared to unobscured AGN. In addition to the X-ray datasets, deep optical/infrared imaging is also needed in order to associate the host galaxy with the corresponding X-ray source. This is needed to determine the redshift of the AGN and to calculate the AGN luminosity for statistical analysis. As a result, investigation of the fraction of luminous obscured AGN requires a multiwavelength dataset with a wide survey area and sufficient survey depth to detect luminous obscured sources that are rare and faint.

Multi-wavelength survey fields generally balance survey depth with survey area resulting in a "wedding cake" like strategy. That is, the survey is focused on a small area of the sky with ultra-deep survey depth or focused on a large area but with shallow depth. Examples of the first case include the survey area of the Chandra Deep Field South (Luo et al., 2017) or the Aegis-X (Nandra et al., 2015) survey while examples of the latter include those of the ROSAT all-sky survey (Boller et al., 2016) or the XMM-XXL survey (Pierre et al., 2016). These survey strategies also are sensitive to different populations of AGNs. Ultra-deep pencil beam surveys are most sensitive to faint sources due to their larger number density while wide-shallow surveys are efficient in picking up rare luminous AGN thanks to the large survey area they can access. However, they cannot detect faint sources due to the shallowness of the surveys. The energy band in which the survey is carried in also affects the efficiency of detecting obscured sources. Hard-band surveys (E> 10keV) are more efficient in detecting absorbed sources since high(er) energy X-rays are more resistant to X-ray absorption. Some examples of hard-band surveys include the SWIFT/BAT All-sky Hard X-Ray Survey (Oh et al., 2018) or NuSTAR Extragalactic surveys (Civano et al., 2015; Masini et al., 2018). Soft-band surveys are less efficient in detecting obscured AGN because the soft-band X-ray photons are more sensitive to absorption. However, soft-band photons are easier to focus in the X-ray telescope which results in higher sensitivity (and deeper depth) which makes it easier to detect faint sources than hard-band surveys.

1.7 Project Goals and Overview of the Thesis

As described in section 1.2 and 1.4, the obscured fraction is an important parameter in the study of cosmological SMBH growth. However, the fraction of obscured AGN at comic noon (and above) is poorly constrained especially among luminous AGN (log $L_{\rm X}$[erg s^{-1}] ≥ 44) which corresponds to the break in the luminosity function and contribute the majority of cosmological SMBH growth. At the time of writing, previous results of the obscured fraction on the luminous end were constrained by deep pencil beam surveys which are not large enough to detect a significant sample of luminous obscured AGN. Therefore, luminous obscured AGN which may contribute a significant fraction to the total SMBH during cosmic noon may have been missed by previous studies.

Recently, attempts to address the weak points in the wedding cake strategy have led to the development of **deep and wide** X-ray datasets. An example is the deep and wide XMM-SERVS dataset in the XMM-LSS which covers an area of 5.3 Deg^2 of the XMM-LSS and overlaps with the Hyper-Suprime Cam Subaru Strategic Program (HSC-SSP) Deep layer and several other deep infrared imaging datasets. These surveys address the need for an X-ray dataset with sufficient area and depth to construct a statistically significant sample of obscured AGN with moderate to high luminosity.

The goal of this thesis is to 1). evaluate the fraction of obscured CTN-AGN by using the deep and wide X-ray dataset and 2). evaluate the mechanism of AGN obscuration at cosmic noon. The content of the work is separated into 3 chapters. The construction of the multiwavelength dataset in the HSC-Deep XMM-LSS field is described in chapter 2.

In chapter 3, the obscured fraction of luminous AGN above $z \sim 2$ is described in chapter 2. Estimation of the hydrogen column density using the X-ray hardness ratios is described in section 3.1.1 based on an assumption of an X-ray spectral model. The parametric model adopted for the analysis of the obscured fraction as well as the maximum-likelihood method is described in section 3.2. The sample used for the analysis is explained in section 3.4 as well as the result of the analysis in section 3.5.

Chapter 4 described the investigation of the obscuration process at redshift 0.8-1.8 based on obscuration scenarios in the local universe such as the radiation pressure regulated nuclear obscuration. In order to perform the analysis, the Eddington ratio needs to be determined. At this redshift range, the MgII emission line is accessible in type-1 AGN which is a more reliable virial mass estimator than the CIV emission line observed at $z > 2$. Section 4.3 describes the construction of the sample of Type-1 and Type-2 AGN. The spectroscopic and SED analysis is discussed in section 4.4 and 4.5. The results are presented in section 4.8.

In this work, the metal abundances of Anders and Grevesse (1989) was. Obscured and unobscured AGN are referred to specifically to X-ray classification while type-1 and type-2 AGN refer to optical/IR classification. A galactic hydrogen column density of 3.57×10^{20}cm^{-2} (Chen et al., 2018) and a flat standard ΛCDM cosmology with $H_0 = 70$km s^{-1} Mpc^{-1},$\Omega_{\rm M} = 0.3$, and $\Omega_\lambda = 0.7$ was assumed. Magnitudes are reported in the AB magnitude system.

Chapter 2

Multi-wavelength Datasets & Catalog Construction

2.1 Deep & Wide X-ray Datasets

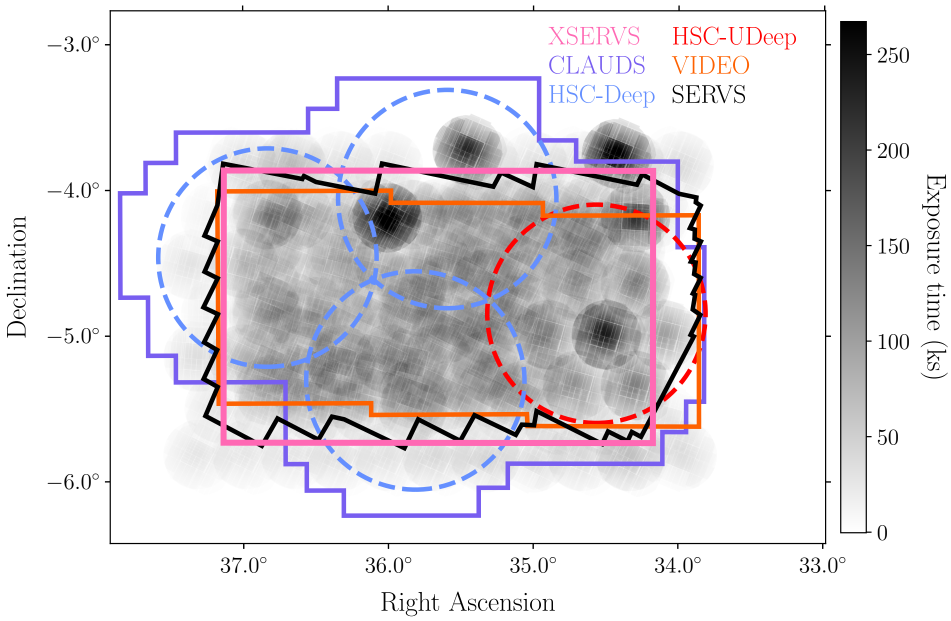

Figure 2.1: 0.5-10 keV flare-filtered exposure map in the HSC Deep XMM-LSS survey area (Chen et al., 2018). The coverage of CLAUDS, HSC-Deep, HSC-UDeep, VIDEO, and SERVS is shown in purple solid, blue dashed, red dashed, orange solid, and black solid lines, respectively. The pink boundary shows the area of the XMM-SERVS datasets. The color bar represents the commutative exposure time. This figure was reproduced with permission from Vijarnwannaluk et al. (2022).

The XMM-SERVS X-ray point-source catalog in the XMM-LSS region (Chen et al., 2018) was used to identify AGN in the HSC-Deep field XMM-LSS region. The area was observed by the *XMM-Newton* satellite over a total survey area of 5.3 Deg^2. *XMM-Newton* has 2 main instruments, an X-ray imager called the European Photon Imaging Camera (EPIC) and an X-ray spectrograph called the Reflection Grating Spectrometers (RGS). The EPIC camera has three detectors, MOS1, MOS2, and PN which were used to perform the survey in the 0.5-2 keV, 2-10 keV, and 0.5-10 keV energy bands. A total of 5242 X-ray point sources were detected.

The whole survey area was observed at an average flair-filtered exposure time of $\sim$ 50ks for each pointing. Deeper X-ray observations are available in some regions from projects listed in table 2 of

Chen et al. (2018). The survey flux limits over 90% of the total area are $1.7 \times 10^{-15}, 1.3 \times 10^{-14}$, and 6.5×10^{-15} erg cm^{-2} s^{-1} in the 0.5-2 keV, 2-10 keV, and 0.5-10 keV bands, respectively.

The flux measured by each detector was derived using an energy conversion factor (ECF) assuming a power-law continuum with photon index, $\Gamma = 1.7$, and galactic absorption column density. The error-weighted average of the flux estimated by all three detectors was adopted for the combined source flux. The error-weighted average count rates were converted to the expected count rates detected with the PN-detector, also known as PN-equivalent count rates. The conversion to count rates was performed using the ECF of the PN detector reported by Chen et al. (2018)

2.2 Deep & Wide Optical & Infrared Imaging Datasets

2.2.1 Hyper-Suprime Cam Subaru Strategic Program

The Hyper-Suprime Cam Subaru Strategic Program (HSC-SSP) is an optical survey performed by the 8.2-meter Subaru telescope. The survey has 3 layers of depth including wide, deep, and ultra-deep. This study uses imaging data from the S19A and S20A data release of the deep and ultra-deep layers within the XMM-LSS survey field. For these datasets broadband optical imaging are available in the *grizy* bands.

The HSC-SSP survey was performed with the Hyper-Suprime Cam (HSC) wide-field imager (Miyazaki et al., 2018). The field-of-view is 1.5 square degrees and comprises 116 2K $\times$ 4K fully-depleted back-illuminated CCDs (FDCCD; Kamata et al. 2012). The images were reduced by the HSC-SSP team using the HSC pipeline (Jurić et al., 2017; Bosch et al., 2018, 2019; Ivezić et al., 2019). The first data release of the panoramic survey telescope and rapid response system (Pan-STARRS1; Schlafly et al. 2012; Tonry et al. 2012; Magnier et al. 2013; Chambers et al. 2016; Magnier et al. 2020) was used to calibrate the photometry and astrometry.

2.2.2 CFHT Large Area U-band Deep Survey

CFHT Large Area U-band Deep Survey (Sawicki et al., 2019) or CLAUDS is a deep U-band imaging survey conducted by the 3.6m CFHT with Megacam (Sawicki et al., 2019) in the HSC-Deep fields.

The survey was performed using Megacam (Boulade et al., 2003) which is a wide field camera with 40 2048$\times$4612 pixel back-illuminated CCDs and a field-of-view of 1.02 Deg^2. Unlike HSC, Megacam has better sensitivity in the U-band than HSC, which was optimized to be sensitive at longer wavelengths.

Two u-band filters were used in the CLAUDS survey; u^* and U. Unlike the old u^*-band filter, the newer U-band filter has a better transmission and no red-leak at 5000 $\mathring{A}$. The CLAUDS survey in the XMM-LSS area was conducted entirely using the u^*-band filter at a depth of 26.6 magnitudes (5 sigma detection in $2''$ diameter aperture). The depth in the ultradeep area which overlaps with the Subaru XMM-Newton Deep Survey (SXDS; Furusawa et al. 2008) reaches 1 magnitude deeper.

The CLAUDS data were reduced and calibrated with the Elixir data reduction software (Magnier and Cuillandre, 2004) at CFHT before further processing with MegaPipe (Gwyn, 2008) at the Canadian Astronomy Data Centre. Astrometric calibration was performed by MegaPipe performs against Gaia astrometry while photometry was calibrated against SDSS u band photometry and cross-checked against synthetic u-band photometry produced from a combination of Pan-STARRS (Magnier et al., 2020) g-band and GALEX NUV photometry.

2.2.3 VISTA Deep Extragalactic Observations Survey

The VISTA deep extragalactic observations survey (VIDEO; Jarvis et al. 2013) is a deep near-infrared imaging survey of 3 extragalactic survey fields including the XMM-LSS. The survey was performed with the VISTA InfraRed CAMera (VIRCAM; Dalton et al. 2006) on the 4.1 meter visible and infrared survey telescope for astronomy (VISTA) at Cerro Paranal. VIRCAM consists of 16 2K $\times$ 2K Raytheon VIRGO HgCdTe detectors and has a field of view of 1.65 Deg^2.

The mosaic images of VIDEO Data-release 5 in the HSC-Deep XMM-LSS field were obtained through the ESO Phase 3 data archive.[1] The survey area in each band is separated into 3 smaller mosaics

[1] http://eso.org/rm/publicAccess#/dataReleases

designated as XMM1, XMM2, and XMM3. Among them, XMM1 covers the SXDS. Data reduction was performed by the VISTA data flow system (VDFS; Irwin et al. 2004) at the Cambridge astronomical survey unit (CASU) The astrometry and photometry of the survey were calibrated against the 2MASS point-source catalog (Skrutskie et al., 2006).

2.2.4 Spitzer Extragalactic Representative Volume Survey

The Spitzer Extragalactic Representative Volume Survey (Mauduit et al., 2012) or SERVS is a deep mid-infrared imaging survey. The survey was performed by the *Spitzer* space telescope using the Infrared Array Camera (IRAC;Fazio et al. 2004) during the post-cryogenic mission. During this time, only the IRAC channel 1 (3.6 μm) and channel 2 (4.5 μm) are operable due to the high background in channel 3 and 4 from the lack of coolant.

SERVS covers 5 deep multiwavelength extragalactic fields including ELAIS-N1, ELAIS-S1, Lockman Hole, Chandra Deep Field South, and XMM-LSS. The total survey area is 18 square degrees but for the XMM-LSS it is $\sim$5.3 square degrees. The survey depth was designed to be close to the confusion limit of the Spitzer IRAC data with a mean integration time per pixel of $\sim 1200s$. The 5-sigma depths in 3.6 and 4.5 μm bands are 1.9 and 2.2 μJy in 3.8-arcsecond diameter aperture.

The data was processed at the Spitzer science center (SSC) using the standard image reduction and additional detector-specific processing pipelines. MOPEX was used to reproject the images to a pixel scale of 0.6 arcseconds per pixel. Photometric calibration was performed against dedicated calibration observations and was cross-checked against the SWIRE survey(Lonsdale et al., 2003). The analysis suggests that the 3.6μm band flux requires an additional 1.02 correction factor. The mosaic and uncertainty images are obtained from the NASA/IPAC Infrared Science Archive[2].

2.2.5 Optical & Infrared Spectroscopic Datasets

Several public spectroscopic datasets are available in the XMM-LSS region. Spectroscopic redshift measurements were collected from various spectroscopic surveys including those from the Sloan Digital Sky Survey data release 9 & 16 (SDSS;Ahumada et al. 2020; Ahn et al. 2012), VIMOS Public Extragalactic Redshift Survey (VIPERS; Scodeggio et al. 2018), Galaxy and Mass Assembly (GAMA; Liske et al. 2015), VIMOS VLT Deep Survey (VVDS; Le Fèvre et al. 2013), VANDELS (Garilli et al., 2021), MOSFIRE Deep Evolution Field Survey (MOSDEF; Kriek et al. 2015), Ultradeep Survey[3] (UDS; McLure et al. 2013; Bradshaw et al. 2013), 3D-HST (Brammer et al., 2012; Momcheva et al., 2016), and the SXDS multiwavelength catalog (Akiyama et al., 2015). Also included, are spectroscopic redshifts reported by individual studies in the SXDS and XMM-LSS regions (Yamada et al. 2005; Geach et al. 2007; Ouchi et al. 2008; Saito et al. 2008; Smail et al. 2008; van Breukelen et al. 2009; Ono et al. 2010; Simpson et al. 2012; Díaz Tello et al. 2013; Melnyk et al. 2013; Yabe et al. 2014; Wang et al. 2016; Menzel et al. 2016; Ono et al. 2018).

Although the depth of the SDSS and VIPERS survey is only up to an i-band magnitude of 22.5, deeper spectroscopic surveys were also conducted in the area. To sum up, 294,536 secure spectroscopic redshifts of 238,403 unique galaxies and AGN were collected. While the majority are from wide and shallow spectroscopic surveys, VVDS-UDEEP, 3D-HST, and follow-up optical spectroscopic of X-ray sources in the SXDS from Akiyama et al. (2015) reach an i-band magnitude of 24.75 mags.

2.3 PSF-Convolved Photometry

When combined together, photometric data in 13 photometric bands were obtained from the deep imaging surveys previously described. Because the instruments used to perform each survey is different and each of them was conducted in different seeing conditions, the shape, and sizes of the point-spread function are different. PSF-convolved photometry was performed to obtain accurate colors and flux measurements of the AGNs.

Proper treatment of the PSF and deblending of the sources using PSF-convolved photometry is important for photometric redshift estimation and SED fitting. This is because photo-z analysis relies

[2] SERVS Team 2020
[3] https://www.nottingham.ac.uk/astronomy/UDS/data/data.html

on comparing the observed colors and fluxes with those estimated from template models. This process is especially important for the mid-infrared dataset such as SERVS which suffers from severe blending due to the larger PSF size compared to the other datasets.

Prior-based PSF-convolved photometry was performed using T-PHOT (Merlin et al., 2015, 2016). Morphological information of an object from a high angular resolution image is used to measure its flux in images with low angular resolution. The HSC r-band was used as the high angular resolution prior thanks to the better depth and angular resolution compared to the other bands. In this work, the WCS system defined in the HSC S19A internal dataset was adopted and other datasets were resampled to it. The process of image alignment, background subtraction, and preparation of variance images are described in appendix A.

2.4 Multi-band Survey Area

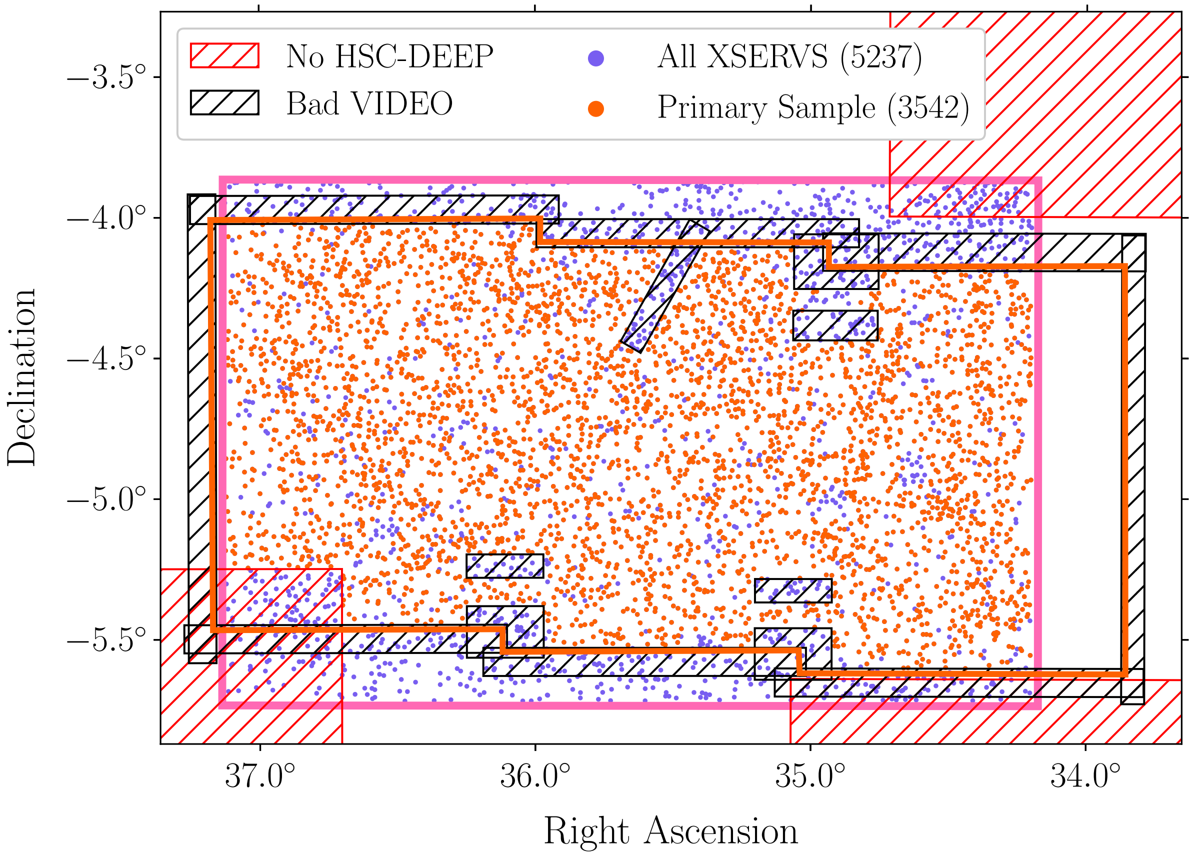

Figure 2.2: The distribution of X-ray sources from the XMM-SERVS point source catalog in the HSC-Deep field. X-ray sources within the multi-band survey area are shown in orange. The black hatched area shows the edge and bad detector regions of the VIDEO dataset. The red-hatched region shows the area covered by the HSC survey. This figure was reproduced with permission from Vijarnwannaluk et al. (2022).

The quality of photometric redshifts depends strongly on the number of photometric bands used. In order to ensure that the AGN sample contains optical/infrared data of equal quality and with a similar number of bands, the survey area of the X-ray sample was redefined based on the availability of multiband photometry. Two conditions were considered including 1)The X-ray counterpart is in the optical infrared survey coverage and 2) The counterpart is not in any bright star masks of HSC or in the bad regions of VIDEO H-band.

The first condition maximizes the coverage of multiband photometry since some portions of X-ray datasets lack some imaging datasets. The second condition removes regions affected by image artifacts

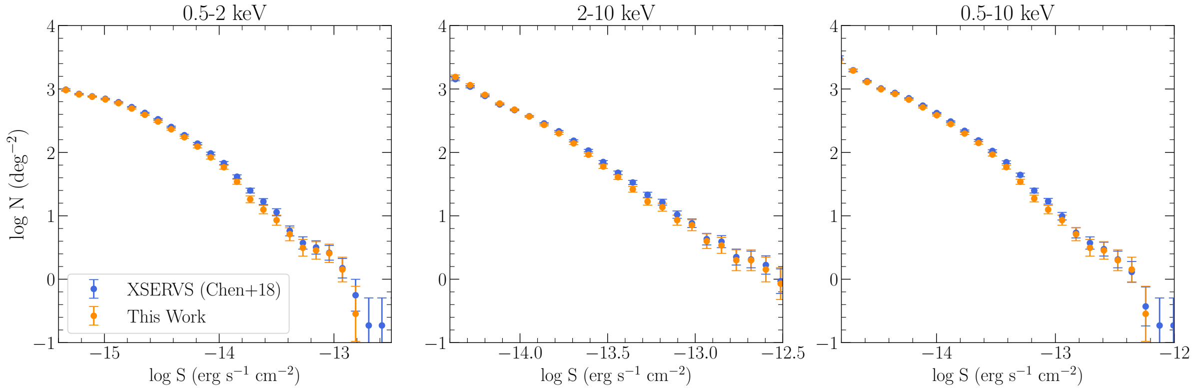

Figure 2.3: $\log N - \log S$ of the X-ray sources in the redefined survey area (orange) compared with that of the full XMM-SERVS (blue) in the 0.5-2 keV, 2-10 keV, and 0.5-10 keV bands. This figure was reproduced with permission from Vijarnwannaluk et al. (2022).

such as stray light, bright star halos, and edges of the images. Figure 2.3 shows the distribution of the X-ray and the boundary of the multiband survey. Only 3542 X-ray sources out of the 5237 XMM-SERVS X-ray sources fall in the multiband survey area which was used for statistical analysis.

A Monte Carlo simulation was performed in order to estimate the size of the multiband survey area. 100,000 mock data points were randomly distributed within the XMM-SERVS area in Chen et al. (2018) and the fraction of data points that fall into the multiband survey area over the total X-ray survey area was calculated. The multiband survey area for statistical analysis is 3.52 square degrees. In order to ensure that the statistical properties of X-ray sources in the redefined survey area are conserved, the $\log N - \log S$ diagram in each band was constructed and compared with that from Mauduit et al. (2012) shown in figure 2.3. There is no significant difference in the measurements hence the survey area is appropriate for statistical analysis.

2.5 Matching with X-ray Dataset

The optical-infrared counterpart has already been determined by Chen et al. (2018) using a maximum-likelihood crossmatch with optical-infrared catalogs in the survey area. The counterpart was matched with the multi-band photometric catalog using a $2''$ radius and found 3180 sources with a counterpart in the PSF-convolved photometric catalog. The majority of X-ray sources (2762 sources) were matched with the mid-infrared source which has the lowest angular resolution. Hence, the source may be blended due to the large PSF size. The number of r-band detected neighbors within a $2''$ radius of the SERVS-matched counterpart was examined and 342 sources have multiple optical counterparts. This suggests that they are blended in the mid-infrared. The source with the brightest 3.6μm magnitude was chosen as the optical counterpart which changes the optical counterpart of 23 AGN.

2.6 Recovery of r-band Non-detected X-ray Source

362 ($\sim 10\%$) sources have no corresponding optical counterpart in the PSF-convolved catalog but have a significant detection in the NIR bands. This suggests that they are either high redshift galaxies ($z > 4$) or they are in heavily dust-obscured host galaxies. Figure 2.4 shows an example of these sources.

PSF-matched photometry was performed using the VIDEO H-band photometry as the detection image, in order to recover the photometry of the r-band non-detected AGN. PSF-matched cutouts of each AGN after matching the PSF of each dataset to that of VIDEO H-band. Aperture photometry was performed using a $2''$ diameter aperture with SExtractor in dual-image mode. Aperture loss was corrected using growth curves calculated from the VIDEO H-band and were constructed in each patch individually. The $2''$ diameter aperture contains $\sim 80\%$ of the PSF flux. By performing the correction patch by patch, the PSF variability in H-band is taken into account over the survey area. Prior-based PSF convolved photometry was performed using the VIDEO H-band images as the high-resolution images instead of the r-band for the mid-infrared datasets.

For 282 of the 362 HSC S19A r-band non-detected sources, the photometry was obtained based on near-infrared detection. The remaining 80 sources lack both HSC S19A r-band and VIDEO H-band detection but faint HSC S19A i-band objects close to the detection limit can be seen in some objects. These remaining sources were not recovered due to their faintness which results in uncertain optical identification. Lastly, the r-band detected PSF-convolved catalog was combined with the H-band detected PSF-matched catalog into a single AGN catalog. In total, multi-wavelength photometry for 3462 (97.7%) out of the 3542 primary X-ray sources was obtained. The catalog was presented as part of Vijarnwannaluk et al. (2022).

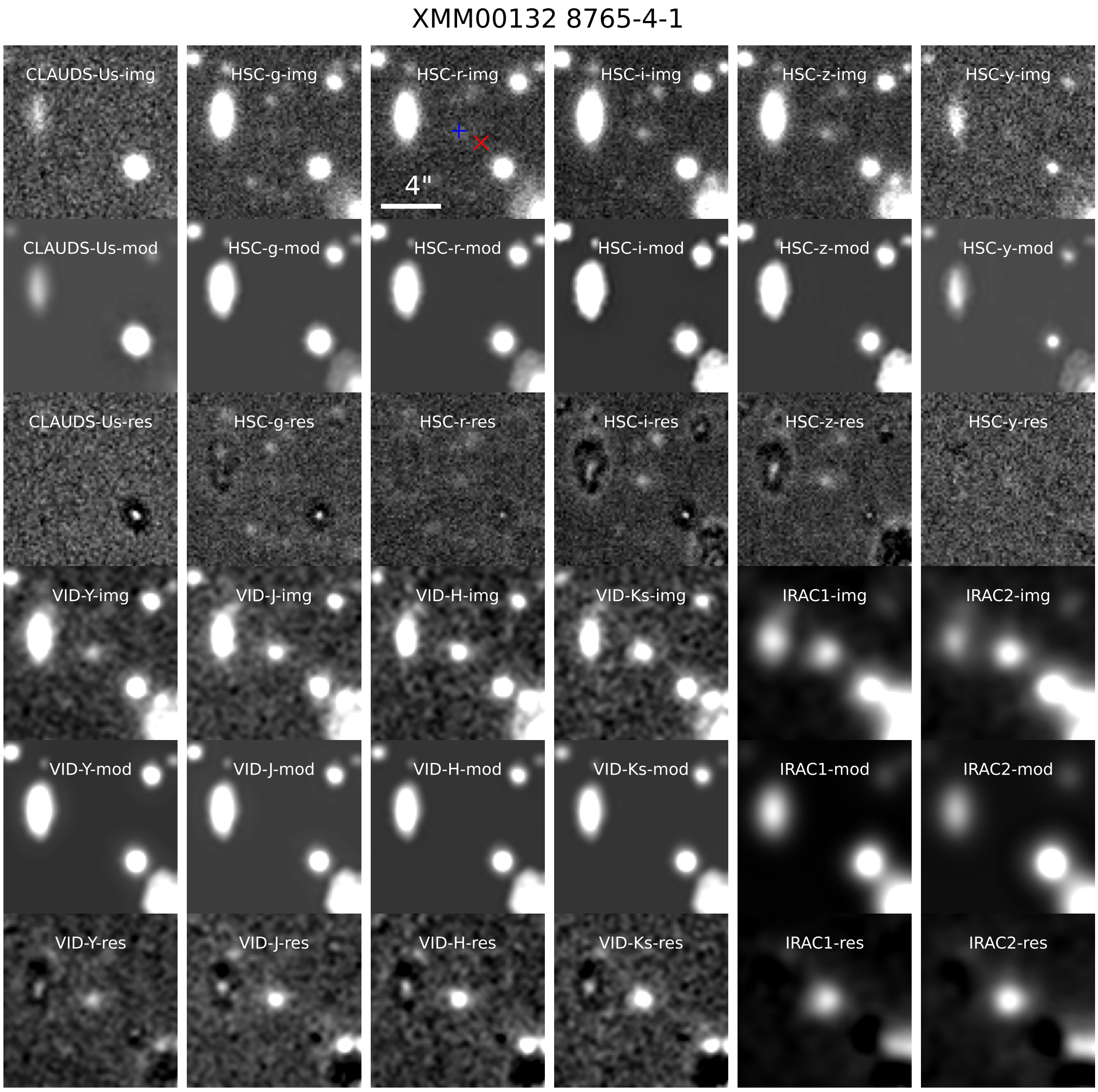

Figure 2.4: The first and fourth row shows the cutout images of an optical-IR counterpart of an X-ray source in each photometric band. The second and fifth rows show the model images from the T-PHOT fitting process. The third and sixth rows show the residual images of the model fitting. The red cross and blue plus show the center of the X-ray source and optical counterpart, respectively. This figure was reproduced with permission from Vijarnwannaluk et al. (2022).

2.7 Photometric Redshift

Only 1321 or 3462 of the X-ray sources have spectroscopic redshift from spectroscopic surveys. The photometric redshift code LePhare (Arnouts et al., 1999; Ilbert et al., 2006) was used to calculate the photometric redshift of the remaining X-ray sources and galaxies.

Galaxy templates from Ilbert et al. (2009) were used for spectroscopically confirmed galaxies. For X-ray sources, templates from Ilbert et al. (2009) which includes templates of the galaxy from Ilbert et al. (2009), AGN templates, and hybrid templates were used instead.

The model magnitudes were calculated between redshift 0 to 6 in steps of 0.05. Both SMC and Calzetti extinction laws were used (Prevot et al., 1984; Calzetti et al., 1994) and fit the reddening as a free parameter with E(B-V) of 0, 0.025, 0.005, 0.075, 0.01, 0.02, 0.03, 0.04, 0.05, 0.06, 0.07, 0.08, 0.09, 0.1, 0.125, 0.15, 0.175, 0.2, 0.25, 0.3, 0.35, 0.4, 0.45, 0.5, 0.55 and 0.6 mag. The contribution from emission lines was added in spectroscopically confirmed galaxies but not for X-ray sources. The systematic zero-point shifts were estimated automatically by LePhare using a spectroscopically confirmed galaxy sample and applied to the X-ray-detected AGN sample. The correction values are shown in Table 2.1. Additional photometric uncertainty (ERR_SCALE) of 0.05 mag was added into the quadrature to include any additional systematic uncertainty in the photometry.

Band	δmag	Band	δmag
CLAUDS-u^*	0.156	VIDEO-Y	0.002
HSC-g	-0.027	VIDEO-J	0.049
HSC-r	-0.037	VIDEO-H	0.070
HSC-i	-0.0254	VIDEO-Ks	-0.021
HSC-z	-0.022	SERVS-3.6μm	-0.005
HSC-y	-0.044	SERVS-4.5μm	0.003

Table 2.1: The zero point shifts calculated with LePHARE.

The photometric redshift performance was evaluated against spectroscopically confirm samples of the same population (eg. AGN or galaxy). In the literature, photometric redshift performance is judged with two parameters. First, the median absolute deviation or NMAD ($\sigma_{\rm NMAD}$: Hoaglin et al. (1983)). NMAD is defined as

$$\sigma_{\rm NMAD} = 1.48 \times \text{Median}\left(\frac{|z_{\rm phz} - z_{\rm spec}|}{1 + z_{\rm spec}}\right)$$

where $z_{\rm phz}$ and $z_{\rm spec}$ are the photometric redshift and spectroscopic redshift, respectively. Second, the outlier fraction ($f_{\rm out}$) which is the fraction of objects whose normalized absolution deviation $(z_{\rm phot} - z_{\rm spec})/(1+z_{\rm spec})$ is larger than 0.15 in the spectroscopic redshift sample. While the threshold to consider a photo-z estimate as an outlier is arbitrary, a value of 0.15 was adopted following studies in deep multiwavelength fields (Ilbert et al., 2009; Laigle et al., 2016).

The photometric redshift performance was evaluated for non-stellar sources outside the stellar locus of the $g - z$ against $z - 3.6\mu$m plane. In the $g - z$ against $z - 3.6\mu$m plane, the boundary is defined as

$$(g - z) - 0.5937(z - [3.6]) < -1.7$$

where g, z and [3.6] are the g, z, and 3.6μm band magnitudes. The performance of sources using galaxy templates was considered for spectroscopically confirmed galaxies and AGN templates for X-ray sources. A comparison between photo-z and spec-z of X-ray non-detected and X-ray detected sources are shown in the left and right panels of figure 2.5. For the spectroscopically confirmed galaxies, a photometric redshift scatter $\sigma_{\rm NMAD}$ of 0.031 and outlier fraction $f_{\rm out}$ of 3% was achieved. For X-ray detected AGN, a photometric redshift scatter ($\sigma_{\rm NMAD}$) of 0.07 and an outlier fraction ($f_{\rm out}$) of 26% was achieved with 4 catastrophic failures where the photometric redshift cannot be determined. The $\sigma_{\rm NMAD}$ and $f_{\rm out}$ for X-ray detected sources are worse than X-ray non-detected sources. It is well known that accurate photometric redshifts of AGNs are challenging to obtain especially for unobscured AGN which tends to have a flat featureless UV-optical continuum. However, for discussing the obscured fraction over a broad redshift range which is presented in chapter 3, the photometric redshift performance is sufficient.

The redshift distribution of the AGNs is shown in figure 2.6. Thanks to the deep multiwavelength datasets and the abundance of spectroscopic surveys in the area, redshift completeness of 99.8% was reached.

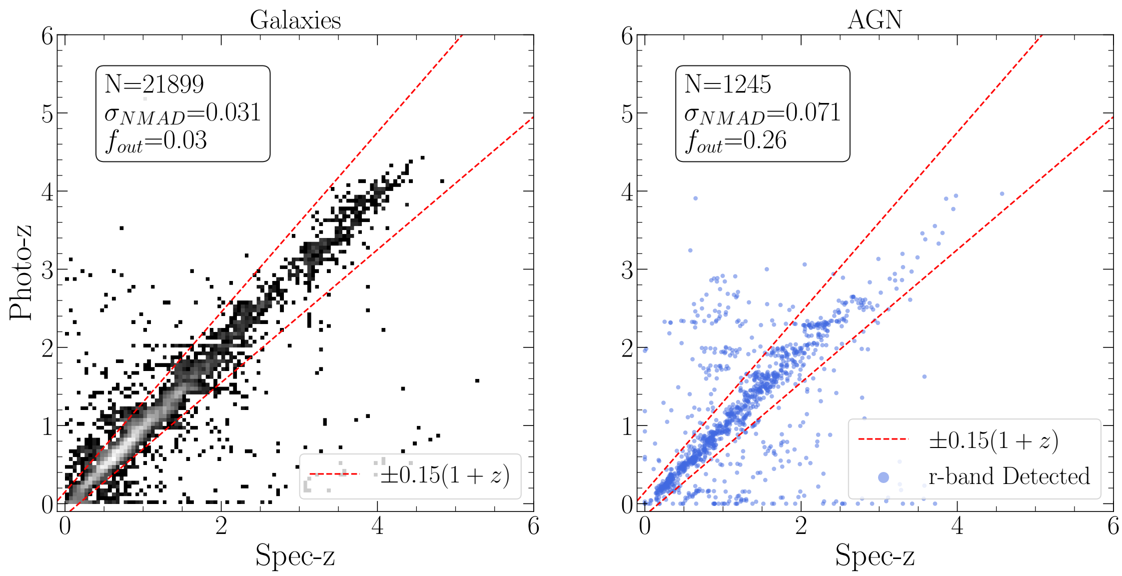

Figure 2.5: Photometric redshift compared with spectroscopic redshift measurements of galaxies without X-ray detection (left) and X-ray detected galaxies (right). The photometric redshift estimation performance statistics are shown at the top left. This figure was reproduced with permission from Vijarnwannaluk et al. (2022).

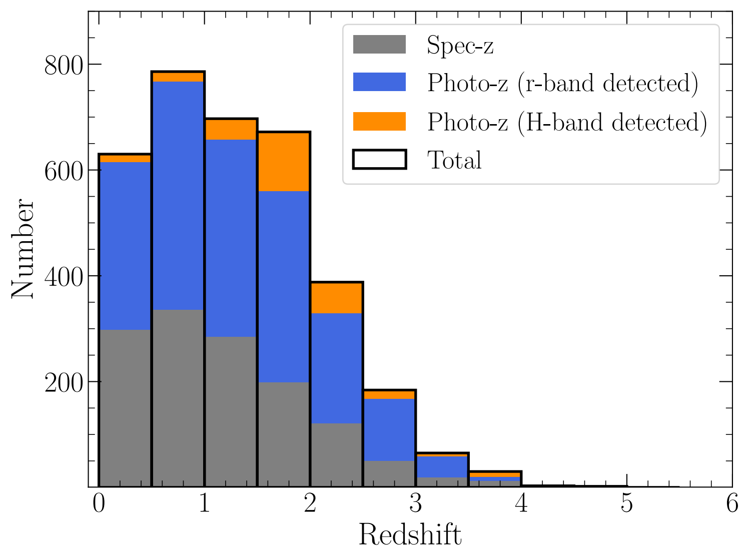

Figure 2.6: The redshift distribution of the X-ray sources. Spectroscopic redshift, photometric redshift from r-band detected source, and photometric redshift from H-band selected sources are shown in gray, blue, and orange from bottom to top, respectively. This figure was reproduced with permission from Vijarnwannaluk et al. (2022).

Chapter 3

The Fraction of Luminous Obscured AGN at $z \geq 2$

Abstract

Statistical studies of X-ray selected Active Galactic Nuclei (AGN) indicate that the fraction of obscured AGN increases with increasing redshift, and the results suggest that a significant part of the accretion growth occurs behind obscuring material in the early universe. The obscured fraction of highly accreting X-ray AGN at around the peak epoch of supermassive black hole growth was investigated using the wide and deep X-ray and optical/IR imaging datasets. The photometric redshift, hydrogen column density, and 2-10 keV AGN luminosity of 306 2-10 keV detected AGN above redshift 2 was estimated. The obscured fraction of AGN was estimated assuming parametric X-ray luminosity and absorption functions. The results suggest that $76^{+4}_{-3}\%$ of luminous quasars ($\log L_X$ (erg s^{-1}) > 44.5) above redshift 2 are obscured. Both the obscured and unobscured $z > 2$ AGN show a broad range of SEDs and morphology, which may reflect the broad variety of host galaxy properties and physical processes associated with the obscuration.

3.1 X-ray Count-rate Analysis

3.1.1 X-ray Spectral Model

An X-ray AGN spectral model needs to be assumed in order to calculate the AGN properties. The most basic model for AGN is a power-law spectrum with a slope (also known as photon-index, Γ). This model works well in most cases of unobscured AGN where there is no photoelectric absorption. However, the spectral model of obscured AGN is much more complex due to reprocessing of the AGN X-ray continuum by absorption, scattering, and reflection as shown in figure 3.1. A phenomenological X-ray AGN model which includes the following main components was adopted for analysis. The XSPEC model names are listed in parentheses.

1. An Exponential cutoff power-law (zcutoffpl): The exponential decaying power-law represents the intrinsic AGN X-ray continuum emission. The continuum us modeled with a power-law with a roll-off at high energy X-rays ($\sim$ 300 keV). It is a multiplicative model combined with a typical power law and an exponentially decaying function at high energy. The spectrum is expressed as $A(E) = K[E(1+z)]^{-\alpha} \exp(-E(1+z)/\beta)$ where A(E) is the photon flux density (photons keV cm^{-2} s^{-1}), E is the energy, z is the redshift α is the photon-index, and β is the e-folding energy of exponential roll-off.

2. Reflection component (Pexrav) : Pexrav (Magdziarz and Zdziarski, 1995) represents the reflected AGN continuum off a neutral material. This appears as a "bump" in the X-ray spectral at approximately $\sim$ 30 keV. Currently, the geometry and the origin of the reflector is highly debated with some studies suggesting the reflection is due to the AGN accretion disk while other suggest that the reflection is due to the dusty torus (Panagiotou and Walter, 2019; Ricci et al., 2011). The model is

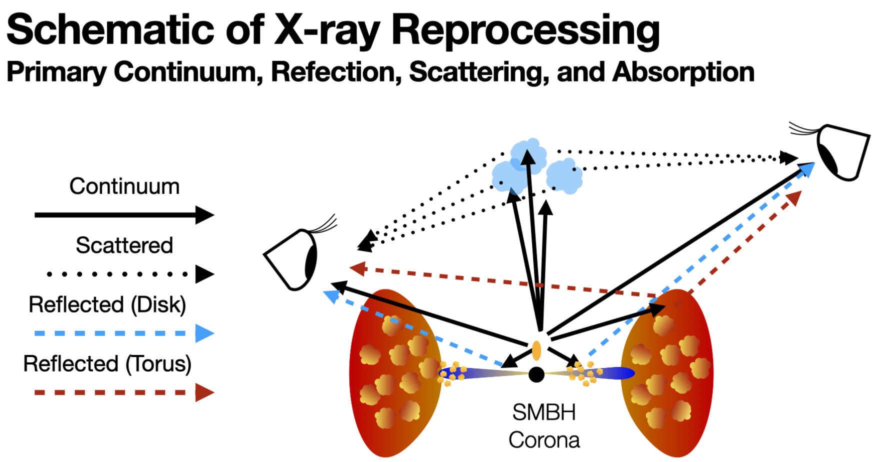

Figure 3.1: Reprocessing of the AGN continuum (thick line) by Thomson scattering (dotted line) and reflection by the AGN torus (red dashed line) and the AGN disk (blue dashed lines). The left-hand side shows the case of an obscured AGN where the continuum is absorbed while the right-hand side for the case of an unobscured AGN.

a tabulated model based on a Monte Carlo simulation. The parameters include the photon index, the cutoff energy, the reflection scaling factor, the redshift, the abundance of elements heavier than He relative to solar, the relative abundance of iron, and the cosine inclination angle. By itself, the model includes the exponential decaying power law but can be removed by setting the relative reflection to negative values.

3. Scattered component (f_{scat}): A portion of the AGN continuum is scattered into the line of sight by photoionized gas by Thomson scattering (Noguchi et al., 2010; Gupta et al., 2021). The strength of the scattering is approximately 1-5% of the intrinsic continuum. The scattered emission was modeled using the same exponential cutoff power law but at a 1% intensity.

4. Photoelectric absorption (zphabs): zphabs represents the main X-ray absorber along the line of sight. The parameters include the redshift (z) and the Hydrogen column density ($N_{\rm H}$).

These models are combined together to construct the intrinsic X-ray spectral model as

$$\mathrm{TBabs(zphabs * cabs * zcutoffpl + pexrav + f_{scat} * zcutoffpl)}$$

where optically-thin Compton Scattering (cabs) and galactic absorption (Tbabs) in the model was included. In this phenomenological model, the hydrogen column density affects solely the AGN continuum emission and not the scattered component or the reflection component of the AGN. An example of the obscured and unobscured AGN model is shown in figure 3.2.

3.1.2 Hydrogen Column Density

The most accurate method to determine the hydrogen column density is to perform an X-ray spectral analysis of the AGN. However, a large number of counts (> 100) is required in order to perform accurate spectral analysis. This can be difficult to obtain for faint sources at high redshift and especially difficult for obscured sources due to the long integration time needed. An alternative approach to determine the hydrogen column density is to use the X-ray hardness ratios. This method uses the observed count rates in broad energy bands which have many more counts to estimate the hydrogen column density but with an increased accuracy.

The X-ray hardness ratio (HR) describes the shape of the X-ray spectra using two or more broad X-ray bands such as the 0.5-2 keV and 2-10 keV bands. In the current literature, HR is typically defined

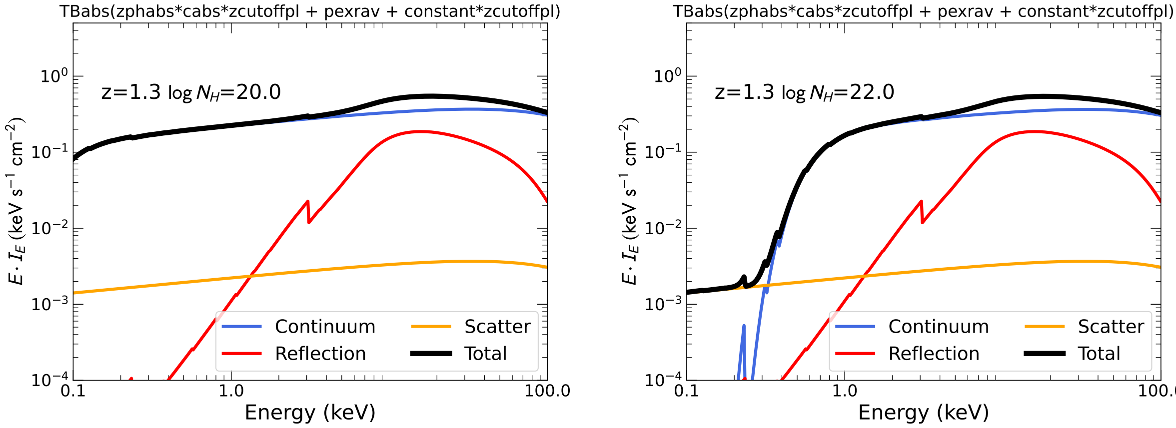

(a) Unobscured **(b)** Obscured

Figure 3.2: The unfolded X-ray spectra of an unobscured AGN with $\log N_{\mathrm{H}}$ [cm^{-2}] = 20 (a) and an obscured AGN with $\log N_{\mathrm{H}}$ [cm^{-2}] = 22 (b) at $z \sim 1.3$. The AGN transmitted continuum, reflected component and scattered component are shown in blue, red, and orange, respectively. The total spectrum is shown in black.

as

$$HR = \frac{H - S}{H + S}$$

where S is the count-rates in the soft 0.5-2 keV band and H is the count-rates in the 2-10 keV band. As shown in figure 3.2, the lower(softer) energy X-rays are more affected by obscuration than the higher(harder) energy X-rays. As the column density increases, more of the harder X-rays will be absorbed. Therefore, the X-ray hardness ratio will increase as a function of column density. In principle, this allows us to trace back the observed hydrogen column density based on the observed hardness ratio.[1]

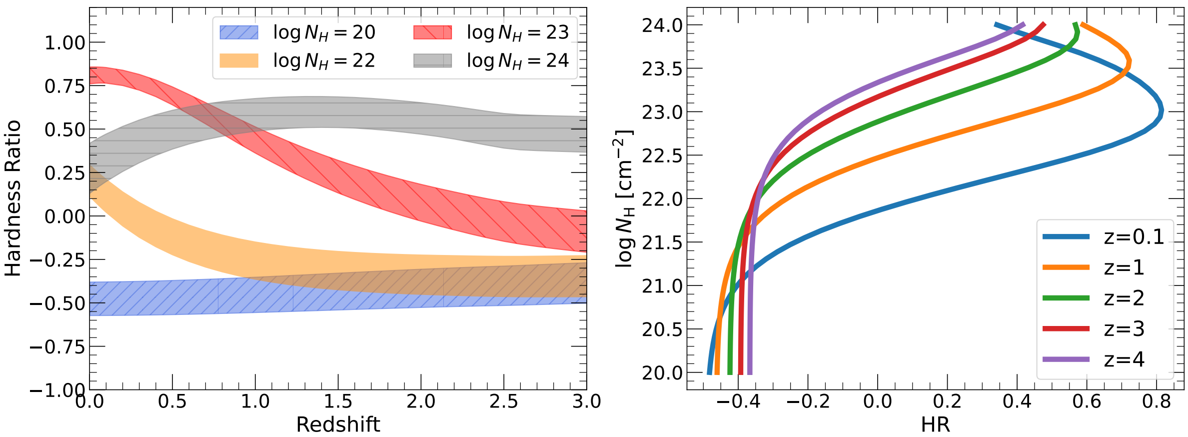

Figure 3.3: (Left) The expected hardness ratio based on the phenomenological AGN model as a function of redshift for hydrogen column density of $\log N_{\mathrm{H}}$ [cm^{-2}] $= 20, 22, 23$ and 24 shown in blue, orange, red, and gray, respectively. The width of each band shows the range of hardness ratio when assuming a photon index of 2 (bottom) to 1.5 (top). (Right) The hydrogen column density as a function of hardness ratio for z =0.1,1,2,3 and 4 is shown in blue, orange, green, red, and purple, respectively.

An X-ray spectral model and the corresponding calibration files of the detector must be assumed in order to use this method. Figure 3.3 shows the X-ray hardness ratio as a function of redshift assuming the phenomenological X-ray model described in section 3.1.1. The width of each band shows the HR

[1]The true N_{H} is unknown and this method estimates N_{H} under a model assumption and observed HR.

assuming a photon index of 1.5-2.0 which is the typical range of the photon index of AGN with a photon index of 1.8 as a nominal value. Here, the redistribution matric files (RMF) and auxiliary response files (ARF) of the PN detector were used. It should be pointed out that in practice, determining the hydrogen column density from X-ray hardness ratio is much more uncertain than using X-ray spectra due to degeneracy in the hardness ratio which arises from the model assumptions but is one of the only methods available to constrain the hydrogen column density for faint sources.

3.1.3 X-ray Survey Sensitivity

Because obscured AGN appears fainter than unobscured AGN and X-ray survey depth is not completely uniform over the survey area, the effective survey area with sufficient survey depth to detect obscured AGN is smaller than unobscured AGN of the same intrinsic luminosity. The survey area function ($\Omega(L_X, z, \log N_{\rm H})$) is used to represent the survey area as a function of the intrinsic AGN properties. This function is used to account for bias in the survey area due to absorption and flux limit.

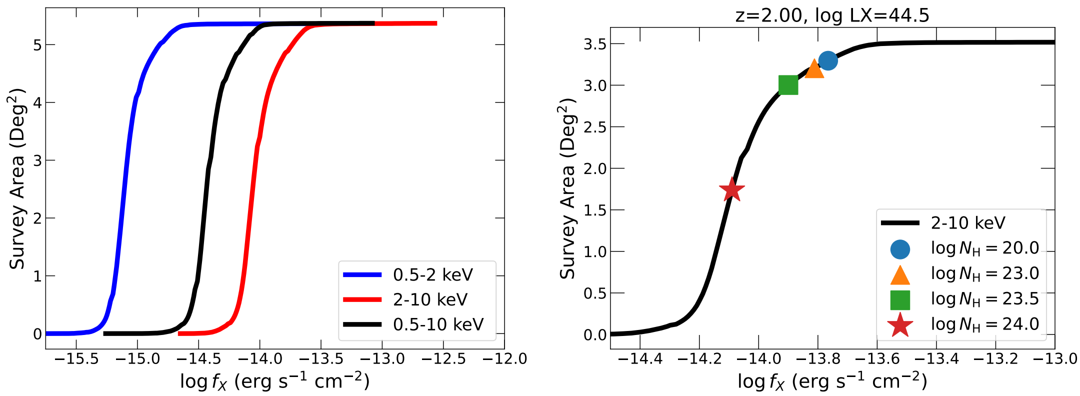

Figure 3.4: (Left) The survey area as a function of survey flux limit in 0.5-2, 2-10, and 0.5-10 keV shown in blue, red, and black, respectively. (Right) The survey area in the 2-10 keV band with sufficient survey depth to detect an AGN at $z = 2$ AGN with 2-10 keV luminosity of $\log L_{\rm X}$ [erg s^{-1}] $= 44.5$ assuming a hydrogen column density of $\log N_{\rm H}$ [cm^{-2}] =20, 23, 23.5, and 24, respectively.

The phenomenological AGN model and PN-detector calibration files were used to construct the survey area function $\Omega(L_X, z, \log N_{\rm H})$ as a function of redshift, 2-10 keV AGB luminosity, and $\log N_{\rm H}$. The original survey area curve reported by Chen et al. (2018) is considered and is shown in the left figure of figure 3.4. The effect of X-ray absorption is shown in the right figure of figure 3.4. For unobscured AGN with $\log N_{\rm H} = 20$ and a 2-10 keV luminosity of $\log L_X$ [ergs^{-1}] $= 44.5$ at $z = 2$, the survey area with sufficient depth to detect it is 3.52 Deg^2. However, for obscured AGN with large column density near Compton-thick, the survey area drops by half. The calculation was performed over a range of redshift, $\log N_{\rm H}$, and 2-10 keV luminosity. An example of the survey area is shown in figure 3.4 for redshift 1 and 2.5.

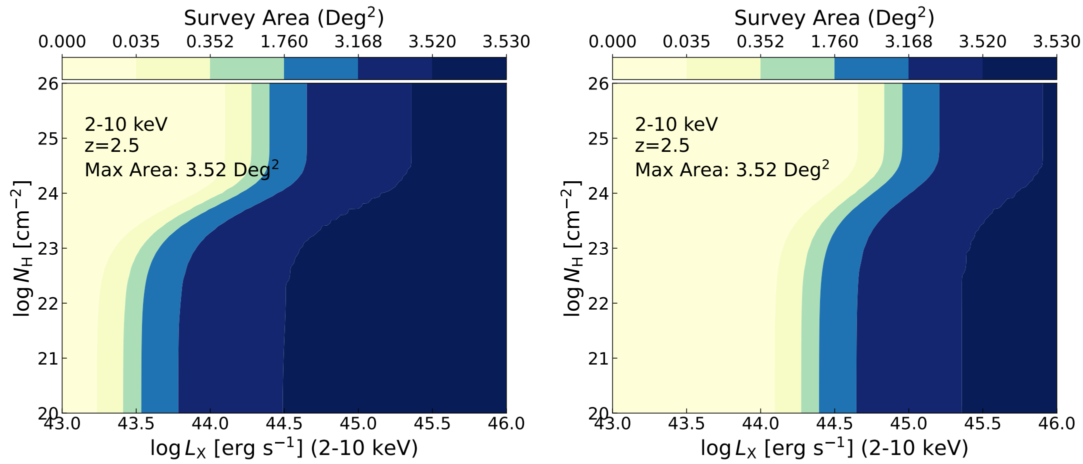

Figure 3.5: The survey area function $\Omega(L_{\mathrm{X}}, z, \log N_{\mathrm{H}})$ for AGN at $z = 1$ (left) and $z = 2.5$ (right).

3.2 Absorption Function

The absorption function f_{abs} was introduced in Ueda et al. (2003). It is a probability distribution function defined between $\log N_{\mathrm{H}}$ (cm^{-2}) $= 20 - 26$. The shape of the absorption function reflects the column density distribution at that redshift and by integrating the column density bins with the luminosity function, the intrinsic number of AGN with $\log N_{\mathrm{H}}$ can be estimated. The function is normalized to 1 between $\log N_{\mathrm{H}}$ (cm^{-2}) $= 20 - 24$ as follows,

$$\int_{20}^{24} f_{abs}(L_X, z; N_{\mathrm{H}}) d\log N_{\mathrm{H}} = 1$$

However at high redshift, the amount of absorption between $\log N_{\mathrm{H}}$ (cm^{-2}) $= 20 - 22$ cannot be distinguished with the HR. Modification of the absorption function was performed by combining the $\log N_{\mathrm{H}}$ bins between 20-22 together and re-normalizing the function. The definition is as follows,

$$f_{abs}(L_X, z; N_{\mathrm{H}}) = \begin{cases} \frac{1-\psi(L_X,z)}{2} & [20 \leq \log N_{\mathrm{H}} < 22] \\ \frac{1}{1+\epsilon}\psi(L_X, z) & [22 \leq \log N_{\mathrm{H}} < 23] \\ \frac{\epsilon}{1+\epsilon}\psi(L_X, z) & [23 \leq \log N_{\mathrm{H}} < 24] \\ \frac{f_{\mathrm{CTK}}}{2}\psi(L_X, z) & [24 \leq \log N_{\mathrm{H}} < 26] \end{cases} \tag{3.1}$$

where $\psi(L_X, z)$ is the fraction of CTN-AGN with $\log N_{\mathrm{H}}$ (cm^{-2}) ≥ 22 and ϵ is the ratio of AGN with $\log N_{\mathrm{H}}$ (cm^{-2}) $= 23 - 24$ to those with $\log N_{\mathrm{H}}$ (cm^{-2}) $= 22 - 23$, and f_{CTK} is the relative number of Compton-thick AGN (CTK-AGN) relative to obscured CTN-AGN, which is fixed to 1.

$\psi(L_X, z)$ describes the dependency on redshift and luminosity of the absorption function. The obscured fraction in the local universe is parameterized as a linearly decreasing function of X-ray luminosity:

$$\begin{aligned} \psi(L_X, z) =& \min[\psi_{max},\ \max[\psi_{43.75}(z) \\ & - \beta(\log L_X - 43.75), \psi_{min}]] \end{aligned} \tag{3.2}$$

where ψ_{min} and ψ_{max} is the minimum and maximum obscured fraction of CTN-AGN, which is determined to be 0.2 and 0.84, respectively (Ueda et al., 2014). The original formalism of the absorption function will return negative probability in $\log N_{\mathrm{H}}$ (cm^{-2}) $= 20-21$ bin at large obscured fraction larger than 0.82. However, by combining the $\log N_{\mathrm{H}}$ (cm^{-2}) $= 20 - 22$ bin, this effect is removed. Hence, larger values of ψ_{max} are allowed as discussed in the later sections. β is the slope of the decrease which is set to 0.24 (Ueda et al., 2014) and $\psi_{43.75}(z)$ is the obscured fraction at a 2-10 keV luminosity of $\log L_X$ (erg s^{-1}) $= 43.75$.

$\psi(L_X, z)$ describes the redshift evolution of the obscured fraction as a function of $\psi_{43.75}(z)$

$$\psi_{43.75}(z) = \begin{cases} \psi^0_{43.75}(1+z)^{a1} & z < 2.0 \\ \psi^0_{43.75}(1+2)^{a1} = \psi^2_{43.75} & z \geq 2.0 \end{cases} \tag{3.3}$$

where $\psi^0_{43.75}$ is the obscured fraction in the local universe at 2-10 keV luminosity of $\log L_X$ (erg s^{-1}) = 43.75 which is set to 0.43 ± 0.03 (Ueda et al. (2014)). a_1 describes the evolution of the obscured fraction with the best-fitted value of 0.48 ± 0.05. A constant $\psi_{43.75}(z = 2) = \psi^2_{43.75}$ in the redshift range above redshift 2 was assumed.

The parameter $\psi_{43.75}(z)$ is not limited to between ψ_{min} and ψ_{max} and solely describes the evolution of the obscured fraction $\psi(L_X, z)$. $\psi_{43.75}(z)$ is equal to $\psi(43.75, z)$ only when $\psi_{43.75}(z) \leq \psi_{max}$ but the obscured fraction of higher luminosity AGN can still be lower. Therefore, interpretation of the obscured fraction is $\psi(L_X, z)$ and not solely on $\psi_{43.75}(z)$. For the remaining free parameters of the luminosity function, the best-fitted values provided by Ueda et al. (2014) were adopted.

3.3 Maximum Likelihood Fitting

The maximum likelihood (ML) method is a parametric fitting method that does not require any binning of the dataset. It relies on each sample to estimate the likelihood function from individual probability. The product of all probability densities (P) in the sample is called the likelihood (L). The probability density of finding the i-th object with $\log N^i_{\mathrm{H}}$ at $\log L^i_X$ and z^i is defined as P_i

$$P_i = \frac{f_{abs}(L^i_X, z^i; \log N^i_{\mathrm{H}})\Omega(L^i_X, z^i, \log N^i_{\mathrm{H}})}{\int_{20}^{24} f_{abs}(L^i_X, z^i; \log N_{\mathrm{H}})\Omega(L^i_X, z^i, \log N_{\mathrm{H}}) d\log N_{\mathrm{H}}}$$

where f_{abs} and Ω is the absorption function and survey area function, respectively.

It is more convenient to calculate the likelihood function in the logarithmic form $\mathcal{M}$ where the product becomes a sum of the probability density instead

$$\mathcal{M}(\psi^2_{43.75}, \epsilon) = -2 \sum_i \ln P_i(\psi^2_{43.75}, \epsilon).$$

The minimum point of the likelihood gives the best-fitted parameter of interest. In this case, the parameter ϵ and $\psi^2_{43.75}$ were set free parameters for the fitting routine and the 1-sigma uncertainty is defined as the range where the log-likelihood value changes from minimum by one.

3.4 High Redshift AGN Sample Selection

I selected a sample of 672 AGN between redshift 2-5 based on the best available redshift (spec-z or photo-z) to estimate the obscured fraction. Among them, 37%(251) was detected in both energy bands. 40% (275) was detected only in the 0.5-2 keV band. 7% (53) were detected only in the 2-10 keV band. The remaining, 13%(93) were detected only in the 0.5-10 keV band and not the other two. The spectroscopic completeness of the sample is 30%(203 AGN) but most of the AGN are broad-line AGN(71%). The extinction-corrected X-ray 2-10 keV luminosity can be calculated using

$$L_X = \mathrm{ext}(z, N_{\mathrm{H}}) k(z) 4\pi D^2_L(z) f_X$$

where $k(z)$ is the k-correction term, and $\mathrm{ext}(z, N_{\mathrm{H}})$ is the absorption correction in the observed frame assuming the best available redshift and $\log N_{\mathrm{H}}$, D_L is the luminosity distance, and f_X is the observed X-ray flux in 2-10 keV band. The PN-equivalent count-rate in the 2-10 keV band was converted into 2-10 keV flux assuming an ECF of 1.26×10^{11} counts^{-1} / erg s^{-1}cm^{-2}.[2] The phenomenological AGN model presented in section 3.1.1 as well as the PN-detector calibration files were used to calculate the extinction correction and the k-correction. The model without absorption was used to calculate the ECF. The flux ratio between the model without absorption to that with $\log N_{\mathrm{H}} = 20 - 24$ is adopted as the extinction correction factor.

The 2-10 keV luminosity and $\log N_{\mathrm{H}}$ of the high redshift AGN are shown in figure 3.6 and 3.7. Most of the AGN possess quasar level luminosity ($\log L_X$ (erg s^{-1}) > 44.5) and are mostly obscured by hydrogen column density larger than $\log N_{\mathrm{H}}$ (cm^{-2}) > 21. Only upper limits can be placed on $\log N_{\mathrm{H}}$ and $\log L_X$ for 0.5-2 keV detected AGN and they show a large scatter. On the other hand, lower limits of $\log N_{\mathrm{H}}$

[2] For 0.5-2 keV and 0.5-10 keV bands, the ECF are 6.84×10^{11} and 3.36×10^{11} counts^{-1}/erg s^{-1}cm^{-2}, respectively

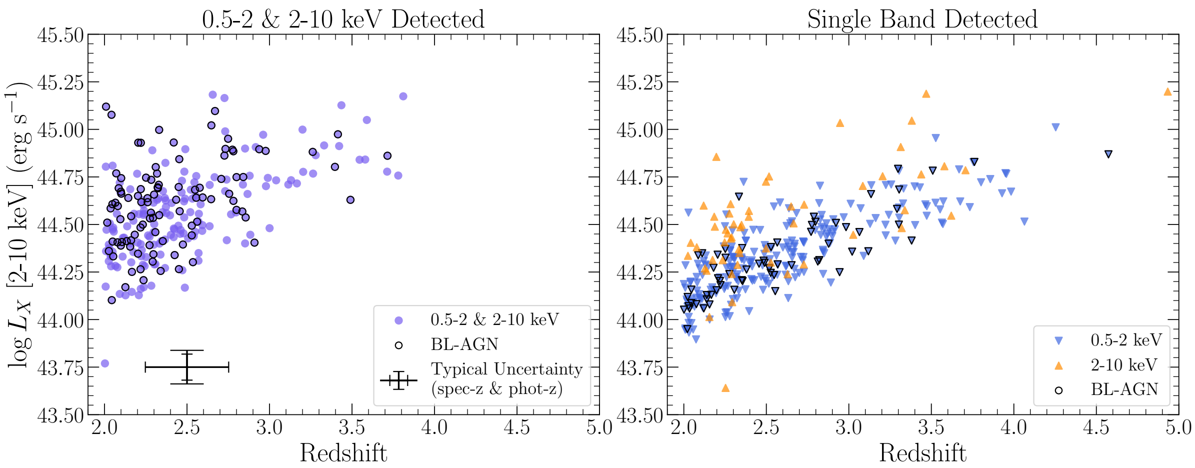

Figure 3.6: The extinction-corrected 2-10 keV luminosity of z=2-5 AGN that is detected in both 0.5-2 keV and 2-10 keV as a function of redshift (purple) is shown in the left-hand panel while the right-hand panel shows for AGN detected only in either the 0.5-2 keV band (blue downward triangle) or the 2-10 keV bands (orange upward triangle). Black open circles represent broad-line AGN. The faceless error bar shows the typical uncertainty for spec-z (long caps) and photo-z samples (long caps). respectively.

and $\log L_X$ are obtained for AGN detected only in the 2-10 keV band. Most of them are located above $\log N_{\rm H} > 23$, which implies that they are heavily obscured AGN.

In the end, only the 304 AGN which was detected in the 2-10 keV band was selected for the statistical analysis since those detected only in the 0.5-2 keV band have uncertain hydrogen column density. The possibility of detecting each AGN was calculated using the survey area function and one AGN was removed because the corresponding survey area is zero. For the AGN detected only in the 2-10 keV band, the Hydrogen column density was assigned to $\log N_{\rm H}$ (cm^{-2}) = 23.5.

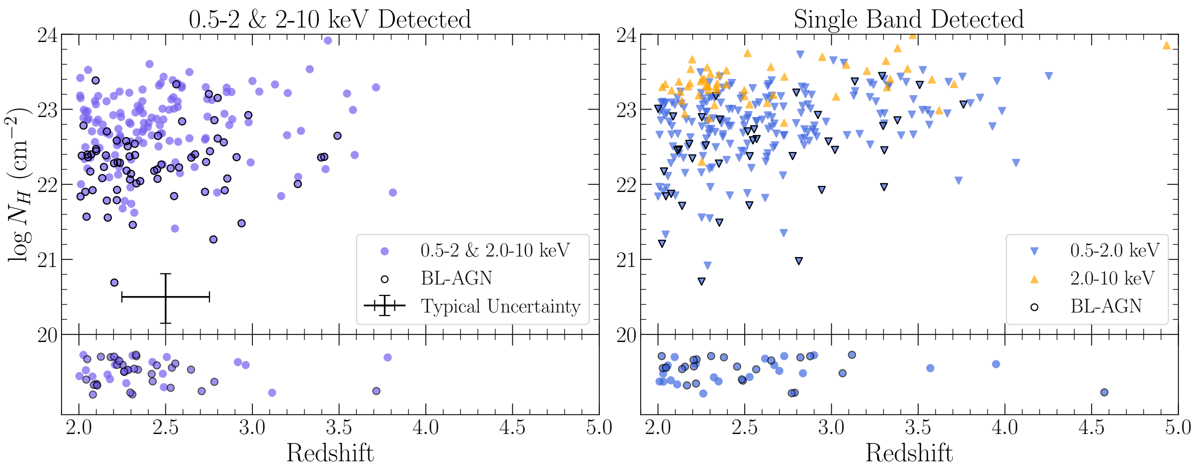

Figure 3.7: The hydrogen column density of z=2-5 AGN that are detected in both 0.5-2 keV and 2-10 keV as a function of redshift (purple) is shown in the left-hand panel while the right-hand panel shows for AGN detected only in either the 0.5-2 keV band (blue downward triangle) or the 2-10 keV bands (orange upward triangle). Black open circles represent broad-line AGN. The faceless error bar shows the typical uncertainty. The bottom panel shows the redshift distribution of AGN with HR softer than the model and is set to $\log N_{\rm H}$ (cm^{-2}) = 20, the data-points in this panel are randomly shifted in y-axis for clarity.

3.5 Results

3.5.1 The Obscured fraction at $z \geq 2$

The fitting was performed under two conditions. First is the 1D fitting where ϵ is fixed to 1.7 as seen in the local universe and $\psi^2_{43.75}$ is set as a free parameter. The 2nd is the 2D where both of $\psi^2_{43.75}$ and ϵ simultaneously. The 1D case was performed as a comparison with the work of Ueda et al. (2014). In addition, I also examined the effect of the choice of the maximum obscured fraction (ψ_{max}). ψ_{max}) was first set to 0.84 following Ueda et al. (2014). Under this setting, the best-fit results are the same as ψ_{max} which suggests that ψ_{max} affects the fitting. Hence, ψ_{max} was set to 0.99 instead. Table 3.1 shows the best-fitted results of both cases.

Parameter	1D	2D
ϵ	1.7 (fixed)	1.4 ± 0.3
$\psi^2_{43.75}$	$1.01^{+0.03}_{-0.04}$	$0.99^{+0.04}_{-0.03}$

Table 3.1: Maximum Likelihood Fitting Results

The obscured fraction was calculated from the intrinsic number of luminous obscured CTN-AGN. The intrinsic number of AGN in each $\log N_{\rm H}$ bin is calculated with the following equation:

$$N = \int\int\int f_{abs}(\log L_X, z, N_{\rm H}) \frac{d\Phi(\log L_X, z)}{d\log L_X} \Omega(1+z)^3 d_A(z)^2 \frac{d\tau}{dz} d\log L_X \; dz \; d\log N_{\rm H} \tag{3.4}$$

where f_{abs}, $d\Phi$, Ω, $d\log L_X$, d_A, and τ are the absorption function, 2-10 keV luminosity function, survey area, angular size distance, and look-back time, respectively. The integration limits are between the redshift, luminosity, and column density of interest. Replacing the survey area with the survey area function $\Omega(L_X, z, \log N_{\rm H})$ gives the expected number of AGN instead.

The expected number of AGNs from the fitting was calculated to examine the reliability of the fitting. The observed $\log N_{\rm H}$ distribution of the 2-10 keV band detected AGN is shown in figure 3.8 and shows that the 2D case reproduces the observed distribution better than 1D. Figure 3.9 based on the best-fitted parameters from the 2D ML-fit shows the distribution of AGN in the 2-10 keV luminosity, $\log N_{\rm H}$, and

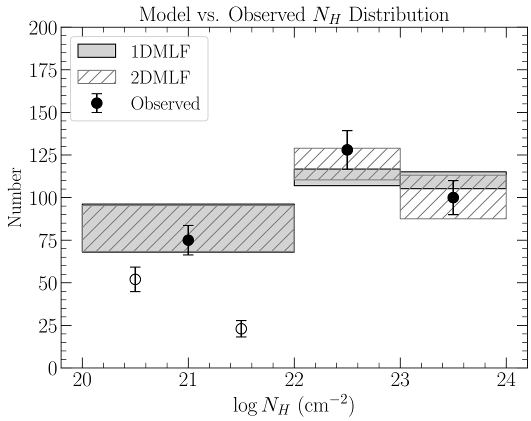

Figure 3.8: Comparison between the $\log N_{\rm H}$ distribution (filled data points) with the expected number of AGN (hatched and shaded area). The filled gray and hatched gray boxes show the 1D and 2D cases, respectively. The vertical width of each box represents the uncertainty of the models. Open round symbols show the unbinned observed number of AGN with $\log N_{\rm H}(\mathrm{cm}^{-2}) < 22$. The expected distributions from 1D and 2D fits are scaled by a factor of 1.72 and 1.68 so that the total number of CTN-AGN is consistent with observation.

redshift plane. The predicted distributions reproduce the observed distribution well and the best-fitted 2D-ML parameters were adopted for further discussion.

To estimate the obscured fraction of luminous AGN, the lower limit of the luminosity integration was set to $\log L_X$ (erg s^{-1}) $= 44.5$ and corresponds to an obscured fraction of $0.76^{+0.04}_{-0.03}$. This boundary corresponds to the break in the hard X-ray luminosity function at $z \sim 2$. In order to compare with other studies, the luminosity limit was set to $\log L_X$ (erg s^{-1}) $= 44 - 45$ which corresponds to an obscured fraction is $0.85^{+0.04}_{-0.03}$ for $\log N_{\rm H}(\mathrm{cm}^{-2}) = 22 - 24$ while obscured fraction with $\log N_{\rm H}(\mathrm{cm}^{-2}) = 23 - 24$ is $0.50^{+0.07}_{-0.06}$.

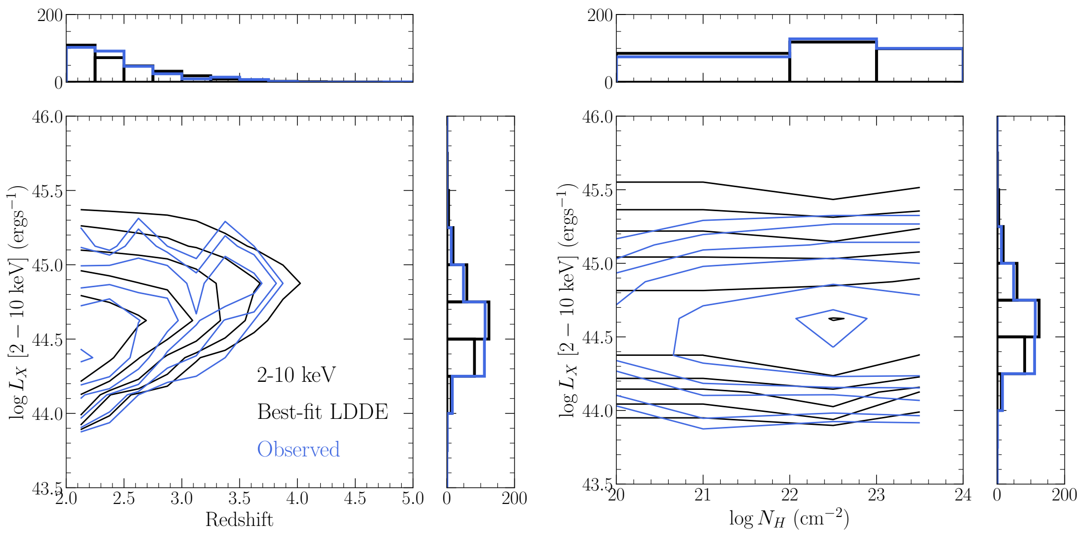

Figure 3.9: 2-10 keV luminosity, redshift, and hydrogen column density distribution. The observed, and expected distribution is shown in blue and black, respectively. The expected distribution was scaled by a factor of 1.68 so that the total number of CTN-AGN is consistent with observation. The projected distribution is shown on the top and right sides of each diagram.

3.5.2 The Slope of the Luminosity Dependence

The model of the obscured fraction assumes dependence on luminosity and does not depend on redshift. This means that the obscured fraction increases at the same rate at all luminosity. In this section, I investigate the slope of the luminosity dependence by allowing the slope parameter β to be a free parameter instead of the obscured fraction which represents the overall normalization. The obscured fraction at $\log L_X$ (erg s^{-1}) ~ 43.5 was set to $\psi^2_{43.75} = 0.73$ following Ueda et al. (2014) and ϵ is set to 1.4 following the 2D ML-fit results.

The fitting suggest that the slope is $\beta = -0.09^{+0.04}_{-0.03}$ and the obscured fraction of luminous CTN-AGN with $\log L_X$ (erg s^{-1}) $= 44 - 45$ is 0.78 ± 0.02. The slope suggests there is nearly no luminosity dependence on the obscured fraction. However, due to the limited luminosity coverage of the sample ($\log L_X$ (erg s^{-1}) $\sim 44 - 45$), the obscured fraction at the most luminous end cannot be reliably constrained.

3.5.3 Obscured Fraction at High Redshift

Here, the best-fitted results are compared with the previous estimations of the obscured fraction in the literature assuming a luminosity range of $\log L_X$ (erg s^{-1}) $\sim 44 - 45$. The best-fit obscured fraction based on the 2D ML best-fit parameters compared with previous measurements in the local universe and at $z > 2$ in figure 3.10. The results suggest that the obscured fraction at high redshift is larger than in the local universe which supports the increasing evolution of the obscured fraction toward high redshift. Again, my results are the largest compared to previous results in the same redshift range except against Liu et al. (2017). They determined the obscured fraction at $\log L_X$ (erg s^{-1}) $= 43.5 - 44.2$ as 0.91 ± 0.03 which is consistent with my results if extrapolated toward lower luminosity without the maximum limit.

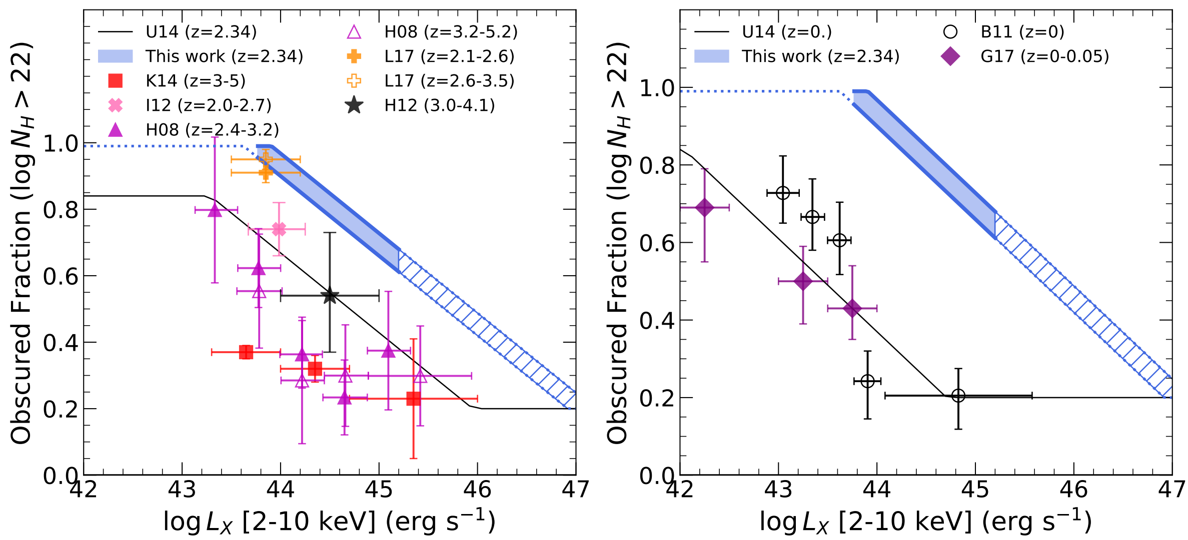

Figure 3.10: Obscured fraction as a function of 2-10 keV luminosity. The left panel shows the results at $z > 2$ compared with Hasinger (2008) (H08; opened and closed magenta triangles), Iwasawa et al. (2012) (I12; pink cross), Hiroi et al. (2012) (H12; black star), Kalfountzou et al. (2014) (K14; red squares), and Liu et al. (2017)(L17; opened and closed plus symbols), and Ueda et al. (2014) (U14, thin black line), respectively. (Right) Same as left but compared with the results at low redshift compared with Burlon et al. (2011) (B11; open black circles), Georgakakis et al. (2017) (G17; purple diamonds), and Ueda et al. (2014)(U14; solid black line), respectively. The lower and upper limit of the model is shown with thick blue lines. The luminosity range of the sample is shown with the shaded area.

The obscured fraction of AGN with $\log N_{\rm H}$ (cm^{-2}) $= 22 - 24$ and $23 - 24$ compared with the results in different redshifts are shown on the left and right panels of figure 3.11, respectively. The results are larger than previous results in the same luminosity range from Ueda et al. (2014) (black solid line).

In a similar redshift, Liu et al. (2017) estimated the obscured fraction using AGN in the C-COSMOS legacy catalog (Civano et al., 2011, 2016) combined with the Chandra deep field south 7M catalog

(CDF-S, Luo et al. 2017). The obscured fraction of AGN with $\log N_{\rm H}({\rm cm}^{-2}) = 22 - 23$ among those with $\log N_{\rm H}({\rm cm}^{-2}) < 23$. For AGN with $\log L_X$ (erg s^{-1}) $= 44.1 - 44.9$ at redshift 2-3, the fraction is 0.67 ± 0.07. Under similar luminosity between $\log L_X$ (erg s^{-1}) $= 44 - 45$ the obscured fraction is $0.70^{+0.05}_{-0.01}$ which is consistent to the above value within 1σ uncertainty.

At redshift 3-5, Vito et al. (2014) estimated the obscured fraction of $\log N_{\rm H}$ (cm^{-2}) $= 23 - 24$ and $\log L_X$ (erg s^{-1}) ≥ 43 as 0.54 ± 0.05. Under the same luminosity and redshift range, the obscured fraction based on the best-fitted results is 0.57 ± 0.05 which is consistent with that of Vito et al. (2014) within 1σ uncertainty.

My results are the largest compared to others that use the LDDE model and are in the same redshift and luminosity range. Hiroi et al. (2012) estimated the obscured fraction of quasars with $\log L_X$ (erg s^{-1}) $= 44 - 45$ at redshift 3-5 to be $0.54^{+0.17}_{-0.19}$, while the best-fit parameters of Ueda et al. (2014) suggest an obscured fraction of 0.50 ± 0.09 above redshift 2.

In order to reconcile the obscured fraction at redshift $z > 2$ with the evolution from the local universe, the evolution parameter (a1) must be $0.75^{+0.10}_{-0.08}$, stronger than that determined by previous studies at lower redshift. However, this change will systematically increase the obscured fraction at $z < 2$. Another possibility is that the obscured fraction may still evolve above redshift 2, and the obscured fraction of high luminosity AGN saturates at a higher redshift than that of low luminosity AGN.

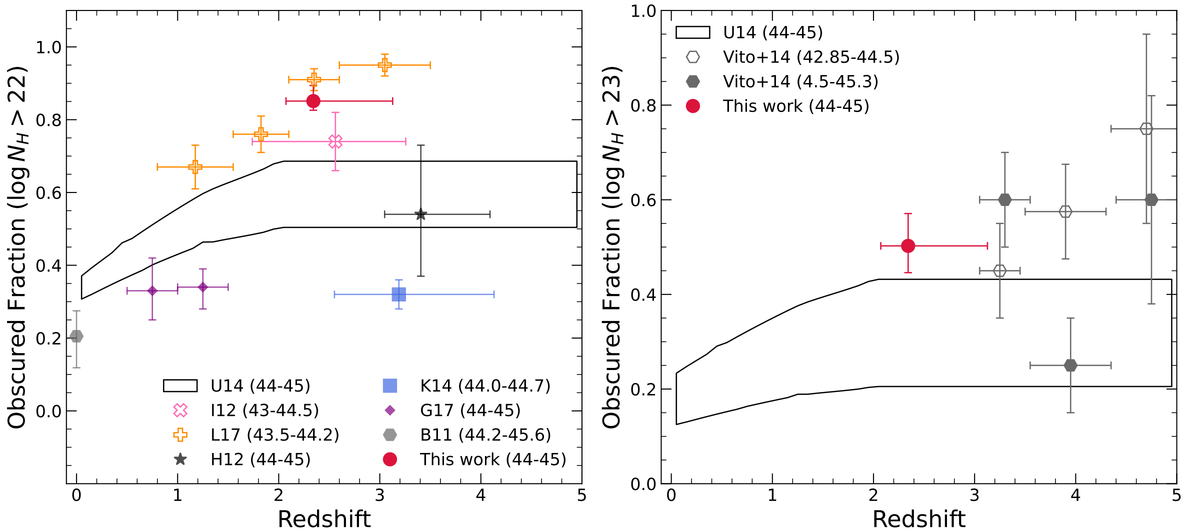

Figure 3.11: The obscured fraction at different redshifts compared with the obscured fraction of AGN with $\log L_X$ (erg s^{-1}) $= 44 - 45$ from the 2D ML best-fit parameters shown with the red round symbol. (Left) Obscured fraction of AGN with $\log N_{\rm H}$ (cm^{-2}) $= 22 = 24$ with redshift. The result is compared with Burlon et al. (2011)(B11; grey hexagon), Iwasawa et al. (2012)(I12; pink cross), Hiroi et al. (2012)(H12; black star) Kalfountzou et al. (2014)(K12; blue square), Liu et al. (2017)(L17; orange plus), and Georgakakis et al. (2017) (G17; purple diamonds), respectively. (Right) The obscured fraction of AGN with $\log N_{\rm H}$ (cm^{-2}) > 23 among CTN-AGN. The results are compared with Vito et al. (2014) shown with gray hexagons. In both panels, The black solid line shows the lower and upper limits of Ueda et al. (2014)(U14). The $\log L_X$ (ergs^{-1}) range are shown in parenthesis.

Recently, Gilli et al. (2022) constructed a model describing the evolution of the ISM hydrogen column density using data from ALMA. Using their model, they estimated the evolution of the obscured fraction as a function of redshift. The best-fitted 2D results in this work is consistent with Gilli et al. (2022) for AGN with $\log N_{\rm H}$ (cm^{-2}) $= 23 - 24$ with $\log L_X$ (erg s^{-1}) ~ 44. but not with the obscured fraction of AGN with $\log N_{\rm H}$ (cm^{-2}) > 22 at the same luminosity. The discrepancy in the latter case may be due to the difficulty in separating unobscured AGN from mildly obscured AGN ($\log N_{\rm H}$ (cm^{-2}) ~ 22) through the hardness ratios.

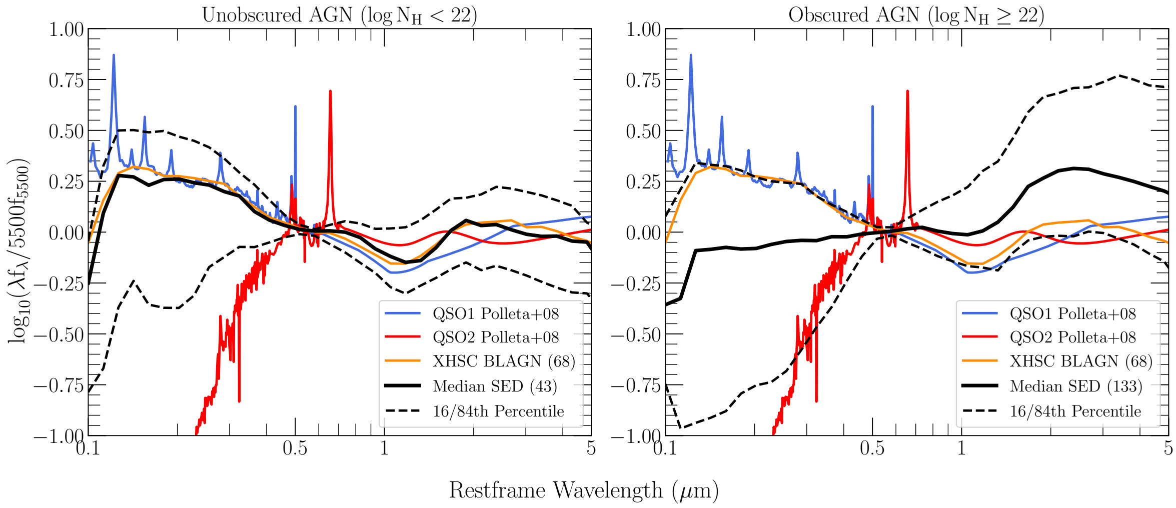

Figure 3.12: (Left) The median SED of unobscured AGN. (Right) The median SED of obscured AGN. In both panels, the dashed line shows the 16th and 84th percentile SED uncertainty. The orange SED represents the median SED of broad-line AGN. The SED are compared with QSO1 and QSO2 SED from Polletta et al. (2007).

3.5.4 The Rest-frame Spectral Energy Distribution

As discussed in the introduction, X-ray absorption is due to metals in gas while optical attenuation is due to dust. A trend in the AGN SED can be expected where unobscured AGN have bluish SED and obscured AGN have redded SED since gas and dust are expected to coexist with each other. I examine the correspondence between the X-ray absorption and the SED shapes by constructing the restframe SED of the high redshift quasars ($\log L_X$ (erg s^{-1}) > 44.5) detected in the 2-10 keV band. For each quasar, I interpolated between the 12-band photometry that was shifted to restframe and normalized at 5500$\mathring{A}$. Additional IRAC3 (5.8μm), IRAC4 (8μm), and MIPS 24μm bands photometry from the SWIRE dataset (Lonsdale et al., 2003) were also include. I separated the sample into unobscured ($\log N_{\rm H}$ (cm^{-2}) < 22) and obscured ($\log N_{\rm H}$ (cm^{-2}) ≥ 22) AGN based on the column density. The median SED of unobscured and obscured quasars was constructed by median-combining the individual SED of X-ray unobscured and obscured quasars, respectively.

The median SED of the high redshift quasars are shown in figure 3.12, I also compared the SED with type-1 and type-2 QSO SEDs from Polletta et al. (2007) as well as the median SED of high redshift BL-AGN. Unobscured AGN have a flat SED similar to the median SED of the BL-AGN. On the other hand, the median SED of obscured AGN is reddened compared to the BL-AGN model or median SED of unobscured AGN.

In each figure, the distribution of SED for each case is shown with dashed lines which represent the 16th and 84th percentile SED distribution. More than 16% of the obscured AGN have a blue UV continuum similar to the median SED of the BL-AGN, while 16% of the unobscured AGN are redder than the median SED of the obscured AGN. This large scatter suggests that the correspondence between the shape of the SED and X-ray absorption is not strong as previously expected.

To further examine the correspondence between optical properties, UV-optical-near-infrared color and morphology, and X-ray absorption, the AGN were separated into 4 groups based on the restframe u^*-H color and UV morphology. The restframe colors were calculated from the SED fitting results of LePhare. The morphology was inferred from the HSC i-band flux ratio between the HSC S20A i-band PSF and cmodel flux. The PSF (cmodel) flux is derived by fitting PSF (PSF or galaxy) model. If the AGN appears as a point source on the image then the ratio is expected to approach 1 while extended AGN will have a smaller flux ratio. AGN with a flux ratio larger than 0.95 is considered a point source.

Figure 3.13 shows the distribution of the high redshift AGN on the rest-frame u^*-H color and the flux ratio plane. Most of the unobscured AGNs have blue rest-frame color and morphology similar to a point source. On the other hand, approximately 49% of obscured AGN have extended morphology. Obscured AGN also has a broader color distribution with colors consistent with the unobscured AGN.

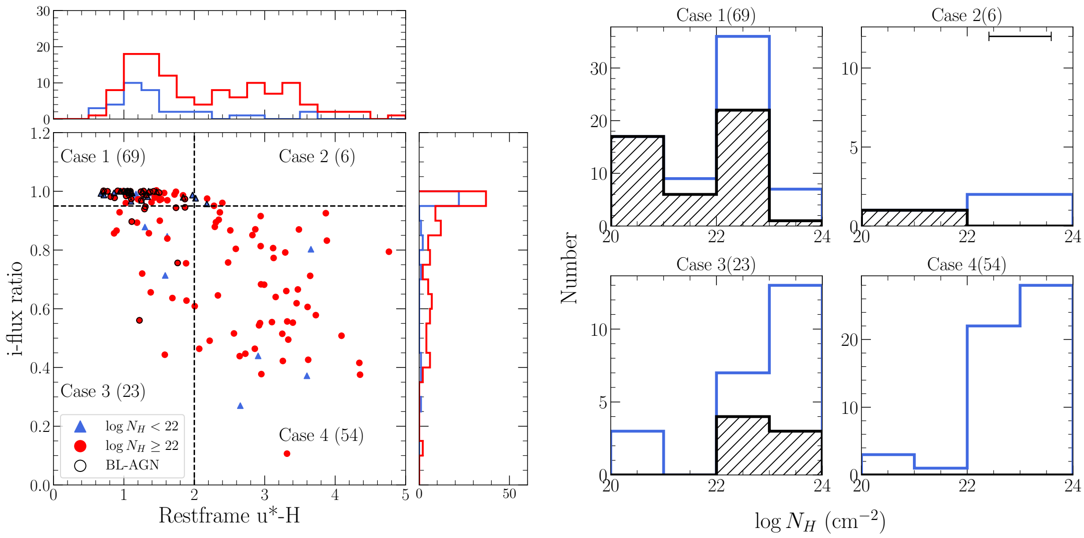

Figure 3.13: (Left) Rest-frame u^*-H colors vs. the HSC i-band flux-ratio. Red round and blue triangles symbols represent obscured and unobscured AGN respectively. Black-rimmed symbols are broad-line AGN. The distribution is separated into 4 quadrants based on the restframe color and morphology. The numbers in parentheses represent the number of objects in each quadrant. The side histograms show the projected morphology distribution (right) and color distribution (top). (Right) The hydrogen column density distribution in each sector. The hatched histogram shows the distribution of broad-line AGN.

Figure 3.13 show the distribution of the high-redshift AGN sample divided into 4 samples based on the color against the morphology plane. The column density distribution of each sample is shown in the right panel. Most of the AGN with extended morphology have log $N_{\rm H}$ consistent with the obscured AGN with log $N_{\rm H}$ (cm^{-2}) > 22. On the other hand, blue point source AGN (case 1) has a mixture of column density log $N_{\rm H}$ both consistent with obscured and unobscured AGN.

For each type of morphology, I performed a KS-test between the log $N_{\rm H}$ distribution of point source and extended objects. The test suggest that the blue and red point source (case 1 & case 2) were not drawn from the same parent distribution at a 0.01 level of significance ($D_{\rm max} = 0.391$, $D_{crit} = 0.277$). However, the number of samples compared between case 1 and case 2 is small. On the other hand, the test suggest that blue and red extended sources (case 3 & case 4) were drawn from the same parent distribution at a 0.01 level of significance ($D_{\rm max} = 0.256$, $D_{crit} = 0.405$). This suggests that both red and blue extended sources may contain obscured AGN.

The largest difference between the cumulative distribution of log $N_{\rm H}$ of blue extended AGN and red extended AGN comes from the log $N_{\rm H}$ (cm^{-2}) = 22 − 23 bin. Absorption of the largest column densities (log $N_{\rm H}$ (cm^{-2}) > 23) generally occurs in the dusty torus while moderate absorption can occur on kpc scale (Hickox and Alexander, 2018). Red-extended obscured AGN may have larger amounts of gas and dust in the host galaxy scale compared to blue-extended obscured AGN. Therefore the large dust attenuation results in redder colors. Another possibility is that the blue UV optical near-infrared colors seen in blue extended obscured AGN is scattered light from central engine (Alexandroff et al., 2013; Assef et al., 2016; Alexandroff et al., 2018; Assef et al., 2020) or light from ongoing unobscured star-formation in the host galaxy.

I also examined the relationship between UV spectral properties and X-ray absorption. I examined the optical spectra of 26 AGN with SDSS spectroscopic data. The morphology of 21 of these AGNs is consistent with a point source object. Three sources have flux ratios > 0.90 close to the stellarity threshold. Of the 26 AGN, two AGN has flux ratios consistent with an extended source with one AGN showing a narrow CIV emission line ($\sigma < 1000$ km s^{-1}). Among these 26 AGN, 2 AGN show absorption lines associated with the CIV emission line. The detection of broad emission lines and a blue continuum suggests that the line of sight towards the BLR and accretion disk has low dust content but is gas-rich since the hydrogen column density is large enough to be classified as an obscured AGN. The dust-free X-ray absorption may be due to ionized or dust-free gas along the line of sight due to the strong UV radiation from the AGN accretion disk (Piconcelli et al., 2005; Merloni et al., 2014). Alternatively, it may be due to dust-free disk winds driven from the AGN accretion disk Gallagher et al. (2002, 2006).

I conclude that the large variety in the SED shapes may be due to different types of X-ray absorbers, scattered AGN emission, and the variety of host galaxy star formation and dust content along the AGN line of sight. This results in a large scatter in the shape of the optical/infrared SED of unobscured and obscured AGN.

3.6 Discussion

3.6.1 Implications on The Source of Obscuration

The increasing trend of the obscured fraction implies changes either in the physical structure and the environment of the AGN. In a broader sense, the large obscured fraction implies that the majority of black hole growth occurs behind large amounts of gas and dust, away from detection by optical detectors. As discussed in the introduction, the increasing trend of the obscured fraction cannot simply be explained by torus obscuration. My belief is that the additional obscuration to the AGN is from the host galaxy ISM but under two major scenarios previously mentioned in section 1.4.

The first scenario is an increase in obscuration due to the cosmological increase in the ISM gas density. The gas fraction in high redshift galaxies is larger than that of local galaxies of the same stellar mass and also more compact (Tacconi et al., 2010; Carilli and Walter, 2013; van der Wel et al., 2014). It suggests that the ISM gas density is higher on all spatial scales of the host galaxy compared to those in the local universe. Therefore, a higher incidence of obscuration by the ISM may explain the increasing trend of the obscured fraction of CTN-AGN (Buchner and Bauer, 2017; Buchner et al., 2017; Circosta et al., 2019; Fabian et al., 2008; Gilli et al., 2022) and may explain the Compton-thick fraction (D'Amato et al., 2020). Trebitsch et al. (2019) used hydrodynamical simulations to investigate the obscuration of high redshift AGN host galaxies. They suggest that AGN feedback is less efficient in clearing lines of sight since dense ISM gas can easily cool and replenish the obscuring material.

The second scenario is that the incidence of obscuration is induced by galaxy mergers. In this scenario, strong gravitational effects by merging galaxies can funnel large amounts of gas and dust towards the nuclear region, which results in a heavily obscured AGN activity (Hopkins et al., 2006, 2008a; Hickox et al., 2009). During the obscured quasar phase, absorption with a large column density ($\log N_{\mathrm{H}}$ (cm^{-2}) > 22) as well as near Eddington limited accretion are induced. This phase is expected to last as long as 10 times the following blow-out phase, in which strong winds driven by the AGN blow out the obscuring material leaving an unobscured quasar at the end of the sequence. observations of merging galaxies in the local universe show that they are heavily obscured compared to those triggered in other processes (Ricci et al., 2017a, 2021). It is possible that the fraction of AGN triggered by a major merger is larger at higher redshifts and the observations of high redshift AGN catch the in the obscured phase more frequent

The decrease in the obscured fraction from high to low redshift may then be explained due to gas consumption by star-formation and AGN accretion (Hirschmann et al., 2014). Feedback by AGN-driven winds further reduces the obscuration within and possibly beyond the nuclear region, as spectroscopic observations of high redshift AGN show that AGN can drive winds with velocities from several hundred up to a thousand kilometers per second, such outflows can reach out to several kiloparsecs beyond the nuclear region (Collet et al., 2016; Nesvadba et al., 2017; Davies et al., 2020).

3.6.2 Implications on Blackhole Growth

In chapter 1, I introduced the importance of cosmic noon as the peak era of SMBH mass growth as shown in figure 1.1 which showed that roughly 70% of the black hole mass density was obtained between redshift 1-3. I also showed that compared to previous work such as Ueda et al. (2014), the fraction of obscured AGN with 2-10 keV luminosity of $\log L_X$ [erg s^{-1}] $\sim 44-45$ is larger than previously estimated thanks to the increased survey area which picked up the rare luminous AGN that is obscured. At face value, this has large implications for models of SMBH growth due to two reasons. First, the larger fraction of obscured AGN that I measure suggests that previous X-ray studies missed a fraction of obscured SMBH growth due to the narrow survey area of deep X-ray datasets. Second, the mass density of SMBH at high redshift was grown by AGN with 2-10 keV luminosity $\log L_X$ [erg s^{-1}] $\sim 44-45$.

Assuming that the increase in the obscured fraction in my work is due to obscured AGN not accounted for in previous studies while unobscured AGN is complete, then the black hole mass density at high redshift estimated by previous studies may be underestimated as high as a factor of 2 assuming the standard radiation efficiency of 0.1. It should be pointed out that radiation efficiency has a large range of possible values from ~ 0.05 in the case of non-rotating black holes to 0.4 in the case of Kerr black holes as discussed in Ueda et al. (2014). However, due to the limited range of luminosity and redshift of the current sample. I was unable to reconstruct the hard X-ray luminosity function which is needed to construct a SMBH growth model. Additional datasets and better modeling of the uncertainties due to the continuum slope is needed in order to fully trace the SMBH growth.

3.6.3 Systematic Uncertainties

Here, the various selection effects which may affect the results are discussed. First, systematic uncertainties arise from the photon index and the reflection strength assumed in the phenomenological AGN model which is used to calculate the column density using the hardness ratio. Assuming a photon index of 1.7 with the same reflection strength, the obscured fraction for luminous quasars with $\log L_X$ (erg s^{-1}) $= 44 - 45$ is estimated to be $0.77^{+0.03}_{-0.04}$, which is approximately 9% lower than when assuming a photon index of 1.8 ($0.85^{+0.04}_{-0.03}$). Assuming a photon index of 1.8 with a stronger reflection strength of 1.3 reduces the obscured fraction to 0.82 ± 0.03 for luminous quasars, corresponding to a systematic change of approximately 3%. The assumption of the photon index and the reflection strength does not strongly affect the estimate of the column density ratio (ϵ) since the results are consistent with each other within uncertainties.

Second, the obscured fraction based on a hard X-ray selected AGN sample could suffer from a bias in which the 2-10 keV count rates close to the detection limit are larger than the true count rates due to statistical fluctuations of the photon count rates (Eddington bias). As a result, hard X-ray-selected AGN samples may have harder hardness ratios and as a result, larger column densities overall. This statistical fluctuation may also affect intrinsically unobscured AGN which makes them show large column density consistent with obscured AGN due to positive fluctuation in the 2-10 keV band.

Third, the estimates of the column density and luminosity may also be affected by the uncertainty in the photometric redshift. Contamination from low-redshift AGNs ($z < 2$) can also affect the best-fit results. The contamination rate from low-redshift AGN ($z_{\rm spec} < 2$) was calculated from the fraction of outlier spectroscopically confirmed quasars above redshift two (AGN above the red-dashed line with $z_{\rm phz} > 2$ as shown in Figure 2.5) overall AGN above redshift two ($z_{\rm phz} > 2$) to be 31%.

3.7 Summary & Conclusion

The obscured fraction of high-redshift luminous quasars ($\log L_X$ (erg s^{-1}) > 44.5 & $z > 2$) was determined as 76^{+4}_{-3}% thanks to the deep and wide datasets in the HSC-deep region which is able to pick up a significant number of luminous obscured AGN. In the luminosity range of $\log L_X$ (erg s^{-1}) $= 44 - 45$ the obscured fraction is 85^{+4}_{-3}% for $\log N_{\rm H}$ (cm^{-2}) > 22 and 50^{+7}_{-6}% for $\log N_{\rm H}$ (cm^{-2}) > 23. The large obscured fraction indicates that a large fraction of luminous accretion activity of black holes occurs under large amounts of gas and dust which may have been missed from previous studies but could be recovered thanks to the large and deep survey area of the XMM-SERVS dataset.

The shape of the optical infrared SED of the AGNs at redshift two was investigated. As expected, unobscured AGNs have a blue power-law or flat SED while obscured AGNs have a redden optical/infrared SED. However, the SED shows a large scatter in both cases. This is consistent with reddening due to dusty gas along the line of sight seen as redden unobscured AGN. On the other hand, evidence of dust-free X-ray absorption or unobscured star formation is present among obscured AGNs.

Chapter 4

The Obscuration Process at $z = 0.8 - 1.8$

Abstract

I investigated the obscuration and host galaxy properties of active galactic nuclei (AGN) during the peak of cosmic accretion growth of SMBHs at redshift 0.8-1.8. The sample was selected from among X-ray-detected AGN with mid-infrared and far-infrared detection and was classified as type-1 and type-2 AGN using optical spectral and morphological classification. The host galaxy properties were estimated with multiwavelength SED fitting. For type-1 AGN, the supermassive black hole mass was determined from MgII emission lines while the black hole mass of type-2 AGN was inferred from the host galaxy stellar mass. By evaluating the Eddington ratio and the distribution in the $\log N_{\mathrm{H}} - \lambda$ diagram, I conclude that obscuration of the majority of AGN at redshift 0.8-1.8 is consistent with that obscured by a radiation pressure regulated dusty torus. However, there is an increased fraction of AGN that is obscured by interstellar matter (ISM) which occupy the in the forbidden zone from $11 \pm 3\%$ in the local universe to $26 \pm 3\%$ at redshift 0.8-1.8. I discuss the possibility of dust-free absorption in type-1 AGN and heavy ISM absorption in type-2 AGN for AGN which reside in the forbidden zone. There is no statistical difference in the star-formation activity between type-1 and type-2 AGN which suggests that obscuration triggered by a gas-rich merging is not a common occurrence in this epoch.

4.1 Additional Far-infrared & Spectroscopic Data

In order to estimate the star-formation rate and decompose the AGN hot dust emission, additional mid-infrared and far-infrared datasets were added from the Spitzer data fusion catalog Vaccari (2015). The Spitzer data fusion catalog contains both IRAC and MIPS 24μm aperture photometry. The catalog also contains Herschel PACS (Poglitsch et al., 2010) and SPIRE (Griffin et al., 2010) 250, 350, and 500 μm PRF-photometry based on 24 μm prior positions. Both MIPS 24μmand the FIR photometry fully cover the multiwavelength survey area presented in V22. First, the two catalogs were matched using a 2" radius aperture. The band merged IRAC channel 1 & 2 coordinates were used for the matching with the optical counterpart of V22. 1445 mid-infrared counterparts from the data fusion catalog which have 24 μm photometry were found out of the original 3462 AGN. For the remaining objects no 24 μmdetection (and subsequently, no FIR data) was found in a 5.25 arcsecond aperture. Visual inspection of the original images was performed to assess the quality of the far-infrared data. After adding the confusion noise with the photometric noise in the quadrature, no clear detection in the far infrared bands was seen in sources with S/N below 3. Therefore, the flux was replaced with 3σ upper limits.

4.2 Sample Selection

The sample was limited to those which have shape measurements and i-band cmodel and PSF flux from the HSC catalog. In addition, the sample was limited to those above redshift 0 and are not within the same region as the local galaxy sample in the HyperLEDA catalog (Makarov et al., 2014). 3203 AGN remain after the selection and only 3150 AGN within redshift 0.8-1.8 were detected in the 0.5-10 keV band. 666 AGN have 24μmdetection from the Spitzer data fusion catalog. The 24μmdetected AGN was selected as the sample. Among them, 395 AGN are detected in both 0.5-2 and 2-10 keV bands. 171 and 72 AGN have single band detection in 0.5-2 keV band and 2-10 keV band, respectively. The number of spectroscopic redshifts among the 24μmsample is 363. Archival optical spectra from the SDSS DR16 archive(Ahumada et al., 2020) were obtained for 239 AGN in order to construct a comparison sample of Type-1 AGN in the survey area. In this redshift range, the MgII emission line is expected to fall into the detector with sufficient continuum emission on both sides of the line.

4.3 Type-1 & Type-2 Classification

The classification of AGN depends strongly on the wavelength used to identify the AGN. From X-ray, the classification of AGN between obscured and unobscured is based on the hydrogen column density. Obscured AGN are typically defined as AGN with hydrogen column density of $\log N_{\rm H}$ [cm^{-2}] $= 22-24$. Some recent studies define obscured AGN as those with hydrogen column density of $\log N_{\rm H}$ [cm^{-2}] $= 23-24$ (Vito et al., 2014, 2018; Georgantopoulos et al., 2023a). From optical/UV, type-1 and type-2 AGN were classified based on the optical spectra. AGN that show broad emission lines are classified as type-1 AGN and those that lack broad emission lines are considered as type-2 AGN. From hereafter, obscured AGN refers to those with hydrogen column density $\log N_{\rm H}$ [cm^{-2}] $= 22-24$. Type-1 AGN refers to those with confirmed broad-line detection (broad-line AGN) or with morphology consistent with a point source. Type-2 AGN refers to those with extended morphology and are not confirmed to possess broad-emission lines. In order to classify the AGN as type-1 or type-2 AGN, the spectroscopic classification presented by Chen et al. (2018) which is based on the classification presented in the compilation of the spectroscopic surveys was adopted.

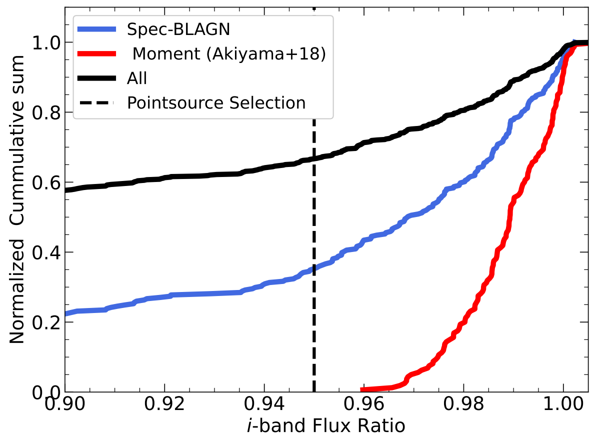

Figure 4.1: The normalized cumulative distribution of the ratio between i-band cmodel flux over PSF flux. The black line represents the full AGN sample with MIPs 24 μm detection. The blue line represent spectroscopically confirmed broad-line AGN. The red line represents X-ray detected point sources classified using the 2nd-moment classification presented by Akiyama et al. (2018).

In order to classify sources as point sources or extended sources, the ratio between the cmodel and PSF flux in HSC i-band is used. Sources whose morphology is close to a point source will have a flux ratio near unity. An alternative method to classify point-source was presented in Akiyama et al. (2018) using the 2nd moment of the PSF. Figure 4.1 shows the normalized cumulative distribution of the i-band flux ratio of the whole sample of AGNs, the sample of spectroscopic broad-line AGN, and AGN which were classified as point-sources based on the 2nd moment classification in thick black, blue, and red lines. It was shown in Akiyama et al. (2018) that the 2nd-moment classification is highly efficient in classifying point source objects but the performance declines at faint magnitudes $i > 24$. AGN are classified as point sources when they have i-band flux-ratio larger than 0.95. This threshold will select more than half of the spectroscopically confirmed broad-line AGN and all AGN classified as point sources with the

2nd moment classification. 36 more AGNs were classified as type-1 AGNs using this method. The final classification in the sample is 328 Type-1 AGN and 338 Type-2 AGN. For the sample of type-1 AGN and type-2 AGN, 291 and 72 have spectroscopic redshifts from the literature, respectively.

4.4 Optical Spectral Analysis

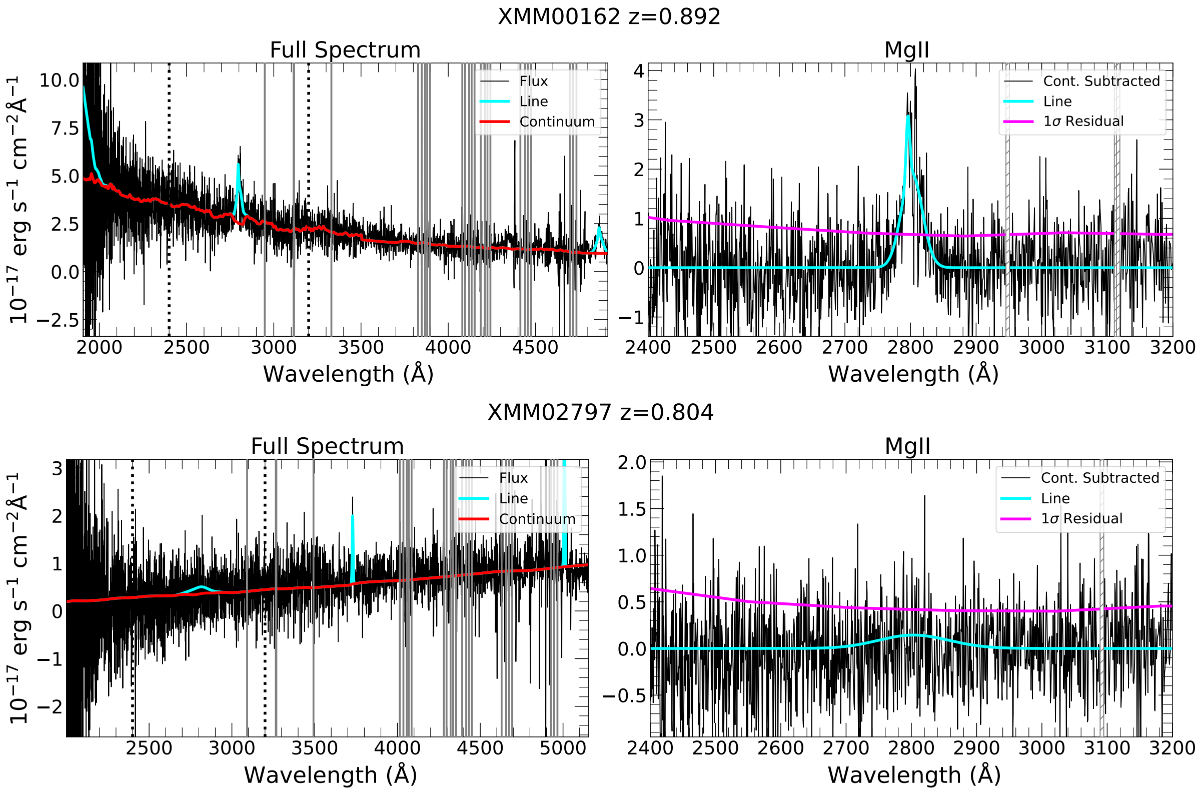

Figure 4.2: Example fitting of AGN with SDSS spectra. The top panel shows a type-1 AGN with clear MgII detection while the bottom AGN shows the spectra of an AGN with no MgII detection. The left panel shows the full restframe spectra while the right panel shows a zoomed-in on position of the MgII emission line. The best-fitted pseudo-continuum model is shown with the red line while the emission lines are shown in cyan. The magenta line in the right panel shows the level of the 1σ residual. Hatched regions are wavelengths that are affected by strong sky emission lines of telluric absorption.

The black hole mass of broad-line AGN can be estimated using single-epoch virial black hole mass relationships (Greene and Ho, 2005; Vestergaard and Peterson, 2006; Vestergaard and Osmer, 2009) with which the black hole mass is estimated with the broad emission line FWHM and the continuum luminosity. The spectral fitting code PyQSOFit (Guo et al., 2018) was used to fit the MgII emission line and the AGN continuum of the AGN with SDSS spectra. The AGN continuum was fitted with a power-law continuum model combined with FeII emission lines. The maximum FWHM of the FeII emission lines was limited to 10,000 kms^{-1}. Regions in the spectra that are affected by strong optical sky emission lines and telluric absorption were masked. The MgII emission line was first fitted with 1 single broad Gaussian component and then add a second broad emission line component after visually examining the initial fitting results. For each AGN, 25 mock spectra were constructed for each AGN by randomizing flux based on the photometric uncertainty assuming a Gaussian distribution, and then performing the spectral fitting again for each realization. The median FWHM of the mock distribution was adopted for later calculations. The lower and upper uncertainty of each fitting parameter was determined based on the 16th and 84th percentile of the mock distribution and range of the uncertainty of the MgII FWHM $R_{84-16} = P_{84} - P_{16}$ where P_{84} is the 84th percentile and P_{16} is the 16th percentile of the fitting results was calculated.

Figure 4.2 shows the fitting results of an AGN with a clear detection of MgII and an AGN with no clear broad MgII emission lines. 92 AGN require 2 broad-line components while 124 AGN require a single broad component. 23 AGN have no broad emission lines based on visual examination. The 23 AGN with no broad emission lines was classified as 17 narrow-line AGN and 6 AGN with low-S/N spectra. The narrow-line AGN generally shows a reddened continuum with no obvious broad lines. The spectroscopic redshift was determined from the [OII] emission lines at 3737Åand is consistent with the redshift determined by SDSS. In some cases, [OIII] emission lines and weak narrow Hβ. were also detected. For AGN with low-S/N spectra, reliable spectroscopic redshift can not be determined, nor can broad emission lines be confirmed. The spectroscopic redshift previously adopted from SDSS was replaced with the photometric redshift instead.

The signal-to-noise is defined as the peak flux over the noise level. Figure 4.3 shows the S/N of the broad component of the MgII emission line against the MgII FWHM. Spectra with low S/N have large MgII FWHM due to variations in the continuum noise and not from an emission line. In addition, the range of the MgII FWHM uncertainty $R_{84-16} = P_{84} - P_{16}$ was calculated, where P_{84} is the 84th percentile and P_{16} is the 16th percentile of the fitting results. The MgII emission line was considered as detected if the S/N is larger than 1.5 and median FWHM over the uncertainty range is larger than 1 ($FWHM_{\mathrm{MgII}}/R_{84-16} > 1$). 257 broad-line AGN satisfy this criterion.

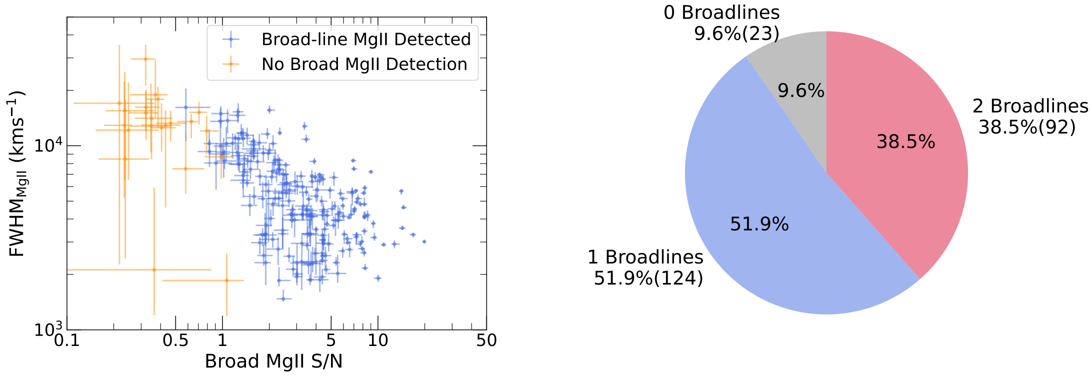

Figure 4.3: (left) The signal-to-noise ratio against the FWHM of the broad MgII emission line component. Blue data points are those which show clear MgII emission lines from visual inspection while orange data points are those which do not show clear MgII emission lines in the spectra. (right) The number of broad components fitted to the MgII emission lines.

The single-epoch virial mass relationship of Vestergaard and Osmer (2009) was adopted in order to infer the supermassive black hole mass of the type-1. The relationship presented in Nobuta et al. (2012) uses the FWHM of the MgII emission line and the continuum luminosity at 3000Åto determine the SMBH mass. The relationship is expressed as

$$M_{\mathrm{BH}}[\mathrm{M}_{\odot}] = 10^{6.86} \left[\frac{\mathrm{FWHM}_{\mathrm{MgII}}}{1000\ \mathrm{km\ s}^{-1}}\right]^2 \left[\frac{3000 L_{3000}}{10^{44}\ \mathrm{erg\ s}^{-1}}\right]^{0.5} \tag{4.1}$$

where FWHM$_{\mathrm{MgII}}$ is the FWHM of the MgII emission line and L_{3000} is the continuum luminosity at 3000 Å. 216 black hole mass estimates were obtained using the SDSS spectra.

In addition to the SDSS broad-line AGN, an additional 109 SMBH mass measurements from Nobuta et al. (2012) were added. Nobuta et al. (2012) estimated the SMBH mass of broad-line AGN within the SXDS survey region (Sekiguchi and SXDS Team, 2004; Akiyama et al., 2015) using the MgII emission line observed using the FOCAS spectrograph (Kashikawa et al., 2002) mounted on the Subaru telescope. They also use the virial mass relationship of Vestergaard and Osmer (2009) to estimate the SMBH mass of the AGN. For a sub-sample of AGN observed in the near-infrared with the FMOS spectrograph (Kimura et al., 2010), they also determined SMBH mass using the H$_{\alpha}$ emission line which is in good agreement with MgII selected sample. A sub-sample of 42 AGN has black hole mass measurements from both SDSS and from Nobuta et al. (2012). The difference between the two samples is the instruments used and how the emission line fitting is carried out. Figure 4.4 shows the black hole mass estimated by (Nobuta et al.,

2012) using the MgII or Hα emission lines against the black hole mass estimated with the MgII emission line detected in SDSS spectra. A linear regression fit was performed to examine the consistency between the two samples. The black hole mass determination of the two samples is statistically consistent with each other within 1σ scatter of the data (ϵ). The measurements from (Nobuta et al., 2012) were adopted in place of the SDSS when available due to the deeper spectroscopic observation performed in the SXDS. The final number of black hole mass estimations contains 106 from Nobuta et al. (2012) and 148 from SDSS.

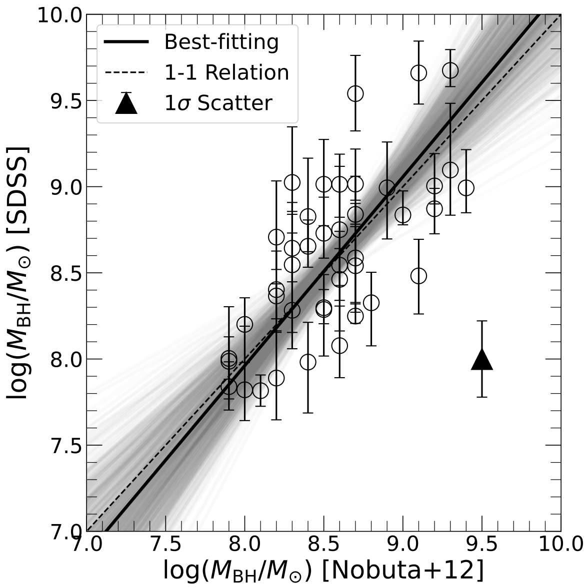

Figure 4.4: Comparison between the black hole mass estimated by Nobuta et al. (2012) from FOCAS spectra against SDSS spectra shown in orange. The best-fitted relation is shown with a thick black line. The dashed line shows the 1-1 relation. The filled black data triangle shows the 1σ scatter of the data points.

4.5 Spectral Energy Distribution (SED) Fitting

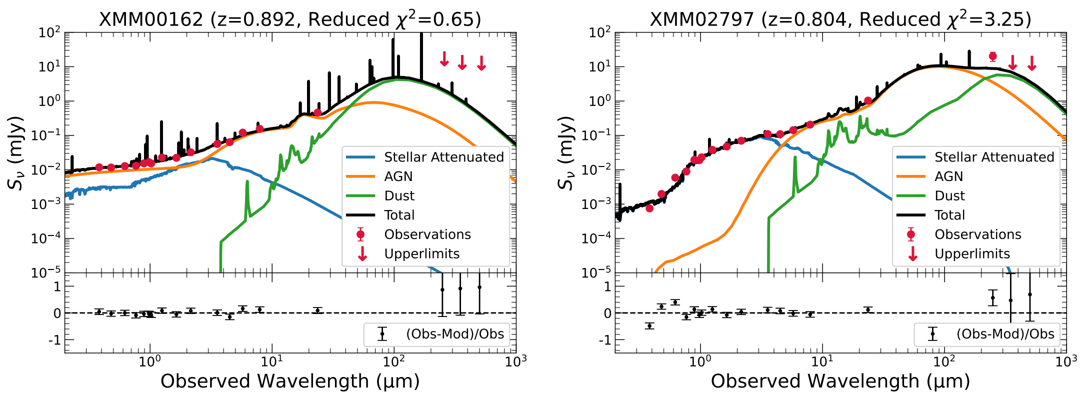

Figure 4.5: The best-fitted observed SED of the type-1 and type-2 on the left and right, respectively. The top panels show the model fitting while the bottom panels show the relative uncertainty. The observations are shown with red datapoint while upper limits are shown with downward arrows. The attenuated stellar, AGN, dust, and total models show blue, orange, green, and black respectively.

SED fitting was performed using CIGALE 2022(Boquien et al., 2019; Yang et al., 2020) in order to estimate the host galaxy stellar mass and the total star-formation rate from the best-fit SED. CIGALE is a SED fitting code that performs SED fitting by balancing the energy absorbed by dust from optical/UV and is re-emitted in the infrared. The parameters on the host galaxy properties were computed using Bayesian posterior distributions.

A simple delayed star-formation history combined with the Chabrier initial mass function (Chabrier, 2003) was adopted for the host galaxy models since only broad-band photometry information is available. Most of the FIR datasets from Herschel have detection in only one or two bands and with S/N less than 10 for most cases. Due to this limitation, the empirical models from Dale et al. (2014), which contains only two parameters were adopted instead.

SKIRTOR AGN models (Stalevski et al., 2012, 2016) were used to fit the mid-infrared and optical/UV continuum of the AGN. CIGALE 2022 can fit the X-ray continuum assuming a power and $\alpha_{\rm OX}$ value. However, this model was not used since it requires absorption-corrected flux. The parameter set used for the SED fitting is presented in Table 4.1. The fitting was performed separately for the type-1 and type-2 AGN samples.

For the spectroscopically confirmed broad-line AGN and the morphologically selected type-1 AGN sample, the inclination angle in the SKIRTOR AGN model to 30 degrees (face-on) and the AGN fraction ($f_{\rm AGN}$) was set to be calculated between 0.1-1 μm and assumed to be $f_{\rm AGN} > 0.5$. By doing so, the optical/UV continuum was forced to be dominated by the AGN continuum emission. For the type-2 AGN sample, the inclination angle was set to 70 degrees instead (edge-on), and the AGN fraction was set to be calculated between 2-10 μm instead, where the AGN torus emission is expected to dominate the emission with $f_{\rm AGN} > 0.5$. Figure 4.5 shows the best-fitted SED of the type-1 and type-2 AGN presented in figure 4.2. For the type-1 AGN, the AGN component dominates the UV/optical emission over the host galaxy emission and simultaneously dominates the mid-infrared emission. For the type-2 case, the AGN torus emission dominates the mid-infrared emission over the dust emission. The reduced χ^2 distribution of the type-1 and type-2 AGN samples show a similar distribution with 95% of each sample having a reduced $\chi^2 < 5$. For comparison in the later sections, the sample was limited to those with the SED fitting has reduced $\chi^2 < 5$. In addition for type-1 AGN, the sample was limited to AGN that have reliable detection of the MgII emission line. This reduces the sample of type-1 AGN to 205 AGN and type-2 AGN to 284 AGN.

Table 4.1: SED fitting parameters used in CIGALE

Star-formation History (sfhdelayed)	
e-folding time of main population ($\tau_{\rm Main}$)	500,1000,2000,4000,6000,8000 Myr
Age of the main stellar population ($\rm Age_{Main}$)	500,2000,3000,4000,6000,8000,10000 Myr
e-folding time of the late starburst population ($\tau_{\rm Burst}$)	3,80.0
Age of the late burst in Myr ($\rm Age_{Burst}$)	20.0
Mass fraction of the late burst population ($\rm f_{Burst}$)	0.0,0.01,0.1
SSP Model (BC03)	
Initial mass function (IMF)	Chabrier
Metallicity	0.02
Separation Age	10.0 Myr
Dust Attenuation (Modified Calzetti et al. (2000) law)	
The color excess of the nebular lines (E(B-V))	0,0.2,0.4,0.6,0.8,1.0,1.5,2.0
Stellar E(B-V) conversion factor	0.44
Ext law emission lines	Cardelli et al. (1989)
Ratio of total to selective extinction ($\rm R_V$)	3.1
Dust Emission (Dale et al., 2014)	
AGN fraction ($\rm f_{AGN}$)	0
Alpha slope (α)	0.0625,1.0,2.0,3.0,4.0
AGN Model (SKIRTOR 2016)	
Average edge-on optical depth at 9.7μm (τ)	3,7
Power-law exponent (pl)	0.5
Dust density gradient index (q)	0.5
Torus equatorial plane and edge angle (oa)	40 Deg
Ratio of torus outer to inner radius (R)	20
Inclination angle (i)	30(70) Deg
Optical power-law of index (δ)	-0.36
AGN fraction $\rm f_{AGN}$	0.5,0.6,0.7,0.8,0.99
AGN fraction band	0.1/1.0 (2.0/10.0) μm
Extinction law	SMC
Polar dust E(B-V)	0.0,0.25,0.5,0.75,1,2
Polar dust temperature	100 Kelvin
Emissivity index of the polar dust	1.6

4.6 Estimation of the Star-formation Rates

In order to calculate the star-formation properties of the host galaxies without the contamination from the AGN emission, the best-fitted models from CIGALE with all the AGN components removed were used for the calculation. Firstly, the restframe $U-V$, and $V-J$ band colors were calculated assuming the the Subaru U and V filters and the UKIRT J-band filters. Secondly, the total star formation rate (SFR) and specific star-formation rate (SSFR) were calculated from the host galaxy optical and far infrared emission using the relationship presented by Murphy et al. (2011) which is given as

$$\frac{\rm SFR_{tot}}{M_{\odot}{\rm yr}^{-1}} = 4.42 \times 10^{-44} \left(\frac{L_{\rm FUV} + 0.88 L_{IR}}{\rm erg\ s^{-1}} \right)$$

where $L_{\rm FUV}$ is the FUV luminosity assuming the GALEX FUV transmission curve and $L_{\rm IR}$ is the infrared 8-1000μmluminosity. Similar to that done for the UVJ diagram, $L_{\rm FUV}$ and $L_{\rm IR}$ were calculated from the best-fitted model without the AGN component.

CIGALE provides the uncertainty for the total (AGN and host galaxy) FUV luminosity and the total dust emission. In order to estimate the star-formation rate uncertainty, the uncertainty of the best-fit AGN FUV luminosity was assumed to be the same as the total FUV luminosity when the AGN components are removed and assumed that the relative uncertainty of the 8-1000μmis the same as the relative uncertainty of the total dust luminosity. The uncertainties are then propagated through the star-formation rate relationship.

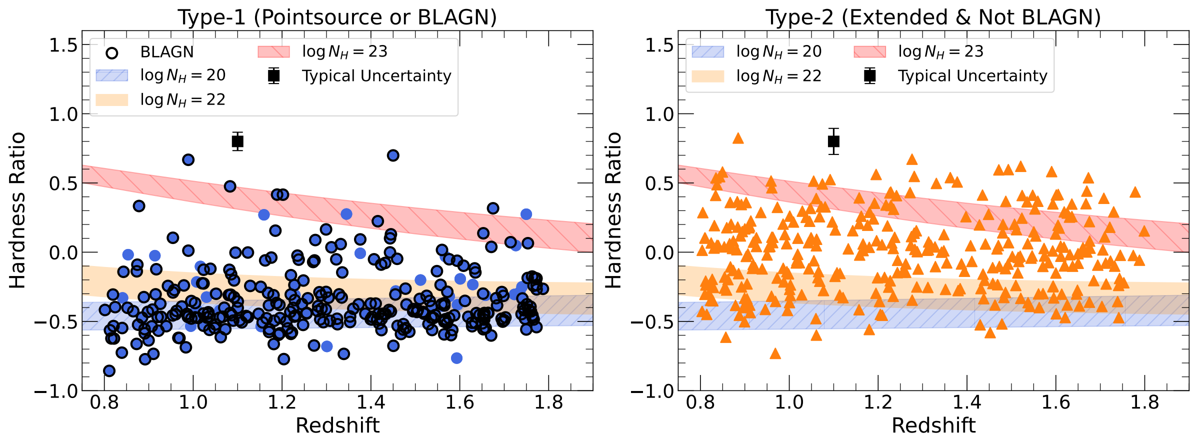

Figure 4.6: The X-ray hardness ratios of type-1 AGN on the left panel and type-2 AGN on the right panel are shown with blue round and orange triangle symbols, respectively. Spectroscopically confirmed broad-line AGN are shown with black-rimmed symbols. The black square symbol shows the typical uncertainty of the AGN in each sample. The blue, yellow, and red bands show the hardness ratio tracks assuming $\log N_{\rm H}$ [cm^{-2}]=20,22, and 23. The bottom edge to the top edge of each band shows the HR tracks assuming a photon index of 2.0 to 1.5.

4.7 $\log N_{\rm H}$ and 2-10 keV AGN luminosity

The hydrogen column density ($\log N_{\rm H}$) can be determined by using the X-ray hardness ratios assuming an X-ray spectral model and redshift. The X-ray hardness ratio is defined as $HR = (H - S)/(H + S)$ where S is the count rate detected in the 0.5-2 keV band and H is the count rate detected in the 2-10 keV band. The same phenomenological X-ray spectral model and process to calculate the hydrogen column density presented in 3.1.2 was adopted in this section.

Figure 4.7 shows the hydrogen column density determined from the X-ray hardness ratio. The left panel shows the sample of AGN which is detected in both the 0.5-2 keV band and the 2-10 keV band while the right-hand panel shows the sample of AGN which is detected only in a single energy band. The bottom part of each panel shows the AGN that has an X-ray hardness < -0.5, softer than the model assumed. For these AGN, the hydrogen column density was set to $\log N_{\rm H}$ [cm^{-2}] $= 20$. As previously mentioned, there is a degeneracy in the hardness ratio when assuming a hydrogen column density and photon index. This systematic effect was included in the calculations of the hydrogen column density uncertainty. For objects that are detected only in the 0.5-2 keV band (down arrows), only upper limits on the hydrogen column density can be determined. On the other hand, for objects that are detected only in 2-10 keV bands (up arrows), only lower limits on the hydrogen column density can be determined.

In Chen et al. (2018), the flux presented is the weighted average of the flux measured in the PN, MOS1, and MOS2 detectors. The flux in each detector was converted from the count rates using a power-law model with a photon index (Γ) of 1.7 for each detector. In Vijarnwannaluk et al. (2022), the flux was converted back to "PN-equivalent" count rates using the energy conversion factor (ECF) presented in Chen et al. (2018) and then recalculated assuming a power law model with a photon index of 1.8 instead. The ECF in soft-band, hard-band, and full-band is $6.84 \times 10^{11}, 1.26 \times 10^{11}$, and 3.36×10^{11} count s^{-1} /erg s^{-1}cm^{-2}. Using the best available redshift and hydrogen column density, the intrinsic 2-10 keV X-ray AGN luminosity (L_X) was calculated using

$$L_X = \mathrm{ext}(z, N_{\rm H}) k(z) 4\pi D_L^2(z) f_X$$

where f_X is the X-ray flux in either soft-band, hard-band, or full-band. $\mathrm{ext}(z, N_{\rm H})$ is the absorption correction which is a function of redshift and Hydrogen column density, $k(z)$ is the X-ray k-correction factor, and D_L is the luminosity distance.

The relationship between the X-ray 2-10 keV luminosity and the 6μmAGN luminosity was used to evaluate the reliability of the SED fitting results. The two 2-10 keV luminosity and the 6μmAGN luminosity correlate with each other over 3 orders of magnitude (Fiore et al., 2009; Stern, 2015; Toba et al.,

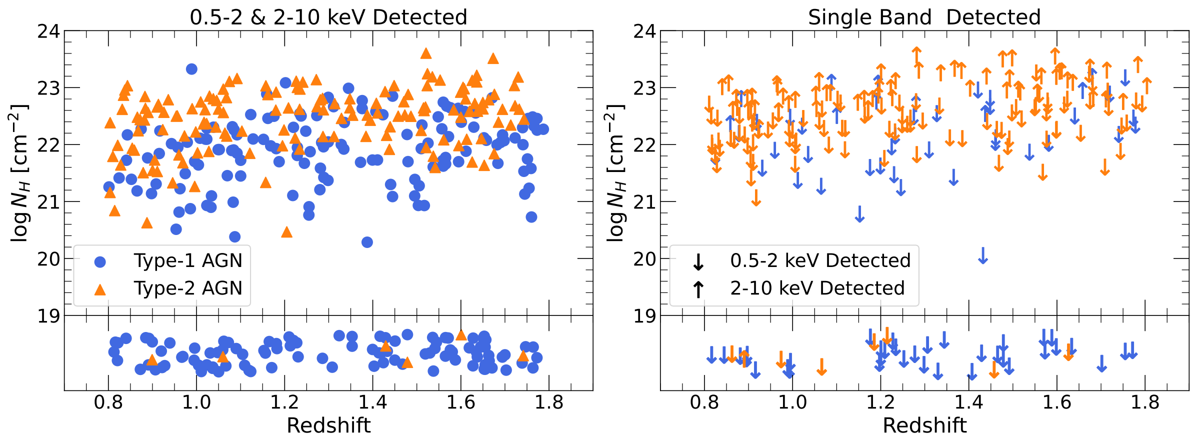

Figure 4.7: The hydrogen column density of AGN detected in both 0.5-2 and 2-10 keV bands (left) and single band detected AGN (right). The top panel shows the AGN which has HR within the model grid. The bottom panel shows the AGN which has an HR softer than the model grid and is set to have $\log N_{\mathrm{H}} = 20$. Type-1 AGN are shown with blue round symbols while type-2 AGN are shown with orange triangle symbols. For single band detected AGN, lower limits are shown with up arrows while upper limits are shown with down arrows.

2022). Since the X-ray model in the SED fitting routine of CIGALE was not used, the measurements of the X-ray luminosity and the infrared luminosity can be considered independent of each other. Linear regression using the Bayesian linear regression routine[1] presented by Kelly (2007) was used to perform the fitting. The lower and upper uncertainties of the linear regression coefficients were estimated based on the 16th and 84th percentiles of 10,000 mock-fitting results.

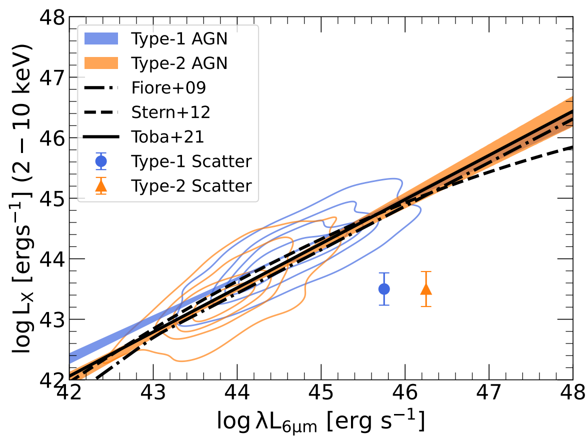

Figure 4.8: The best-fitted $L_{6\mu m} - L_{\mathrm{X}}$ relationship of type-1 and type-2 AGN shown in blue and orange bands, respectively. The width of each band represents the 1σ confidence interval. The distribution of type-1 and type-2 AGN are shown in blue and orange contours. The blue round and orange triangle data point shows the 1σ scatter of the type-1 and type-2 AGN samples. The best-fitted relationships are compared to the results from Fiore et al. (2009); Stern (2015) and Toba et al. (2022)

Figure 4.8 shows the 2-10 keV X-ray luminosity vs. the $6\mu m$ AGN luminosity relationship of the hard-band detected sample of AGN with spectroscopic redshift. The hard-band selected sample was used since it is least affected by obscuration as compared to the other bands. Here redshift range was not limited to 0.8-1.8 as most type-2 AGN with spectroscopic redshift are at $z < 0.8$. The results are consistent with all of the relationships determined by previous studies within the scatter parameter (ϵ)

[1] https://github.com/jmeyers314/linmix

determined by the linear regression. Equation 4.2 shows the best-fit linear relationship between the $6\mu m$ infrared AGN luminosity and 2-10 keV AGN luminosity based on the hard-band selected sample.

$$\log L_{\mathrm{X}} = 0.66(\pm0.03) \log L_{6\mu\mathrm{m}} + 17.04^{+0.28}_{-0.25} : \epsilon = 0.27 \tag{4.2}$$

Observations of high luminosity AGN ($\log L_{6\mu m}$ [erg s^{-1}] > 46) suggest that the X-ray emission becomes weak at high luminosity, high Eddington ratio systems. This may be due to disruption of the corona by radiatively inefficient accretion flows or shielding from winds (Nardini et al., 2019; Zappacosta et al., 2020; Duras et al., 2020). Therefore above $\log L_{6\mu m}$ [erg s^{-1}] > 46, the $L_X - L_{6\mu m}$ relationship deviates from linear relationships and has to be fitted by a polynomial equation. The results are not strongly affected by this effect since the luminosity has not entered the hyper-luminous regime and is still consistent with a linear relationship.

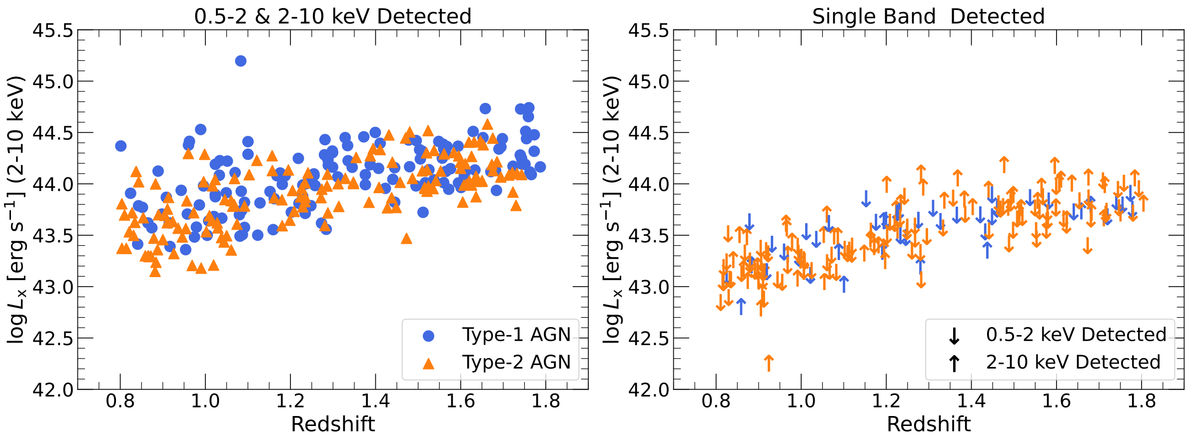

Figure 4.9: The 2-10 keV luminosity of AGN detected in both 0.5-2 and 2-10 keV bands (left) and single band detected AGN (right). Type-1 AGN are shown with blue round symbols while type-2 AGN are shown with orange triangle symbols. For single band detected AGN, lower limits are shown with up arrows while upper limits are shown with down arrows.

4.8 Results

4.8.1 Host Galaxy Stellar Mass

In order to examine the difference between type-1 and type-2 AGN, the host galaxy stellar estimated from the SED fitting with type-1 and type-2 AGN models were first examined. Figure 4.10 shows the stellar mass and 6-micron AGN luminosity of type-1 and type-2 AGN. On average, Type-1 AGN and Type-2 AGN in the sample have an average host galaxy stellar mass of$\log M_{\mathrm{stellar}} = 10.6^{+0.4}_{-0.3}$ and $\log M_{\mathrm{stellar}} = 10.9^{+0.3}_{-0.3}$, respectively. The stellar mass uncertainty of type-1 AGN is on average a factor of 2 larger than Type-2 AGN. This is because the optical wavelength of type-1 AGN is contaminated by the AGN optical emission whereas the optical wavelength of type-2 AGN is dominated mainly by stellar emission of the host galaxy.

The sample of type-1 and type-2 AGN cover a broad range in redshift and luminosity and can be affected by the cosmological increase of luminous AGN towards redshift ~ 2. In order to perform a fair comparison between the host galaxy's stellar mass, a sub-sample of type-1 and type-2 AGN which has the same redshift and luminosity distribution was constructed using a matching process similar to that of Zou et al. (2019) and Georgantopoulos et al. (2023b). The sample was simultaneously divided into redshift bins of 0.2 between redshift 0.8-1.8 while the luminosity was divided in bins of 0.25 between $\log L_{6\mu\mathrm{m}} = 43 - 46$. This results in a two-dimensional grid in redshift luminosity space with $N^{\mathrm{t1}}_{L,z}$ type-1 AGN and $N^{\mathrm{t2}}_{L,z}$ type-2 AGN. The luminosity matching was also performed using the 2-10 keV luminosity. In this case, the 2-10 keV luminosity was divided between $\log L_{\mathrm{X}}$ [erg s^{-1}] $= 42.5 - 45.5$ in bins of 0.25 dex.For each (L, z) bin, minimum number of AGN between type-1 and type-2 $N^{\mathrm{match}}_{L,z} = \min(N^{\mathrm{t1}}_{L,z}, N^{\mathrm{t2}}_{L,z})$

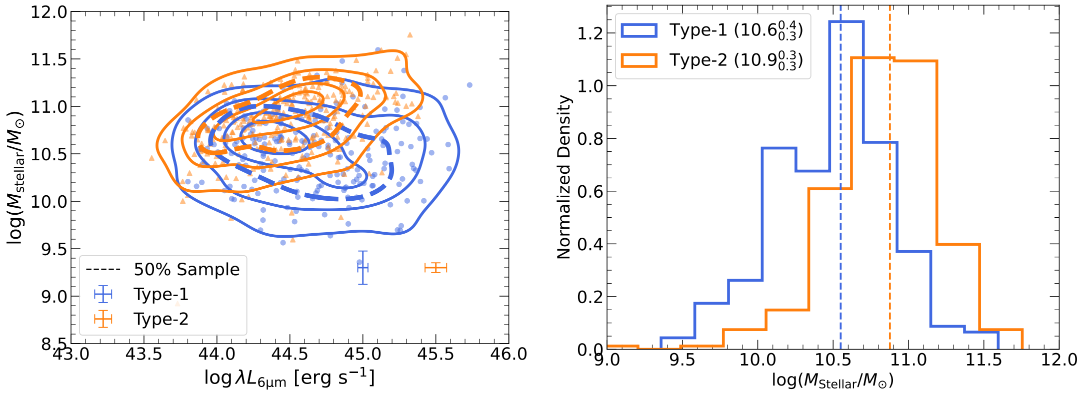

Figure 4.10: The 6-micron luminosity against stellar mass $M_{\rm stellar}$ of type-1 AGN and type-2 AGN shown as blue and orange contours, respectively. The contour levels show the area which 10-90% of the datasets lays under. The 50% level is shown with dashed contours. The faceless data point with error bars shows the typical uncertainty of the AGN.

was chosen. 10,000 mock samples of type-1 and type-2 AGN were then constructed. For each trial, $N^{\rm match}_{L,z}$ were randomly selected among type-1 and type-2 AGNs. A boot-strap style analysis was adopted where AGN already randomly selected can be selected again.

After constructing the mock samples, an Anderson-Darling k-sample test[2] (Anderson and Darling, 1952) was performed between the mock type-1 AGN sample and the mock type-2 AGN sample. Similar to the KS-test, the Anderson-Darling K-sample test is used to test if two samples are drawn from the same parent distribution (null hypothesis). A significance level of 5% was assumed for the test. To take into account the uncertainties in the stellar mass of each AGN into consideration, the stellar mass was randomly drawn from a Gaussian distribution with a width equal to the 1σ uncertainty of the stellar mass including an additional uncertainty of 0.1 dex to the quadrature. For a two-sample test with a significance of 5%, the critical value is 1.96 however all mock sample tests are larger than the critical value.

The AGN sample contains a mixture of AGN detected in 0.5-2, 2-10 keV, and both bands. There is a possibility that the type-1 AGN sample contains more luminous AGN than the type-2 AGN due to the deeper depth of the 0.5-2 keV detected sample which is also more sensitive to unobscured AGN. For the type-1 AGN sample, this results in an overall bias towards less luminous AGNs in less massive galaxies since fainter AGNs have smaller black holes and reside in less massive galaxies. In order to investigate this effect, the test was performed again but limited to those with detection in the 2-10 keV band and those with detection in both 0.5-2 and 2-10 keV bands. Table 4.2 shows the Anderson-Darling test statistics for each exercise.

In all cases, type-1 and type-2 AGN have different stellar mass with type-2 AGN residing in more massive galaxies than type-1 AGN by ~ 0.3 dex. The results follow the same trend as recent studies such as Zou et al. (2019); Mountrichas et al. (2021); Koutoulidis et al. (2022) and Georgantopoulos et al. (2023a) which suggest that type-2 AGN reside in more massive galaxies than type-1 AGN. However, is in tension with Suh et al. (2019) which concluded that type-1 AGN reside in more massive galaxies, as well as Bongiorno et al. (2012) who find no significant difference between obscured and unobscured AGN host.

4.8.2 The Black Hole mass of Type 1 & 2 AGN

In order to estimate the Eddington ratio of the type-2, the SMBH mass of type-2 AGN was inferred using the $M_{\rm stellar} - M_{\rm BH}$. The black hole mass of broad-line type-1 AGN can be estimated from the FWHM of the broad emission lines. This method is currently the only method to directly estimate the SMBH mass of AGN at this redshift and is only applicable to broad-line AGN. For type-2 AGN which shows no broad emission lines in the optical/UV spectrum, there is no direct method to estimate the

[2] https://docs.scipy.org/doc/scipy/reference/generated/scipy.stats.anderson_ksamp.html

Type-1 vs. Type-2			
Case	Match Luminosity	Nmatch	Test Statistics
All AGN	6 μm	171	$34.9^{+8.0}_{-7.2}$
All AGN	2-10 keV	172	$35.4^{+8.3}_{-7.4}$
2-10 keV	6 μm	128	$28.9^{7.0}_{-6.4}$
2-10 keV	2-10 keV	134	$27.8^{7.4}_{-6.6}$
0.5-2 & 2-10 keV	6 μm	106	$24.2^{6.5}_{-5.7}$
0.5-2 & 2-10 keV	2-10 keV	105	$21.7^{6.3}_{-5.7}$

Table 4.2: Anderson-Darling test statistics for stellar mass.

SMBH mass at this redshift but the black hole mass can be inferred from the host galaxy stellar mass assuming an $M_{\rm BH} - M_{\rm Stellar}$ relationship.

Figure 4.11 shows the distribution of the host galaxy stellar mass and black hole mass of type-1 AGN from the spectral analysis and previously reported values from Nobuta et al. (2012). The sample is compared to $M_{\rm BH} - M_{\rm Stellar}$ in the local universe from Kormendy and Ho (2013) and Reines and Volonteri (2015). Although the scatter is large (∼0.5 dex), the stellar mass to black hole mass ratio for the type-1 AGN is consistent with the $M_{\rm BH} - M_{\rm Stellar}$ of local early-type galaxies but is inconsistent with $M_{\rm BH} - M_{\rm Stellar}$ relationship of broad-line AGN in the local universe in which is ~ 1.5 dex away from the distribution of the datapoint. The results are consistent with previous results of $M_{\rm BH} - M_{\rm Stellar}$ of broad-line AGN in a similar redshift which suggest the $M_{\rm BH} - M_{\rm Stellar}$ of high-z broad-line AGN are consistent with local passive galaxies (Jahnke et al., 2009; Schramm and Silverman, 2013; Ding et al., 2020; Setoguchi et al., 2021; Mountrichas, 2023; Suh et al., 2020).

To calculate the black hole mass of the type-2 AGN sample, the $M_{\rm BH} - M_{\rm Stellar}$ of local early-type galaxies from Kormendy and Ho (2013) were adopted. This relationship is consistent with that of early-type galaxies from Reines and Volonteri (2015). Figure 4.12 shows the distribution in the 6-micron luminosity and black hole mass compared between type-1 and type-2 AGN. The result suggests that type-2 AGN have $M_{\rm BH}$ of $10^{8.5}$ $M_\odot$ which is similar to the type-1 AGN sample. The hard X-ray bolometric correction of type-1 and type-2 AGN from Duras et al. (2020) were used to calculate the bolometric luminosity. The hard X-ray BC has been shown to be a function of the intrinsic bolometric luminosity (Lusso et al., 2012) as opposed to those from optical or infrared bands.

4.8.3 Star Formation Activity

In this section, the results related to the star-formation properties of the AGN host galaxies are discussed. Firstly, the host galaxy colors in the restframe UVJ diagram were examined.

The UVJ diagram galaxies classifies galaxies into two major groups including; star-forming galaxies on the bottom right side and passive galaxies on the top left wedge. Figure 4.13 show the distribution of the AGN on the UVJ diagram with the star-forming/passive boundary of $z = 1 - 2$ galaxies from (Williams et al., 2009).

The majority of type-1 and type-2 AGN reside in the star-forming portion of the diagram while 13(6%) of type-1 AGN and of 83(29%) type-2 AGN objects reside in the passive region but close to the boundary of the diagram. A portion of the type-1 AGN occupies the bluer part of the UVJ diagram at $V - J < 0.6$ and $U - V < 1$. It should be pointed out that the host galaxy colors of type-1 on bluer colors of the diagram may be contaminated by AGN light.

Figure 4.14 shows the distribution of type-1 and type-2 AGN in the SFR $- M_{\rm stellar}$ diagram. The samples were separated into smaller redshift bins in order to mitigate the effect of the increasing cosmological evolution of star-formation towards cosmic noon and compare with the star-formation main sequence of Popesso et al. (2023). In order to be consistent with the IMF assumed in of Popesso et al. (2023), the stellar mass was converted to that when assuming a Kroupa IMF (Kroupa, 2001) with a 1.06 conversion factor (Popesso et al., 2023). A limit of 1% of the main-sequence SFR was adopted as the fiducial quenched limit.

For the majority of the AGN population, the star-formation rates are consistent with the SFR of main-sequence galaxies of the same stellar mass or are lower but not quenched. An Anderson-Darling test was performed to test the similarity between the SFR and the specific star formation rate (SSFR)

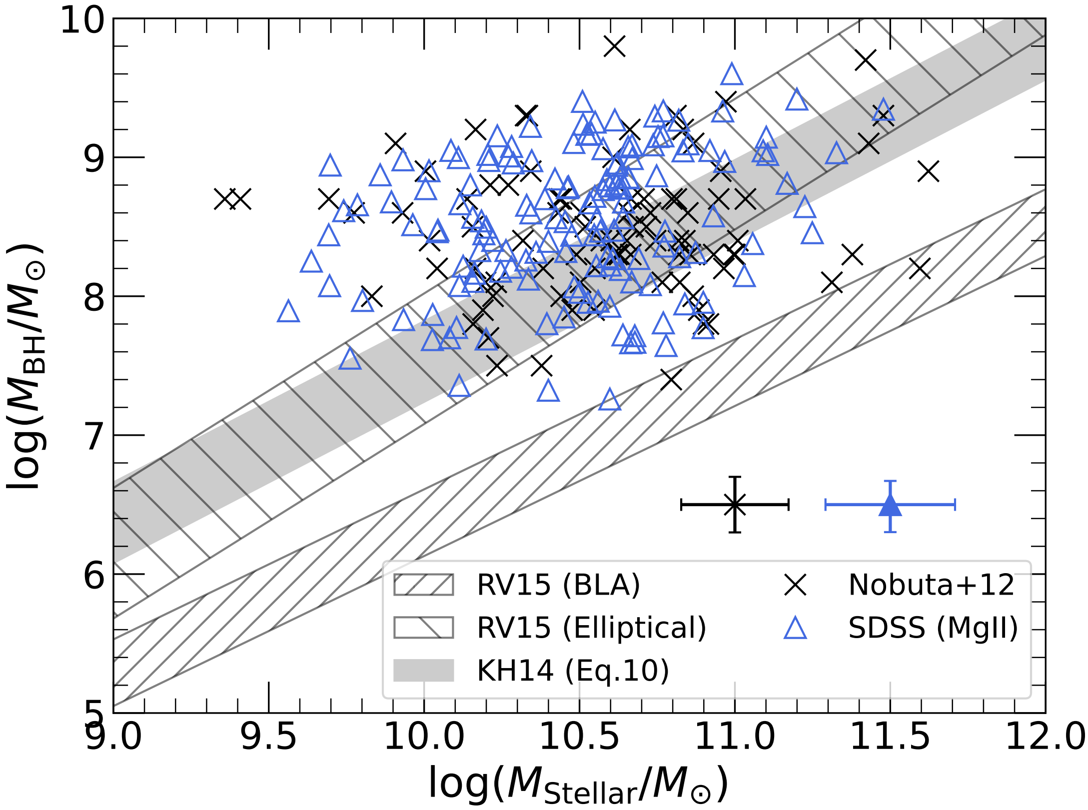

Figure 4.11: Comparison between the host galaxy stellar mass of type-1 AGN. Black crosses and blue open triangle shows measurements obtained from Nobuta et al. (2012) and from spectral analysis, respectively. The data points with error bars show the typical uncertainties of the measurements. The right-hatched and left-hatched areas show the $M_{\rm stellar} - M_{\rm BH}$ relationship for broad-line AGN and early-type galaxies in the early universe from Reines and Volonteri (2015). The gray shaded area shows the the $M_{\rm stellar} - M_{\rm BH}$ relationship for local early-type galaxies from Kormendy and Ho (2013).

of type-1 and type-2 AGN. The test was performed using the same redshift and luminosity matching as described in section 4.8.1, but in addition also matched the host galaxy stellar mass distribution since both SFR and SSFR is a function of host galaxy stellar mass(Feulner et al., 2005; Karim et al., 2011; Ilbert et al., 2015). The stellar mass distribution was matched between $\log M_{\rm stellar} = 9 - 12$ in bins of 0.5 dex. Both FIR-detected and FIR-non-detected AGN were used in the analysis since not enough FIR-detected AGN were available for statistical analysis after matching redshift, AGN luminosity, and stellar mass.

The results suggest no difference between the SFR and SSFR of type-1 and type-2 AGN at a 95% confidence and are shown in table 4.3. The results are consistent with Zou et al. (2019); Mountrichas et al. (2021); Koutoulidis et al. (2022); Suh et al. (2019) who concluded that the SFR of type-1 and type-2 AGN are statistically consistent with each other and are consistent with typical main-sequenced galaxies or those below.

4.8.4 $N_H - \lambda_{\rm Edd}$ Diagram

The obscuration of type-1 and type-2 AGN was investigated based on scenarios in the local universe such as the radiation pressure-regulated unified model. The observed Eddington ratio distribution for type-1 and type-2 AGN detected in the 2-10 keV band is shown in figure 4.15. The effective Eddington ratio for the median column density is shown with the thick black line. The majority of type-1 AGN are

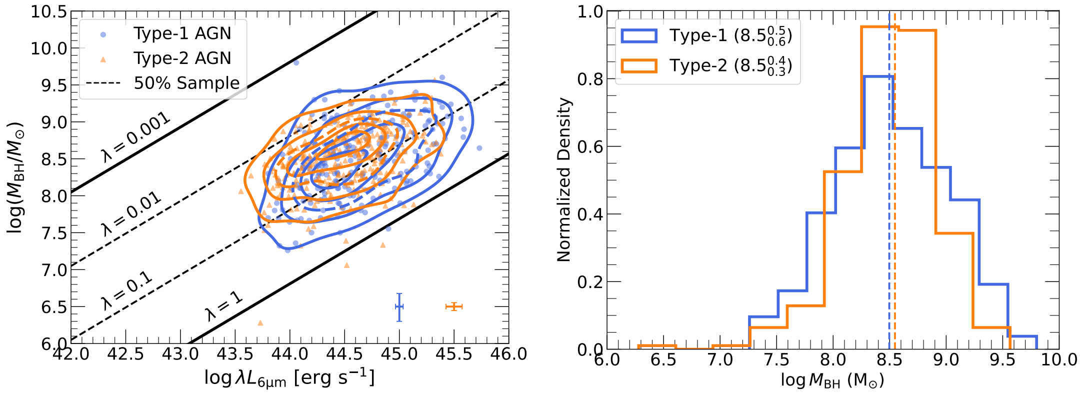

Figure 4.12: The 6-micron luminosity against black hole mass $M_{\rm BH}$ of type-1 AGN and type-2 AGN shown as blue and orange contours, respectively. The contour levels show the area which 10-90% of the datasets lays under. The 50% level is shown with dashed contours. The lines show the Eddington-ratio assuming the infrared bolometric correction from Runnoe et al. (2012). The faceless data point with error bars shows the typical uncertainty of the AGN.

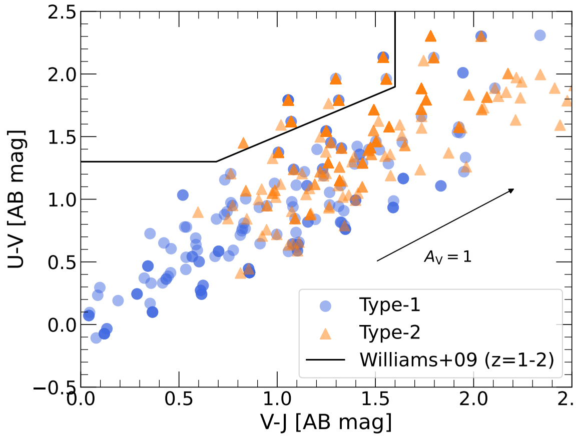

Figure 4.13: UVJ Diagram of Type-1 and Type-2 AGN assuming the boundary of Williams et al. (2009). The reddening vector with $A_{\rm V} = 1$ is shown on the right.

above the effective Eddington ratio for type-1 AGN while the opposite is true for type-2 AGN. When examining the shape of the distribution, the Eddington ratio distribution of type-2 AGN is skewered distribution towards the lower Eddington ratio while the type-1 AGN shows a symmetric distribution. There is no strong difference between the median Eddington ratio between type-1 and type-2 AGN. For both samples, the typical completeness limit is at an Eddington ratio of $\log \lambda_{\rm Edd} \sim -1.9$.

Figure 4.16 shows the distribution of type-1 and type-2 AGN at redshift 0.8-1.8 in $\log N_{\rm H} - \lambda_{\rm Edd}$ diagram on the left and right-hand side, respectively. The bottom of each plot shows the distribution of sources whose hydrogen column density cannot be constrained with the X-ray hardness ratio because they have a softer hardness ratio than the intrinsic power-law model. Their position along the Eddington ratio axis is shown but they are randomly distributed vertically for clarity.

For type-1 AGN, only 82 of the 166 2-10 keV detected type-1 AGN sample which $\log N_{\rm H}$ can be constrained with the hardness ratio, the values are distributed between $\log N_{\rm H}$ $[{\rm cm}^{-2}] = 21 - 23$. Broad lines are observed among this sample hence the column density for the majority should be lower than $\log N_{\rm H}$ $[{\rm cm}^{-2}] = 22$ otherwise the optical attenuation will extinguish the AGN emission. Some type-1 AGN has hydrogen column density larger than $\log N_{\rm H}$ $[{\rm cm}^{-2}] = 22$ but since the optical spectra show broad-lines, it implies that the X-ray absorption is caused by material with low dust content of free dust.

For type-2 AGN, most of them have a column density larger than $\log N_{\rm H}$ $[{\rm cm}^{-2}] = 22$ consistent with the typical classification of AGN in X-rays. However, 24% of the sample of type-2 AGN with

Star formation Rate			
Sample	Match Luminosity	Nmatch	Statistics
All	6 μm	113	$0.3^{+1.5}_{-0.7}$
All	2-10 keV	114	$0.1^{+1.4}_{-0.6}$
2-10 keV	6μm	73	$0.9^{+1.8}_{-1.1}$
2-10 keV	2-10 keV	84	$0.1^{+1.1}_{-0.5}$
0.5-2 & 2-10 keV	6 μm	56	$-0.2^{+1.0}_{-0.5}$
0.5-2 & 2-10 keV	2-10 keV	64	$-0.3^{+0.8}_{-0.4}$
Specific Star Formation Rate			
Sample	Match Luminosity	Nmatch	Statistics
All	6μm	113	$0.3^{+1.3}_{-0.7}$
All	2-10 keV	114	$0.3^{+1.1}_{-0.6}$
2-10 kev	6μm	73	$0.9^{+1.7}_{-0.9}$
2-10 kev	2-10 keV	84	$0.1^{+1.2}_{-0.6}$
0.5-2 & 2-10 keV	6μm	56	$-0.1^{+0.9}_{-0.5}$
0.5-2 & 2-10 keV	2-10 keV	56	$-0.1^{+0.7}_{-0.5}$

Table 4.3: Anderson-Darling Test statistics between type-1 and type-2 AGN for the host galaxy star-formation rate and specific star-formation rates.

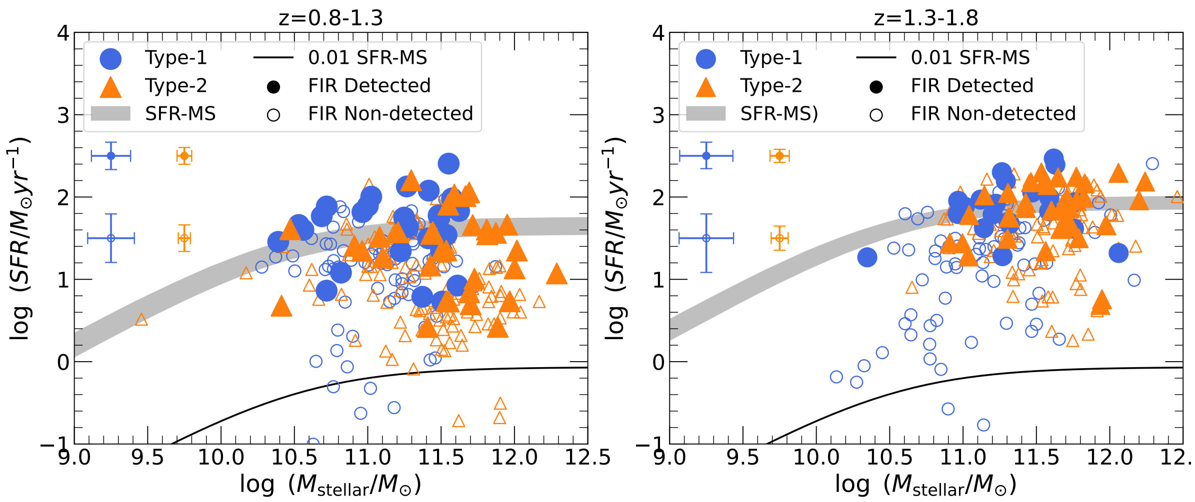

Figure 4.14: The SFR $-$ $M_{\rm stellar}$ distribution at $z = 0.8 - 1.3$ (left) and at $z = 1.3 - 1.8$ (right). FIR-detected AGNs are shown as filled data points. The contours show the distribution of FIR non-detected AGN. The star formation main sequence of Popesso et al. (2023) is shown as the gray area where the with represents 1σ the confidence interval of the relationship.

$\log N_{\rm H}$ [cm^{-2}] ≥ 22 reside above the effective Eddington ratio limit in the forbidden zone. These type-2 AGNs are expected to produce dusty outflows. An alternative explanation is that the X-ray emission is affected by ISM absorption.

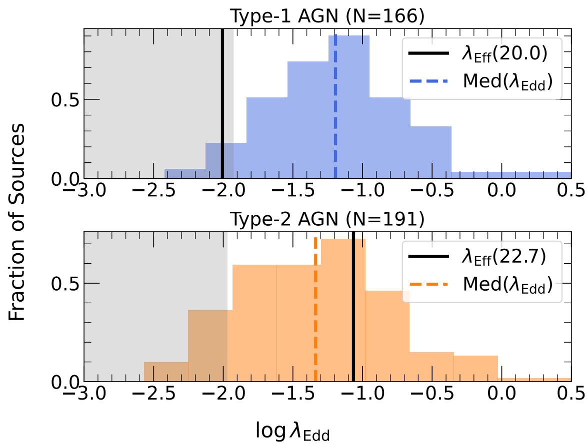

Figure 4.15: The observed Eddington-ratio distribution of Type-1 AGN (top) and type-2 AGN (bottom). The thick black lines show the effective Eddington ratio at the median hydrogen column density of each sample. The dashed line shows the median Eddington ratio of each sample.

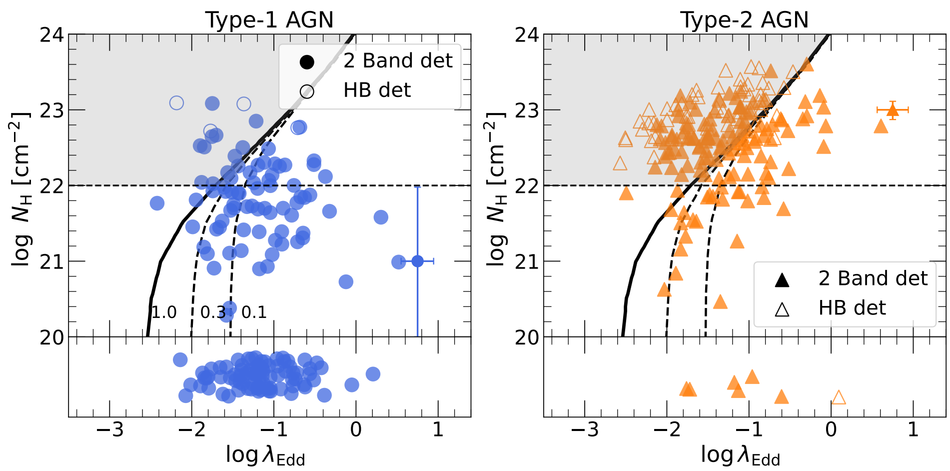

Figure 4.16: The $N_H - \lambda_{\rm Edd}$ diagram of type-1 AGN (left, blue round symbols) and type-2 AGN (right, orange triangles). The hydrogen column density uncertainty is shown assuming an intrinsic column density of $\log N_{\rm H}$ [cm^{-2}] = 21 and $\log N_{\rm H}$ [cm^{-2}] = 23 and the typical Eddington-ratio uncertainty for type-1 and type-2 AGN with the data points with error bars. In both panels, the curved thick and dashed line shows the effective Eddington ratio assuming a dust abundance of 1,0.3, and 0.1, from left to right. The horizontal dashed line shows the fiducial ISM absorption in the local universe. The bottom panel shows the Eddington-ratio distribution of AGN which the Hydrogen column density can not be constrained with the X-ray hardness ratio.

4.9 Discussion

4.9.1 The Obscuration of Type-1 AGN

In this section, the obscuration in type-1 AGN based on the $\log N_{\rm H} - \lambda$ diagram is discussed. The detection of broad AGN emission lines in the optical spectra and the point source morphology implies that the dust attenuation is modest compared with type-2 AGN. In principle, the line of sight of type-1 AGN passes through both the host galaxy ISM and the polar dust region. Therefore, the X-ray absorption can be due to modest ISM obscuration in the line of sight. Since the hydrogen column density of the majority of type-1 AGN can not be constrained, the effect of ISM obscuration was examined through the effects on the restframe colors of the AGN.

A toy model to simulate the observed colors when the AGN optical emission is affected by ISM

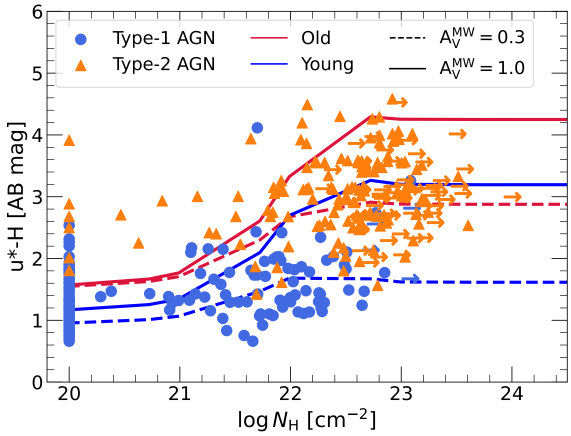

Figure 4.17: Rest-frame u*-H color distribution of type-1 and type-2 AGN. shown as blue round and orange triangles, respectively. The gray shaded area shows the expected color space as a function of increasing ISM column density near the AGN.

attenuation as a function of ISM hydrogen column density was constructed. In CIGALE, the polar dust attenuation in the AGN model is applied to the AGN component and independent from the dust attenuation applied to the stellar component. Since distinguishing between polar dust and the ISM is not straightforward, no distinction is made between the two here. The component was used to represent the attenuation by the kpc-scale ISM ($< 1kpc$) or circumnuclear scale ($\sim$ 100 pc) in the case of $\log N_{\mathrm{H}}$ [cm^{-2}] ~ 24. The SMC extinction curve was adopted to calculate the dust attenuation applied to the AGN component and convert $\log N_{\mathrm{H}}$ to E(B-V) assuming $A_{\mathrm{V}}/N_{\mathrm{H}}$ from Dobashi et al. (2009) and $R_{\mathrm{V}} = 2.93$ from (Pei, 1992).

Two sets of host galaxy models were adopted from the best-fitted parameters SED fitting parameters of type-1 AGN. Firstly, a 3 Gyr old stellar population with an e-folding time of 0.5 Gyr and secondly a 1.5 Gyr old stellar population with an e-folding time of 6 Gyr. The dust extinction curves of Cardelli et al. (1989) with $R_{\mathrm{V}} = 3.1$ with A_V of 0.3 and 1 was assumed. In order to realistically set the ratio between the host galaxy luminosity and the AGN luminosity, the AGN fraction in 2-10 μmwas set to the best-fitted type-1 AGN AGN fraction in 2-10 μm.

In figure 4.17, the $u * -H$ color distribution of type-1 AGN against the total hydrogen column density. The $u * -H$ colors of the two models are shown as a function of kpc-scale ISM-only hydrogen column density. The colors of type-2 AGN are shown as a reference for host galaxy-dominated colors. With increasing kpc-scale ISM obscuration which affects the AGN emission, the contamination by the host galaxy increases as seen as the increasingly red colors at $\log N_{\mathrm{H}}$ [cm^{-2}] $\sim 21.5 - 22$. At above $\log N_{\mathrm{H}}$ [cm^{-2}] $= 22$, the colors become dominated by the host stellar emission as there is no longer any change in the colors.

For type-1 AGN with $\log N_{\mathrm{H}}$ [cm^{-2}] < 22, the colors are consistent with those which are dominated by the blue unobscured AGN emission or those affected by mild kpc-scale ISM obscuration of less than $A_V \sim 1.5$ mag. Some type-1 AGN have hydrogen column density larger than $\log N_{\mathrm{H}}$ [cm^{-2}] > 22 but have colors consistent with the unobscured type-1 AGN or obscured AGN in host galaxies with young stellar populations with low dust attenuation. However, the latter case cannot explain the broad emission lines detected in the optical emission of the type-1 AGN since the latter model suggest the AGN emission is extinct due to the large kpc-scale dust attenuation.

The type-1 AGN with $\log N_{\mathrm{H}}$ [cm^{-2}] > 22 can be explained if the X-ray absorption occurs from dust-free gas. Merloni et al. (2014) showed that obscured broad-line AGN make up $\sim 10 - 20\%$ of the luminous AGN population ($\log L_{\mathrm{X}}$ [erg s^{-1}] > 44). Ichikawa et al. (2019) investigated the X-ray and mid-infrared dust covering factor of SWIFT/BAT AGN. They found that for typical AGN with $\log L_{\mathrm{Bol}}$ [ergs^{-1}] > 42.5 the covering factor of X-ray absorbing material is larger than that of the mid-infrared emitting dusty material. Liu et al. (2018) concluded that partial obscuration in lines-of-sight near the torus edge can result in dust-free obscuration. Another possibility is that dust-free lines of sight are due to a gas-rich extended time variable dust sublimation zone within the nuclear torus (Kudoh et al., 2023).

Obscured broad-line AGN may also be due to accretion disk winds within the dust sublimation radius which coincide with the line-of-sight. Since these winds occur within the dust sublimation radius, their content is dust-free ionized gas. An example of such a case is broad-absorption line quasars (BAL-QSO) which tend to show complex ionized X-ray absorption (Gallagher et al., 2002, 2006) and broad absorption features associated with SiV, CIV, or MgII. Since most of the samples are at redshift below that which CIV can be detected in the optical spectrum, the statistical significance among the sample cannot be discussed. However, 5 cases of absorption associated with the CIV emission line of type-1 AGN are seen. For one of the BAL quasars candidates, the column density is $\log N_{\rm H}$ [cm^{-2}] $= 22.5$ under the assumption of a neutral photoelectric absorber (phabs) while the hydrogen column density of the remaining AGN cannot be constrained. BAL-QSO tends to have more complex absorption including both ionized and partially X-ray absorption (Gallagher et al., 2006) which requires X-ray spectral analysis with higher signal-to-noise.

4.9.2 The Obscuration of Type-2 AGN

In this section, the X-ray absorption of type-2 AGN on the $N_{\rm H} - \lambda_{\rm Edd}$ diagram is discussed. Unlike type-1 AGN, the lack of broad emission lines and the host galaxy-dominated continuum requires large amounts of dust along the line of sight. In figure 4.16, the X-ray absorption of 76% of hard band detected type-2 AGN can be explained by radiation pressure-regulated torus obscuration.

In figure 4.16, 24% of type-2 AGN reside in the forbidden zone which may imply that they are actively producing outflows. Lansbury et al. (2020) suggest that the time scale in which dusty outflows clear out Compton-thick line of sight ($\log N_{\rm H}$ [cm^{-2}] $= 24$) is very short ($\sim 10^4$ yr) compared to a lifetime of the AGN ($\sim 10^{7-8}$ yr) and for lower hydrogen column density, the time scale should be shorter. Jun et al. (2021) estimated that $\leq 20\%$ of the AGN population should occupy the blow-out region of the $N_{\rm H} - \lambda_{\rm Edd}$ diagram. Hence, only a small fraction of the entire sample of type-2 AGN should occupy the forbidden zone. The large number of AGN in the forbidden zone can be explained if the X-ray absorption in these AGN is associated with the heavy nuclear ISM absorption. Therefore, the obscuration can be kept at accretion rates above the effective Eddington ratio. As shown by Gilli et al. (2022), the ISM absorption beyond the local universe can reach above $\log N_{\rm H}$ [cm^{-2}] ≥ 22.

In order to quantify the increased incidence of ISM-obscured AGN due to the cosmological evolution of the gas fraction, the fraction of type-2 AGN within the forbidden zone was compared with the fraction in the local universe. The second data release of the Swift-BAT AGN Spectroscopic Survey (BASS DR2, Koss et al. (2022); Oh et al. (2022)) was adopted as the local universe sample. BASS is a highly complete sample of local AGN($z < 0.1$) thanks to the detection of hard X-rays (> 10 keV) and high spectroscopic completeness from dedicated follow-up efforts to measure the black hole mass from broad emission lines or stellar velocity dispersion. The hydrogen column density from Ricci et al. (2017b) was added and the sample was limited to 681 non-beamed and non-lensed AGN that have similar redshift ($|\Delta z| < 0.01$) between the two reports. The spectral classification presented in Koss et al. (2022) was adopted to classify the AGN into type-1 or type-2. The $N_{\rm H} - \lambda$ diagram of BASS AGN is shown in the 4.18.

In the local universe, the fraction of Compton-thin type-2 AGN in the forbidden zone among AGN with Eddington ratio larger than $\lambda_{\rm Edd} \geq -2$ is $11 \pm 3\%$. If Seyfert 1.9 are considered as type-1 AGN due to the detection of broad Hα emission line then the fraction is reduced to $7 \pm 2\%$. In comparison, the fraction of type-2 AGN at z=0.8-1.8 in the forbidden zone with Eddington ratio larger than $\lambda_{\rm Edd} \geq -2$ is $26 \pm 5\%$. The fraction was also examined in the case of the Eddington ratio larger than $\lambda_{\rm Edd} \geq -1$ which is less affected by the detection limits. Overall, the results support the increased fraction of obscured AGN due to the cosmological evolution of the galaxy's ISM.

Since ISM gas is dusty, the large ISM hydrogen column density will also affect the AGN optical/UV emission. As a brief reminder, the sample of type-2 AGN was selected based on their extended morphology. The torus hydrogen column density in the observed line of sight should be low because the Eddington ratio of type-2 AGN in the forbidden zone is above the effective Eddington ratio. Hence, without the ISM, The AGN should appear similar to a typical unobscured AGN or broad-line AGN. For ISM dust, Zhu et al. (2017) presented the Milky-way gas-to-attenuation ratio as $N_{\rm H}/A_{\rm V} = (2.08 \pm 0.02) \times 10^{21}$ H cm^{-2} mag^{-1}. Therefore, ISM hydrogen column densities of $\log N_{\rm H}$ [cm^{-2}] $= 22$ will produce a V-band attenuation of $A_{\rm V} \sim 4$ magnitudes and is much larger by a factor of 2-5 times for the UV emission when assuming ISM extinction curves (Cardelli et al., 1989; Calzetti et al., 2000). As shown in figure 4.17 above

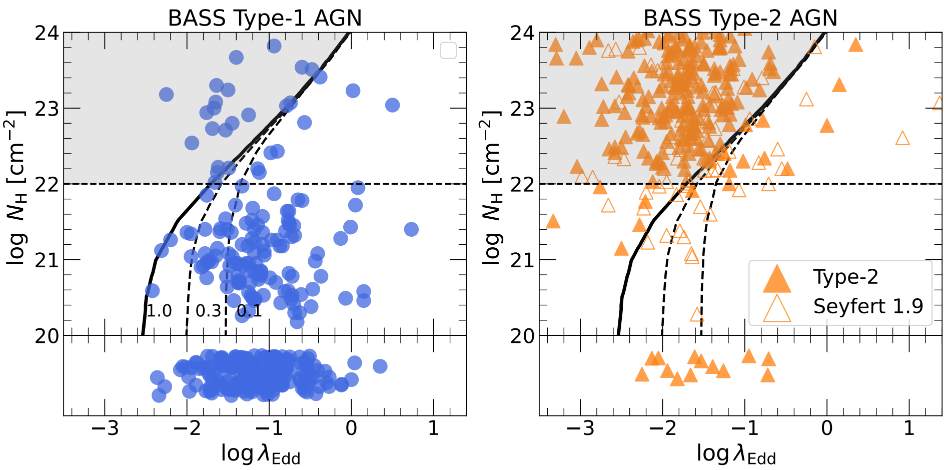

Figure 4.18: The observed Eddington-ratio distribution of Type-1 AGN (top) and type-2 AGN (bottom) in the local universe from the BASS survey. The thick black lines show the effective Eddington ratio at the median hydrogen column density of each sample. The dashed line shows the median Eddington ratio of each sample.

$\log N_{\rm H}$ [cm^{-2}] ≥ 22, the colors become dominated by the host galaxy even for type-1 AGN. Hence, the observed morphology may be dominated by the host galaxy because the contrast between AGN and the host galaxy emission is reduced due to ISM obscuration.

The effects are similar to intermediate Seyfert galaxies in the local universe (Maiolino and Rieke, 1995) but at a higher severity. In the most severe case, the ISM obscuration may be enough to obscure the whole galaxy as seen in SMG populations. Among the sample of AGN, 14 of the type-2 AGN were not detected in the HSC bands but are detected in the NIR bands. Their column density exceeds $\log N_{\rm H}$ [cm^{-2}] $= 22$ and the SED-fitting based ISM V-band attenuation distributes between $A_{\rm V} = 1 - 6$ magnitudes. However, the nuclear ISM attenuation must be larger the that estimated by SED fitting since this SED fitting attenuation represents the average optical attenuation over the whole galaxies. These AGNs may be analogous to SMG-AGN at $z \geq 2$ which show heavy X-ray absorption from the ISM components (Circosta et al., 2019; D'Amato et al., 2020)

4.9.3 Star-formation Activity and Obscuration

In this section, the properties of the star formation of type-1 and type-2 AGN in the context of the evolutionary scenario are discussed. Intense star formation is expected to occur simultaneously with obscured AGN activity following a gas-rich merger event as seen in local ULIRGs. If gas-rich merger-triggered obscuration is common in the AGN population at high redshift, the star-formation activity in type-2 AGN should be more intense than unobscured AGN (Hopkins et al., 2006, 2008b).

However, firstly the statistical analysis suggests no significant difference between the SFR or SSFR of type-1 and type-2 AGN. Secondly, the SFR of type-1 and type-2 AGN is consistent with the typical star-formation rate main sequence. Thirdly, the Eddington ratio distribution of the majority of type-2 AGN is lower than the effective Eddington ratio of their respective hydrogen column density. Based on these facts, I believe that the majority of type-2 AGN are obscured by a radiation pressure-regulated torus or obscuration due to the cosmological evolution of galaxies and not kpc-scale obscuration as a result of gas-rich mergers.

Although the results support the scenario of the radiation pressure-regulated torus, selection effects may affect the result. During the coalescent phase which corresponds to peak accretion and star-formation activity, the large influx of gas towards the nuclear regions may result in near Compton-thick absorption (Blecha et al., 2018), which can be missed from X-ray selection due to their faintness. This would suggest that the sample of type-2 AGN which I selected may be analogous to galaxies in the early stage of coalescence where the AGN is triggered by the gravitational disturbance of nearby galaxies. Their SFR and SSFR are consistent with the main-sequence galaxies and the absorption is due to torus or nuclear ISM obscuration. On the other hand, type-1 AGN are those in the post-blowout stage after a decline in SFR but not quenched due to the longer time scale of star formation compared to the AGN. High angular resolution deep imaging and spectroscopic follow-up will be required to identify AGN in a merger sequence.

4.9.4 Systematic Uncertainties

In this section, the systematic uncertainties which may affect the analysis are discussed. First, the effects of AGN light on the estimation of stellar mass. For type-1 AGN, estimation of the stellar mass can be uncertain due to the dominance of AGN emission in the optical/UV. Due to contamination from the AGN emission, the SED can be fitted with a younger stellar population with lower stellar mass or a SED with a larger burst fraction. It should be pointed out that reliable stellar age indicators from spectral analysis are not available. The stellar age of the best-fitted SED does not show any strong difference between type-1 and Type-2 AGN and the burst fraction used in the fitting is limited to at most 10% of the total stellar mass.

Second, the choice of the $M_{\rm BH} - M_{\rm Stellar}$ relationship can affect the determination of the Eddington ratio through the black hole mass estimate. There is currently no reliable direct estimate of black hole mass available for most of the sample at z=0.8-1.8. Hence, the $M_{\rm BH} - M_{\rm Stellar}$ was adopted based on the assumption that type-2 AGN follows a similar $M_{\rm BH} - M_{\rm Stellar}$ relationship as type-1 AGN samples shown in figure 4.11.

On the one hand, assuming $M_{\rm BH} - M_{\rm Stellar}$ of local broad-line AGN will decrease the black hole mass of type-2 AGN by approximately 1.5 dex and will increase the Eddington ratio by a similar amount. In such a case, most of the type-2 AGN will appear in the forbidden region near the Eddington limit above the effective Eddington ratio limit. Under such a scenario, all type-2 AGN are affected by ISM absorption instead of a mixture of nuclear and ISM obscuration.

On the other hand, the $M_{\rm BH} - M_{\rm Stellar}$ of high redshift AGN may have a higher normalization than that of local passive galaxies. Merloni et al. (2010) showed that the deviation from the local black hole mass to stellar mass ratio of type-1 evolves with redshift as $(1+z)^{0.68}$. Hence, accounting for the redshift evolution of the $M_{\rm BH} - M_{\rm Stellar}$, the mass of type-2 AGN is larger by $\sim 0.62 \log(1+z) \sim 0.27$ which reduces the Eddington ratio for type-2 AGN. In this case, the fraction of AGN in the forbidden zone is reduced, and most AGN is obscured by the dusty torus.

Recently, there has been development of a virial mass calibration using the Paschen-β emission lines (Onori et al., 2017a) which suggest that type-2 AGN have a smaller black hole masses than type-1 AGN by $\sim 0.8 - 1$ dex (Onori et al., 2017b; Ricci et al., 2017d). While there are differences in the AGN luminosity compared to the sample, future observations of Paschen-β emission lines may shed light on the mass of type-2 AGN.

4.10 Summary & Conclusion

In this work, I investigated the incidence of obscuration, stellar mass, and star-formation rate of X-ray selected type-1 and type-2 AGN at $z = 0.8 - 1.8$ in the HSC-Deep XMM-LSS survey field. I performed a spectral analysis of the MgII emission lines to determine the black hole mass of type-1 AGN. For type-2 AGN, I inferred the blackhole mass by assuming a $M_{\rm BH} - M_{\rm stellar}$ relationship where the stellar mass was estimated using SED fitting. I estimated the hydrogen column density using the X-ray hardness ratio by a phenomenological X-ray spectral model. The important results are summarized as follows.

1. The majority of type-1 AGN have an Eddington ratio above the effective Eddington ratio whereas most type-2 AGN are below. The observed Eddington ratio distribution of type-2 AGN is skewed towards a lower value than type-1 AGN consistent with the radiation-regulated unified model. (section 4.8.4)

2. The X-ray absorption of type-1 AGN may be due to mild ISM obscuration $\log N_{\rm H}$ [cm^{-2}] < 22 but for larger hydrogen column density dust-free sight lines or disk-winds are needed. (section 4.9.1)

3. Among the type-2 AGN sample, 24% reside in the forbidden zone. The X-ray absorption among type-2 AGN in the forbidden zone can be explained by additional ISM obscuration which is not strongly affected by the AGN radiation pressure. (section 4.9.2)

4. The fraction of type-2 AGN in the forbidden zone increased from $11 \pm 3\%$ in the local universe to $26 \pm 5\%$ at redshift 0.8-1.8. The increased fraction of AGN in the forbidden zone supports the increasing incidence of ISM absorption due to the cosmological evolution of galaxy ISMs 4.9.2).
5. There is no trend between star-formation activity and obscuration. The total star-formation rate of AGN host galaxies is consistent with typical main sequence galaxies in the same redshift or lower but not quenched (1% SFR-MS). The star-formation rate and specific star-formation rate of type-1 and type-2 AGN are consistent with each other at a 95% confidence level. (section 4.9.3)

The results indicate that the main obscuration mechanism for the majority of AGN at redshift 0.8-1.8 is due to radiation pressure-regulated dusty torus. However, the incidence of obscuration above $\log N_{\rm H}$ [cm^{-2}] ≥ 22 by the galaxy ISM is larger than that in the local universe, as seen by the increased fraction of AGN occupying the forbidden zone. I believe that this is increase can be due to the cosmological evolution of the host galaxy ISM.

Chapter 5

Summary & Conclusion

In this study, I investigated the obscuration of active galactic nuclei during the peak of SMBH growth by using deep and wide multiwavelength datasets. In chapter 2, I explained the construction of a multiband photometric catalog using the deep and wide optical infrared datasets in the HSC-Deep field, XMM-LSS survey area which covers 13-band of photometry from u*-band to 4.5 μm. PSF-convolved photometry was performed in order to obtain accurate colors and fluxes of optical/infrared counterparts of X-ray sources. This is especially important for mid-infrared datasets such as SERVS 3.6 and 4.5 μm which are heavily affected by blending. By using this photometry, the photometric redshift was estimated using AGN and galaxy models for sources with no prior spectroscopic redshift. Good photo-z statistics scatter of 0.1 when compared with spectroscopic redshift was achieved and a sample of 3462 X-ray detected AGN with multiband photometry up to redshift 5 was presented.

A sub-sample of 2-10 keV detected AGN was used to study the obscured fraction of Compton-thin AGN above redshift 2 as described in chapter 3. Here, I adopted a modified version of the absorption function model described in Ueda et al. (2014) to estimate the obscured fraction. Thanks to the deep and wide X-ray dataset, luminous obscured AGN which may have been missed in shallower or narrow field X-ray surveys have been detected. Using the best-fit parameters I estimated that 76^{+4}_{-3}% of Compton-thin AGN with 2-10 keV luminosity above $\log L_{\rm X}$ [erg s^{-1}] ≥ 44.5 at above redshift 2 are obscured which is a factor of ~ 2 large than that in the local universe. The large obscured fraction of AGN could be a result of the cosmological evolution of the ISM component in normal star-forming galaxies or due to a large fraction of mergers triggered AGN at high redshift.

Using the multiwavelength photometry, I further examined the optical infrared SED of obscured and unobscured AGN at $z > 2$. On average, unobscured AGNs have a flat optical infrared SED as opposed to obscured AGNs which have a reddened SED. However, the scatter in the median SED is large. This indicates that a significant fraction of the AGN are affected by dust reddening or contain dust-free X-ray absorption.

Inspired by the large scatter in the SED. I further investigated the obscuration properties of AGN at redshift 0.8-1.8 using the $\log N_{\rm H} - \lambda_{\rm Edd}$ in chapter 4. The AGN was classified into type-1 and type-2 AGN based on the spectroscopic classification and the optical morphology. For broad-line AGN, the black hole mass was estimated from the MgII emission lines while for type-2 AGN, the black hole mass was inferred from the host galaxy stellar mass assuming a stellar mass to black hole mass of local passive galaxies. On average, type-2 AGN has a lower Eddington ratio than type-1 AGN and has a distribution of Eddington ratios skewed towards a lower Eddington ratio. My investigation of the star-formation rate of type-1 and type-2 AGN also suggest no difference between the two population and both are consistent with the typical star-forming galaxies.

A larger fraction of type-2 AGN is within the forbidden zone of the $\log N_{\rm H} - \lambda_{\rm Edd}$ as compared to the local universe. The increased fraction suggests an increased incidence of ISM absorption in the sample of type-2 AGN which is due to the cosmological evolution of galaxy ISMs. For type-1, the large column density above $\log N_{\rm H}$ [cm^{-2}] ≥ 22 can be explained by dust-free absorption. Figure 5.1 summarizes the mechanism of AGN obscuration for type-1 and type-2 AGN as well as for unobscured and obscured AGN. All in all, it suggests that most of the AGN are obscured by radiation pressure-regulated dusty torus with an increased fraction of ISM obscuration due to the cosmological evolution of the host galaxy ISM.

<table>
<tr><th rowspan="4" colspan="2">Obstructing Material</th><th colspan="4">X-ray Obscuration</th></tr>
<tr><th colspan="3">Compton-Thin AGN (CTN-AGN)</th><th>Compton-Thick AGN (CTK-AGN)</th></tr>
<tr><th>Log N_H = <22</th><th>Log N_H = 22-23</th><th>Log N_H = 23-24</th><th>Log N_H = 24-26</th></tr>
<tr><th>Unobscured</th><th colspan="2">Obscured</th><th>CTK</th></tr>
<tr><td rowspan="2">Dust Obscuration</td><td>Type-1 AGN</td><td>• Dusty ISM
• Polar Dust</td><td colspan="2">• Dust-Free LOS
• Accretion Disk Winds
• ISM+Outflows</td><td></td></tr>
<tr><td>Type-2 AGN</td><td></td><td colspan="2">• Torus
• High-z Dusty ISM</td><td>• Torus</td></tr>
</table>

Figure 5.1: The mechanism of AGN obscuration broken down by classification.

As mentioned in the introduction, the obscured fraction shows an increase from the local universe up to high redshift as summarized in chapter 3. My investigation of the obscuration properties in chapter 4 at redshift 0.8-1.8 suggest that radiation pressure-regulated dusty torus is the primary mechanism of obscuration but with an increased fraction of ISM absorption. These results show that the inclination angle of the line of sight may not simply explain the mechanism of AGN obscuration. Therefore, the cosmological evolution of the obscured fraction may be driven by the cosmological evolution of the AGN host galaxy ISM. Figure 5.2 shows the summary phenomenological view of AGN obscuration at low and at high redshift including each mechanism of AGN obscuration.

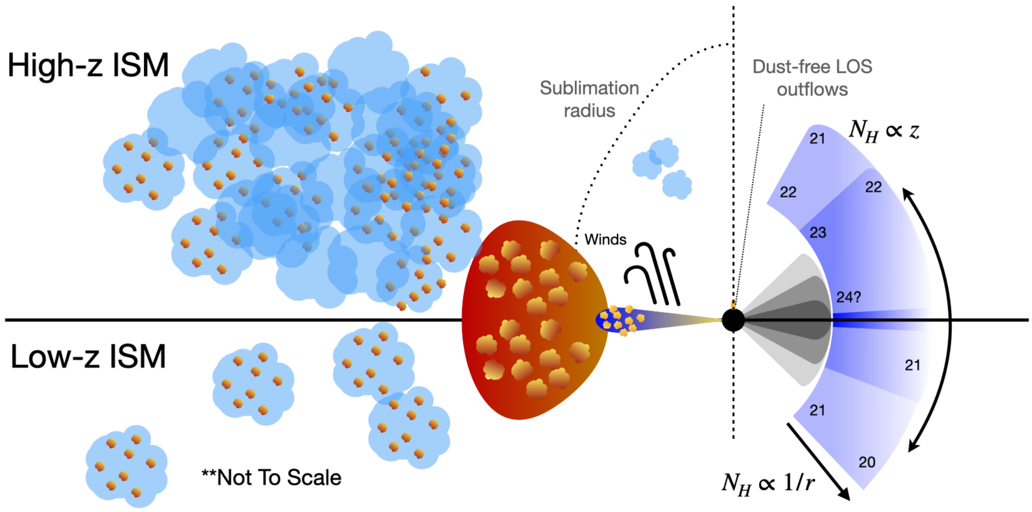

Figure 5.2: The current schematic image of AGN obscuration. The left-hand side shows the physical structure of obscuration including the ISM, torus, winds, and dust-free lines of sight. The right-hand side shows the phenomenological view in terms of covering factors of each mechanism. At high redshift, the evolution of the galaxy ISM increases the ISM covering factor (blue-shaded area) in both the height and hydrogen column density. The torus covering factor is shown in gray and is assumed to have no evolution.

5.1 Future Prospects

It is becoming increasingly clear that the build-up of black holes and stellar mass at high redshift universe occurs under heavy obscuration. Although our statistical understanding of the increased obscuration has progressed significantly, the reality is that the obscuration has decreased since the formation of those galaxies. The process by which a galaxy has become less obscured is still not well understood. Some possible processes include intense AGN feedback which can blow out even the ISM or consumption of the ISM by star formation and accretion. For the former, high angular resolution imaging of the AGN and spectroscopic confirmation of merging galaxies is needed in order to determine the fraction of AGN in a merger sequence.

In this work, I used the hardness ratio to estimate the hydrogen column density of the AGN. As mentioned, this method is subject to the assumption of the model especially the photon index of the AGN. With recent advancements in computation power, a Bayesian spectral analysis of the X-ray sources would provide a better understanding of the uncertainties of the AGN properties.

As described in section 4.9.4, gas-rich mergers may result in Compton-thick levels of absorption which can be missed by the X-ray surveys. In order to investigate the obscuration of luminous CTK-AGN near the knee of the luminosity function, deep & wide mid-infrared and far infrared datasets are needed to identify CTK-AGN without X-rays. Future projects such as PRIMA Bradford et al. (2022) and GREX+ (Inoue et al., 2022) would aid in this investigation.

Appendix A

Multi-band Photometry

A.1 Image Alignment and Background Subtraction

For HSC images, we perform global background subtraction to the image in each patch image. The background levels were determined from the mean pixel value of the image after applying a 3σ clip. After that, 200 blank pixels were padded to each side of the image.

CLAUDS data used in this work were aligned to the tract-patch definition as of the HSC S16A dataset which is a prior version to the HSC data. Hence, there is a 1-2 pixel offset in the image pixel grid compared to the S19A and S20A data used in this work. We match the astrometry to the HSC S19A dataset and apply an additional local background subtraction using SWarp (Bertin, 2010).

For the pipeline-reduced VIDEO DR5 images of the XMM1, 2, and 3, the background of each area was subtracted using SExtractor (Bertin and Arnouts, 1996). The images were then resampled into the same pixel scale as in the HSC images and combined together into a single mosaic using SWarp. Resampled variance images on the same pixel scale were also produced using SWarp. However, these variance images do not preserve the original variance. We created new variance images by converting the original weight images to variance and then passing them to SWarp as images to be combined. This method preserves the original variance measured from the background images. Cutouts in the same tract and patch as HSC images were created from the mosaics and resampled to the same S19A WCS system.

SERVS mid-infrared images are provided as a single mosaic with the RMS image. We use SWARP to resample the image to the same WCS coordinates as the HSC S19A dataset and to perform background subtraction. The RMS image was converted to a variance image and resampled in the same manner applied to the VIDEO images. We then cut the mosaic images according to each patch and tract defined in the S19A dataset using SWARP.

A.2 PSF Modeling and Kernel Construction

Measurements of the color of an object can be affected by the PSF difference between the images in two bands. This is because the amount of flux measured in the two bands using the same aperture size is systematically off due to the difference in the PFS shape and size. In order to obtain accurate colors either the PFS of each dataset needs to be normalized to the same shape and size or a template-fitting type of photometry should be used.

The point-spread function gives the distribution of the intensity that falls on the detector by a point source. Its shape and size are governed by the instrument's optical system. For seeing limited observations, the size of the PSF is limited by the sky conditions at the time of the observations. This differs for each dataset due to different locations, times, and instruments that were used to obtain the data. In the case of observations taken with space-based facilities, the angular resolution depends solely on the instrument. A convolution kernel is needed in order to convert an image with one angular resolution to another. The convolution kernel is a 2-dimensional matrix that converts the PSF shape of the high-resolution image (HRI) to the PSF shape of the low-resolution image (LRI). It can be constructed by deconvolving the LRI PSF with the HRI PSF.

In this work, we construct a PSF in each patch in order to take into account the PSF variation over the survey area. However, PSF variation within each patch is ignored. The PSF of the HSC datasets were obtained from the HSC database while the PSF models for CLAUDS, VIDEO, and SERVS were constructed directly from the images of stellar objects which were chosen from the 2MASS point-source catalog (Skrutskie et al., 2006)[1].

At first, catalogs in each patch produced using SExtractor are matched with Ks band sources in the 2MASS point-source catalog. For CLAUDS and VIDEO, 2MASS sources with $15 \leq K_s < 17$ were selected for the PSF modeling. Due to the low angular resolution of 2MASS, some extended sources were identified as point sources in the 2MASS point-source catalog. We remove these extended sources using CLASS_STAR < 0.9 and ELLIPTICITY > 0.2 measured in the CLAUDS and VIDEO catalogs.

For SERVS, sources with $14 \leq \mathrm{K_s} < 17$ were selected for the PSF modeling. Since the PSFs of Spitzer IRAC are asymmetric, the same criteria as the CLAUDS and VIDEO datasets cannot be used to remove extended sources. Extended sources were rejected by examining the FWHM distribution; sources whose FWHM exceeds 2σ scatter were removed.

After removing extended sources from the models, the individual images of stellar sources were re-centered, background subtracted, and normalized to unity. The final PSF images were constructed using a median combination of each individual stellar source. Finally, the final PSF image is re-centered and normalized once again, and the images are padded to 55×55 pixels.

Local PSF images were constructed only for patches with more than 7 individual stellar sources. A median PSF image of each tract is used for patches with fewer than 7 individual sources. The HSC S19A r-band PSF images were adopted as the HRI PSF and Pypher (Boucaud et al., 2016) was used to construct the convolution kernels of images in other bands.

A.3 Pixel-to-Pixel Correlation Correction

Pixel-Pixel correlation is an effect that occurs due to the resampling of pixelated images. Resampling smooths the image thus the variance in the image becomes artificially smaller than the original image. Therefore, it is necessary to correct the underestimation of the variance in order to obtain accurate photometric uncertainties for each pixel.

The HSC pipeline has already performed the correction for pixel-pixel correlation and no resampling was done for the reduced image. For CLAUDS, VIDEO, and SERVS, we examine the effects of pixel-pixel correlation by performing a fixed-aperture analysis similar to Bielby et al. (2012). SExtractor was used to produce segmentation images of all CLAUDS and VIDEO images and 1000 fixed apertures of $2''$ radius were placed in regions with no source detections. We use PhotUtils to measure the sky background from the science images in the 1000 apertures while the photometric uncertainties were estimated from the weight images in the same aperture. Since some apertures may overlap with the image boundary or a bad detector region, we use a 4σ clip was used to remove these apertures. The sky background variance (σ^2_{sky}) was estimated by fitting a Gaussian distribution to the distribution of the sky background values and compared the variance with the median of the variance image in the same aperture (σ^2_{wei}). If there is no pixel-pixel correlation, the two values are consistent with each other.

For the SERVS dataset, thanks to the resampling process described in section A.1, the SERVS variance data preserved correct variance and is consistent with the variance in the sky background. On the other hand, The variances measured in CLAUDS and VIDEO were significantly smaller than the variance measured in the sky background. The correction factor $k = \sigma^2_{sky}/\sigma^2_{wei}$ was estimated in each patch of CLAUDS and VIDEO data.

The correction factors for the VIDEO images are relatively constant over the survey area of the VIDEO survey. This is expected since the survey depth of VIDEO is the same over the full survey area. Therefore, we adopt a single correction factor determined from the median of the correction factors in all of the VIDEO images for simplicity. On the other hand, the correction factor of CLAUDS shows significant variation due to the variation in the survey depth in each area. The correction factor was applied individually in each patch. We used the median of all correction factors in each tract when the correction factor cannot be determined within the patch itself.

[1] 2MASS Collaboration 2003

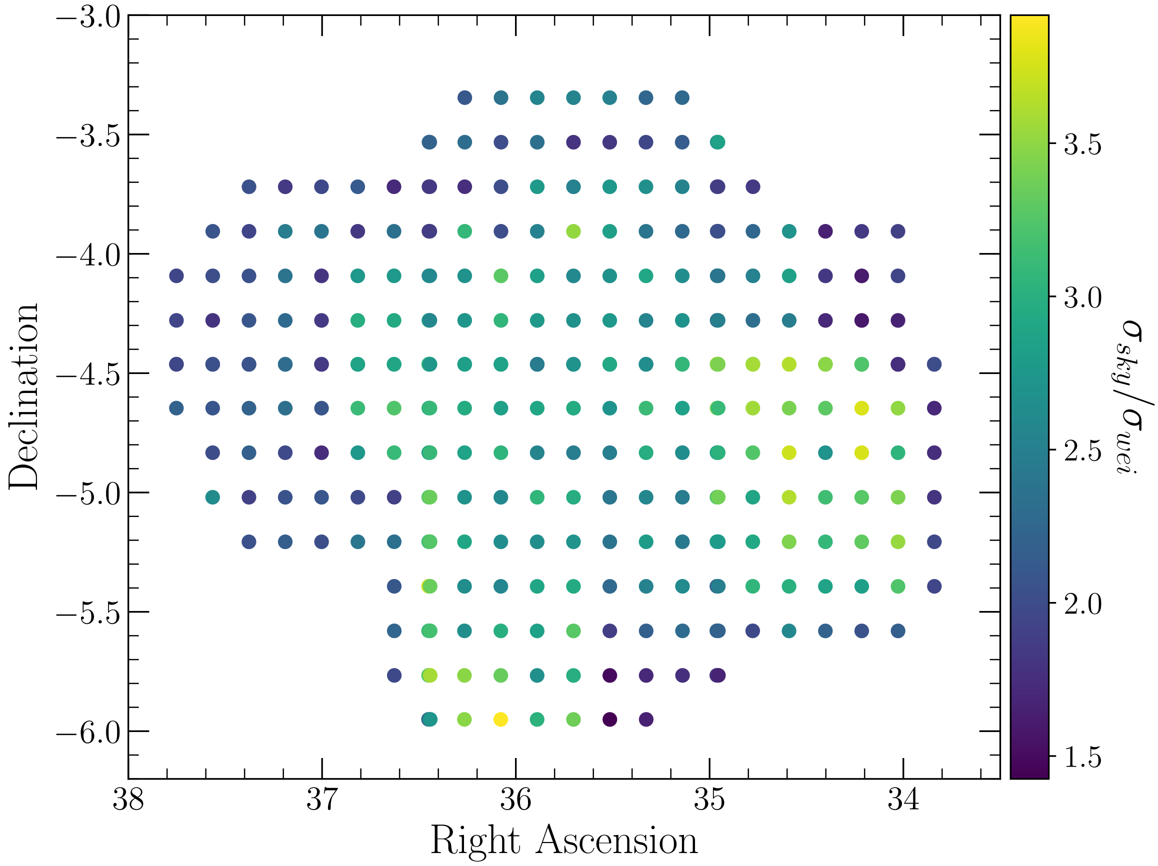

Figure A.1: The distribution of pixel-pixel correlation correction factor among the CLAUDS datasets.

A.4 Source Detection & T-Phot photometry

Among all datasets, the HSC S19A r-band image has the highest angular resolution among the imaging datasets and is deep enough to detect a large fraction of objects in the other bands. Therefore, we use the r-band image as the high-resolution prior and perform source detection and constructed segmentation images using SExtractor. We then use the images to perform PSF-convolved photometry using T-Phot.

The T-PHOT fitting process fails in some regions where bright stars are present in the image. This is likely due to the fact that the SExtractor deblending algorithm divides the star and halo into many individual sources. Therefore, we remove any source that lies within the HSC S19A r-band bright star masks (Coupon et al., 2018). T-PHOT was run twice in each patch to take into account small sub-pixel astrometric offsets that were determined in the first run and applied automatically during the second run. The results include catalogs containing the fitting results, model images, residual images, and residual statistics. The residual images in the 3.6 and 4.5 μm bands show systematic residuals. This is possibly due to the PSF asymmetry and its variation over the field of view of the IRAC datasets.

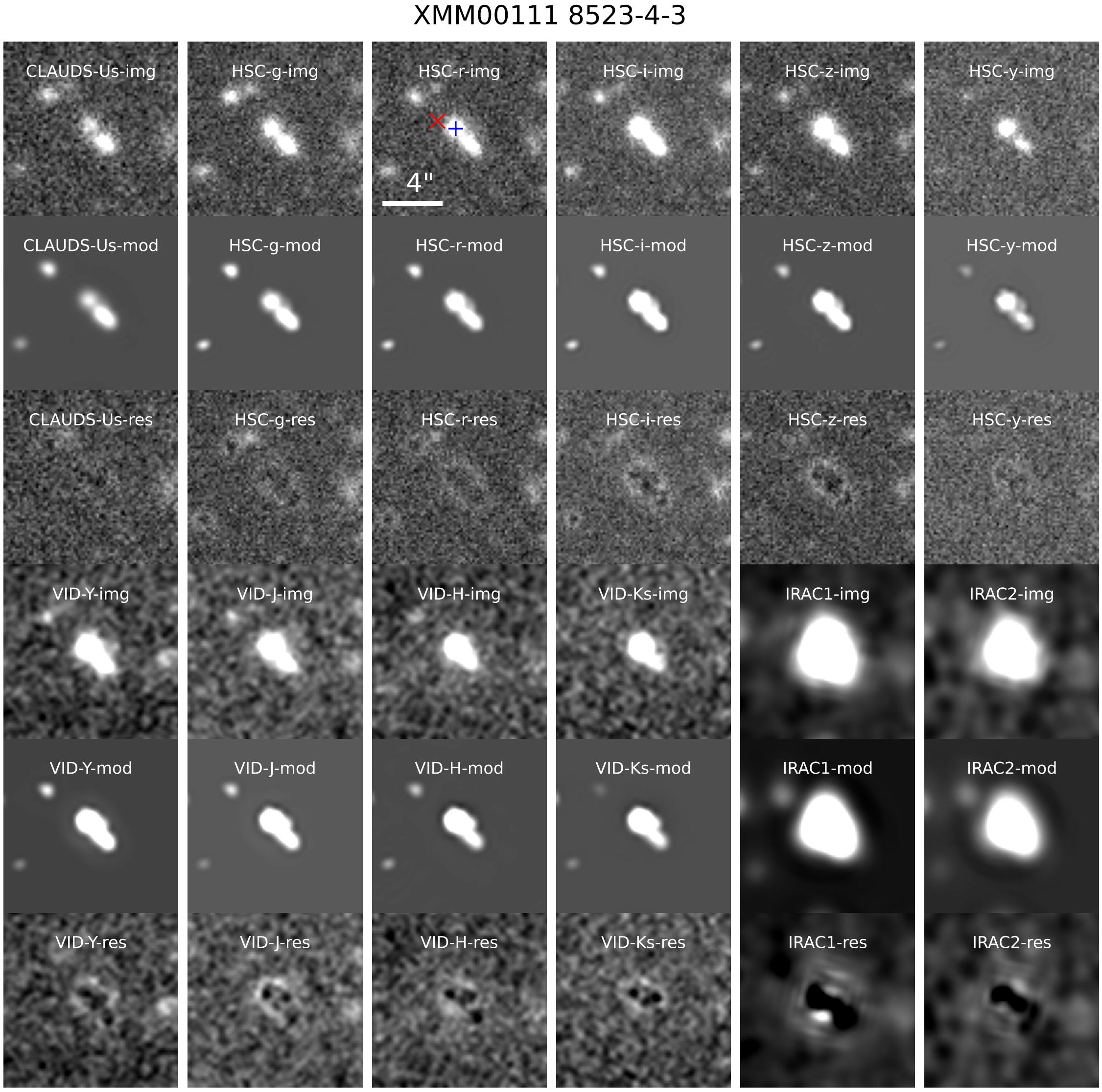

Figure A.2: (First and fourth rows) cutout images of an optical-IR counterpart of an X-ray source in each photometric band. (Second and fifth rows) model images from the T-PHOT fitting process. (Third and sixth rows) residual images of the model fitting. The blue plus and red cross symbols mark the center of the optical-infrared counterpart and X-ray source center, respectively.

A.5 Multi-band Catalog Construction

We combine the T-PHOT catalogs of each patch together to remove duplicated objects that lie in overlapping regions of the patch and tracts. We then calculated the photometric magnitudes and uncertainties in each band using the zero-points and zero-point uncertainties shown in Table A.1. The 2σ upper limits were calculated instead if the signal-to-noise ratio of the measurement is below 2σ.

We flag objects that fall into the HSC S20A bright star mask, bad detector regions affected by stray light, or detector defects, sources on the edge of the survey area, saturated sources, and sources with failed fitting results. In addition, sources that are likely local galaxies and were broken up by the detection algorithm were also identified using region files created from the Hyper-LEDA catalog (Makarov et al., 2014). The galactic reddening value for each object was retrieved from the IRAS reddening map[2] of Schlegel et al. (1998) and we calculate the dust attenuation by galactic dust in each band assuming the galactic dust extinction law of Fitzpatrick 1999.

Band	Zero-point	Uncertainty
CLAUDS-u^*	30.0	0.035
HSC-g	27.0	0.010
HSC-r	27.0	0.010
HSC-i	27.0	0.010
HSC-z	27.0	0.011
HSC-y	27.0	0.013
VIDEO-YJHKs	30.0	0.020
SERVS 3.6 & 4.5μm	23.9	0.030

Table A.1: Zeropoint uncertainty of each dataset.

[2]https://irsa.ipac.caltech.edu/applications/DUST/

Appendix B

The Forbidden Zone

The discussion of radiation pressure on dusty gas and the $N_{\mathrm{H}} - \lambda$ was first discussed in Fabian et al. (2006) and Fabian et al. (2008). Their prescription of radiation pressure ignores the radiation pressure from the infrared emission effect which was not considered in previous studies. In Fabian et al. (2008), infrared radiation was assumed to radiate away without interaction due to the low optical depth of infrared radiation. However as discussed in recent work, at high hydrogen column density the optical depth of the dusty gas can be optically thick to infrared radiation (Schulze et al., 2015; Ishibashi and Fabian, 2016). Ishibashi et al. (2018) presented a revision of the forbidden zone previous work which includes the effect of infrared radiation pressure (AKA infrared trapping) and is shown here.

For spherical shell of mass with a hydrogen column density of N_{H}, the magnitude of the total gravitational force on the shell of mass is

$$F_{\mathrm{Grav}} = -\frac{GM_{\mathrm{BH}}(4\pi r^2 m_p N_{\mathrm{H}})}{r^2}$$

where G is the gravitational constant, M_{BH} is the supermassive black hole mass, m_p is the mass of a proton, N_{H} is the hydrogen column density, and r is the radius to the shell. The total radiation pressure upon the shell of gas by radiation from the AGN is expressed as

$$F_{\mathrm{rad}} = F_{\mathrm{UV}} + F_{\mathrm{IR}} = \frac{(L - Le^{-\tau_{\mathrm{UV}}})}{c} + \frac{L}{c}\tau_{\mathrm{IR}}$$

where L is the total luminosity of the AGN, c is the speed of light, τ_{UV} is the UV optical depth, and τ_{IR} is the infrared optical depth. both of the optical depths depend on the hydrogen column density which can be expressed as $\tau_{\mathrm{UV}} = \tau_{\mathrm{UV}}(N_{\mathrm{H}}) = \kappa_{\mathrm{UV}} m_p N_{\mathrm{H}}$ and $\tau_{\mathrm{IR}} = \tau_{\mathrm{IR}}(N_{\mathrm{H}}) = \kappa_{\mathrm{IR}} m_p N_{\mathrm{H}}$ where κ_{UV} and κ_{IR} is the UV and infrared opacity, respectively. The equation of motion of the shell can be expressed as

$$F_{tot} = -4\pi GM_{\mathrm{BH}} m_p N_{\mathrm{H}} + \frac{L}{c}(1 - e^{-\tau_{\mathrm{UV}}} + \tau_{\mathrm{IR}}) \tag{B.1}$$

The critical luminosity is the luminosity in which the radiation pressure balances the gravitational force of the gas shell. Therefore, the total force is set to zero. Hence

$$4\pi GM_{\mathrm{BH}} m_p N_{\mathrm{H}} = \frac{L}{c}(1 - e^{-\tau_{\mathrm{UV}}} + \tau_{\mathrm{IR}})$$

and can be rearranged in terms of luminosity as

$$L_{\mathrm{Eff}} = \frac{4\pi GM_{\mathrm{BH}} c m_p N_{\mathrm{H}}}{(1 - e^{-\tau_{\mathrm{UV}}} + \tau_{\mathrm{IR}})} \tag{B.2}$$

Here, L_{Eff} is the effective Eddington luminosity of partially ionized or dusty gas. The generalized Eddington ratio is then expressed as $\Lambda = L/L_{\mathrm{Eff}}$. The generalized Eddington can also be expressed in terms of the classical Eddington ratio limit

$$\Lambda = \frac{L}{L_{\mathrm{Eff}}} = \frac{\lambda L_{\mathrm{Edd}}}{L_{\mathrm{Eff}}} = \lambda \frac{4\pi G m_p c M_{\mathrm{BH}}}{\sigma_{\mathrm{T}}} \cdot \frac{(1 - e^{-\tau_{\mathrm{UV}}} + \tau_{\mathrm{IR}})}{4\pi GM_{\mathrm{BH}} c m_p N_{\mathrm{H}}} = \frac{(1 - e^{-\tau_{\mathrm{UV}}} + \tau_{\mathrm{IR}})}{\sigma_{\mathrm{T}} N_{\mathrm{H}}}\lambda$$

.

By setting $\Lambda = 1$ where the AGN luminosity has reached the effective Eddington luminosity, the effective Eddington ratio can be expressed in terms of the hydrogen column density.

$$\lambda_{\mathrm{Eff}} = \frac{\sigma_{\mathrm{T}}}{(1 - e^{-\tau_{\mathrm{UV}}} + \tau_{\mathrm{IR}})} N_{\mathrm{H}} \tag{B.3}$$

We expressed equation B.3 different from that presented in Ishibashi et al. (2018) because both τ_{UV} and τ_{IR} are depends on the hydrogen column density. The fiducial UV and IR opacities are $\kappa_{\mathrm{UV}} = 200 f_{\mathrm{dust,MW}}\ \mathrm{cm^2 g^{-1}}$ and $\kappa_{\mathrm{IR}} = 4 f_{\mathrm{dust,MW}}\ \mathrm{cm^2 g^{-1}}$ where $f_{dust,MW}$ is the dust-to-gas ratio normalized to the Milky way value. Figure B.1 show the $N_{\mathrm{H}} - \lambda$ based on the formalization presented here and compared with previous work.

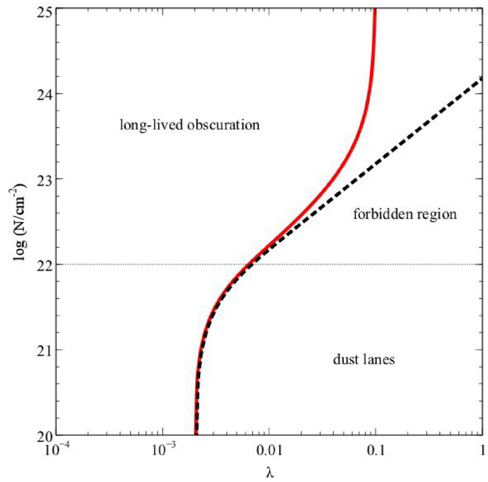

Figure B.1: The $N_{\mathrm{H}} - \lambda$ diagram presented from Ishibashi et al. (2018). The effective Eddington ratio including the effect of infrared trapping is shown as a thick red line. The relationship presented by Fabian et al. (2008) without infrared trapping is shown as a black dashed line. This figure was reproduced with permission from figure 1 of Ishibashi et al. (2018).

At low hydrogen column density (and hence low optical depth), the infrared optical depth approaches 0 at quicker than the UV optical depth. The term $e^{\tau_{\mathrm{UV}}}$ can be approximated as $e^{-\tau_{\mathrm{UV}}} \sim 1 + \tau_{\mathrm{UV}}$ and therefore equation B.3 can be written has

$$\lambda_{\mathrm{Eff}} \sim \frac{\sigma_{\mathrm{T}}}{\tau_{\mathrm{UV}}} N_{\mathrm{H}} = \frac{\sigma_{\mathrm{T}}}{\kappa_{\mathrm{UV}} m_p} = \frac{6 \times 10^{-25}}{200 \cdot 1 \cdot 1.66 \times 10^{-24}} \sim 0.002$$

when assuming a Milky way gas to dust ratio.

At large hydrogen column density ($\log N_{\mathrm{H}}\ [\mathrm{cm^{-2}}] \geq 24$) both infrared and UV emission becomes optically thick ($\tau_{\mathrm{IR}} = 4 \cdot 1.66 \times 10^{-24} \cdot 10^{24} \geq 1$), the term $e^{-\tau_{\mathrm{UV}}}$ can be approximated as $e^{-\tau_{\mathrm{UV}}} \sim 0$ since the UV optical depth is a few hundred times larger than the infrared optical depth. Assuming Milky way gas to dust ratio, equation B.3 can be approximated similarly as

$$\lambda_{\mathrm{Eff}} \sim \frac{\sigma_{\mathrm{T}}}{1 + \tau_{\mathrm{IR}}} N_{\mathrm{H}} \sim \frac{\sigma_{\mathrm{T}}}{\tau_{\mathrm{IR}}} N_{\mathrm{H}} = \frac{\sigma_{\mathrm{T}}}{\kappa_{\mathrm{IR}} m_p} = \frac{6 \times 10^{-25}}{4 \cdot 1 \cdot 1.66 \times 10^{-24}} \sim 0.1$$

. Here, I also assume that $\tau_{\mathrm{IR}} \gg 1$ therefore absorbed 1 into τ_{IR}.

The difference of the $N_{\mathrm{H}} - \lambda$ in this work as compared to previous studies can be seen in the optical thick regime $\log N_{\mathrm{H}}\ [\mathrm{cm^{-2}}] \geq 24$. In the original prescription which ignores infrared trapping, the effective Eddington ratio at large hydrogen column density can be approximated as $\lambda_{\mathrm{Eff}} \sim \sigma_{\mathrm{T}} N_{\mathrm{H}}$ which is shown as the black dashed lines in figure B.1. Ignoring the infrared trapping would imply that the obscuration of most of the heavily obscured AGN is static and will never blow out. The inclusion of infrared trapping reduces the effective Eddington ratio because of the additional radiation pressure from the infrared radiation.

Bibliography

2MASS Collaboration. 2mass all-sky point source catalog, 2003. URL https://catcopy.ipac.caltech.edu/dois/doi.php?id=10.26131/IRSA2.

C. P. Ahn, R. Alexandroff, C. Allende Prieto, S. F. Anderson, T. Anderton, B. H. Andrews, É. Aubourg, S. Bailey, E. Balbinot, R. Barnes, J. Bautista, T. C. Beers, A. Beifiori, A. A. Berlind, V. Bhardwaj, D. Bizyaev, C. H. Blake, M. R. Blanton, M. Blomqvist, J. J. Bochanski, A. S. Bolton, A. Borde, J. Bovy, W. N. Brandt, J. Brinkmann, P. J. Brown, J. R. Brownstein, K. Bundy, N. G. Busca, W. Carithers, A. R. Carnero, M. A. Carr, D. I. Casetti-Dinescu, Y. Chen, C. Chiappini, J. Comparat, N. Connolly, J. R. Crepp, S. Cristiani, R. A. C. Croft, A. J. Cuesta, L. N. da Costa, J. R. A. Davenport, K. S. Dawson, R. de Putter, N. De Lee, T. Delubac, S. Dhital, A. Ealet, G. L. Ebelke, E. M. Edmondson, D. J. Eisenstein, S. Escoffier, M. Esposito, M. L. Evans, X. Fan, B. Femenía Castellá, E. Fernández Alvar, L. D. Ferreira, N. Filiz Ak, H. Finley, S. W. Fleming, A. Font-Ribera, P. M. Frinchaboy, D. A. García-Hernández, A. E. García Pérez, J. Ge, R. Génova-Santos, B. A. Gillespie, L. Girardi, J. I. González Hernández, E. K. Grebel, J. E. Gunn, H. Guo, D. Haggard, J.-C. Hamilton, D. W. Harris, S. L. Hawley, F. R. Hearty, S. Ho, D. W. Hogg, J. A. Holtzman, K. Honscheid, J. Huehnerhoff, I. I. Ivans, Ž. Ivezić, H. R. Jacobson, L. Jiang, J. Johansson, J. A. Johnson, G. Kauffmann, D. Kirkby, J. A. Kirkpatrick, M. A. Klaene, G. R. Knapp, J.-P. Kneib, J.-M. Le Goff, A. Leauthaud, K.-G. Lee, Y. S. Lee, D. C. Long, C. P. Loomis, S. Lucatello, B. Lundgren, R. H. Lupton, B. Ma, Z. Ma, N. MacDonald, C. E. Mack, S. Mahadevan, M. A. G. Maia, S. R. Majewski, M. Makler, E. Malanushenko, V. Malanushenko, A. Manchado, R. Mandelbaum, M. Manera, C. Maraston, D. Margala, S. L. Martell, C. K. McBride, I. D. McGreer, R. G. McMahon, B. Ménard, S. Meszaros, J. Miralda-Escudé, A. D. Montero-Dorta, F. Montesano, H. L. Morrison, D. Muna, J. A. Munn, H. Murayama, A. D. Myers, A. F. Neto, D. C. Nguyen, R. C. Nichol, D. L. Nidever, P. Noterdaeme, S. E. Nuza, R. L. C. Ogando, M. D. Olmstead, D. J. Oravetz, R. Owen, N. Padmanabhan, N. Palanque-Delabrouille, K. Pan, J. K. Parejko, P. Parihar, I. Pâris, P. Pattarakijwanich, J. Pepper, W. J. Percival, I. Pérez-Fournon, I. Pérez-Ràfols, P. Petitjean, J. Pforr, M. M. Pieri, M. H. Pinsonneault, G. F. Porto de Mello, F. Prada, A. M. Price-Whelan, M. J. Raddick, R. Rebolo, J. Rich, G. T. Richards, A. C. Robin, H. J. Rocha-Pinto, C. M. Rockosi, N. A. Roe, A. J. Ross, N. P. Ross, G. Rossi, J. A. Rubiño-Martin, L. Samushia, J. Sanchez Almeida, A. G. Sánchez, B. Santiago, C. Sayres, D. J. Schlegel, K. J. Schlesinger, S. J. Schmidt, D. P. Schneider, M. Schultheis, A. D. Schwope, C. G. Scóccola, U. Seljak, E. Sheldon, Y. Shen, Y. Shu, J. Simmerer, A. E. Simmons, R. A. Skibba, M. F. Skrutskie, A. Slosar, F. Sobreira, J. S. Sobeck, K. G. Stassun, O. Steele, M. Steinmetz, M. A. Strauss, A. Streblyanska, N. Suzuki, M. E. C. Swanson, T. Tal, A. R. Thakar, D. Thomas, B. A. Thompson, J. L. Tinker, R. Tojeiro, C. A. Tremonti, M. Vargas Magaña, L. Verde, M. Viel, S. K. Vikas, N. P. Vogt, D. A. Wake, J. Wang, B. A. Weaver, D. H. Weinberg, B. J. Weiner, A. A. West, M. White, J. C. Wilson, J. P. Wisniewski, W. M. Wood-Vasey, B. Yanny, C. Yèche, D. G. York, O. Zamora, G. Zasowski, I. Zehavi, G.-B. Zhao, Z. Zheng, G. Zhu, and J. C. Zinn. The Ninth Data Release of the Sloan Digital Sky Survey: First Spectroscopic Data from the SDSS-III Baryon Oscillation Spectroscopic Survey. ApJS, 203(2): 21, Dec. 2012. doi: 10.1088/0067-0049/203/2/21.

R. Ahumada, C. A. Prieto, A. Almeida, F. Anders, S. F. Anderson, B. H. Andrews, B. Anguiano, R. Arcodia, E. Armengaud, M. Aubert, S. Avila, V. Avila-Reese, C. Badenes, C. Balland, K. Barger, J. K. Barrera-Ballesteros, S. Basu, J. Bautista, R. L. Beaton, T. C. Beers, B. I. T. Benavides, C. F. Bender, M. Bernardi, M. Bershady, F. Beutler, C. M. Bidin, J. Bird, D. Bizyaev, G. A. Blanc, M. R. Blanton, M. Boquien, J. Borissova, J. Bovy, W. N. Brandt, J. Brinkmann, J. R. Brownstein, K. Bundy, M. Bureau, A. Burgasser, E. Burtin, M. Cano-Díaz, R. Capasso, M. Cappellari, R. Carrera, S. Chabanier, W. Chaplin, M. Chapman, B. Cherinka, C. Chiappini, P. Doohyun Choi, S. D. Chojnowski, H. Chung, N. Clerc, D. Coffey, J. M. Comerford, J. Comparat, L. da Costa, M.-C. Cousinou, K. Covey, J. D. Crane, K. Cunha, G. d. S. Ilha, Y. S. Dai, S. B. Damsted, J. Darling, J. Davidson, James W., R. Davies, K. Dawson, N. De, A. de la Macorra, N. De Lee, A. B. d. A. Queiroz, A. Deconto Machado, S. de la Torre, F. Dell'Agli, H. du Mas des Bourboux, A. M. Diamond-Stanic, S. Dillon, J. Donor, N. Drory, C. Duckworth, T. Dwelly, G. Ebelke, S. Eftekharzadeh, A. Davis Eigenbrot, Y. P. Elsworth, M. Eracleous, G. Erfanianfar, S. Escoffier, X. Fan, E. Farr, J. G. Fernández-Trincado, D. Feuillet, A. Finoguenov, P. Fofie, A. Fraser-McKelvie, P. M. Frinchaboy, S. Fromenteau, H. Fu, L. Galbany, R. A. Garcia, D. A. García-Hernández, L. A. G. Oehmichen, J. Ge, M. A. G. Maia, D. Geisler, J. Gelfand, J. Goddy, V. Gonzalez-Perez, K. Grabowski, P. Green, C. J. Grier, H. Guo, J. Guy, P. Harding, S. Hasselquist, A. J. Hawken, C. R. Hayes, F. Hearty, S. Hekker, D. W. Hogg, J. A. Holtzman, D. Horta, J. Hou, B.-C. Hsieh, D. Huber, J. A. S. Hunt, J. I. Chitham, J. Imig, M. Jaber, C. E. J. Angel, J. A. Johnson, A. M. Jones, H. Jönsson, E. Jullo, Y. Kim, K. Kinemuchi, I. Kirkpatrick, Charles C., G. W. Kite, M. Klaene, J.-P. Kneib, J. A. Kollmeier, H. Kong, M. Kounkel, D. Krishnarao, I. Lacerna, T.-W. Lan, R. R. Lane, D. R. Law, J.-M. Le Goff, H. W. Leung, H. Lewis, C. Li, J. Lian, L. Lin, D. Long, P. Longa-Peña, B. Lundgren, B. W. Lyke, J. Ted Mackereth, C. L. MacLeod, S. R. Majewski, A. Manchado, C. Maraston, P. Martini, T. Masseron, K. L. Masters, S. Mathur, R. M. McDermid, A. Merloni, M. Merrifield, S. Mészáros, A. Miglio, D. Minniti, R. Minsley, T. Miyaji, F. G. Mohammad, B. Mosser, E.-M. Mueller, D. Muna, A. Muñoz-Gutiérrez,

A. D. Myers, S. Nadathur, P. Nair, K. Nandra, J. C. do Nascimento, R. J. Nevin, J. A. Newman, D. L. Nidever, C. Nitschelm, P. Noterdaeme, J. E. O'Connell, M. D. Olmstead, D. Oravetz, A. Oravetz, Y. Osorio, Z. J. Pace, N. Padilla, N. Palanque-Delabrouille, P. A. Palicio, H.-A. Pan, K. Pan, J. Parker, R. Paviot, S. Peirani, K. P. Ramŕez, S. Penny, W. J. Percival, I. Perez-Fournon, I. Pérez-Ràfols, P. Petitjean, M. M. Pieri, M. Pinsonneault, V. J. Poovelil, J. T. Povick, A. Prakash, A. M. Price-Whelan, M. J. Raddick, A. Raichoor, A. Ray, S. B. Rembold, M. Rezaie, R. A. Riffel, R. Riffel, H.-W. Rix, A. C. Robin, A. Roman-Lopes, C. Román-Zúñiga, B. Rose, A. J. Ross, G. Rossi, K. Rowlands, K. H. R. Rubin, M. Salvato, A. G. Sánchez, L. Sánchez-Menguiano, J. R. Sánchez-Gallego, C. Sayres, A. Schaefer, R. P. Schiavon, J. S. Schimoia, E. Schlafly, D. Schlegel, D. P. Schneider, M. Schultheis, A. Schwope, H.-J. Seo, A. Serenelli, A. Shafieloo, S. J. Shamsi, Z. Shao, S. Shen, M. Shetrone, R. Shirley, V. S. Aguirre, J. D. Simon, M. F. Skrutskie, A. Slosar, R. Smethurst, J. Sobeck, B. C. Sodi, D. Souto, D. V. Stark, K. G. Stassun, M. Steinmetz, D. Stello, J. Stermer, T. Storchi-Bergmann, A. Streblyanska, G. S. Stringfellow, A. Stutz, G. Suárez, J. Sun, M. Taghizadeh-Popp, M. S. Talbot, J. Tayar, A. R. Thakar, R. Theriault, D. Thomas, Z. C. Thomas, J. Tinker, R. Tojeiro, H. H. Toledo, C. A. Tremonti, N. W. Troup, S. Tuttle, E. Unda-Sanzana, M. Valentini, J. Vargas-González, M. Vargas-Magaña, J. A. Vázquez-Mata, M. Vivek, D. Wake, Y. Wang, B. A. Weaver, A.-M. Weijmans, V. Wild, J. C. Wilson, R. F. Wilson, N. Wolthuis, W. M. Wood-Vasey, R. Yan, M. Yang, C. Yèche, O. Zamora, P. Zarrouk, G. Zasowski, K. Zhang, C. Zhao, G. Zhao, Z. Zheng, Z. Zheng, G. Zhu, and H. Zou. The 16th Data Release of the Sloan Digital Sky Surveys: First Release from the APOGEE-2 Southern Survey and Full Release of eBOSS Spectra. ApJS, 249 (1):3, July 2020. doi: 10.3847/1538-4365/ab929e.

J. Aird, A. L. Coil, A. Georgakakis, K. Nandra, G. Barro, and P. G. Pérez-González. The evolution of the X-ray luminosity functions of unabsorbed and absorbed AGNs out to z∼ 5. MNRAS, 451(2):1892–1927, Aug. 2015. doi: 10.1093/mnras/stv1062.

M. Akiyama, Y. Ueda, M. G. Watson, H. Furusawa, T. Takata, C. Simpson, T. Morokuma, T. Yamada, K. Ohta, F. Iwamuro, K. Yabe, N. Tamura, Y. Moritani, N. Takato, M. Kimura, T. Maihara, G. Dalton, I. Lewis, H. Lee, E. Curtis-Lake, E. Macaulay, F. Clarke, J. D. Silverman, S. Croom, M. Ouchi, H. Hanami, J. Díaz Tello, T. Yoshikawa, N. Fujishiro, and K. Sekiguchi. The Subaru-XMM-Newton Deep Survey (SXDS). VIII. Multi-wavelength identification, optical/NIR spectroscopic properties, and photometric redshifts of X-ray sources. PASJ, 67(5):82, Oct. 2015. doi: 10.1093/pasj/psv050.

M. Akiyama, W. He, H. Ikeda, M. Niida, T. Nagao, J. Bosch, J. Coupon, M. Enoki, M. Imanishi, N. Kashikawa, T. Kawaguchi, Y. Komiyama, C.-H. Lee, Y. Matsuoka, S. Miyazaki, A. J. Nishizawa, M. Oguri, Y. Ono, M. Onoue, M. Ouchi, A. Schulze, J. D. Silverman, M. M. Tanaka, M. Tanaka, Y. Terashima, Y. Toba, and Y. Ueda. The quasar luminosity function at redshift 4 with the Hyper Suprime-Cam Wide Survey. PASJ, 70:S34, Jan. 2018. doi: 10.1093/pasj/psx091.

R. Alexandroff, M. A. Strauss, J. E. Greene, N. L. Zakamska, N. P. Ross, W. N. Brandt, G. Liu, P. S. Smith, J. Ge, F. Hamann, A. D. Myers, P. Petitjean, D. P. Schneider, H. Yesuf, and D. G. York. Candidate type II quasars at 2 ¡ z ¡ 4.3 in the Sloan Digital Sky Survey III. MNRAS, 435 (4):3306–3325, Nov. 2013. doi: 10.1093/mnras/stt1500.

R. M. Alexandroff, N. L. Zakamska, A. J. Barth, F. Hamann, M. A. Strauss, J. Krolik, J. E. Greene, I. Pâris, and N. P. Ross. Spectropolarimetry of high-redshift obscured and red quasars. MNRAS, 479(4):4936–4957, Oct. 2018. doi: 10.1093/mnras/sty1685.

E. Anders and N. Grevesse. Abundances of the elements: Meteoritic and solar. Geochim. Cosmochim. Acta, 53(1): 197–214, Jan. 1989. doi: 10.1016/0016-7037(89)90286-X.

T. W. Anderson and D. A. Darling. Asymptotic Theory of Certain "Goodness of Fit" Criteria Based on Stochastic Processes. *The Annals of Mathematical Statistics*, 23(2): 193 – 212, 1952. doi: 10.1214/aoms/1177729437. URL https://doi.org/10.1214/aoms/1177729437.

R. Antonucci. Unified models for active galactic nuclei and quasars. ARA&A, 31:473–521, Jan. 1993. doi: 10.1146/annurev.aa.31.090193.002353.

S. Arnouts, S. Cristiani, L. Moscardini, S. Matarrese, F. Lucchin, A. Fontana, and E. Giallongo. Measuring and modelling the redshift evolution of clustering: the Hubble Deep Field North. MNRAS, 310(2):540–556, Dec. 1999. doi: 10.1046/j.1365-8711.1999.02978.x.

R. J. Assef, D. J. Walton, M. Brightman, D. Stern, D. Alexander, F. Bauer, A. W. Blain, T. Diaz-Santos, P. R. M. Eisenhardt, S. L. Finkelstein, R. C. Hickox, C. W. Tsai, and J. W. Wu. Hot Dust Obscured Galaxies with Excess Blue Light: Dual AGN or Single AGN Under Extreme Conditions? ApJ, 819(2):111, Mar. 2016. doi: 10.3847/0004-637X/819/2/111.

R. J. Assef, M. Brightman, D. J. Walton, D. Stern, F. E. Bauer, A. W. Blain, T. Díaz-Santos, P. R. M. Eisenhardt, R. C. Hickox, H. D. Jun, A. Psychogyios, C. W. Tsai, and J. W. Wu. Hot Dust-obscured Galaxies with Excess Blue Light. ApJ, 897(2):112, July 2020. doi: 10.3847/1538-4357/ab9814.

J. A. Baldwin, M. M. Phillips, and R. Terlevich. Classification parameters for the emission-line spectra of extragalactic objects. PASP, 93:5–19, Feb. 1981. doi: 10.1086/130766.

D. R. Ballantyne, J. E. Everett, and N. Murray. Connecting Galaxy Evolution, Star Formation, and the Cosmic X-Ray Background. ApJ, 639(2):740–752, Mar. 2006. doi: 10.1086/499558.

E. Bertin. SWarp: Resampling and Co-adding FITS Images Together, Oct. 2010.

E. Bertin and S. Arnouts. SExtractor: Software for source extraction. A&AS, 117:393–404, June 1996. doi: 10.1051/aas:1996164.

R. Bielby, P. Hudelot, H. J. McCracken, O. Ilbert, E. Daddi, O. Le Fèvre, V. Gonzalez-Perez, J. P. Kneib, C. Marmo, Y. Mellier, M. Salvato, D. B. Sanders, and C. J. Willott. The WIRCam Deep Survey. I. Counts, colours, and mass-functions derived from near-infrared imaging in the CFHTLS deep fields. A&A, 545:A23, Sept. 2012. doi: 10.1051/0004-6361/201118547.

F. Bigiel and L. Blitz. A Universal Neutral Gas Profile for nearby Disk Galaxies. ApJ, 756(2):183, Sept. 2012. doi: 10.1088/0004-637X/756/2/183.

L. Blecha, G. F. Snyder, S. Satyapal, and S. L. Ellison. The power of infrared AGN selection in mergers: a theoretical study. MNRAS, 478(3):3056–3071, Aug. 2018. doi: 10.1093/mnras/sty1274.

T. Boller, M. J. Freyberg, J. Trümper, F. Haberl, W. Voges, and K. Nandra. Second ROSAT all-sky survey (2RXS) source catalogue. A&A, 588:A103, Apr. 2016. doi: 10.1051/0004-6361/201525648.

A. Bongiorno, A. Merloni, M. Brusa, B. Magnelli, M. Salvato, M. Mignoli, G. Zamorani, F. Fiore, D. Rosario, V. Mainieri, H. Hao, A. Comastri, C. Vignali, I. Balestra, S. Bardelli, S. Berta, F. Civano, P. Kampczyk, E. Le Floc'h, E. Lusso, D. Lutz, L. Pozzetti, F. Pozzi, L. Riguccini, F. Shankar, and J. Silverman. Accreting supermassive black holes in the COSMOS field and the connection to their host galaxies. MNRAS, 427(4):3103–3133, Dec. 2012. doi: 10.1111/j.1365-2966.2012.22089.x.

M. Boquien, D. Burgarella, Y. Roehlly, V. Buat, L. Ciesla, D. Corre, A. K. Inoue, and H. Salas. CIGALE: a python Code Investigating GALaxy Emission. A&A, 622:A103, Feb. 2019. doi: 10.1051/0004-6361/201834156.

J. Bosch, R. Armstrong, S. Bickerton, H. Furusawa, H. Ikeda, M. Koike, R. Lupton, S. Mineo, P. Price, T. Takata, M. Tanaka, N. Yasuda, Y. AlSayyad, A. C. Becker, W. Coulton, J. Coupon, J. Garmilla, S. Huang, K. S. Krughoff, D. Lang, A. Leauthaud, K.-T. Lim, N. B. Lust, L. A. MacArthur, R. Mandelbaum, H. Miyatake, S. Miyazaki, R. Murata, S. More, Y. Okura, R. Owen, J. D. Swinbank, M. A. Strauss, Y. Yamada, and H. Yamanoi. The Hyper Suprime-Cam software pipeline. PASJ, 70:S5, Jan. 2018. doi: 10.1093/pasj/psx080.

J. Bosch, Y. AlSayyad, R. Armstrong, E. Bellm, H.-F. Chiang, S. Eggl, K. Findeisen, M. Fisher-Levine, L. P. Guy, A. Guyonnet, Ž. Ivezić, T. Jenness, G. Kovács, K. S. Krughoff, R. H. Lupton, N. B. Lust, L. A. MacArthur, J. Meyers, F. Moolekamp, C. B. Morrison, T. D. Morton, W. O'Mullane, J. K. Parejko, A. A. Plazas, P. A. Price, M. L. Rawls, S. L. Reed, P. Schellart, C. T. Slater, I. Sullivan, J. D. Swinbank, D. Taranu, C. Z. Waters, and W. M. Wood-Vasey. An Overview of the LSST Image Processing Pipelines. In P. J. Teuben, M. W. Pound, B. A. Thomas, and E. M. Warner, editors, *Astronomical Data Analysis Software and Systems XXVII*, volume 523 of *Astronomical Society of the Pacific Conference Series*, page 521, Oct. 2019.

A. Boucaud, M. Bocchio, A. Abergel, F. Orieux, H. Dole, and M. A. Hadj-Youcef. Convolution kernels for multi-wavelength imaging. A&A, 596:A63, Dec. 2016. doi: 10.1051/0004-6361/201629080.

O. Boulade, X. Charlot, P. Abbon, S. Aune, P. Borgeaud, P.-H. Carton, M. Carty, J. Da Costa, H. Deschamps, D. Desforge, D. Eppellé, P. Gallais, L. Gosset, R. Granelli, M. Gros, J. de Kat, D. Loiseau, J. . Ritou, J. Y. Roussé, P. Starzynski, N. Vignal, and L. G. Vigroux. MegaCam: the new Canada-France-Hawaii Telescope wide-field imaging camera. In M. Iye and A. F. M. Moorwood, editors, *Instrument Design and Performance for Optical/Infrared Ground-based Telescopes*, volume 4841 of *Society of Photo-Optical Instrumentation Engineers (SPIE) Conference Series*, pages 72–81, Mar. 2003. doi: 10.1117/12.459890.

C. Bradford, J. Glenn, L. Armus, C. Battersby, A. Bolatto, B. Hensley, M. Meixner, E. Mills, K. Pontoppidan, A. Pope, J.-D. Smith, J. Staguhn, and Prima Science Working Groups. The PRIMA Far-Infrared Probe: Observatory and Instrumentation. In *American Astronomical Society Meeting Abstracts*, volume 54 of *American Astronomical Society Meeting Abstracts*, page 304.07, June 2022.

E. J. Bradshaw, O. Almaini, W. G. Hartley, K. T. Smith, C. J. Conselice, J. S. Dunlop, C. Simpson, R. W. Chuter, M. Cirasuolo, S. Foucaud, R. J. McLure, A. Mortlock, and H. Pearce. High-velocity outflows from young star-forming galaxies in the UKIDSS Ultra-Deep Survey. MNRAS, 433(1):194–208, July 2013. doi: 10.1093/mnras/stt715.

G. B. Brammer, P. G. van Dokkum, M. Franx, M. Fumagalli, S. Patel, H.-W. Rix, R. E. Skelton, M. Kriek, E. Nelson, K. B. Schmidt, R. Bezanson, E. da Cunha, D. K. Erb, X. Fan, N. Förster Schreiber, G. D. Illingworth, I. Labbé, J. Leja, B. Lundgren, D. Magee, D. Marchesini, P. McCarthy, I. Momcheva, A. Muzzin, R. Quadri, C. C. Steidel, T. Tal, D. Wake, K. E. Whitaker, and A. Williams. 3D-HST: A Wide-field Grism Spectroscopic Survey with the Hubble Space Telescope. ApJS, 200(2):13, June 2012. doi: 10.1088/0067-0049/200/2/13.

J. Buchner and F. E. Bauer. Galaxy gas as obscurer - II. Separating the galaxy-scale and nuclear obscurers of active galactic nuclei. MNRAS, 465(4):4348–4362, Mar. 2017. doi: 10.1093/mnras/stw2955.

J. Buchner, A. Georgakakis, K. Nandra, M. Brightman, M.-L. Menzel, Z. Liu, L.-T. Hsu, M. Salvato, C. Rangel, J. Aird, A. Merloni, and N. Ross. Obscuration-dependent Evolution of Active Galactic Nuclei. ApJ, 802(2):89, Apr. 2015. doi: 10.1088/0004-637X/802/2/89.

J. Buchner, S. Schulze, and F. E. Bauer. Galaxy gas as obscurer - I. GRBs x-ray galaxies and find an $\mathrm{N}_H{}^3\propto$ M_{star} relation. MNRAS, 464(4):4545–4566, Feb. 2017. doi: 10.1093/mnras/stw2423.

D. Burlon, M. Ajello, J. Greiner, A. Comastri, A. Merloni, and N. Gehrels. Three-year Swift-BAT Survey of Active Galactic Nuclei: Reconciling Theory and Observations? ApJ, 728(1):58, Feb. 2011. doi: 10.1088/0004-637X/728/1/58.

D. Calzetti, A. L. Kinney, and T. Storchi-Bergmann. Dust Extinction of the Stellar Continua in Starburst Galaxies: The Ultraviolet and Optical Extinction Law. ApJ, 429: 582, July 1994. doi: 10.1086/174346.

D. Calzetti, L. Armus, R. C. Bohlin, A. L. Kinney, J. Koornneef, and T. Storchi-Bergmann. The Dust Content and Opacity of Actively Star-forming Galaxies. ApJ, 533(2): 682–695, Apr. 2000. doi: 10.1086/308692.

J. A. Cardelli, G. C. Clayton, and J. S. Mathis. The Relationship between Infrared, Optical, and Ultraviolet Extinction. ApJ, 345:245, Oct. 1989. doi: 10.1086/167900.

C. L. Carilli and F. Walter. Cool Gas in High-Redshift Galaxies. ARA&A, 51(1):105–161, Aug. 2013. doi: 10.1146/annurev-astro-082812-140953.

G. Chabrier. Galactic Stellar and Substellar Initial Mass Function. PASP, 115(809):763–795, July 2003. doi: 10.1086/376392.

K. C. Chambers, E. A. Magnier, N. Metcalfe, H. A. Flewelling, M. E. Huber, C. Z. Waters, L. Denneau, P. W. Draper, D. Farrow, D. P. Finkbeiner, C. Holmberg, J. Koppenhoefer, P. A. Price, A. Rest, R. P. Saglia, E. F. Schlafly, S. J. Smartt, W. Sweeney, R. J. Wainscoat, W. S. Burgett, S. Chastel, T. Grav, J. N. Heasley, K. W.

Hodapp, R. Jedicke, N. Kaiser, R. P. Kudritzki, G. A. Luppino, R. H. Lupton, D. G. Monet, J. S. Morgan, P. M. Onaka, B. Shiao, C. W. Stubbs, J. L. Tonry, R. White, E. Bañados, E. F. Bell, R. Bender, E. J. Bernard, M. Boegner, F. Boffi, M. T. Botticella, A. Calamida, S. Casertano, W. P. Chen, X. Chen, S. Cole, N. Deacon, C. Frenk, A. Fitzsimmons, S. Gezari, V. Gibbs, C. Goessl, T. Goggia, R. Gourgue, B. Goldman, P. Grant, E. K. Grebel, N. C. Hambly, G. Hasinger, A. F. Heavens, T. M. Heckman, R. Henderson, T. Henning, M. Holman, U. Hopp, W. H. Ip, S. Isani, M. Jackson, C. D. Keyes, A. M. Koekemoer, R. Kotak, D. Le, D. Liska, K. S. Long, J. R. Lucey, M. Liu, N. F. Martin, G. Masci, B. McLean, E. Mindel, P. Misra, E. Morganson, D. N. A. Murphy, A. Obaika, G. Narayan, M. A. Nieto-Santisteban, P. Norberg, J. A. Peacock, E. A. Pier, M. Postman, N. Primak, C. Rae, A. Rai, A. Riess, A. Riffeser, H. W. Rix, S. Röser, R. Russel, L. Rutz, E. Schilbach, A. S. B. Schultz, D. Scolnic, L. Strolger, A. Szalay, S. Seitz, E. Small, K. W. Smith, D. R. Soderblom, P. Taylor, R. Thomson, A. N. Taylor, A. R. Thakar, J. Thiel, D. Thilker, D. Unger, Y. Urata, J. Valenti, J. Wagner, T. Walder, F. Walter, S. P. Watters, S. Werner, W. M. Wood-Vasey, and R. Wyse. The Pan-STARRS1 Surveys. *arXiv e-prints*, art. arXiv:1612.05560, Dec. 2016.

C. T. J. Chen, W. N. Brandt, B. Luo, P. Ranalli, G. Yang, D. M. Alexander, F. E. Bauer, D. D. Kelson, M. Lacy, K. Nyland, P. Tozzi, F. Vito, M. Cirasuolo, R. Gilli, M. J. Jarvis, B. D. Lehmer, M. Paolillo, D. P. Schneider, O. Shemmer, I. Smail, M. Sun, M. Tanaka, M. Vaccari, C. Vignali, Y. Q. Xue, M. Banerji, K. E. Chow, B. Häußler, R. P. Norris, J. D. Silverman, and J. R. Trump. The XMM-SERVS survey: new XMM-Newton point-source catalogue for the XMM-LSS field. MNRAS, 478(2):2132–2163, Aug. 2018. doi: 10.1093/mnras/sty1036.

C. Circosta, C. Vignali, R. Gilli, A. Feltre, F. Vito, F. Calura, V. Mainieri, M. Massardi, and C. Norman. X-ray emission of z ¿ 2.5 active galactic nuclei can be obscured by their host galaxies. A&A, 623:A172, Mar. 2019. doi: 10.1051/0004-6361/201834426.

F. Civano, M. Brusa, A. Comastri, M. Elvis, M. Salvato, G. Zamorani, P. Capak, F. Fiore, R. Gilli, H. Hao, H. Ikeda, Y. Kakazu, J. S. Kartaltepe, D. Masters, T. Miyaji, M. Mignoli, S. Puccetti, F. Shankar, J. Silverman, C. Vignali, A. Zezas, and A. M. Koekemoer. The Population of High-redshift Active Galactic Nuclei in the Chandra-COSMOS Survey. ApJ, 741(2):91, Nov. 2011. doi: 10.1088/0004-637X/741/2/91.

F. Civano, R. C. Hickox, S. Puccetti, A. Comastri, J. R. Mullaney, L. Zappacosta, S. M. LaMassa, J. Aird, D. M. Alexander, D. R. Ballantyne, F. E. Bauer, W. N. Brandt, S. E. Boggs, F. E. Christensen, W. W. Craig, A. Del-Moro, M. Elvis, K. Forster, P. Gandhi, B. W. Grefenstette, C. J. Hailey, F. A. Harrison, G. B. Lansbury, B. Luo, K. Madsen, C. Saez, D. Stern, E. Treister, M. C. Urry, D. R. Wik, and W. Zhang. The Nustar Extragalactic Surveys: Overview and Catalog from the COSMOS Field. ApJ, 808(2):185, Aug. 2015. doi: 10.1088/0004-637X/808/2/185.

F. Civano, S. Marchesi, A. Comastri, M. C. Urry, M. Elvis, N. Cappelluti, S. Puccetti, M. Brusa, G. Zamorani, G. Hasinger, T. Aldcroft, D. M. Alexander, V. Allevato, H. Brunner, P. Capak, A. Finoguenov, F. Fiore, A. Fruscione, R. Gilli, K. Glotfelty, R. E. Griffiths, H. Hao, F. A. Harrison, K. Jahnke, J. Kartaltepe, A. Karim, S. M. LaMassa, G. Lanzuisi, T. Miyaji, P. Ranalli, M. Salvato, M. Sargent, N. J. Scoville, K. Schawinski, E. Schinnerer, J. Silverman, V. Smolcic, D. Stern, S. Toft, B. Trakhtenbrot, E. Treister, and C. Vignali. The Chandra Cosmos Legacy Survey: Overview and Point Source Catalog. ApJ, 819(1):62, Mar. 2016. doi: 10.3847/0004-637X/819/1/62.

C. Collet, N. P. H. Nesvadba, C. De Breuck, M. D. Lehnert, P. Best, J. J. Bryant, R. Hunstead, D. Dicken, and H. Johnston. Kinematic signatures of AGN feedback in moderately powerful radio galaxies at z ~2 observed with SINFONI. A&A, 586:A152, Feb. 2016. doi: 10.1051/0004-6361/201526872.

A. Comastri, G. Setti, G. Zamorani, and G. Hasinger. The contribution of AGNs to the X-ray background. A&A, 296:1, Apr. 1995.

J. Coupon, N. Czakon, J. Bosch, Y. Komiyama, E. Medezinski, S. Miyazaki, and M. Oguri. The bright-star masks for the HSC-SSP survey. PASJ, 70:S7, Jan. 2018. doi: 10.1093/pasj/psx047.

E. Daddi, F. Bournaud, F. Walter, H. Dannerbauer, C. L. Carilli, M. Dickinson, D. Elbaz, G. E. Morrison, D. Riechers, M. Onodera, F. Salmi, M. Krips, and D. Stern. Very High Gas Fractions and Extended Gas Reservoirs in z = 1.5 Disk Galaxies. ApJ, 713(1):686–707, Apr. 2010. doi: 10.1088/0004-637X/713/1/686.

D. A. Dale, G. Helou, G. E. Magdis, L. Armus, T. Díaz-Santos, and Y. Shi. A Two-parameter Model for the Infrared/Submillimeter/Radio Spectral Energy Distributions of Galaxies and Active Galactic Nuclei. ApJ, 784 (1):83, Mar. 2014. doi: 10.1088/0004-637X/784/1/83.

G. B. Dalton, M. Caldwell, A. K. Ward, M. S. Whalley, G. Woodhouse, R. L. Edeson, P. Clark, S. M. Beard, A. M. Gallie, S. P. Todd, J. M. D. Strachan, N. N. Bezawada, W. J. Sutherland, and J. P. Emerson. The VISTA infrared camera. In I. S. McLean and M. Iye, editors, *Society of Photo-Optical Instrumentation Engineers (SPIE) Conference Series*, volume 6269 of *Society of Photo-Optical Instrumentation Engineers (SPIE) Conference Series*, page 62690X, June 2006. doi: 10.1117/12.670018.

Q. D'Amato, R. Gilli, C. Vignali, M. Massardi, F. Pozzi, G. Zamorani, C. Circosta, F. Vito, J. Fritz, G. Cresci, V. Casasola, F. Calura, A. Feltre, V. Manieri, D. Rigopoulou, P. Tozzi, and C. Norman. Dust and gas content of high-redshift galaxies hosting obscured AGN in the Chandra Deep Field-South. A&A, 636:A37, Apr. 2020. doi: 10.1051/0004-6361/201936175.

R. L. Davies, N. M. Förster Schreiber, D. Lutz, R. Genzel, S. Belli, T. T. Shimizu, A. Contursi, R. I. Davies, R. Herrera-Camus, M. M. Lee, T. Naab, S. H. Price, A. Renzini, A. Schruba, A. Sternberg, L. J. Tacconi, H. Übler, E. Wisnioski, and S. Wuyts. From Nuclear to Circumgalactic: Zooming in on AGN-driven Outflows at $z \sim 2.2$ with SINFONI. ApJ, 894(1):28, May 2020. doi: 10.3847/1538-4357/ab86ad.

I. Delvecchio, C. Gruppioni, F. Pozzi, S. Berta, G. Zamorani, A. Cimatti, D. Lutz, D. Scott, C. Vignali, G. Cresci, A. Feltre, A. Cooray, M. Vaccari, J. Fritz, E. Le Floc'h, B. Magnelli, P. Popesso, S. Oliver, J. Bock, M. Carollo, T. Contini, O. Le Févre, S. Lilly, V. Mainieri, A. Renzini, and M. Scodeggio. Tracing the cosmic growth of supermassive black holes to $z \sim 3$ with Herschel. MNRAS, 439 (3):2736–2754, Apr. 2014. doi: 10.1093/mnras/stu130.

J. Díaz Tello, C. Donzelli, N. Padilla, N. Fujishiro, H. Hanami, T. Yoshikawa, and B. Hatsukade. Physical Properties, Star Formation, and Active Galactic Nucleus Activity in Balmer Break Galaxies at 0 ¡ z ¡ 1. ApJ, 771 (1):7, July 2013. doi: 10.1088/0004-637X/771/1/7.

X. Ding, J. Silverman, T. Treu, A. Schulze, M. Schramm, S. Birrer, D. Park, K. Jahnke, V. N. Bennert, J. S. Kartaltepe, A. M. Koekemoer, M. A. Malkan, and D. Sanders. The Mass Relations between Supermassive Black Holes and Their Host Galaxies at 1 ¡ z ¡ 2 HST-WFC3. ApJ, 888(1):37, Jan. 2020. doi: 10.3847/1538-4357/ab5b90.

K. Dobashi, J.-P. Bernard, A. Kawamura, F. Egusa, A. Hughes, D. Paradis, C. Bot, and W. T. Reach. Extinction Map of the Small Magellanic Cloud Based on the SIRIUS and 6X 2MASS Point Source Catalogs. AJ, 137 (6):5099–5109, June 2009. doi: 10.1088/0004-6256/137/6/5099.

F. Duras, A. Bongiorno, F. Ricci, E. Piconcelli, F. Shankar, E. Lusso, S. Bianchi, F. Fiore, R. Maiolino, A. Marconi, F. Onori, E. Sani, R. Schneider, C. Vignali, and F. La Franca. Universal bolometric corrections for active galactic nuclei over seven luminosity decades. A&A, 636:A73, Apr. 2020. doi: 10.1051/0004-6361/201936817.

A. C. Fabian, A. Celotti, and M. C. Erlund. Radiative pressure feedback by a quasar in a galactic bulge. MNRAS, 373(1):L16–L20, Nov. 2006. doi: 10.1111/j.1745-3933.2006.00234.x.

A. C. Fabian, R. V. Vasudevan, and P. Gandhi. The effect of radiation pressure on dusty absorbing gas around active galactic nuclei. MNRAS, 385(1):L43–L47, Mar. 2008. doi: 10.1111/j.1745-3933.2008.00430.x.

A. C. Fabian, R. V. Vasudevan, R. F. Mushotzky, L. M. Winter, and C. S. Reynolds. Radiation pressure and absorption in AGN: results from a complete unbiased sample from Swift. MNRAS, 394(1):L89–L92, Mar. 2009. doi: 10.1111/j.1745-3933.2009.00617.x.

G. G. Fazio, J. L. Hora, L. E. Allen, M. L. N. Ashby, P. Barmby, L. K. Deutsch, J. S. Huang, S. Kleiner, M. Marengo, S. T. Megeath, G. J. Melnick, M. A. Pahre, B. M. Patten, J. Polizotti, H. A. Smith, R. S. Taylor, Z. Wang, S. P. Willner, W. F. Hoffmann, J. L. Pipher, W. J. Forrest, C. W. McMurty, C. R. McCreight, M. E. McKelvey, R. E. McMurray, D. G. Koch, S. H. Moseley, R. G. Arendt, J. E. Mentzell, C. T. Marx, P. Losch, P. Mayman, W. Eichhorn, D. Krebs, M. Jhabvala, D. Y. Gezari, D. J. Fixsen, J. Flores, K. Shakoorzadeh, R. Jungo, C. Hakun, L. Workman, G. Karpati, R. Kichak, R. Whitley, S. Mann, E. V. Tollestrup, P. Eisenhardt, D. Stern, V. Gorjian, B. Bhattacharya, S. Carey, B. O. Nelson, W. J. Glaccum, M. Lacy, P. J. Lowrance, S. Laine, W. T. Reach, J. A. Stauffer, J. A. Surace, G. Wilson, E. L. Wright, A. Hoffman, G. Domingo, and M. Cohen. The Infrared Array Camera (IRAC) for the Spitzer Space Telescope. ApJS, 154(1):10–17, Sept. 2004. doi: 10.1086/422843.

G. Feulner, A. Gabasch, M. Salvato, N. Drory, U. Hopp, and R. Bender. Specific Star Formation Rates to Redshift 5 from the FORS Deep Field and the GOODS-S Field. ApJ, 633(1):L9–L12, Nov. 2005. doi: 10.1086/498109.

F. Fiore, S. Puccetti, M. Brusa, M. Salvato, G. Zamorani, T. Aldcroft, H. Aussel, H. Brunner, P. Capak, N. Cappelluti, F. Civano, A. Comastri, M. Elvis, C. Feruglio, A. Finoguenov, A. Fruscione, R. Gilli, G. Hasinger, A. Koekemoer, J. Kartaltepe, O. Ilbert, C. Impey, E. Le Floc'h, S. Lilly, V. Mainieri, A. Martinez-Sansigre, H. J. McCracken, N. Menci, A. Merloni, T. Miyaji, D. B. Sanders, M. Sargent, E. Schinnerer, N. Scoville, J. Silverman, V. Smolcic, A. Steffen, P. Santini, Y. Taniguchi, D. Thompson, J. R. Trump, C. Vignali, M. Urry, and L. Yan. Chasing Highly Obscured QSOs in the COSMOS Field. ApJ, 693(1):447–462, Mar. 2009. doi: 10.1088/0004-637X/693/1/447.

E. L. Fitzpatrick. Correcting for the Effects of Interstellar Extinction. PASP, 111(755):63–75, Jan. 1999. doi: 10.1086/316293.

H. Furusawa, G. Kosugi, M. Akiyama, T. Takata, K. Sekiguchi, I. Tanaka, I. Iwata, M. Kajisawa, N. Yasuda, M. Doi, M. Ouchi, C. Simpson, K. Shimasaku, T. Yamada, J. Furusawa, T. Morokuma, C. M. Ishida, K. Aoki, T. Fuse, M. Imanishi, M. Iye, H. Karoji, N. Kobayashi, T. Kodama, Y. Komiyama, Y. Maeda, S. Miyazaki, Y. Mizumoto, F. Nakata, J. Noumaru, R. Ogasawara, S. Okamura, T. Saito, T. Sasaki, Y. Ueda, and M. Yoshida. The Subaru/XMM-Newton Deep Survey (SXDS). II. Optical Imaging and Photometric Catalogs. ApJS, 176(1):1–18, May 2008. doi: 10.1086/527321.

S. C. Gallagher, W. N. Brandt, G. Chartas, and G. P. Garmire. X-Ray Spectroscopy of Quasi-Stellar Objects with Broad Ultraviolet Absorption Lines. ApJ, 567(1): 37–41, Mar. 2002. doi: 10.1086/338485.

S. C. Gallagher, W. N. Brandt, G. Chartas, R. Priddey, G. P. Garmire, and R. M. Sambruna. An Exploratory Chandra Survey of a Well-defined Sample of 35 Large Bright Quasar Survey Broad Absorption Line Quasars. ApJ, 644 (2):709–724, June 2006. doi: 10.1086/503762.

B. Garilli, R. McLure, L. Pentericci, P. Franzetti, A. Gargiulo, A. Carnall, O. Cucciati, A. Iovino, R. Amorin, M. Bolzonella, A. Bongiorno, M. Castellano, A. Cimatti, M. Cirasuolo, F. Cullen, J. Dunlop, D. Elbaz, S. Finkelstein, A. Fontana, F. Fontanot, M. Fumana, L. Guaita, W. Hartley, M. Jarvis, S. Juneau, D. Maccagni, D. McLeod, K. Nandra, E. Pompei, L. Pozzetti, M. Scodeggio, M. Talia, A. Calabrò, G. Cresci, J. P. U. Fynbo, N. P. Hathi, P. Hibon, A. M. Koekemoer, M. Magliocchetti, M. Salvato, G. Vietri, G. Zamorani, O. Almaini, I. Balestra, S. Bardelli, R. Begley, G. Brammer, E. F. Bell, R. A. A. Bowler, M. Brusa, F. Buitrago, C. Caputi, P. Cassata, S. Charlot, A. Citro, S. Cristiani, E. Curtis-Lake, M. Dickinson, G. Fazio, H. C. Ferguson, F. Fiore, M. Franco, A. Georgakakis, M. Giavalisco, A. Grazian, M. Hamadouche, I. Jung, S. Kim, Y. Khusanova, O. Le Fèvre, M. Longhetti, J. Lotz, F. Mannucci, D. Maltby, K. Matsuoka, H. Mendez-Hernandez, J. Mendez-Abreu, M. Mignoli, M. Moresco, M. Nonino, M. Pannella, C. Papovich, P. Popesso, G. Roberts-Borsani, D. J. Rosario, A. Saldana-Lopez, P. Santini, A. Saxena, D. Schaerer, C. Schreiber, D. Stark, L. A. M. Tasca, R. Thomas, E. Vanzella, V. Wild, C. Williams, and E. Zucca. The VANDELS ESO public spectroscopic survey. Final data release of 2087 spectra and spectroscopic measurements. A&A, 647:A150, Mar. 2021. doi: 10.1051/0004-6361/202040059.

J. E. Geach, C. Simpson, S. Rawlings, A. M. Read, and M. Watson. Low-power radio galaxy environments in the Subaru?/XMM-Newton Deep Field at z ~0.5. MNRAS, 381(4):1369–1380, Nov. 2007. doi: 10.1111/j.1365-2966.2007.12329.x.

R. Genzel, A. Eckart, T. Ott, and F. Eisenhauer. On the nature of the dark mass in the centre of the Milky Way. MNRAS, 291(1):219–234, Oct. 1997. doi: 10.1093/mnras/291.1.219.

A. Georgakakis, J. Aird, J. Buchner, M. Salvato, M. L. Menzel, W. N. Brandt, I. D. McGreer, T. Dwelly, G. Mountrichas, C. Koki, I. Georgantopoulos, L. T. Hsu, A. Merloni, Z. Liu, K. Nandra, and N. P. Ross. The X-ray luminosity function of active galactic nuclei in the redshift interval z=3-5. MNRAS, 453(2):1946–1964, Oct. 2015. doi: 10.1093/mnras/stv1703.

A. Georgakakis, M. Salvato, Z. Liu, J. Buchner, W. N. Brandt, T. T. Ananna, A. Schulze, Y. Shen, S. LaMassa, K. Nandra, A. Merloni, and I. D. McGreer. X-ray constraints on the fraction of obscured active galactic nuclei at high accretion luminosities. MNRAS, 469(3):3232–3251, Aug. 2017. doi: 10.1093/mnras/stx953.

I. Georgantopoulos, E. Pouliasis, G. Mountrichas, A. Van der Wel, S. Marchesi, and G. Lanzuisi. Comparing the host galaxy ages of X-ray selected AGN in COSMOS. Obscured AGN are associated with older galaxies. A&A, 673: A67, May 2023a. doi: 10.1051/0004-6361/202244875.

I. Georgantopoulos, E. Pouliasis, G. Mountrichas, A. Van der Wel, S. Marchesi, and G. Lanzuisi. Comparing the host galaxy ages of X-ray selected AGN in COSMOS: Obscured AGN are associated with older galaxies. *arXiv e-prints*, art. arXiv:2302.00530, Feb. 2023b. doi: 10.48550/arXiv.2302.00530.

A. M. Ghez, B. L. Klein, M. Morris, and E. E. Becklin. High Proper-Motion Stars in the Vicinity of Sagittarius A*: Evidence for a Supermassive Black Hole at the Center of Our Galaxy. ApJ, 509(2):678–686, Dec. 1998. doi: 10.1086/306528.

R. Gilli, A. Comastri, and G. Hasinger. The synthesis of the cosmic X-ray background in the Chandra and XMM-Newton era. A&A, 463(1):79–96, Feb. 2007. doi: 10.1051/0004-6361:20066334.

R. Gilli, C. Norman, F. Calura, F. Vito, R. Decarli, S. Marchesi, K. Iwasawa, A. Comastri, G. Lanzuisi, F. Pozzi, Q. D'Amato, C. Vignali, M. Brusa, M. Mignoli, and P. Cox. Supermassive black holes at high redshift are expected to be obscured by their massive host galaxies' interstellar medium. A&A, 666:A17, Oct. 2022. doi: 10.1051/0004-6361/202243708.

T. Goto, S. Arnouts, H. Inami, H. Matsuhara, C. Pearson, T. T. Takeuchi, E. Le Floc'h, T. Takagi, T. Wada, T. Nakagawa, S. Oyabu, D. Ishihara, H. Mok Lee, W.-S. Jeong, C. Yamauchi, S. Serjeant, C. Sedgwick, and E. Treister. Luminosity functions of local infrared galaxies with AKARI: implications for the cosmic star formation history and AGN evolution. MNRAS, 410(1):573–584, Jan. 2011. doi: 10.1111/j.1365-2966.2010.17466.x.

J. E. Greene and L. C. Ho. Estimating Black Hole Masses in Active Galaxies Using the Hα Emission Line. ApJ, 630 (1):122–129, Sept. 2005. doi: 10.1086/431897.

M. J. Griffin, A. Abergel, A. Abreu, P. A. R. Ade, P. André, J. L. Augueres, T. Babbedge, Y. Bae, T. Baillie, J. P. Baluteau, M. J. Barlow, G. Bendo, D. Benielli, J. J. Bock, P. Bonhomme, D. Brisbin, C. Brockley-Blatt, M. Caldwell, C. Cara, N. Castro-Rodriguez, R. Cerulli, P. Chanial, S. Chen, E. Clark, D. L. Clements, L. Clerc, J. Coker, D. Communal, L. Conversi, P. Cox, D. Crumb, C. Cunningham, F. Daly, G. R. Davis, P. de Antoni, J. Delderfield, N. Devin, A. di Giorgio, I. Didschuns, K. Dohlen, M. Donati, A. Dowell, C. D. Dowell, L. Duband, L. Dumaye, R. J. Emery, M. Ferlet, D. Ferrand, J. Fontignie, M. Fox, A. Franceschini, M. Frerking, T. Fulton, J. Garcia, R. Gastaud, W. K. Gear, J. Glenn, A. Goizel, D. K. Griffin, T. Grundy, S. Guest, L. Guillemet, P. C. Hargrave, M. Harwit, P. Hastings, E. Hatziminaoglou, M. Herman, B. Hinde, V. Hristov, M. Huang, P. Imhof, K. J. Isaak, U. Israelsson, R. J. Ivison, D. Jennings, B. Kiernan, K. J. King, A. E. Lange, W. Latter, G. Laurent, P. Laurent, S. J. Leeks, E. Lellouch, L. Levenson, B. Li, J. Li, J. Lilienthal, T. Lim, S. J. Liu, N. Lu, S. Madden, G. Mainetti, P. Marliani, D. McKay, K. Mercier, S. Molinari, H. Morris, H. Moseley, J. Mulder, M. Mur, D. A. Naylor, H. Nguyen, B. O'Halloran, S. Oliver, G. Olofsson, H. G. Olofsson, R. Orfei, M. J. Page, I. Pain, P. Panuzzo, A. Papageorgiou, G. Parks, P. Parr-Burman, A. Pearce, C. Pearson, I. Pérez-Fournon, F. Pinsard, G. Pisano, J. Podosek, M. Pohlen, E. T. Polehampton, D. Pouliquen, D. Rigopoulou, D. Rizzo, I. G. Roseboom, H. Roussel, M. Rowan-Robinson, B. Rownd, P. Saraceno, M. Sauvage, R. Savage, G. Savini, E. Sawyer, C. Scharmberg, D. Schmitt, N. Schneider, B. Schulz, A. Schwartz, R. Shafer, D. L. Shupe, B. Sibthorpe, S. Sidher, A. Smith, A. J. Smith, D. Smith, L. Spencer, B. Stobie, R. Sudiwala, K. Sukhatme, C. Surace, J. A. Stevens, B. M. Swinyard, M. Trichas, T. Tourette, H. Triou, S. Tseng, C. Tucker, A. Turner, M. Vaccari, I. Valtchanov, L. Vigroux, E. Virique, G. Voellmer, H. Walker, R. Ward, T. Waskett, M. Weilert, R. Wesson, G. J. White, N. Whitehouse, C. D. Wilson, B. Winter, A. L. Woodcraft, G. S. Wright, C. K. Xu, A. Zavagno, M. Zemcov, L. Zhang, and E. Zonca. The Herschel-SPIRE instrument and its in-flight performance. A&A, 518:L3, July 2010. doi: 10.1051/0004-6361/201014519.

H. Guo, Y. Shen, and S. Wang. PyQSOFit: Python code to fit the spectrum of quasars. Astrophysics Source Code Library, record ascl:1809.008, Sept. 2018.

K. K. Gupta, C. Ricci, A. Tortosa, Y. Ueda, T. Kawamuro, M. Koss, B. Trakhtenbrot, K. Oh, F. E. Bauer, F. Ricci, G. C. Privon, L. Zappacosta, D. Stern, D. Kakkad, E. Piconcelli, S. Veilleux, R. Mushotzky, T. Caglar, K. Ichikawa, A. Elagali, M. C. Powell, C. M. Urry, and F. Harrison. BAT AGN Spectroscopic Survey XXVII: scattered X-Ray radiation in obscured active galactic nuclei. MNRAS, 504(1):428–443, June 2021. doi: 10.1093/mnras/stab839.

S. D. J. Gwyn. MegaPipe: The MegaCam Image Stacking Pipeline at the Canadian Astronomical Data Centre. PASP, 120(864):212, Feb. 2008. doi: 10.1086/526794.

G. Hasinger. Absorption properties and evolution of active galactic nuclei. A&A, 490(3):905–922, Nov. 2008. doi: 10.1051/0004-6361:200809839.

R. C. Hickox and D. M. Alexander. Obscured Active Galactic Nuclei. ARA&A, 56:625–671, Sept. 2018. doi: 10.1146/annurev-astro-081817-051803.

R. C. Hickox, C. Jones, W. R. Forman, S. S. Murray, C. S. Kochanek, D. Eisenstein, B. T. Jannuzi, A. Dey, M. J. I. Brown, D. Stern, P. R. Eisenhardt, V. Gorjian, M. Brodwin, R. Narayan, R. J. Cool, A. Kenter, N. Caldwell, and M. E. Anderson. Host Galaxies, Clustering, Eddington Ratios, and Evolution of Radio, X-Ray, and Infrared-Selected AGNs. ApJ, 696(1):891–919, May 2009. doi: 10.1088/0004-637X/696/1/891.

K. Hiroi, Y. Ueda, M. Akiyama, and M. G. Watson. Comoving Space Density and Obscured Fraction of High-redshift Active Galactic Nuclei in the Subaru/XMM-Newton Deep Survey. ApJ, 758(1):49, Oct. 2012. doi: 10.1088/0004-637X/758/1/49.

M. Hirschmann, K. Dolag, A. Saro, L. Bachmann, S. Borgani, and A. Burkert. Cosmological simulations of black hole growth: AGN luminosities and downsizing. MNRAS, 442(3):2304–2324, Aug. 2014. doi: 10.1093/mnras/stu1023.

D. C. Hoaglin, F. Mosteller, and J. W. Tukey. *Understanding robust and exploratory data anlysis.* 1983.

P. F. Hopkins, L. Hernquist, T. J. Cox, T. Di Matteo, P. Martini, B. Robertson, and V. Springel. Black Holes in Galaxy Mergers: Evolution of Quasars. ApJ, 630(2): 705–715, Sept. 2005. doi: 10.1086/432438.

P. F. Hopkins, L. Hernquist, T. J. Cox, T. Di Matteo, B. Robertson, and V. Springel. A Unified, Merger-driven Model of the Origin of Starbursts, Quasars, the Cosmic X-Ray Background, Supermassive Black Holes, and Galaxy Spheroids. ApJS, 163(1):1–49, Mar. 2006. doi: 10.1086/499298.

P. F. Hopkins, T. J. Cox, D. Kereš, and L. Hernquist. A Cosmological Framework for the Co-Evolution of Quasars, Supermassive Black Holes, and Elliptical Galaxies. II. Formation of Red Ellipticals. ApJS, 175(2):390–422, Apr. 2008a. doi: 10.1086/524363.

P. F. Hopkins, L. Hernquist, T. J. Cox, and D. Kereš. A Cosmological Framework for the Co-Evolution of Quasars, Supermassive Black Holes, and Elliptical Galaxies. I. Galaxy Mergers and Quasar Activity. ApJS, 175(2):356–389, Apr. 2008b. doi: 10.1086/524362.

K. Ichikawa, C. Ricci, Y. Ueda, F. E. Bauer, T. Kawamuro, M. J. Koss, K. Oh, D. J. Rosario, T. T. Shimizu, M. Stalevski, L. Fuller, C. Packham, and B. Trakhtenbrot. BAT AGN Spectroscopic Survey. XI. The Covering Factor of Dust and Gas in Swift/BAT Active Galactic Nuclei. ApJ, 870(1):31, Jan. 2019. doi: 10.3847/1538-4357/aaef8f.

O. Ilbert, S. Arnouts, H. J. McCracken, M. Bolzonella, E. Bertin, O. Le Fèvre, Y. Mellier, G. Zamorani, R. Pellò, A. Iovino, L. Tresse, V. Le Brun, D. Bottini, B. Garilli, D. Maccagni, J. P. Picat, R. Scaramella, M. Scodeggio, G. Vettolani, A. Zanichelli, C. Adami, S. Bardelli, A. Cappi, S. Charlot, P. Ciliegi, T. Contini, O. Cucciati, S. Foucaud, P. Franzetti, I. Gavignaud, L. Guzzo, B. Marano, C. Marinoni, A. Mazure, B. Meneux, R. Merighi, S. Paltani, A. Pollo, L. Pozzetti, M. Radovich, E. Zucca, M. Bondi, A. Bongiorno, G. Busarello, S. de La Torre, L. Gregorini, F. Lamareille, G. Mathez, P. Merluzzi, V. Ripepi, D. Rizzo, and D. Vergani. Accurate photometric redshifts for the CFHT legacy survey calibrated using the VIMOS VLT deep survey. A&A, 457(3): 841–856, Oct. 2006. doi: 10.1051/0004-6361:20065138.

O. Ilbert, P. Capak, M. Salvato, H. Aussel, H. J. McCracken, D. B. Sanders, N. Scoville, J. Kartaltepe, S. Arnouts, E. Le Floc'h, B. Mobasher, Y. Taniguchi, F. Lamareille, A. Leauthaud, S. Sasaki, D. Thompson, M. Zamojski, G. Zamorani, S. Bardelli, M. Bolzonella, A. Bongiorno, M. Brusa, K. I. Caputi, C. M. Carollo, T. Contini, R. Cook, G. Coppa, O. Cucciati, S. de la Torre, L. de Ravel, P. Franzetti, B. Garilli, G. Hasinger, A. Iovino, P. Kampczyk, J. P. Kneib, C. Knobel, K. Kovac, J. F. Le Borgne, V. Le Brun, O. Le Fèvre, S. Lilly, D. Looper, C. Maier, V. Mainieri, Y. Mellier, M. Mignoli, T. Murayama, R. Pellò, Y. Peng, E. Pérez-Montero, A. Renzini, E. Ricciardelli, D. Schiminovich, M. Scodeggio, Y. Shioya, J. Silverman, J. Surace, M. Tanaka, L. Tasca, L. Tresse, D. Vergani, and E. Zucca. Cosmos Photometric Redshifts with 30-Bands for 2-deg^2. ApJ, 690(2):1236–1249, Jan. 2009. doi: 10.1088/0004-637X/690/2/1236.

O. Ilbert, S. Arnouts, E. Le Floc'h, H. Aussel, M. Bethermin, P. Capak, B. C. Hsieh, M. Kajisawa, A. Karim, O. Le Fèvre, N. Lee, S. Lilly, H. J. McCracken, L. Michel-Dansac, T. Moutard, M. A. Renzini, M. Salvato, D. B. Sanders, N. Scoville, K. Sheth, J. D. Silverman, V. Smolčić, Y. Taniguchi, and L. Tresse. Evolution of the specific star formation rate function at z¡ 1.4 Dissecting the mass-SFR plane in COSMOS and GOODS. A&A, 579:A2, July 2015. doi: 10.1051/0004-6361/201425176.

A. K. Inoue, H. Kaneda, T. Yamada, Y. Harikane, D. Ishihara, T. Kodama, Y. Komiyama, T. Moriya, K. Motohara, H. Nomura, M. Ouchi, S. Oyabu, T. Suzuki, T. Wada, and I. Yamamura. GREX-PLUS: galaxy reionization explorer and planetary universe spectrometer. In L. E. Coyle, S. Matsuura, and M. D. Perrin, editors, *Space Telescopes and Instrumentation 2022: Optical, Infrared, and Millimeter Wave*, volume 12180 of *Society of Photo-Optical Instrumentation Engineers (SPIE) Conference Series*, page 121801I, Aug. 2022. doi: 10.1117/12.2626050.

M. J. Irwin, J. Lewis, S. Hodgkin, P. Bunclark, D. Evans, R. McMahon, J. P. Emerson, M. Stewart, and S. Beard. VISTA data flow system: pipeline processing for WFCAM and VISTA. In P. J. Quinn and A. Bridger, editors, *Optimizing Scientific Return for Astronomy through Information Technologies*, volume 5493 of *Society of Photo-Optical Instrumentation Engineers (SPIE) Conference Series*, pages 411–422, Sept. 2004. doi: 10.1117/12.551449.

W. Ishibashi and A. C. Fabian. AGN-starburst evolutionary connection: a physical interpretation based on radiative feedback. MNRAS, 463(2):1291–1296, Dec. 2016. doi: 10.1093/mnras/stw2063.

W. Ishibashi, A. C. Fabian, C. Ricci, and A. Celotti. Revisiting the 'forbidden' region: AGN radiative feedback with radiation trapping. MNRAS, 479(3):3335–3342, Sept. 2018. doi: 10.1093/mnras/sty1620.

Ž. Ivezić, S. M. Kahn, J. A. Tyson, B. Abel, E. Acosta, R. Allsman, D. Alonso, Y. AlSayyad, S. F. Anderson, J. Andrew, J. R. P. Angel, G. Z. Angeli, R. Ansari, P. Antilogus, C. Araujo, R. Armstrong, K. T. Arndt, P. Astier, É. Aubourg, N. Auza, T. S. Axelrod, D. J. Bard, J. D. Barr, A. Barrau, J. G. Bartlett, A. E. Bauer, B. J. Bauman, S. Baumont, E. Bechtol, K. Bechtol, A. C. Becker, J. Becla, C. Beldica, S. Bellavia, F. B. Bianco, R. Biswas, G. Blanc, J. Blazek, R. D. Blandford, J. S. Bloom, J. Bogart, T. W. Bond, M. T. Booth, A. W. Borgland, K. Borne, J. F. Bosch, D. Boutigny, C. A. Brackett, A. Bradshaw, W. N. Brandt, M. E. Brown, J. S. Bullock, P. Burchat, D. L. Burke, G. Cagnoli, D. Calabrese, S. Callahan, A. L. Callen, J. L. Carlin, E. L. Carlson, S. Chandrasekharan, G. Charles-Emerson, S. Chesley, E. C. Cheu, H.-F. Chiang, J. Chiang, C. Chirino, D. Chow, D. R. Ciardi, C. F. Claver, J. Cohen-Tanugi, J. J. Cockrum, R. Coles, A. J. Connolly, K. H. Cook, A. Cooray, K. R. Covey, C. Cribbs, W. Cui, R. Cutri, P. N. Daly, S. F.

Daniel, F. Daruich, G. Daubard, G. Daues, W. Dawson, F. Delgado, A. Dellapenna, R. de Peyster, M. de Val-Borro, S. W. Digel, P. Doherty, R. Dubois, G. P. Dubois-Felsmann, J. Durech, F. Economou, T. Eifler, M. Eracleous, B. L. Emmons, A. Fausti Neto, H. Ferguson, E. Figueroa, M. Fisher-Levine, W. Focke, M. D. Foss, J. Frank, M. D. Freemon, E. Gangler, E. Gawiser, J. C. Geary, P. Gee, M. Geha, C. J. B. Gessner, R. R. Gibson, D. K. Gilmore, T. Glanzman, W. Glick, T. Goldina, D. A. Goldstein, I. Goodenow, M. L. Graham, W. J. Gressler, P. Gris, L. P. Guy, A. Guyonnet, G. Haller, R. Harris, P. A. Hascall, J. Haupt, F. Hernandez, S. Herrmann, E. Hileman, J. Hoblitt, J. A. Hodgson, C. Hogan, J. D. Howard, D. Huang, M. E. Huffer, P. Ingraham, W. R. Innes, S. H. Jacoby, B. Jain, F. Jammes, M. J. Jee, T. Jenness, G. Jernigan, D. Jevremović, K. Johns, A. S. Johnson, M. W. G. Johnson, R. L. Jones, C. Juramy-Gilles, M. Jurić, J. S. Kalirai, N. J. Kallivayalil, B. Kalmbach, J. P. Kantor, P. Karst, M. M. Kasliwal, H. Kelly, R. Kessler, V. Kinnison, D. Kirkby, L. Knox, I. V. Kotov, V. L. Krabbendam, K. S. Krughoff, P. Kubánek, J. Kuczewski, S. Kulkarni, J. Ku, N. R. Kurita, C. S. Lage, R. Lambert, T. Lange, J. B. Langton, L. Le Guillou, D. Levine, M. Liang, K.-T. Lim, C. J. Lintott, K. E. Long, M. Lopez, P. J. Lotz, R. H. Lupton, N. B. Lust, L. A. MacArthur, A. Mahabal, R. Mandelbaum, T. W. Markiewicz, D. S. Marsh, P. J. Marshall, S. Marshall, M. May, R. McKercher, M. McQueen, J. Meyers, M. Migliore, M. Miller, D. J. Mills, C. Miraval, J. Moeyens, F. E. Moolekamp, D. G. Monet, M. Moniez, S. Monkewitz, C. Montgomery, C. B. Morrison, F. Mueller, G. P. Muller, F. Muñoz Arancibia, D. R. Neill, S. P. Newbry, J.-Y. Nief, A. Nomerotski, M. Nordby, P. O'Connor, J. Oliver, S. S. Olivier, K. Olsen, W. O'Mullane, S. Ortiz, S. Osier, R. E. Owen, R. Pain, P. E. Palecek, J. K. Parejko, J. B. Parsons, N. M. Pease, J. M. Peterson, J. R. Peterson, D. L. Petravick, M. E. Libby Petrick, C. E. Petry, F. Pierfederici, S. Pietrowicz, R. Pike, P. A. Pinto, R. Plante, S. Plate, J. P. Plutchak, P. A. Price, M. Prouza, V. Radeka, J. Rajagopal, A. P. Rasmussen, N. Regnault, K. A. Reil, D. J. Reiss, M. A. Reuter, S. T. Ridgway, V. J. Riot, S. Ritz, S. Robinson, W. Roby, A. Roodman, W. Rosing, C. Roucelle, M. R. Rumore, S. Russo, A. Saha, B. Sassolas, T. L. Schalk, P. Schellart, R. H. Schindler, S. Schmidt, D. P. Schneider, M. D. Schneider, W. Schoening, G. Schumacher, M. E. Schwamb, J. Sebag, B. Selvy, G. H. Sembroski, L. G. Seppala, A. Serio, E. Serrano, R. A. Shaw, I. Shipsey, J. Sick, N. Silvestri, C. T. Slater, J. A. Smith, R. C. Smith, S. Sobhani, C. Soldahl, L. Storrie-Lombardi, E. Stover, M. A. Strauss, R. A. Street, C. W. Stubbs, I. S. Sullivan, D. Sweeney, J. D. Swinbank, A. Szalay, P. Takacs, S. A. Tether, J. J. Thaler, J. G. Thayer, S. Thomas, A. J. Thornton, V. Thukral, J. Tice, D. E. Trilling, M. Turri, R. Van Berg, D. Vanden Berk, K. Vetter, F. Virieux, T. Vucina, W. Wahl, L. Walkowicz, B. Walsh, C. W. Walter, D. L. Wang, S.-Y. Wang, M. Warner, O. Wiecha, B. Willman, S. E. Winters, D. Wittman, S. C. Wolff, W. M. Wood-Vasey, X. Wu, B. Xin, P. Yoachim, and H. Zhan. LSST: From Science Drivers to Reference Design and Anticipated Data Products. ApJ, 873(2):111, Mar. 2019. doi: 10.3847/1538-4357/ab042c.

K. Iwasawa, R. Gilli, C. Vignali, A. Comastri, W. N. Brandt, P. Ranalli, F. Vito, N. Cappelluti, F. J. Carrera, S. Falocco, I. Georgantopoulos, V. Mainieri, and M. Paolillo. The XMM deep survey in the CDF-S. II. A 9-20 keV selection of heavily obscured active galaxies at z ¿ 1.7. A&A, 546:A84, Oct. 2012. doi: 10.1051/0004-6361/201220036.

K. Jahnke, A. Bongiorno, M. Brusa, P. Capak, N. Cappelluti, M. Cisternas, F. Civano, J. Colbert, A. Comastri, M. Elvis, G. Hasinger, O. Ilbert, C. Impey, K. Inskip, A. M. Koekemoer, S. Lilly, C. Maier, A. Merloni, D. Riechers, M. Salvato, E. Schinnerer, N. Z. Scoville, J. Silverman, Y. Taniguchi, J. R. Trump, and L. Yan. Massive Galaxies in COSMOS: Evolution of Black Hole Versus Bulge Mass but not Versus Total Stellar Mass Over the Last 9 Gyr? ApJ, 706(2):L215–L220, Dec. 2009. doi: 10.1088/0004-637X/706/2/L215.

M. J. Jarvis, D. G. Bonfield, V. A. Bruce, J. E. Geach, K. McAlpine, R. J. McLure, E. González-Solares, M. Irwin, J. Lewis, A. K. Yoldas, S. Andreon, N. J. G. Cross, J. P. Emerson, G. Dalton, J. S. Dunlop, S. T. Hodgkin, F. O. Le, M. Karouzos, K. Meisenheimer, S. Oliver, S. Rawlings, C. Simpson, I. Smail, D. J. B. Smith, M. Sullivan, W. Sutherland, S. V. White, and J. T. L. Zwart. The VISTA Deep Extragalactic Observations (VIDEO) survey. MNRAS, 428(2):1281–1295, Jan. 2013. doi: 10.1093/mnras/sts118.

H. D. Jun, R. J. Assef, C. M. Carroll, R. C. Hickox, Y. Kim, J. Lee, C. Ricci, and D. Stern. The Dust-to-gas Ratio and the Role of Radiation Pressure in Luminous, Obscured Quasars. ApJ, 906(1):21, Jan. 2021. doi: 10.3847/1538-4357/abc629.

M. Jurić, J. Kantor, K. T. Lim, R. H. Lupton, G. Dubois-Felsmann, T. Jenness, T. S. Axelrod, J. Aleksić, R. A. Allsman, Y. AlSayyad, J. Alt, R. Armstrong, J. Basney, A. C. Becker, J. Becla, R. Biswas, J. Bosch, D. Boutigny, M. C. Kind, D. R. Ciardi, A. J. Connolly, S. F. Daniel, G. E. Daues, F. Economou, H. F. Chiang, A. Fausti, M. Fisher-Levine, D. M. Freemon, P. Gris, F. Hernandez, J. Hoblitt, Z. Ivezić, F. Jammes, D. Jevremović, R. L. Jones, J. B. Kalmbach, V. P. Kasliwal, K. S. Krughoff, J. Lurie, N. B. Lust, L. A. MacArthur, P. Melchior, J. Moeyens, D. L. Nidever, R. Owen, J. K. Parejko, J. M. Peterson, D. Petravick, S. R. Pietrowicz, P. A. Price, D. J. Reiss, R. A. Shaw, J. Sick, C. T. Slater, M. A. Strauss, I. S. Sullivan, J. D. Swinbank, S. Van Dyk, V. Vujčić, A. Withers, and P. Yoachim. The LSST Data Management System. In N. P. F. Lorente, K. Shortridge, and R. Wayth, editors, *Astronomical Data Analysis Software and Systems XXV*, volume 512 of *Astronomical Society of the Pacific Conference Series*, page 279, Dec. 2017.

D. Kakkad, V. Mainieri, P. Padovani, G. Cresci, B. Husemann, S. Carniani, M. Brusa, A. Lamastra, G. Lanzuisi, E. Piconcelli, and M. Schramm. Tracing outflows in the AGN forbidden region with SINFONI. A&A, 592:A148, Aug. 2016. doi: 10.1051/0004-6361/201527968.

E. Kalfountzou, F. Civano, M. Elvis, M. Trichas, and P. Green. The largest X-ray-selected sample of z¿3 AGNs: C-COSMOS and ChaMP. MNRAS, 445(2):1430–1448, Dec. 2014. doi: 10.1093/mnras/stu1745.

Y. Kamata, S. Miyazaki, H. Nakaya, Y. Komiyama, Y. Obuchi, S. Kawanomoto, F. Uraguchi, Y. Utsumi, H. Suzuki, Y. Miyazaki, and M. Muramatsu. Hyper Suprime-Cam: characteristics of 116 fully depleted back-illuminated CCDs. In A. D. Holland and J. W. Beletic, editors, *High Energy, Optical, and Infrared Detectors for Astronomy V*, volume 8453 of *Society of Photo-Optical Instrumentation Engineers (SPIE) Conference Series*, page 84531X, July 2012. doi: 10.1117/12.927234.

A. Karim, E. Schinnerer, A. Martínez-Sansigre, M. T. Sargent, A. van der Wel, H. W. Rix, O. Ilbert, V. Smolčić, C. Carilli, M. Pannella, A. M. Koekemoer, E. F. Bell, and M. Salvato. The Star Formation History of Mass-selected

Galaxies in the COSMOS Field. ApJ, 730(2):61, Apr. 2011. doi: 10.1088/0004-637X/730/2/61.

N. Kashikawa, K. Aoki, R. Asai, N. Ebizuka, M. Inata, M. Iye, K. S. Kawabata, G. Kosugi, Y. Ohyama, K. Okita, T. Ozawa, Y. Saito, T. Sasaki, K. Sekiguchi, Y. Shimizu, H. Taguchi, T. Takata, Y. Yadoumaru, and M. Yoshida. FOCAS: The Faint Object Camera and Spectrograph for the Subaru Telescope. PASJ, 54(6):819–832, Dec. 2002. doi: 10.1093/pasj/54.6.819.

B. C. Kelly. Some Aspects of Measurement Error in Linear Regression of Astronomical Data. ApJ, 665(2):1489–1506, Aug. 2007. doi: 10.1086/519947.

M. Kimura, T. Maihara, F. Iwamuro, M. Akiyama, N. Tamura, G. B. Dalton, N. Takato, P. Tait, K. Ohta, S. Eto, D. Mochida, B. Elms, K. Kawate, T. Kurakami, Y. Moritani, J. Noumaru, N. Ohshima, M. Sumiyoshi, K. Yabe, J. Brzeski, T. Farrell, G. Frost, P. R. Gillingham, R. Haynes, A. M. Moore, R. Muller, S. Smedley, G. Smith, D. G. Bonfield, C. B. Brooks, A. R. Holmes, E. Curtis Lake, H. Lee, I. J. Lewis, T. R. Froud, I. A. Tosh, G. F. Woodhouse, C. Blackburn, R. Content, N. Dipper, G. Murray, R. Sharples, and D. J. Robertson. Fibre Multi-Object Spectrograph (FMOS) for the Subaru Telescope. PASJ, 62:1135–1147, Oct. 2010. doi: 10.1093/pasj/62.5.1135.

M. Kishimoto, S. F. Hönig, T. Beckert, and G. Weigelt. The innermost region of AGN tori: implications from the HST/NICMOS type 1 point sources and near-IR reverberation. A&A, 476(2):713–721, Dec. 2007. doi: 10.1051/0004-6361:20077911.

J. Kormendy and L. C. Ho. Coevolution (Or Not) of Supermassive Black Holes and Host Galaxies. ARA&A, 51(1):511–653, Aug. 2013. doi: 10.1146/annurev-astro-082708-101811.

M. J. Koss, C. Ricci, B. Trakhtenbrot, K. Oh, J. S. den Brok, J. E. Mejía-Restrepo, D. Stern, G. C. Privon, E. Treister, M. C. Powell, R. Mushotzky, F. E. Bauer, T. T. Ananna, M. Baloković, R. E. Bär, G. Becker, P. Bessiere, L. Burtscher, T. Caglar, E. Congiu, P. Evans, F. Harrison, M. Heida, K. Ichikawa, N. Kamraj, I. Lamperti, F. Pacucci, F. Ricci, R. Riffel, A. F. Rojas, K. Schawinski, M. J. Temple, C. M. Urry, S. Veilleux, and J. Williams. BASS. XXII. The BASS DR2 AGN Catalog and Data. ApJS, 261(1):2, July 2022. doi: 10.3847/1538-4365/ac6c05.

L. Koutoulidis, G. Mountrichas, I. Georgantopoulos, E. Pouliasis, and M. Plionis. Host galaxy properties of X-ray active galactic nuclei in the local Universe. A&A, 658:A35, Feb. 2022. doi: 10.1051/0004-6361/202142466.

M. Kriek, A. E. Shapley, N. A. Reddy, B. Siana, A. L. Coil, B. Mobasher, W. R. Freeman, L. de Groot, S. H. Price, R. Sanders, I. Shivaei, G. B. Brammer, I. G. Momcheva, R. E. Skelton, P. G. van Dokkum, K. E. Whitaker, J. Aird, M. Azadi, M. Kassis, J. S. Bullock, C. Conroy, R. Davé, D. Kereš, and M. Krumholz. The MOSFIRE Deep Evolution Field (MOSDEF) Survey: Rest-frame Optical Spectroscopy for ~1500 H-selected Galaxies at 1.37 ¡ z ¡ 3.8. ApJS, 218(2):15, June 2015. doi: 10.1088/0067-0049/218/2/15.

P. Kroupa. On the variation of the initial mass function. MNRAS, 322(2):231–246, Apr. 2001. doi: 10.1046/j.1365-8711.2001.04022.x.

Y. Kudoh, K. Wada, N. Kawakatu, and M. Nomura. Multiphase Gas Nature in the Sub-parsec Region of the Active Galactic Nuclei. I. Dynamical Structures of Dusty and Dust-free Outflow. ApJ, 950(1):72, June 2023. doi: 10.3847/1538-4357/accc2b.

F. La Franca, F. Fiore, A. Comastri, G. C. Perola, N. Sacchi, M. Brusa, F. Cocchia, C. Feruglio, G. Matt, C. Vignali, N. Carangelo, P. Ciliegi, A. Lamastra, R. Maiolino, M. Mignoli, S. Molendi, and S. Puccetti. The HELLAS2XMM Survey. VII. The Hard X-Ray Luminosity Function of AGNs up to z = 4: More Absorbed AGNs at Low Luminosities and High Redshifts. ApJ, 635(2): 864–879, Dec. 2005. doi: 10.1086/497586.

C. Laigle, H. J. McCracken, O. Ilbert, B. C. Hsieh, I. Davidzon, P. Capak, G. Hasinger, J. D. Silverman, C. Pichon, J. Coupon, H. Aussel, D. Le Borgne, K. Caputi, P. Cassata, Y. Y. Chang, F. Civano, J. Dunlop, J. Fynbo, J. S. Kartaltepe, A. Koekemoer, O. Le Fèvre, E. Le Floc'h, A. Leauthaud, S. Lilly, L. Lin, S. Marchesi, B. Milvang-Jensen, M. Salvato, D. B. Sanders, N. Scoville, V. Smolcic, M. Stockmann, Y. Taniguchi, L. Tasca, S. Toft, M. Vaccari, and J. Zabl. The COSMOS2015 Catalog: Exploring the 1 ¡ z ¡ 6 Universe with Half a Million Galaxies. ApJS, 224(2):24, June 2016. doi: 10.3847/0067-0049/224/2/24.

G. B. Lansbury, M. Banerji, A. C. Fabian, and M. J. Temple. X-ray observations of luminous dusty quasars at z ¿ 2. MNRAS, 495(3):2652–2663, Jan. 2020. doi: 10.1093/mnras/staa1220.

A. Lawrence. The relative frequency of broad-lined and narrow-lined active galactic nuclei : implications for unified schemes. MNRAS, 252:586, Oct. 1991. doi: 10.1093/mnras/252.4.586.

O. Le Fèvre, P. Cassata, O. Cucciati, B. Garilli, O. Ilbert, V. Le Brun, D. Maccagni, C. Moreau, M. Scodeggio, L. Tresse, G. Zamorani, C. Adami, S. Arnouts, S. Bardelli, M. Bolzonella, M. Bondi, A. Bongiorno, D. Bottini, A. Cappi, S. Charlot, P. Ciliegi, T. Contini, S. de la Torre, S. Foucaud, P. Franzetti, I. Gavignaud, L. Guzzo, A. Iovino, B. Lemaux, C. López-Sanjuan, H. J. McCracken, B. Marano, C. Marinoni, A. Mazure, Y. Mellier, R. Merighi, P. Merluzzi, S. Paltani, R. Pellò, A. Pollo, L. Pozzetti, R. Scaramella, L. Tasca, D. Vergani, G. Vettolani, A. Zanichelli, and E. Zucca. The VIMOS VLT Deep Survey final data release: a spectroscopic sample of 35 016 galaxies and AGN out to z ~6.7 selected with $17.5 \leq i_{AB} \leq 24.75$. A&A, 559:A14, Nov. 2013. doi: 10.1051/0004-6361/201322179.

J. Liske, I. K. Baldry, S. P. Driver, R. J. Tuffs, M. Alpaslan, E. Andrae, S. Brough, M. E. Cluver, M. W. Grootes, M. L. P. Gunawardhana, L. S. Kelvin, J. Loveday, A. S. G. Robotham, E. N. Taylor, S. P. Bamford, J. Bland-Hawthorn, M. J. I. Brown, M. J. Drinkwater, A. M. Hopkins, M. J. Meyer, P. Norberg, J. A. Peacock, N. K. Agius, S. K. Andrews, A. E. Bauer, J. H. Y. Ching, M. Colless, C. J. Conselice, S. M. Croom, L. J. M. Davies, R. De Propris, L. Dunne, E. M. Eardley, S. Ellis, C. Foster, C. S. Frenk, B. Häußler, B. W. Holwerda, C. Howlett, H. Ibarra, M. J. Jarvis, D. H. Jones, P. R. Kafle, C. G. Lacey, R. Lange, M. A. Lara-López, Á. R. López-Sánchez, S. Maddox, B. F. Madore, T. McNaught-Roberts, A. J. Moffett, R. C. Nichol, M. S. Owers, D. Palamara, S. J. Penny, S. Phillipps, K. A. Pimbblet, C. C. Popescu, M. Prescott, R. Proctor, E. M. Sadler, A. E. Sansom, M. Seibert, R. Sharp, W. Sutherland, J. A. Vázquez-Mata, E. van Kampen, S. M. Wilkins, R. Williams, and A. H. Wright. Galaxy And Mass Assembly (GAMA): end of survey report and data release 2. MNRAS, 452(2): 2087–2126, Sept. 2015. doi: 10.1093/mnras/stv1436.

T. Liu, P. Tozzi, J.-X. Wang, W. N. Brandt, C. Vignali, Y. Xue, D. P. Schneider, A. Comastri, G. Yang, F. E. Bauer, M. Paolillo, B. Luo, R. Gilli, Q. D. Wang, M. Giavalisco, Z. Ji, D. M. Alexander, V. Mainieri, O. Shemmer, A. Koekemoer, and G. Risaliti. X-Ray Spectral Analyses of AGNs from the 7Ms Chandra Deep Field-South Survey: The Distribution, Variability, and Evolutions of AGN Obscuration. ApJS, 232(1):8, Sept. 2017. doi: 10.3847/1538-4365/aa7847.

T. Liu, A. Merloni, J.-X. Wang, P. Tozzi, Y. Shen, M. Brusa, M. Salvato, K. Nandra, J. Comparat, Z. Liu, G. Ponti, and D. Coffey. Probing AGN inner structure with X-ray obscured type 1 AGN. MNRAS, 479(4):5022–5034, Oct. 2018. doi: 10.1093/mnras/sty1751.

C. J. Lonsdale, H. E. Smith, M. Rowan-Robinson, J. Surace, D. Shupe, C. Xu, S. Oliver, D. Padgett, F. Fang, T. Conrow, A. Franceschini, N. Gautier, M. Griffin, P. Hacking, F. Masci, G. Morrison, J. O'Linger, F. Owen, I. Pérez-Fournon, M. Pierre, R. Puetter, G. Stacey, S. Castro, M. d. C. Polletta, D. Farrah, T. Jarrett, D. Frayer, B. Siana, T. Babbedge, S. Dye, M. Fox, E. Gonzalez-Solares, M. Salaman, S. Berta, J. J. Condon, H. Dole, and S. Serjeant. SWIRE: The SIRTF Wide-Area Infrared Extragalactic Survey. PASP, 115(810):897–927, Aug. 2003. doi: 10.1086/376850.

B. Luo, W. N. Brandt, Y. Q. Xue, B. Lehmer, D. M. Alexander, F. E. Bauer, F. Vito, G. Yang, A. R. Basu-Zych, A. Comastri, R. Gilli, Q. S. Gu, A. E. Hornschemeier, A. Koekemoer, T. Liu, V. Mainieri, M. Paolillo, P. Ranalli, P. Rosati, D. P. Schneider, O. Shemmer, I. Smail, M. Sun, P. Tozzi, C. Vignali, and J. X. Wang. The Chandra Deep Field-South Survey: 7 Ms Source Catalogs. ApJS, 228(1):2, Jan. 2017. doi: 10.3847/1538-4365/228/1/2.

E. Lusso, A. Comastri, B. D. Simmons, M. Mignoli, G. Zamorani, C. Vignali, M. Brusa, F. Shankar, D. Lutz, J. R. Trump, R. Maiolino, R. Gilli, M. Bolzonella, S. Puccetti, M. Salvato, C. D. Impey, F. Civano, M. Elvis, V. Mainieri, J. D. Silverman, A. M. Koekemoer, A. Bongiorno, A. Merloni, S. Berta, E. Le Floc'h, B. Magnelli, F. Pozzi, and L. Riguccini. Bolometric luminosities and Eddington ratios of X-ray selected active galactic nuclei in the XMM-COSMOS survey. MNRAS, 425(1):623–640, Sept. 2012. doi: 10.1111/j.1365-2966.2012.21513.x.

P. Madau and M. Dickinson. Cosmic Star-Formation History. ARA&A, 52:415–486, Aug. 2014. doi: 10.1146/annurev-astro-081811-125615.

P. Magdziarz and A. A. Zdziarski. Angle-dependent Compton reflection of X-rays and gamma-rays. MNRAS, 273 (3):837–848, Apr. 1995. doi: 10.1093/mnras/273.3.837.

E. A. Magnier and J. C. Cuillandre. The Elixir System: Data Characterization and Calibration at the Canada-France-Hawaii Telescope. PASP, 116(819):449–464, May 2004. doi: 10.1086/420756.

E. A. Magnier, E. Schlafly, D. Finkbeiner, M. Juric, J. L. Tonry, W. S. Burgett, K. C. Chambers, H. A. Flewelling, N. Kaiser, R. P. Kudritzki, J. S. Morgan, P. A. Price, W. E. Sweeney, and C. W. Stubbs. The Pan-STARRS 1 Photometric Reference Ladder, Release 12.01. ApJS, 205 (2):20, Apr. 2013. doi: 10.1088/0067-0049/205/2/20.

E. A. Magnier, E. F. Schlafly, D. P. Finkbeiner, J. L. Tonry, B. Goldman, S. Röser, E. Schilbach, S. Casertano, K. C. Chambers, H. A. Flewelling, M. E. Huber, P. A. Price, W. E. Sweeney, C. Z. Waters, L. Denneau, P. W. Draper, K. W. Hodapp, R. Jedicke, N. Kaiser, R. P. Kudritzki, N. Metcalfe, C. W. Stubbs, and R. J. Wainscoat. Pan-STARRS Photometric and Astrometric Calibration. ApJS, 251(1):6, Nov. 2020. doi: 10.3847/1538-4365/abb82a.

R. Maiolino and G. H. Rieke. Low-Luminosity and Obscured Seyfert Nuclei in Nearby Galaxies. ApJ, 454:95, Nov. 1995. doi: 10.1086/176468.

R. Maiolino, O. Shemmer, M. Imanishi, H. Netzer, E. Oliva, D. Lutz, and E. Sturm. Dust covering factor, silicate emission, and star formation in luminous QSOs. A&A, 468(3): 979–992, June 2007. doi: 10.1051/0004-6361:20077252.

D. Makarov, P. Prugniel, N. Terekhova, H. Courtois, and I. Vauglin. HyperLEDA. III. The catalogue of extragalactic distances. A&A, 570:A13, Oct. 2014. doi: 10.1051/0004-6361/201423496.

A. Masini, A. Comastri, F. Civano, R. C. Hickox, C. M. Carroll, H. Suh, W. N. Brandt, M. A. DiPompeo, F. A. Harrison, and D. Stern. The NuSTAR Extragalactic Surveys: Unveiling Rare, Buried AGNs and Detecting the Contributors to the Peak of the Cosmic X-Ray Background. ApJ, 867(2):162, Nov. 2018. doi: 10.3847/1538-4357/aae539.

J. C. Mauduit, M. Lacy, D. Farrah, J. A. Surace, M. Jarvis, S. Oliver, C. Maraston, M. Vaccari, L. Marchetti, G. Zeimann, E. A. Gonzáles-Solares, J. Pforr, A. O. Petric, B. Henriques, P. A. Thomas, J. Afonso, A. Rettura, G. Wilson, J. T. Falder, J. E. Geach, M. Huynh, R. P. Norris, N. Seymour, G. T. Richards, S. A. Stanford, D. M. Alexander, R. H. Becker, P. N. Best, L. Bizzocchi, D. Bonfield, N. Castro, A. Cava, S. Chapman, N. Christopher, D. L. Clements, G. Covone, N. Dubois, J. S. Dunlop, E. Dyke, A. Edge, H. C. Ferguson, S. Foucaud, A. Franceschini, R. R. Gal, J. K. Grant, M. Grossi, E. Hatziminaoglou, S. Hickey, J. A. Hodge, J. S. Huang, R. J. Ivison, M. Kim, O. LeFevre, M. Lehnert, C. J. Lonsdale, L. M. Lubin, R. J. McLure, H. Messias, A. Martínez-Sansigre, A. M. J. Mortier, D. M. Nielsen, M. Ouchi, G. Parish, I. Perez-Fournon, M. Pierre, S. Rawlings, A. Readhead, S. E. Ridgway, D. Rigopoulou, A. K. Romer, I. G. Rosebloom, H. J. A. Rottgering, M. Rowan-Robinson, A. Sajina, C. J. Simpson, I. Smail, G. K. Squires, J. A. Stevens, R. Taylor, M. Trichas, T. Urrutia, E. van Kampen, A. Verma, and C. K. Xu. The Spitzer Extragalactic Representative Volume Survey (SERVS): Survey Definition and Goals. PASP, 124(917):714, July 2012. doi: 10.1086/666945.

R. J. McLure, H. J. Pearce, J. S. Dunlop, M. Cirasuolo, E. Curtis-Lake, V. A. Bruce, K. I. Caputi, O. Almaini, D. G. Bonfield, E. J. Bradshaw, F. Buitrago, R. Chuter, S. Foucaud, W. G. Hartley, and M. J. Jarvis. The sizes, masses and specific star formation rates of massive galaxies at 1.3 ¡ z ¡ 1.5: strong evidence in favour of evolution via minor mergers. MNRAS, 428(2):1088–1106, Jan. 2013. doi: 10.1093/mnras/sts092.

O. Melnyk, M. Plionis, A. Elyiv, M. Salvato, L. Chiappetti, N. Clerc, P. Gandhi, M. Pierre, T. Sadibekova, A. Pospieszalska-Surdej, and J. Surdej. VizieR Online Data Catalog: XMM-LSS field X-ray sources classification (Melnyk+, 2013). *VizieR Online Data Catalog*, art. J/A+A/557/A81, Aug. 2013.

M. L. Menzel, A. Merloni, A. Georgakakis, M. Salvato, E. Aubourg, W. N. Brandt, M. Brusa, J. Buchner, T. Dwelly, K. Nandra, I. Pâris, P. Petitjean, and A. Schwope. A spectroscopic survey of X-ray-selected AGNs in the northern XMM-XXL field. MNRAS, 457 (1):110–132, Mar. 2016. doi: 10.1093/mnras/stv2749.

E. Merlin, A. Fontana, H. C. Ferguson, J. S. Dunlop, D. Elbaz, N. Bourne, V. A. Bruce, F. Buitrago, M. Castellano, C. Schreiber, A. Grazian, R. J. McLure, K. Okumura, X. Shu, T. Wang, R. Amorín, K. Boutsia, N. Cappelluti, A. Comastri, S. Derriere, S. M. Faber, and P. Santini. T-PHOT: A new code for PSF-matched, prior-based, multiwavelength extragalactic deconfusion photometry. A&A, 582:A15, Oct. 2015. doi: 10.1051/0004-6361/201526471.

E. Merlin, N. Bourne, M. Castellano, H. C. Ferguson, T. Wang, S. Derriere, J. S. Dunlop, D. Elbaz, and A. Fontana. T-PHOT version 2.0: Improved algorithms for background subtraction, local convolution, kernel registration, and new options. A&A, 595:A97, Nov. 2016. doi: 10.1051/0004-6361/201628751.

A. Merloni, A. Bongiorno, M. Bolzonella, M. Brusa, F. Civano, A. Comastri, M. Elvis, F. Fiore, R. Gilli, H. Hao, K. Jahnke, A. M. Koekemoer, E. Lusso, V. Mainieri, M. Mignoli, T. Miyaji, A. Renzini, M. Salvato, J. Silverman, J. Trump, C. Vignali, G. Zamorani, P. Capak, S. J. Lilly, D. Sanders, Y. Taniguchi, S. Bardelli, C. M. Carollo, K. Caputi, T. Contini, G. Coppa, O. Cucciati, S. de la Torre, L. de Ravel, P. Franzetti, B. Garilli, G. Hasinger, C. Impey, A. Iovino, K. Iwasawa, P. Kampczyk, J. P. Kneib, C. Knobel, K. Kovač, F. Lamareille, J. F. Le Borgne, V. Le Brun, O. Le Fèvre, C. Maier, R. Pello, Y. Peng, E. Perez Montero, E. Ricciardelli, M. Scodeggio, M. Tanaka, L. A. M. Tasca, L. Tresse, D. Vergani, and E. Zucca. On the Cosmic Evolution of the Scaling Relations Between Black Holes and Their Host Galaxies: Broad-Line Active Galactic Nuclei in the zCOSMOS Survey. ApJ, 708(1):137–157, Jan. 2010. doi: 10.1088/0004-637X/708/1/137.

A. Merloni, A. Bongiorno, M. Brusa, K. Iwasawa, V. Mainieri, B. Magnelli, M. Salvato, S. Berta, N. Cappelluti, A. Comastri, F. Fiore, R. Gilli, A. Koekemoer, E. Le Floc'h, E. Lusso, D. Lutz, T. Miyaji, F. Pozzi, L. Riguccini, D. J. Rosario, J. Silverman, M. Symeonidis, E. Treister, C. Vignali, and G. Zamorani. The incidence of obscuration in active galactic nuclei. MNRAS, 437(4): 3550–3567, Feb. 2014. doi: 10.1093/mnras/stt2149.

S. Miyazaki, Y. Komiyama, S. Kawanomoto, Y. Doi, H. Furusawa, T. Hamana, Y. Hayashi, H. Ikeda, Y. Kamata, H. Karoji, M. Koike, T. Kurakami, S. Miyama, T. Morokuma, F. Nakata, K. Namikawa, H. Nakaya, K. Nariai, Y. Obuchi, Y. Oishi, N. Okada, Y. Okura, P. Tait, T. Takata, Y. Tanaka, M. Tanaka, T. Terai, D. Tomono, F. Uraguchi, T. Usuda, Y. Utsumi, Y. Yamada, H. Yamanoi, H. Aihara, H. Fujimori, S. Mineo, H. Miyatake, M. Oguri, T. Uchida, M. M. Tanaka, N. Yasuda, M. Takada, H. Murayama, A. J. Nishizawa, N. Sugiyama, M. Chiba, T. Futamase, S.-Y. Wang, H.-Y. Chen, P. T. P. Ho, E. J. Y. Liaw, C.-F. Chiu, C.-L. Ho, T.-C. Lai, Y.-C. Lee, D.-Z. Jeng, S. Iwamura, R. Armstrong, S. Bickerton, J. Bosch, J. E. Gunn, R. H. Lupton, C. Loomis, P. Price, S. Smith, M. A. Strauss, E. L. Turner, H. Suzuki, Y. Miyazaki, M. Muramatsu, K. Yamamoto, M. Endo, Y. Ezaki, N. Ito, N. Kawaguchi, S. Sofuku, T. Taniike, K. Akutsu, N. Dojo, K. Kasumi, T. Matsuda, K. Imoto, Y. Miwa, M. Suzuki, K. Takeshi, and H. Yokota. Hyper Suprime-Cam: System design and verification of image quality. PASJ, 70:S1, Jan. 2018. doi: 10.1093/pasj/psx063.

S. Mizukoshi, T. Minezaki, S. Tsunetsugu, A. Yoshida, H. Sameshima, M. Kokubo, and H. Noda. Measurement of AGN dust extinction based on the near-infrared flux variability of WISE data. MNRAS, 516(2):2876–2886, Oct. 2022. doi: 10.1093/mnras/stac2307.

I. G. Momcheva, G. B. Brammer, P. G. van Dokkum, R. E. Skelton, K. E. Whitaker, E. J. Nelson, M. Fumagalli, M. V. Maseda, J. Leja, M. Franx, H.-W. Rix, R. Bezanson, E. Da Cunha, C. Dickey, N. M. Förster Schreiber, G. Illingworth, M. Kriek, I. Labbé, J. Ulf Lange, B. F. Lundgren, D. Magee, D. Marchesini, P. Oesch, C. Pacifici, S. G. Patel, S. Price, T. Tal, D. A. Wake, A. van der Wel, and S. Wuyts. The 3D-HST Survey: Hubble Space Telescope WFC3/G141 Grism Spectra, Redshifts, and Emission Line Measurements for ~100,000 Galaxies. ApJS, 225 (2):27, Aug. 2016. doi: 10.3847/0067-0049/225/2/27.

R. Morrison and D. McCammon. Interstellar photoelectric absorption cross sections, 0.03-10 keV. ApJ, 270:119–122, July 1983. doi: 10.1086/161102.

G. Mountrichas. The co-evolution of supermassive black holes and galaxies in luminous AGN over a wide range of redshift. A&A, 672:A98, Apr. 2023. doi: 10.1051/0004-6361/202345924.

G. Mountrichas, V. Buat, I. Georgantopoulos, G. Yang, V. A. Masoura, M. Boquien, and D. Burgarella. Galaxy properties of type 1 and 2 X-ray selected AGN and a comparison among different classification criteria. A&A, 653: A70, Sept. 2021. doi: 10.1051/0004-6361/202141273.

L. A. Mowla, P. van Dokkum, G. B. Brammer, I. Momcheva, A. van der Wel, K. Whitaker, E. Nelson, R. Bezanson, A. Muzzin, M. Franx, J. MacKenty, J. Leja, M. Kriek, and D. Marchesini. COSMOS-DASH: The Evolution of the Galaxy Size-Mass Relation since z $\sim$ 3 from New Widefield WFC3 Imaging Combined with CANDELS/3D-HST. ApJ, 880(1):57, July 2019. doi: 10.3847/1538-4357/ab290a.

E. J. Murphy, J. J. Condon, E. Schinnerer, R. C. Kennicutt, D. Calzetti, L. Armus, G. Helou, J. L. Turner, G. Aniano, P. Beirão, A. D. Bolatto, B. R. Brandl, K. V. Croxall, D. A. Dale, J. L. Donovan Meyer, B. T. Draine, C. Engelbracht, L. K. Hunt, C. N. Hao, J. Koda, H. Roussel, R. Skibba, and J. D. T. Smith. Calibrating Extinction-free Star Formation Rate Diagnostics with 33 GHz Free-free Emission in NGC 6946. ApJ, 737(2):67, Aug. 2011. doi: 10.1088/0004-637X/737/2/67.

K. Nandra, E. S. Laird, J. A. Aird, M. Salvato, A. Georgakakis, G. Barro, P. G. Perez-Gonzalez, P. Barmby, R. R. Chary, A. Coil, M. C. Cooper, M. Davis, M. Dickinson, S. M. Faber, G. G. Fazio, P. Guhathakurta, S. Gwyn, L. T. Hsu, J. S. Huang, R. J. Ivison, D. C. Koo, J. A. Newman, C. Rangel, T. Yamada, and C. Willmer. AEGIS-X: Deep Chandra Imaging of the Central Groth Strip. ApJS, 220(1):10, Sept. 2015. doi: 10.1088/0067-0049/220/1/10.

E. Nardini, E. Lusso, G. Risaliti, S. Bisogni, F. Civano, M. Elvis, G. Fabbiano, R. Gilli, A. Marconi, F. Salvestrini, and C. Vignali. The most luminous blue quasars at 3.0 ¡ z ¡ 3.3. I. A tale of two X-ray populations. A&A, 632:A109, Dec. 2019. doi: 10.1051/0004-6361/201936911.

N. P. H. Nesvadba, C. De Breuck, M. D. Lehnert, P. N. Best, and C. Collet. The SINFONI survey of powerful radio galaxies at z 2: Jet-driven AGN feedback during the Quasar Era. A&A, 599:A123, Mar. 2017. doi: 10.1051/0004-6361/201528040.

K. Nobuta, M. Akiyama, Y. Ueda, M. G. Watson, J. Silverman, K. Hiroi, K. Ohta, F. Iwamuro, K. Yabe, N. Tamura, Y. Moritani, M. Sumiyoshi, N. Takato, M. Kimura, T. Maihara, G. Dalton, I. Lewis, D. Bonfield, H. Lee, E. Curtis-Lake, E. Macaulay, F. Clarke, K. Sekiguchi, C. Simpson, S. Croom, M. Ouchi, H. Hanami, and T. Yamada. Black Hole Mass and Eddington Ratio Distribution Functions of X-Ray-selected Broad-line AGNs at z ~1.4 in the Subaru XMM-Newton Deep Field. ApJ, 761(2):143, Dec. 2012. doi: 10.1088/0004-637X/761/2/143.

K. Noguchi, Y. Terashima, Y. Ishino, Y. Hashimoto, M. Koss, Y. Ueda, and H. Awaki. Scattered X-rays in Obscured Active Galactic Nuclei and Their Implications for Geometrical Structure and Evolution. ApJ, 711(1): 144–156, Mar. 2010. doi: 10.1088/0004-637X/711/1/144.

K. Oh, M. Koss, C. B. Markwardt, K. Schawinski, W. H. Baumgartner, S. D. Barthelmy, S. B. Cenko, N. Gehrels, R. Mushotzky, A. Petulante, C. Ricci, A. Lien, and B. Trakhtenbrot. The 105-Month Swift-BAT All-sky Hard X-Ray Survey. ApJS, 235(1):4, Mar. 2018. doi: 10.3847/1538-4365/aaa7fd.

K. Oh, M. J. Koss, Y. Ueda, D. Stern, C. Ricci, B. Trakhtenbrot, M. C. Powell, J. S. den Brok, I. Lamperti, R. Mushotzky, F. Ricci, R. E. Bär, A. F. Rojas, K. Ichikawa, R. Riffel, E. Treister, F. Harrison, C. M. Urry, F. E. Bauer, and K. Schawinski. BASS. XXIV. The BASS DR2 Spectroscopic Line Measurements and AGN Demographics. ApJS, 261(1):4, July 2022. doi: 10.3847/1538-4365/ac5b68.

Y. Ono, M. Ouchi, K. Shimasaku, M. Akiyama, J. Dunlop, D. Farrah, J. C. Lee, R. McLure, S. Okamura, and M. Yoshida. Stellar populations of Lyα emitters at z = 3-4 based on deep large area surveys in the Subaru-SXDS/UKIDSS-UDS Field. MNRAS, 402(3):1580–1598, Mar. 2010. doi: 10.1111/j.1365-2966.2009.16034.x.

Y. Ono, M. Ouchi, Y. Harikane, J. Toshikawa, M. Rauch, S. Yuma, M. Sawicki, T. Shibuya, K. Shimasaku, M. Oguri, C. Willott, M. Akhlaghi, M. Akiyama, J. Coupon, N. Kashikawa, Y. Komiyama, A. Konno, L. Lin, Y. Matsuoka, S. Miyazaki, T. Nagao, K. Nakajima, J. Silverman, M. Tanaka, Y. Taniguchi, and S.-Y. Wang. Great Optically Luminous Dropout Research Using Subaru HSC (GOLDRUSH). I. UV luminosity functions at z $\sim$ 4-7 derived with the half-million dropouts on the 100 deg^2 sky. PASJ, 70:S10, Jan. 2018. doi: 10.1093/pasj/psx103.

F. Onori, F. La Franca, F. Ricci, M. Brusa, E. Sani, R. Maiolino, S. Bianchi, A. Bongiorno, F. Fiore, A. Marconi, and C. Vignali. Detection of faint broad emission lines in type 2 AGN - I. Near-infrared observations and spectral fitting. MNRAS, 464(2):1783–1832, Jan. 2017a. doi: 10.1093/mnras/stw2368.

F. Onori, F. Ricci, F. La Franca, S. Bianchi, A. Bongiorno, M. Brusa, F. Fiore, R. Maiolino, A. Marconi, E. Sani, and C. Vignali. Detection of faint broad emission lines in type 2 AGN - II. On the measurement of the black hole mass of type 2 AGN and the unified model. MNRAS, 468(1): L97–L102, June 2017b. doi: 10.1093/mnrasl/slx032.

M. Ouchi, K. Shimasaku, M. Akiyama, C. Simpson, T. Saito, Y. Ueda, H. Furusawa, K. Sekiguchi, T. Yamada, T. Kodama, N. Kashikawa, S. Okamura, M. Iye, T. Takata, M. Yoshida, and M. Yoshida. The Subaru/XMM-Newton Deep Survey (SXDS). IV. Evolution of Lyα Emitters from z = 3.1 to 5.7 in the 1 deg^2 Field: Luminosity Functions and AGN. ApJS, 176(2):301–330, June 2008. doi: 10.1086/527673.

C. Panagiotou and R. Walter. Reflection geometries in absorbed and unabsorbed AGN. A&A, 626:A40, June 2019. doi: 10.1051/0004-6361/201935052.

Y. C. Pei. Interstellar Dust from the Milky Way to the Magellanic Clouds. ApJ, 395:130, Aug. 1992. doi: 10.1086/171637.

E. Piconcelli, E. Jimenez-Bailón, M. Guainazzi, N. Schartel, P. M. Rodríguez-Pascual, and M. Santos-Lleó. The XMM-Newton view of PG quasars. I. X-ray continuum and absorption. A&A, 432(1):15–30, Mar. 2005. doi: 10.1051/0004-6361:20041621.

M. Pierre, F. Pacaud, C. Adami, S. Alis, B. Altieri, N. Baran, C. Benoist, M. Birkinshaw, A. Bongiorno, M. N. Bremer, M. Brusa, A. Butler, P. Ciliegi, L. Chiappetti, N. Clerc, P. S. Corasaniti, J. Coupon, C. De Breuck, J. Democles, S. Desai, J. Delhaize, J. Devriendt, Y. Dubois, D. Eckert, A. Elyiv, S. Ettori, A. Evrard, L. Faccioli, A. Farahi, C. Ferrari, F. Finet, S. Fotopoulou, N. Fourmanoit, P. Gandhi, F. Gastaldello, R. Gastaud, I. Georgantopoulos, P. Giles, L. Guennou, V. Guglielmo, C. Horellou, K. Husband, M. Huynh, A. Iovino, M. Kilbinger, E. Koulouridis, S. Lavoie, A. M. C. Le Brun, J. P. Le Fevre, C. Lidman, M. Lieu, C. A. Lin, A. Mantz, B. J. Maughan, S. Maurogordato, I. G. McCarthy, S. McGee, J. B. Melin, O. Melnyk, F. Menanteau, M. Novak, S. Paltani, M. Plionis, B. M. Poggianti, D. Pomarede, E. Pompei, T. J. Ponman, M. E. Ramos-Ceja, P. Ranalli, D. Rapetti, S. Raychaudury, T. H. Reiprich, H. Rottgering, E. Rozo, E. Rykoff, T. Sadibekova, J. Santos, J. L. Sauvageot, C. Schimd, M. Sereno, G. P. Smith, V. Smolčić, S. Snowden, D. Spergel, S. Stanford, J. Surdej, P. Valageas, A. Valotti, I. Valtchanov, C. Vignali, J. Willis, and F. Ziparo. The XXL Survey. I. Scientific motivations - XMM-Newton observing plan - Follow-up observations and simulation programme. A&A, 592:A1, June 2016. doi: 10.1051/0004-6361/201526766.

A. Poglitsch, C. Waelkens, N. Geis, H. Feuchtgruber, B. Vandenbussche, L. Rodriguez, O. Krause, E. Renotte, C. van Hoof, P. Saraceno, J. Cepa, F. Kerschbaum, P. Agnèse, B. Ali, B. Altieri, P. Andreani, J. L. Augueres, Z. Balog, L. Barl, O. H. Bauer, N. Belbachir, M. Benedettini, N. Billot, O. Boulade, H. Bischof, J. Blommaert, E. Callut, C. Cara, R. Cerulli, D. Cesarsky, A. Contursi, Y. Creten, W. De Meester, V. Doublier, E. Doumayrou, L. Duband, K. Exter, R. Genzel, J. M. Gillis, U. Grözinger, T. Henning, J. Herreros, R. Huygen, M. Inguscio, G. Jakob, C. Jamar, C. Jean, J. de Jong, R. Katterloher, C. Kiss, U. Klaas, D. Lemke, D. Lutz, S. Madden, B. Marquet, J. Martignac, A. Mazy, P. Merken, F. Montfort, L. Morbidelli, T. Müller, M. Nielbock, K. Okumura, R. Orfei, R. Ottensamer, S. Pezzuto, P. Popesso, J. Putzeys, S. Regibo, V. Reveret, P. Royer, M. Sauvage, J. Schreiber, J. Stegmaier, D. Schmitt, J. Schubert, E. Sturm, M. Thiel, G. Tofani, R. Vavrek, M. Wetzstein, E. Wieprecht, and E. Wiezorrek. The Photodetector Array Camera and Spectrometer (PACS) on the Herschel Space Observatory. A&A, 518:L2, July 2010. doi: 10.1051/0004-6361/201014535.

M. Polletta, M. Tajer, L. Maraschi, G. Trinchieri, C. J. Lonsdale, L. Chiappetti, S. Andreon, M. Pierre, O. Le Fèvre, G. Zamorani, D. Maccagni, O. Garcet, J. Surdej, A. Franceschini, D. Alloin, D. L. Shupe, J. A. Surace, F. Fang, M. Rowan-Robinson, H. E. Smith, and L. Tresse. Spectral Energy Distributions of Hard X-Ray Selected Active Galactic Nuclei in the XMM-Newton Medium Deep Survey. ApJ, 663(1):81–102, July 2007. doi: 10.1086/518113.

P. Popesso, A. Concas, G. Cresci, S. Belli, G. Rodighiero, H. Inami, M. Dickinson, O. Ilbert, M. Pannella, and D. Elbaz. The main sequence of star-forming galaxies across cosmic times. MNRAS, 519(1):1526–1544, Feb. 2023. doi: 10.1093/mnras/stac3214.

M. L. Prevot, J. Lequeux, E. Maurice, L. Prevot, and B. Rocca-Volmerange. The typical interstellar extinction in the Small Magellanic Cloud. A&A, 132:389–392, Mar. 1984.

A. E. Reines and M. Volonteri. Relations between Central Black Hole Mass and Total Galaxy Stellar Mass in the Local Universe. ApJ, 813(2):82, Nov. 2015. doi: 10.1088/0004-637X/813/2/82.

C. Ricci, R. Walter, T. J. L. Courvoisier, and S. Paltani. Reflection in Seyfert galaxies and the unified model of AGN. A&A, 532:A102, Aug. 2011. doi: 10.1051/0004-6361/201016409.

C. Ricci, F. E. Bauer, E. Treister, K. Schawinski, G. C. Privon, L. Blecha, P. Arevalo, L. Armus, F. Harrison, L. C. Ho, K. Iwasawa, D. B. Sanders, and D. Stern. Growing supermassive black holes in the late stages of galaxy mergers are heavily obscured. MNRAS, 468(2): 1273–1299, June 2017a. doi: 10.1093/mnras/stx173.

C. Ricci, B. Trakhtenbrot, M. J. Koss, Y. Ueda, I. Del Vecchio, E. Treister, K. Schawinski, S. Paltani, K. Oh, I. Lamperti, S. Berney, P. Gandhi, K. Ichikawa, F. E. Bauer, L. C. Ho, D. Asmus, V. Beckmann, S. Soldi, M. Baloković, N. Gehrels, and C. B. Markwardt. BAT AGN Spectroscopic Survey. V. X-Ray Properties of the Swift/BAT 70-month AGN Catalog. ApJS, 233(2):17, Dec. 2017b. doi: 10.3847/1538-4365/aa96ad.

C. Ricci, B. Trakhtenbrot, M. J. Koss, Y. Ueda, K. Schawinski, K. Oh, I. Lamperti, R. Mushotzky, E. Treister, L. C. Ho, A. Weigel, F. E. Bauer, S. Paltani, A. C. Fabian, Y. Xie, and N. Gehrels. The close environments of accreting massive black holes are shaped by radiative feedback. Nature, 549(7673):488–491, Sept. 2017c. doi: 10.1038/nature23906.

C. Ricci, G. C. Privon, R. W. Pfeifle, L. Armus, K. Iwasawa, N. Torres-Albà, S. Satyapal, F. E. Bauer, E. Treister, L. C. Ho, S. Aalto, P. Arévalo, L. Barcos-Muñoz, V. Charmandaris, T. Diaz-Santos, A. S. Evans, T. Gao, H. Inami, M. J. Koss, G. Lansbury, S. T. Linden, A. Medling, D. B. Sanders, Y. Song, D. Stern, V. U, Y. Ueda, and S. Yamada. A hard X-ray view of luminous and ultra-luminous infrared galaxies in GOALS - I. AGN obscuration along the merger sequence. MNRAS, 506(4):5935–5950, Oct. 2021. doi: 10.1093/mnras/stab2052.

C. Ricci, T. T. Ananna, M. J. Temple, C. M. Urry, M. J. Koss, B. Trakhtenbrot, Y. Ueda, D. Stern, F. E. Bauer, E. Treister, G. C. Privon, K. Oh, S. Paltani, M. Stalevski, L. C. Ho, A. C. Fabian, R. Mushotzky, C. S. Chang, F. Ricci, D. Kakkad, L. Sartori, R. Baer, T. Caglar, M. Powell, and F. Harrison. BASS XXXVII: The Role of Radiative Feedback in the Growth and Obscuration Properties of Nearby Supermassive Black Holes. ApJ, 938(1): 67, Oct. 2022. doi: 10.3847/1538-4357/ac8e67.

F. Ricci, F. La Franca, A. Marconi, F. Onori, F. Shankar, R. Schneider, E. Sani, S. Bianchi, A. Bongiorno, M. Brusa, F. Fiore, R. Maiolino, and C. Vignali. Detection of faint broad emission lines in type 2 AGNs - III. On the M_{BH}-$\sigma_\star$ relation of type 2 AGNs. MNRAS, 471 (1):L41–L46, Oct. 2017d. doi: 10.1093/mnrasl/slx103.

J. C. Runnoe, M. S. Brotherton, and Z. Shang. Updating quasar bolometric luminosity corrections - II. Infrared bolometric corrections. MNRAS, 426(4):2677–2688, Nov. 2012. doi: 10.1111/j.1365-2966.2012.21644.x.

A. Saintonge and B. Catinella. The Cold Interstellar Medium of Galaxies in the Local Universe. ARA&A, 60:319–361, Aug. 2022. doi: 10.1146/annurev-astro-021022-043545.

T. Saito, K. Shimasaku, S. Okamura, M. Ouchi, M. Akiyama, M. Yoshida, and Y. Ueda. Deep Spectroscopy of Systematically Surveyed Extended Lyα Sources at z ~3-5. ApJ, 675(2):1076–1094, Mar. 2008. doi: 10.1086/527282.

D. B. Sanders and I. F. Mirabel. Luminous Infrared Galaxies. ARA&A, 34:749, Jan. 1996. doi: 10.1146/annurev.astro.34.1.749.

M. Sawicki, S. Arnouts, J. Huang, J. Coupon, A. Golob, S. Gwyn, S. Foucaud, T. Moutard, I. Iwata, C. Liu, L. Chen, G. Desprez, Y. Harikane, Y. Ono, M. A. Strauss, M. Tanaka, N. Thibert, M. Balogh, K. Bundy, S. Chapman, J. E. Gunn, B.-C. Hsieh, O. Ilbert, Y. Jing, O. LeFèvre, C. Li, Y. Matsuda, S. Miyazaki, T. Nagao, A. J. Nishizawa, M. Ouchi, K. Shimasaku, J. Silverman, S. de la Torre, L. Tresse, W.-H. Wang, C. J. Willott, T. Yamada, X. Yang, and H. K. C. Yee. The CFHT large area U-band deep survey (CLAUDS). MNRAS, 489(4): 5202–5217, Nov. 2019. doi: 10.1093/mnras/stz2522.

E. F. Schlafly, D. P. Finkbeiner, M. Jurić, E. A. Magnier, W. S. Burgett, K. C. Chambers, T. Grav, K. W. Hodapp, N. Kaiser, R. P. Kudritzki, N. F. Martin, J. S. Morgan, P. A. Price, H. W. Rix, C. W. Stubbs, J. L. Tonry, and R. J. Wainscoat. Photometric Calibration of the First 1.5 Years of the Pan-STARRS1 Survey. ApJ, 756(2):158, Sept. 2012. doi: 10.1088/0004-637X/756/2/158.

D. J. Schlegel, D. P. Finkbeiner, and M. Davis. Maps of Dust Infrared Emission for Use in Estimation of Reddening and Cosmic Microwave Background Radiation Foregrounds. ApJ, 500(2):525–553, June 1998. doi: 10.1086/305772.

M. Schramm and J. D. Silverman. The Black Hole-Bulge Mass Relation of Active Galactic Nuclei in the Extended Chandra Deep Field-South Survey. ApJ, 767(1):13, Apr. 2013. doi: 10.1088/0004-637X/767/1/13.

A. Schulze, A. Bongiorno, I. Gavignaud, M. Schramm, J. Silverman, A. Merloni, G. Zamorani, M. Hirschmann, V. Mainieri, L. Wisotzki, F. Shankar, F. Fiore, A. M. Koekemoer, and G. Temporin. The cosmic growth of the active black hole population at 1 ¡z ¡2 in zCOSMOS, VVDS and SDSS. MNRAS, 447(3):2085–2111, Mar. 2015. doi: 10.1093/mnras/stu2549.

M. Scodeggio, L. Guzzo, B. Garilli, B. R. Granett, M. Bolzonella, S. de la Torre, U. Abbas, C. Adami, S. Arnouts, D. Bottini, A. Cappi, J. Coupon, O. Cucciati, I. Davidzon, P. Franzetti, A. Fritz, A. Iovino, J. Krywult, V. Le Brun, O. Le Fèvre, D. Maccagni, K. Małek, A. Marchetti,

F. Marulli, M. Polletta, A. Pollo, L. A. M. Tasca, R. Tojeiro, D. Vergani, A. Zanichelli, J. Bel, E. Branchini, G. De Lucia, O. Ilbert, H. J. McCracken, T. Moutard, J. A. Peacock, G. Zamorani, A. Burden, M. Fumana, E. Jullo, C. Marinoni, Y. Mellier, L. Moscardini, and W. J. Percival. The VIMOS Public Extragalactic Redshift Survey (VIPERS). Full spectroscopic data and auxiliary information release (PDR-2). A&A, 609:A84, Jan. 2018. doi: 10.1051/0004-6361/201630114.

K. Sekiguchi and SXDS Team. Subaru/XMM-Newton Deep Survey (SXDS). In *American Astronomical Society Meeting Abstracts*, volume 205 of *American Astronomical Society Meeting Abstracts*, page 81.05, Dec. 2004.

SERVS Team. Spitzer extragalactic representative volume survey, 2020. URL https://catcopy.ipac.caltech.edu/dois/doi.php?id=10.26131/IRSA407.

K. Setoguchi, Y. Ueda, Y. Toba, and M. Akiyama. Black Hole and Galaxy Coevolution in Moderately Luminous Active Galactic Nuclei at z $\sim$ 1.4 in SXDF. ApJ, 909(2): 188, Mar. 2021. doi: 10.3847/1538-4357/abdf55.

C. Simpson. The luminosity dependence of the type 1 active galactic nucleus fraction. MNRAS, 360(2):565–572, June 2005. doi: 10.1111/j.1365-2966.2005.09043.x.

C. Simpson, S. Rawlings, R. Ivison, M. Akiyama, O. Almaini, E. Bradshaw, S. Chapman, R. Chuter, S. Croom, J. Dunlop, S. Foucaud, and W. Hartley. Radio imaging of the Subaru/XMM-Newton Deep Field- III. Evolution of the radio luminosity function beyond z= 1. MNRAS, 421(4):3060–3083, Apr. 2012. doi: 10.1111/j.1365-2966.2012.20529.x.

M. F. Skrutskie, R. M. Cutri, R. Stiening, M. D. Weinberg, S. Schneider, J. M. Carpenter, C. Beichman, R. Capps, T. Chester, J. Elias, J. Huchra, J. Liebert, C. Lonsdale, D. G. Monet, S. Price, P. Seitzer, T. Jarrett, J. D. Kirkpatrick, J. E. Gizis, E. Howard, T. Evans, J. Fowler, L. Fullmer, R. Hurt, R. Light, E. L. Kopan, K. A. Marsh, H. L. McCallon, R. Tam, S. Van Dyk, and S. Wheelock. The Two Micron All Sky Survey (2MASS). AJ, 131(2): 1163–1183, Feb. 2006. doi: 10.1086/498708.

I. Smail, R. Sharp, A. M. Swinbank, M. Akiyama, Y. Ueda, S. Foucaud, O. Almaini, and S. Croom. A pilot survey for KX QSOs in the UKIDSS Ultra Deep Survey Field. MNRAS, 389(1):407–414, Sept. 2008. doi: 10.1111/j.1365-2966.2008.13579.x.

H. R. Stacey, T. Costa, J. P. McKean, C. E. Sharon, G. Calistro Rivera, E. Glikman, and P. P. van der Werf. Red quasars blow out molecular gas from galaxies during the peak of cosmic star formation. MNRAS, 517(3):3377–3391, Dec. 2022. doi: 10.1093/mnras/stac2765.

M. Stalevski, J. Fritz, M. Baes, T. Nakos, and L. Č. Popović. 3D radiative transfer modelling of the dusty tori around active galactic nuclei as a clumpy two-phase medium. MNRAS, 420(4):2756–2772, Mar. 2012. doi: 10.1111/j.1365-2966.2011.19775.x.

M. Stalevski, C. Ricci, Y. Ueda, P. Lira, J. Fritz, and M. Baes. The dust covering factor in active galactic nuclei. MNRAS, 458(3):2288–2302, May 2016. doi: 10.1093/mnras/stw444.

D. Stern. The X-Ray to Mid-infrared Relation of AGNs at High Luminosity. ApJ, 807(2):129, July 2015. doi: 10.1088/0004-637X/807/2/129.

H. Suh, F. Civano, G. Hasinger, E. Lusso, S. Marchesi, A. Schulze, M. Onodera, D. J. Rosario, and D. B. Sanders. Multi-wavelength Properties of Type 1 and Type 2 AGN Host Galaxies in the Chandra-COSMOS Legacy Survey. ApJ, 872(2):168, Feb. 2019. doi: 10.3847/1538-4357/ab01fb.

H. Suh, F. Civano, B. Trakhtenbrot, F. Shankar, G. Hasinger, D. B. Sanders, and V. Allevato. No Significant Evolution of Relations between Black Hole Mass and Galaxy Total Stellar Mass Up to z $\sim$ 2.5. ApJ, 889 (1):32, Jan. 2020. doi: 10.3847/1538-4357/ab5f5f.

M. Symeonidis and M. J. Page. AGN and star formation across cosmic time. MNRAS, 503(3):3992–4007, May 2021. doi: 10.1093/mnras/stab598.

L. J. Tacconi, R. Genzel, R. Neri, P. Cox, M. C. Cooper, K. Shapiro, A. Bolatto, N. Bouché, F. Bournaud, A. Burkert, F. Combes, J. Comerford, M. Davis, N. M. Förster Schreiber, S. Garcia-Burillo, J. Gracia-Carpio, D. Lutz, T. Naab, A. Omont, A. Shapley, A. Sternberg, and B. Weiner. High molecular gas fractions in normal massive star-forming galaxies in the young Universe. Nature, 463(7282):781–784, Feb. 2010. doi: 10.1038/nature08773.

L. J. Tacconi, R. Genzel, A. Saintonge, F. Combes, S. García-Burillo, R. Neri, A. Bolatto, T. Contini, N. M. Förster Schreiber, S. Lilly, D. Lutz, S. Wuyts, G. Accurso, J. Boissier, F. Boone, N. Bouché, F. Bournaud, A. Burkert, M. Carollo, M. Cooper, P. Cox, C. Feruglio, J. Freundlich, R. Herrera-Camus, S. Juneau, M. Lippa, T. Naab, A. Renzini, P. Salome, A. Sternberg, K. Tadaki, H. Übler, F. Walter, B. Weiner, and A. Weiss. PHIBSS: Unified Scaling Relations of Gas Depletion Time and Molecular Gas Fractions. ApJ, 853(2):179, Feb. 2018. doi: 10.3847/1538-4357/aaa4b4.

R. Tazaki and K. Ichikawa. Dust Destruction by Drift-induced Sputtering in Active Galactic Nuclei. ApJ, 892 (2):149, Apr. 2020. doi: 10.3847/1538-4357/ab72f6.

R. Tazaki, K. Ichikawa, and M. Kokubo. Dust Destruction by Charging: A Possible Origin of Gray Extinction Curves of Active Galactic Nuclei. ApJ, 892(2):84, Apr. 2020. doi: 10.3847/1538-4357/ab7822.

Y. Toba, S. Oyabu, H. Matsuhara, M. A. Malkan, D. Ishihara, T. Wada, Y. Ohyama, S. Takita, and C. Yamauchi. The 9 and 18 Micrometer Luminosity Functions of Various Types of Galaxies with AKARI: Implication for the Dust Torus Structure of AGN. PASJ, 65:113, Oct. 2013. doi: 10.1093/pasj/65.5.113.

Y. Toba, S. Oyabu, H. Matsuhara, M. A. Malkan, P. Gandhi, T. Nakagawa, N. Isobe, M. Shirahata, N. Oi, Y. Ohyama, S. Takita, C. Yamauchi, and K. Yano. Luminosity and Redshift Dependence of the Covering Factor of Active Galactic Nuclei viewed with WISE and Sloan Digital Sky Survey. ApJ, 788(1):45, June 2014. doi: 10.1088/0004-637X/788/1/45.

Y. Toba, Y. Ueda, P. Gandhi, C. Ricci, D. Burgarella, V. Buat, T. Nagao, S. Oyabu, H. Matsuhara, and B.-C. Hsieh. How Does the Polar Dust Affect the Correlation between Dust Covering Factor and Eddington Ratio in Type 1 Quasars Selected from the Sloan Digital Sky Survey Data Release 16? ApJ, 912(2):91, May 2021. doi: 10.3847/1538-4357/abe94a.

Y. Toba, T. Liu, T. Urrutia, M. Salvato, J. Li, Y. Ueda, M. Brusa, N. Yutani, K. Wada, A. J. Nishizawa, J. Buchner, T. Nagao, A. Merloni, M. Akiyama, R. Arcodia, B.-C. Hsieh, K. Ichikawa, M. Imanishi, K. T. Inoue, T. Kawaguchi, G. Lamer, K. Nandra, J. D. Silverman, and Y. Terashima. The eROSITA Final Equatorial-Depth Survey (eFEDS). A multiwavelength view of WISE mid-infrared galaxies/active galactic nuclei. A&A, 661:A15, May 2022. doi: 10.1051/0004-6361/202141547.

J. L. Tonry, C. W. Stubbs, K. R. Lykke, P. Doherty, I. S. Shivvers, W. S. Burgett, K. C. Chambers, K. W. Hodapp, N. Kaiser, R. P. Kudritzki, E. A. Magnier, J. S. Morgan, P. A. Price, and R. J. Wainscoat. The Pan-STARRS1 Photometric System. ApJ, 750(2):99, May 2012. doi: 10.1088/0004-637X/750/2/99.

M. Trebitsch, M. Volonteri, and Y. Dubois. Black hole obscuration and duty-cycles mediated by AGN feedback in high-redshift galaxies. MNRAS, 487(1):819–831, July 2019. doi: 10.1093/mnras/stz1280.

E. Treister and C. M. Urry. The Evolution of Obscuration in Active Galactic Nuclei. ApJ, 652(2):L79–L82, Dec. 2006. doi: 10.1086/510237.

E. Treister, C. M. Urry, and S. Virani. The Space Density of Compton-Thick Active Galactic Nucleus and the X-Ray Background. ApJ, 696(1):110–120, May 2009. doi: 10.1088/0004-637X/696/1/110.

Y. Ueda, M. Akiyama, K. Ohta, and T. Miyaji. Cosmological Evolution of the Hard X-Ray Active Galactic Nucleus Luminosity Function and the Origin of the Hard X-Ray Background. ApJ, 598(2):886–908, Dec. 2003. doi: 10.1086/378940.

Y. Ueda, M. Akiyama, G. Hasinger, T. Miyaji, and M. G. Watson. Toward the Standard Population Synthesis Model of the X-Ray Background: Evolution of X-Ray Luminosity and Absorption Functions of Active Galactic Nuclei Including Compton-thick Populations. ApJ, 786 (2):104, May 2014. doi: 10.1088/0004-637X/786/2/104.

C. M. Urry and P. Padovani. Unified Schemes for Radio-Loud Active Galactic Nuclei. PASP, 107:803, Sept. 1995. doi: 10.1086/133630.

M. Vaccari. The Spitzer Data Fusion: Contents, Construction and Applications to Galaxy Evolution Studies. In *The Many Facets of Extragalactic Radio Surveys: Towards New Scientific Challenges*, page 27, Oct. 2015. doi: 10.22323/1.267.0027.

C. van Breukelen, C. Simpson, S. Rawlings, M. Akiyama, D. Bonfield, L. Clewley, M. J. Jarvis, T. Mauch, T. Readhead, A.-M. Stobbart, M. Swinbank, and M. Watson. Evidence of a link between the evolution of clusters and their AGN fraction. MNRAS, 395(1):11–27, May 2009. doi: 10.1111/j.1365-2966.2009.14513.x.

A. van der Wel, M. Franx, P. G. van Dokkum, R. E. Skelton, I. G. Momcheva, K. E. Whitaker, G. B. Brammer, E. F. Bell, H. W. Rix, S. Wuyts, H. C. Ferguson, B. P. Holden, G. Barro, A. M. Koekemoer, Y.-Y. Chang, E. J. McGrath, B. Häussler, A. Dekel, P. Behroozi, M. Fumagalli, J. Leja, B. F. Lundgren, M. V. Maseda, E. J. Nelson, D. A. Wake, S. G. Patel, I. Labbé, S. M. Faber, N. A. Grogin, and D. D. Kocevski. 3D-HST+CANDELS: The Evolution of the Galaxy Size-Mass Distribution since z = 3. ApJ, 788 (1):28, June 2014. doi: 10.1088/0004-637X/788/1/28.

M. Vestergaard and P. S. Osmer. Mass Functions of the Active Black Holes in Distant Quasars from the Large Bright Quasar Survey, the Bright Quasar Survey, and the Color-selected Sample of the SDSS Fall Equatorial Stripe. ApJ, 699(1):800–816, July 2009. doi: 10.1088/0004-637X/699/1/800.

M. Vestergaard and B. M. Peterson. Determining Central Black Hole Masses in Distant Active Galaxies and Quasars. II. Improved Optical and UV Scaling Relationships. ApJ, 641(2):689–709, Apr. 2006. doi: 10.1086/500572.

B. Vijarnwannaluk, M. Akiyama, M. Schramm, Y. Ueda, Y. Matsuoka, Y. Toba, M. Sawicki, S. Gwyn, and J. Pflugradt. The Obscured Fraction of Quasars at Cosmic Noon. ApJ, 941(1):97, Dec. 2022. doi: 10.3847/1538-4357/ac9c07.

F. Vito, R. Gilli, C. Vignali, A. Comastri, M. Brusa, N. Cappelluti, and K. Iwasawa. The hard X-ray luminosity function of high-redshift (3 ¡ z $\lesssim$ 5) active galactic nuclei. MNRAS, 445(4):3557–3574, Dec. 2014. doi: 10.1093/mnras/stu2004.

F. Vito, R. Gilli, C. Vignali, W. N. Brandt, A. Comastri, G. Yang, B. D. Lehmer, B. Luo, A. Basu-Zych, F. E. Bauer, N. Cappelluti, A. Koekemoer, V. Mainieri, M. Paolillo, P. Ranalli, O. Shemmer, J. Trump, J. X. Wang, and Y. Q. Xue. The deepest X-ray view of high-redshift galaxies: constraints on low-rate black hole accretion. MNRAS, 463(1):348–374, Nov. 2016. doi: 10.1093/mnras/stw1998.

F. Vito, W. N. Brandt, G. Yang, R. Gilli, B. Luo, C. Vignali, Y. Q. Xue, A. Comastri, A. M. Koekemoer, B. D. Lehmer, T. Liu, M. Paolillo, P. Ranalli, D. P. Schneider, O. Shemmer, M. Volonteri, and J. Wang. High-redshift AGN in the Chandra Deep Fields: the obscured fraction and space density of the sub-L_* population. MNRAS, 473 (2):2378–2406, Jan. 2018. doi: 10.1093/mnras/stx2486.

K. Wada. Radiation-driven Fountain and Origin of Torus around Active Galactic Nuclei. ApJ, 758(1):66, Oct. 2012. doi: 10.1088/0004-637X/758/1/66.

K. Wada. Obscuring Fraction of Active Galactic Nuclei: Implications from Radiation-driven Fountain Models. ApJ, 812(1):82, Oct. 2015. doi: 10.1088/0004-637X/812/1/82.

K. Wada, M. Schartmann, and R. Meijerink. Multi-phase Nature of a Radiation-driven Fountain with Nuclear Starburst in a Low-mass Active Galactic Nucleus. ApJ, 828 (2):L19, Sept. 2016. doi: 10.3847/2041-8205/828/2/L19.

F. Wang, X.-B. Wu, X. Fan, J. Yang, W. Yi, F. Bian, I. D. McGreer, Q. Yang, Y. Ai, X. Dong, W. Zuo, L. Jiang, R. Green, S. Wang, Z. Cai, R. Wang, and M. Yue. A Survey of Luminous High-redshift Quasars with SDSS and WISE. I. Target Selection and Optical Spectroscopy. ApJ, 819(1):24, Mar. 2016. doi: 10.3847/0004-637X/819/1/24.

R. J. Williams, R. F. Quadri, M. Franx, P. van Dokkum, and I. Labbé. Detection of Quiescent Galaxies in a Bicolor Sequence from Z = 0-2. ApJ, 691(2):1879–1895, Feb. 2009. doi: 10.1088/0004-637X/691/2/1879.

R. Willingale, R. L. C. Starling, A. P. Beardmore, N. R. Tanvir, and P. T. O'Brien. Calibration of X-ray absorption in our Galaxy. MNRAS, 431(1):394–404, May 2013. doi: 10.1093/mnras/stt175.

K. Yabe, K. Ohta, F. Iwamuro, M. Akiyama, N. Tamura, S. Yuma, M. Kimura, N. Takato, Y. Moritani, M. Sumiyoshi, T. Maihara, J. Silverman, G. Dalton, I. Lewis, D. Bonfield, H. Lee, E. Curtis-Lake, E. Macaulay, and F. Clarke. The mass-metallicity relation at z $\sim$ 1.4 revealed with Subaru/FMOS. MNRAS, 437(4): 3647–3663, Feb. 2014. doi: 10.1093/mnras/stt2185.

S. Yamada, Y. Ueda, A. Tanimoto, M. Imanishi, Y. Toba, C. Ricci, and G. C. Privon. Comprehensive Broadband X-Ray and Multiwavelength Study of Active Galactic Nuclei in 57 Local Luminous and Ultraluminous Infrared Galaxies Observed with NuSTAR and/or Swift/BAT. ApJS, 257(2):61, Dec. 2021. doi: 10.3847/1538-4365/ac17f5.

T. Yamada, T. Kodama, M. Akiyama, H. Furusawa, I. Iwata, M. Kajisawa, M. Iye, M. Ouchi, K. Sekiguchi, K. Shimasaku, C. Simpson, I. Tanaka, and M. Yoshida. The Number Density of Old Passively Evolving Galaxies at z=1 in the Subaru/XMM-Newton Deep Survey Field. ApJ, 634(2):861–878, Dec. 2005. doi: 10.1086/496954.

G. Yang, M. Boquien, V. Buat, D. Burgarella, L. Ciesla, F. Duras, M. Stalevski, W. N. Brandt, and C. Papovich. X-CIGALE: Fitting AGN/galaxy SEDs from X-ray to infrared. MNRAS, 491(1):740–757, Jan. 2020. doi: 10.1093/mnras/stz3001.

L. Zappacosta, E. Piconcelli, M. Giustini, G. Vietri, F. Duras, G. Miniutti, M. Bischetti, A. Bongiorno, M. Brusa, M. Chiaberge, A. Comastri, C. Feruglio, A. Luminari, A. Marconi, C. Ricci, C. Vignali, and F. Fiore. The WISSH quasars project. VII. The impact of extreme radiative field in the accretion disc and X-ray corona interplay. A&A, 635:L5, Mar. 2020. doi: 10.1051/0004-6361/201937292.

H. Zhu, W. Tian, A. Li, and M. Zhang. The gas-to-extinction ratio and the gas distribution in the Galaxy. MNRAS, 471(3):3494–3528, Nov. 2017. doi: 10.1093/mnras/stx1580.

F. Zou, G. Yang, W. N. Brandt, and Y. Xue. The Host-galaxy Properties of Type 1 versus Type 2 Active Galactic Nuclei. ApJ, 878(1):11, June 2019. doi: 10.3847/1538-4357/ab1eb1.